Untersuchungen der Plasmamikrowellenwechselwirkung einer spezifischen Plasmaquelle zur Optimierung deren Einsetzbarkeit

Inauguraldissertation

zur

Erlangung des akademischen Grades eines

Doktors der Naturwissenschaften (Dr. rer. nat)

der

Mathematisch-Naturwissenschaftlichen Fakultät

der

Ernst-Moritz-Arndt-Universität Greifswald

vorgelegt von

Mathias Andrasch

geboren am 04. Oktober 1981

in Stralsund

Greifswald, den 16. Oktober 2014

Dekan:	Prof. Dr. Klaus Fesser
1. Gutachter:	Prof. Dr. Klaus-Dieter Weltmann
2. Gutachter:	Prof. Dr. Uwe Czarnetzki
Tag der Promotion:	21.04.2015

Inhaltsverzeichnis

1. Einleitung

Ein Gas, welches teilweise oder vollständig ionisiert ist, wird in der Physik als Plasma bezeichnet und macht 99 Prozent des sichtbaren Universums aus. Auf Grund der besonderen Eigenschaften von Plasmen entwickelten sich verschiedenste technologische Anwendungen. Diese reichen von der Materialbearbeitung, über die Lichterzeugung bis hin zur Sterilisation und therapeutischen Anwendungen [1, 2].

Um technologische Plasmen zu kategorisieren gibt es unterschiedlichste Ansätze. Eine Möglichkeit stellt dabei die Unterteilung nach der charakteristischen Anregungsfrequenz der elektrischen Energie dar, die in das Plasma zur Heizung eingekoppelt wird. Angefangen bei den am einfachsten zu realisierenden Frequenzen $0\ Hz$ (DC) und Wechselstrom (AC) bei $50\ Hz$ bzw. $60\ Hz$, die im Bereich der Bögen eine wichtige Rolle spielen, bis zum Ende des Niederfrequenzbereiches (NF) bei $100\ kHz$, in dem die Dielektrisch Behinderten Entladungen (DBE) betrieben werden. Bei einer weiteren Vergrößerung der Anregungsfrequenz muss im zunehmenden Maß der Wellencharakter elektromagnetischer Felder berücksichtigt werden, beispielsweise durch den Einsatz von Leitungssystemen mit wohldefinierten Wellenwiderständen. In diesem Bereich bis ca. $100\ MHz$ arbeiten sowohl induktiv und kapazitiv gekoppelte Plasmen als auch Radiofrequenz-Plasmajets. Diesen Entladungen gemeinsam ist, dass ihre Abmessungen klein im Vergleich zur korrespondierenden Wellenlänge der Anregungsfrequenz sind. Durch eine nochmalige Erhöhung der Anregungsfrequenz erreicht man ab ca. $1\ GHz$ den Bereich der Hochfrequenz (HF) und Mikrowellen[1], in dem der gesamte Wellencharakter der elektromagnetischen Felder bei der Wechselwirkung mit der Entladung zum Tragen kommt.

Diese Mikrowellenentladungen haben eine Vielzahl von Anwendungen. Neben klassischen industriellen Applikationen, wie Abscheiden, Ätzen, Funktionalisieren und Beschichten [3], sind vor allem Mikrowellenplasmen bei Normaldruck Gegenstand der aktuellen Forschung. Eine wichtige Rolle hierbei spielen Untersuchungen an umweltrelevanten Prozessen, wie die Reduktion von Stickstoffmonoxid (NO) [4, 5] oder der Abbau von flüchtigen organischen Verbindungen (VOC) [6] auch in halogener Form [7]. In diesem Zusammenhang wurde der Abbau von Methan zu Kohlenstoff und Wasserstoff mit Hilfe der katalytischen Eigenschaften von mikrowelleninduzierten Plasmen untersucht [8, 9]. Im Gegensatz dazu gab es auch Studien, die die Optimierung des Verbrennungsprozesses von Kohlenwasserstoffen [10, 11] zum Inhalt hatten. Im Hinblick auf die erneuerbaren Energien sei auf die Gewinnung von Wasserstoff durch die Dissoziation von Wasser mittels Mikrowel-

---

[1] Der Name ist als Steigerung von Langwelle Mittelwelle Kurzwelle über Ultrakurzwelle hin zur Mikrowelle zu verstehen und nicht auf die räumliche Ausdehnung bezogen, die im Bereich von Dezimetern bis hinunter zu Millimetern liegt.

lenplasmen [12] hingewiesen. Ein weiteres Anwendungsgebiet stellt die Materialbearbeitung (Schweißen, Brennen, Sintern) [13] dar. Das Spektrum möglicher Applikationen erstreckt sich bis hin zu therapeutischen Anwendungen im Bereich der Plasmamedizin [14].

1.1 Stand der Technik

Nach diesem Überblick über die möglichen Anwendungen von Atmosphärendruck Mikrowellenplasmaquellen soll dieser Abschnitt eine Übersicht über die unterschiedlichen Atmosphärendruck Mikrowellenplasmaquellen liefern, mit dem in Abbildung 1.1-1 vorangestellten Schema.

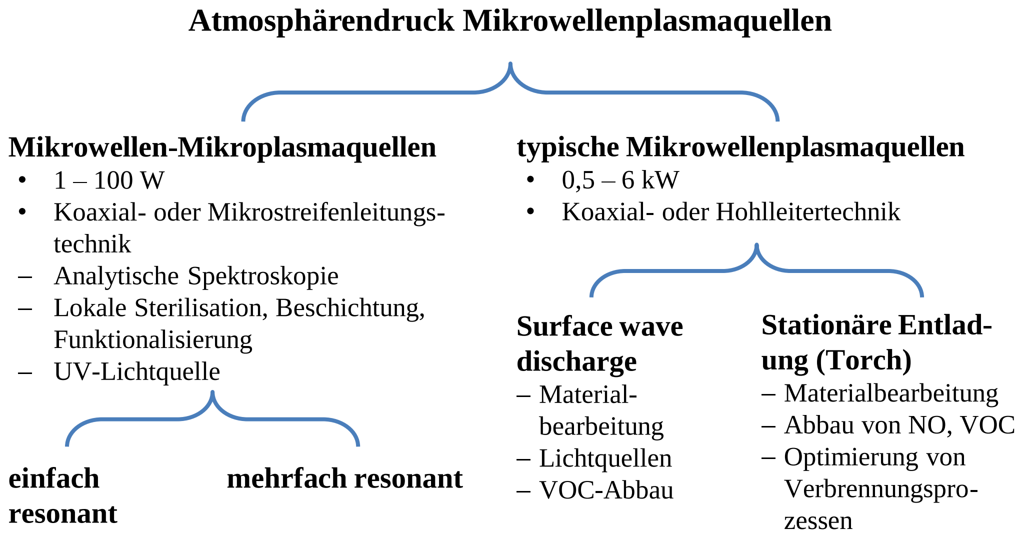

Abbildung 1.1-1 zeigt einen schematischen Überblick über Atmosphärendruck Mikrowellenplasmaquellen.

Als erstes seien die Mikrowellen-Mikroplasmen erwähnt, für die eine geringe umgesetzte Leistung ($1\,W - 100\,W$) typisch ist. Durch diesen geringen Leistungseintrag ist eine Abführung der thermischen Last ohne größeren technischen Aufwand möglich, was viel Raum für unterschiedliche technische Umsetzungen bietet. Kategorisieren lassen sich diese Mikrowellen-Mikroplasmen beispielsweise durch die Art ihrer Resonanzstruktur. Zum einen gibt es die einfach resonanten Systeme, bei denen eine Erhöhung der globalen Feldstärke um den Faktor 2 durch den Abschluss mit Leerlauf oder Kurzschluss erreicht wird. Überlagert man hierzu noch Kanten oder Spitzeneffekte können lokal Feldstärken erreicht werden, die eine Zündung des Plasmas bei Atmosphärendruck möglich machen. Beispiele für diese Entladungsform sind der „quarter-wavelength microwave slot resonator“ [15] und die „small surface wave discharge“[16], welche im Bereich der Analytischen Spektroskopie einsetzbar sind. Plasmaquellen die auf der Mikrostreifentechnologie [17-19] basieren, können unter anderem für die lokale Sterilisation, Beschichtung und Funktionalisierung innerhalb von schwer zugänglichen Strukturen eingesetzt werden.

Neben den einfach resonanten gibt es noch die mehrfach resonanten Systeme. Dabei können durch Mehrfachreflektionen globale Feldstärken größer als Faktor 2 erzielt werden. Es ist ebenfalls möglich zusätzliche lokale Feldstärkeüberhöhungen durch Kanten- und Spitzeneffekte zu realisieren. Diese Systeme können beispielsweise in Koaxialtechnik umgesetzt sein, wie bei Mikrowellen-Plasmajets [20-22] zur Oberflächenmodifikation, oder beim „small plasma torch“ [23] zur Analytischen Spektroskopie. Eine weitere Quelle dieser Kategorie ist der „re-entrant cavity applicator“[11], welcher zur Plasmaunterstützenden Verbrennung eingesetzt wird. Der Einsatz von Mikrostreifenleitungstechnik ist auch hier beim Design möglich, wie beispielsweise beim „microstrip split ring resonator“ [24, 25] zur Sterilisation oder der „microstrip-like transmission line“ [26, 27] als ultraviolette Lichtquelle.

Allen Mikrowellen-Mikroplasmaquellen gemeinsam ist, dass die von ihnen erzeugte Gesamtanzahl an Spezies, auf Grund des geringen Plasmavolumens, zu gering ist für die mit dieser Arbeit in Zusammenhang stehenden Applikationen. Deshalb liegt der Schwerpunkt bei den typischen Mikrowellenplasmen.

Diese setzen im Gegensatz zu den Mikrowellen-Mikroplasmen wesentlich mehr Spezies um, da sie auf Grund ihrer wesentlich höheren Leistung ($500\,W - 6\,kW$) ein erheblich größeres Plasmavolumen haben. Bei der Kategorisierung der unterschiedlichen Quellen gibt es verschiedene Ansätze, beispielsweise die Unterteilung nach Art der Einkopplung [28]. Ein allgemeinerer Ansatz ist dabei die Einteilung in die Gruppen der Wanderwellenentladung und der stationären Entladung [3].

Diese Wanderwellentladungen basieren in den meisten Fällen auf einem Oberflächenwelleneffekt und werden daher als „Surface wave discharges“ [29] bezeichnet. Das Funktionsprinzip beruht dabei auf einer besonderen Form der Mikrowellenplasmawechselwirkung. Ein Plasma wird durch ein dielektrisches Rohr, mit einer Dielektrizitätskonstante abweichend von der äußeren Umgebung, radial begrenzt. Die in dem Rohr angeregten Elektronendichten, mit einer Plasmafrequenz weit oberhalb der Anregungsfrequenz, formen einen Innenleiter. Zusammen mit dem Brechzahlsprung vom dielektrischen Rohr in der Umgebung entsteht in Wellenleitungssystem, in dem sich die anregende Mikrowelle weiter ausbreiten kann und so den Wechselwirkungsbereich zwischen Plasma und elektromagnetischer Welle vergrößert. Diese Entladungsform kann sowohl im Vakuum arbeiten [30-33], was eine Zündung der Entladung ohne weitere Hilfsmittel möglich macht, als auch bei Normaldruck [34-37]. Durch ihren großen Einsatzbereich hinsichtlich Druck und Leistung gibt es eine Vielzahl von Applikationen für die „Surface wave discharge“. Sie erstreckt sich von der Oberflächenbearbeitung, über Lichtquellen inklusive Laser, bis hin zur Gasaufbereitung (Abbau von VOC).

Die Gruppe der stationären Entladungen zeichnet sich dadurch aus, dass ihr Wechselwirkungsbereich durch die Geometrie des Resonators vorgegeben ist und sich im Verlauf der Entladungsdynamik nicht ändert. Auch hier kommt es zum Einsatz von dielektrischen Rohren, die aber die Funktion haben, die Gasströmung zu stabilisieren [4, 5, 7, 38-40] und kein zusätzliches Wellenleitersystem aufbauen. Entladungen, die auf den Einsatz eines solchen

Rohres verzichten, weisen meist ein sehr inhomogenes Plasma auf [10, 41]. Diese Entladungsform wird sowohl für die Materialbearbeitung als auch für den Abbau von NO und VOC eingesetzt. Des Weiteren kann sie zur Optimierung von Verbrennungsprozessen herangezogen werden.

Die hohe umgesetzte Leistung in den Mikrowellenquellen stellt besondere Anforderungen an die Abführung der thermischen Last, vor allem, wenn die Entladungen kontinuierlich betrieben werden. Häufig werden daher hohe Gasflüsse (bis 150 slm) oder Wasserkühlsysteme eingesetzt.

Der Vollständigkeit halber seien Entladungen in Mikrowellenöfen erwähnt [42], die sich zwar einfach umsetzen lassen, aber auf Grund ihrer Mehrmodigkeit nur begrenzt reproduzierbare Resultate liefern können. Des Weiteren ist es möglich, mit ausreichend großer Leistung (größer 1 MW) Mikrowellenplasmen bei Normaldruck im Freifeld zu erzeugen [43]. Diese Entladungen haben, auf Grund ihrer schlechten Reproduzierbarkeit oder der großen Leistung, nur geringes Applikationspotential.

1.2 Motivation der Arbeit

Die Forschung an mikrowelleninduzierten Atmosphärendruckplasmen am INP[1] begann 1997 mit Untersuchungen an einer stationären Entladung zur Reduktion von NO [4]. Daraus entwickelten sich Forschungsprojekte zu unterschiedlichen Anwendungsbereichen, dargestellt in Abbildung 1.2-1.

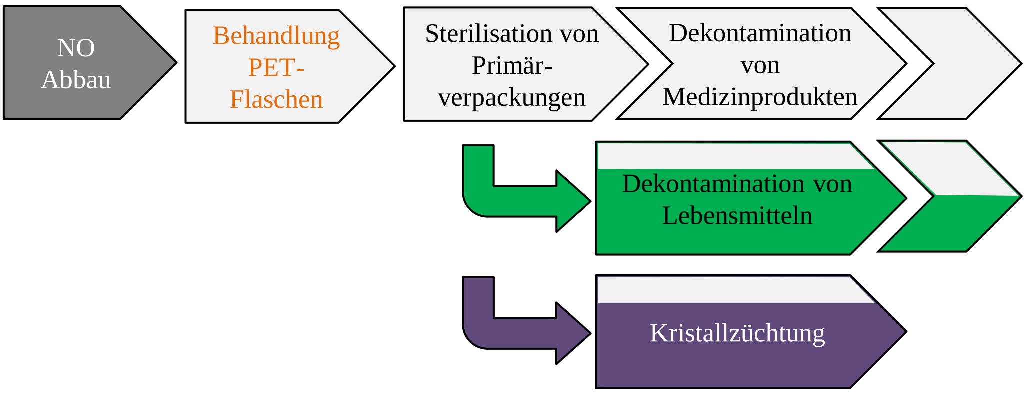

Abbildung 1.2-1 zeigt den zeitlichen Verlauf der Forschungsprojekte in den unterschiedlichen Anwendungsbereichen der Atmosphärendruck Mikrowellenplasmaquellen am INP.

Im Jahr 2003 begannen die Arbeiten an einer Mikrowellenlaufentladung [44] zum Einsatz an thermolabilen Materialen (PET[2] -Flaschen). Dabei stellt sich auf Grund der selbsttätigen Bewegung des Plasmas innerhalb des Mikrowellenreaktors, aus Sicht der Entladung ein, sehr großer Gasstrom ein. Zusammen mit den kurzen Prozesszeiten im Millisekundenbereich kann so die thermische Belastung der thermolabilen Materialien signifikant reduziert

---

[1] Leibniz Institut für Plasmaforschung und Technologie e. V.

[2] Polyethylenterephthalat

werden. Im Rahmen des BMBF-Projektes „Plasmose“ (FKZ 13N8666) wurden die mikrobiologische Wirksamkeit dieser Entladung an thermolabilen Primärverpackungen für pharmazeutische Produkte untersucht. Neben einer Optimierung der Entladung hinsichtlich Energieeinkopplung und des Zündverhaltens [45] konnten auch vielversprechende Resultate bei der Reduktion von Mikroorganismen im Bereich von bis zu sieben Größenordnungen erzielt werden [46]. Ein weiteres wichtiges Resultat war die Etablierung und der patentrechtliche Schutz einer resonanzabgleichsfreien Zündtechnologie für mikrowelleninduzierte Atmosphärendruckplasmen für Leistungen im Bereich von $2\ kW$ [47].

Auf Grund dieser vielversprechenden Resultate wurde in dem anschließenden BMBF-Projekt „Endoplas“ (FKZ 13N9320) unter anderem untersucht, inwieweit sich diese Entladung zur Dekontamination und Sterilisation von thermolabilen Medizinprodukten einsetzen lässt. Dabei wurde der Ansatz einer Separation der Entladung vom zu behandelnden Objekt verfolgt. Dies führt zur Entwicklung eines stationären Atmosphärendruck Mikrowellen-Torches (PLexc®) auf Grundlage der Zündtechnologie der Laufentladung [48]. Mithilfe dieser Entladung wurde an der Technologie eines plasmagenerierten Gas-Sterilisationsverfahrens gearbeitet, welches zur Zeit patentiert wird [49].

Darüber hinaus wurde im Rahmen des BMEL-Projektes „Friplas“ (FKZ 2816300707) untersucht, ob sich dieses Dekontaminationsverfahren auch auf Lebensmittel, beispielsweise Brassica Napus, übertragen lässt. Die erzielten Resultate [50] führten in der Folge zu einer weiteren Finanzierung der Forschung im Rahmen des BMBF-Projektes „SafeFresh“ (FKZ 13N12428).

Um die weitere Einsatzbarkeit der entwickelten Mikrowellenplasmatechnologie zu untersuchen wurde im Projekt „Kriplas“ (Senats Ausschusswettbewerb der Leibniz Gemeinschaft) in Zusammenarbeit mit dem IKZ[1] daran gearbeitet, ein plasmabasiertes Verfahren für die Züchtung von Galliumnitridkristallen (GaN) zu entwickeln [51]. Der neuartige Ansatz ist hierbei die Bereitstellung des notwendigen Stickstoffes mittels eines Plasmas. Das Vorhaben hat dahingehend eine große Bedeutung, dass GaN-Kristalle eine immer wichtigere Rolle in der Halbleiterindustrie spielen. Problematisch dabei ist, dass etablierte Verfahren zur Herstellung dieser GaN-Kristalle, wie die Hydridgasphasenepitaxie (HVPE) [52, 53], auf Grund ihrer geringen Wachstumsraten, nicht geeignet für die Züchtung von massiven Einkristallen sind.

Einige der aufgezeigten Applikationen weisen schon zum jetzigen Zeitpunkt ein hohes Potenzial der Realisierung im industriellen Maßstab auf. Trotz der kontinuierlichen Weiterentwicklung der Mikrowellenplasmaquelle in den letzten Jahren müssen sowohl die Quelle als auch die Prozesse dahingehend optimiert werden, dass die nötigen Stoffmengen mit hinreichender Stabilität zur Verfügung zu stellen. Des Weiteren müssen perspektivisch die Prozesse in den industriellen Maßstab skaliert werden. Damit diese Ziele erreicht werden

---

[1] Leibniz Institut für Kristallzüchtung

können, ist ein grundlegendes Verständnis der vorliegenden Mikrowellenplasmawechselwirkung, vor allem in der Aufbauphase des Volumenplasmas, unabdingbar.

1.3 Lösungsansatz

Auf Grund der Geometrie der Plasmaquelle, die einen entscheidenden Einfluss auf die elektromagnetische Feldverteilung hat, ist ein experimenteller Zugang zur Entladung nur begrenzt gegeben. Um den experimentellen Zugang zur Plasmaquelle zu vergrößern, wären starke konstruktive Änderungen notwendig, die wiederum einen nicht zu vernachlässigenden Effekt auf die Entladung selbst hätten. In [54] wurde gezeigt, dass es möglich ist, die Mikrowellenplasmawechselwirkung einer Argonentladung bei Normaldruck im Rahmen eines selbstkonsistenten, rotationssymmetrischen, zweidimensionalen, Fluidmodells zu simulieren. Daher scheint der Ansatz einer kombinierten Studie aus Experiment und Modell am geeignetsten.

Zu diesem Zweck muss das Modell dahingehend weiterentwickelt werden, dass auch die dynamischen Vorgänge zeitaufgelöst simuliert werden können. Dieser Teil der Arbeit wird in Zusammenarbeit mit Dr. Baeva durchgeführt. Das abschließende Ziel ist die Mikrowellenentladung unter ihren Einsatzbedingungen, Druckluft bei Atmosphärendruck, nachzubilden. Zuvor muss allerdings die Mikrowellenplasmawechselwirkung innerhalb der Quelle erfolgreich simuliert werden.

Die Entladung wird in Argon betrieben damit das Modell vereinfacht und angewendet werden kann. Um filamentierte Strukturen [55] zu vermeiden, die mithilfe eines zweidimensionalen, rotationssymmetrischen Modells nicht abgebildet werden können, muss die Entladung im Grobvakuum (ab $10\ mbar$) betrieben werden. Daraus folgt die Notwendigkeit der Anpassung und Entwicklung der bestehenden Plasmaquelle für den Einsatz unter den beschriebenen Bedingungen. Im Rahmen der geplanten Untersuchungen zur Züchtung von GaN-Kristallen, die sowohl auf Basis von vibrationsangeregten Stickstoffmolekülen [56] als auch auf Basis von atomarem Stickstoff [57] durchgeführt werden sollen, ist ebenfalls die Entwicklung der Mikrowellenplasmaquelle für einen Einsatz im Grobvakuum[1] geplant.

Neben den Arbeiten an der Plasmaquelle müssen diagnostische Methoden etabliert werden, um die Ergebnisse des Modells zu stützen und zu validieren. Die geplanten Untersuchungen fokussieren sich auf die Mikrowellenplasmawechselwirkung. Damit werden sowohl Methoden zur Charakterisierung des Plasmas als auch des Mikrowellenfeldes benötigt. Zu diesem Zweck wird zum einen die Elektronendichte im Afterglow der Entladung bestimmt, was keine störenden diagnostischen Zugänge an der Plasmaquelle bedingt. Zum anderen

---

[1] Durch die Druckreduzierung lassen sich die freien Weglängen vergrößern, um genügend atomaren Stickstoff am Ort des Kristallwachstums bereitzustellen.

wird die elektromagnetische Feldverteilung, im Inneren der Entladung mit Hilfe der Detektion von der hinein- und hinausläufenden Mikrowelle, ermittelt.

Um das Zusammenwirken der einzelnen Teilaspekte dieser Arbeit, mit den dazugehörigen Veröffentlichungen, zur Untersuchung der Plasmamikrowellenwechselwirkung, besser zu veranschaulichen sei auf Abbildung 1.3-1 verwiesen.

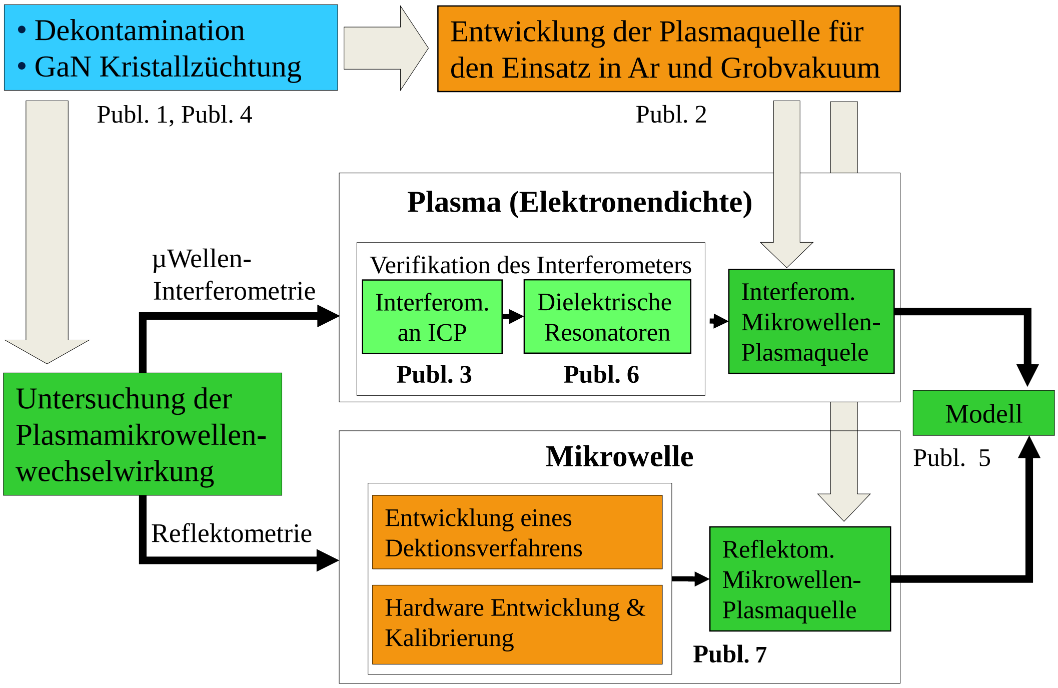

Abbildung 1.3-1 zeigt einen Überblick der einzelnen Arbeiten zur Untersuchung der Plasmamikrowellenwechselwirkung.

2. Experimenteller Teil und seine spezifischen Resultate

Die für die Untersuchung der Mikrowellenplasmawechselwirkung notwendigen experimentellen Arbeiten werden in diesem Kapitel beschrieben. Dies umfasst die Entwicklung der Plasmaquelle für den Einsatz im Grobvakuum, die Etablierung der Mikrowelleninterferometrie zur Elektronendichtebestimmung, sowie die Entwicklung, den Test und die Implementation eines heterodynen Reflektometers zur Charakterisierung des Mikrowellenfeldes. Dabei beinhalteten die diagnostischen Teile umfassende Diskussionen der methodenspezifischen Resultate basierend auf systematischen Untersuchungen zu diesen.

2.1 Die Plasmaquelle

Den Ausgangspunkt der Entwicklung der Mikrowellenplasmaquelle stellt die Zündtechnologie [47] und die darauf basierende Atmosphärendruck Plasmaquelle PLexc® dar. Es handelt sich dabei um eine koaxiale Struktur über die das Mikrowellenfeld mittels TEM-Welle geführt wird. Zur selbsttätigen Zündung des Plasmas befindet sich am Ende des Innenleiters eine resonante Struktur. Diese Plasmaquelle, wie in [48] beschrieben, kann aber nicht im Grobvakuum eingesetzt werden. Grund hierfür sind zum einen Probleme bei der Abführung der thermischen Last im Grobvakuum, zum anderen stellt der Transport der Mikrowellenleistung über die koaxiale Struktur ein enormes Problem dar. Durch den geringen Druck und der damit verringerten Isolationsfestigkeit kommt es zu parasitären Entladungen innerhalb der Plasmaquelle, die zur Zerstörung dieser führen.

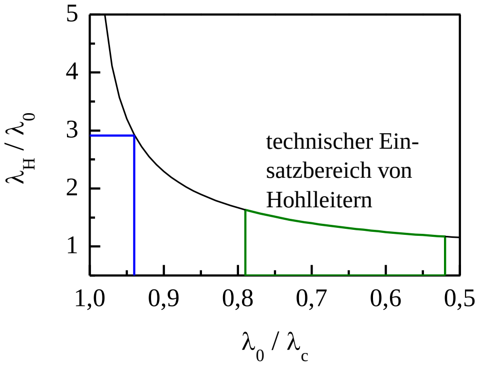

Abbildung 2.1-1 zeigt die Dispersionsrelation von Hohlleitern. Dabei ist in Grün der technische Einsatzbereich gekennzeichnet und in Blau die Dimensionierung des Reaktors.

Parallel wurde die Mikrowellenlaufentladung weiterentwickelt. Das Problem bestand darin, dass die optimale Behandlungsintensität bei der Dekontamination von PET-Flaschen mit einer Höhe von $168\,mm$, nicht erreicht werden konnte. Auf Grund des stehenden Wellenfeldes mit einem Abstand zwischen den Maxima von $\lambda_H/2 = 114{,}5\,mm$ innerhalb der Prozesskammer [45], kommt es zu einem inhomogenen Wärmeeintrag [58], der zur Verformung von Teilen der Flasche führt. Durch die Dimensionierung der Prozesskammer mit einem quadratischen Querschnitt der Kantenlänge $a = 92\,mm$ konnte die Wellenlänge des dominierenden Modus E_{11} um $55\,\%$ ($\lambda_H/2 = 177\,mm$) erhöht werden [59, 60], siehe Abbildung 2.1-1. Der Ansatz, einen Hohlleiter außerhalb des typischen Einsatzbereiches im Dispersionsmodus zu verwenden, konnte gewählt werden, da die verwendete Quelle (Magnetron *NL10250-18*; $2{,}455\,GHz$; $2\,kW$) relativ schmalbandig im Vergleich zur Dispersionsrelation des Hohlleiters ist. Da kleine Schwankungen im Frequenzspektrum der Quelle in diesem Design bereits einen großen Einfluss auf die elektromagnetische Feldverteilung in der Prozesskammer haben, ist eine weitere Verlängerung der Wellenlänge, im Hinblick auf die Stabilität der Entladung nicht sinnvoll. Die in diesem Zusammenhang in Kooperation mit Dr. Pipa durchgeführten zeitaufgelösten Untersuchungen zur Entladungsbildung [61], mittels Aufnahmen einer Hochgeschwindigkeitskamera zeigten, dass mit der zur Verfügung stehenden Technik ein Volumenplasma in Umgebungsluft bei Atmosphärendruck in ca. 5 ms erzeugt werden kann.

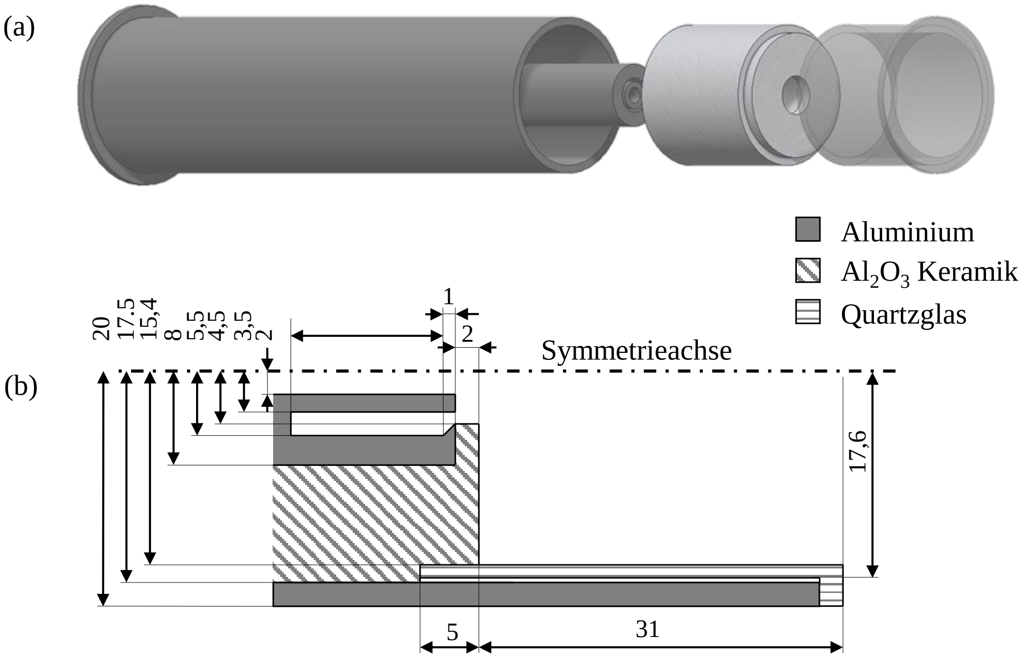

Abbildung 2.1-2 zeigt die schematische Darstellung der Mikrowellenplasmaquelle für den Einsatz im Grobvakuum. (a) stellt die verschiedenen baulichen Komponenten in einer Explosionsdarstellung dar. (b) zeigt den bemaßten Längsschnitt.

Basierend auf den Resultaten zur Entladungsbildung entstand der Ansatz zur Reduzierung der thermischen Belastung der Plasmaquelle. Durch die am INP entwickelten Magnetronnetzteile, mit Anstiegszeiten unterhalb von 50 μs und der Selbstzündung der Entladung, kann diese über einen weiten Bereich gepulst betrieben werden, der auch die komplette Neuzündung in jedem Zyklus einschließt [51]. Nach einem Mikrowellenpuls in der Größenordnung von 10 ms kann, durch die unbeschränkte Dauer der Pulspause, die abzuführende thermische Leistung reguliert werden. Dies eröffnet die Möglichkeit des Einsatzes von polymeerbasierten Dielektrika beim Design der Mikrowellenplasmaquelle, was wiederum zur Erhöhung der Durchschlagsfestigkeit im koaxialen Teil der Plasmaquelle führt.

Der für den Betrieb der Plasmaquelle benötigte Gasstrom wird axial durch den Innenleiter geführt, das Mikrowellenfeld koaxial dazu, siehe Abbildung 2.1-2. Da es keinen standardisierten HF-Verbinder mit Gasdurchführung gibt, kann nur ein Anschluss axial und demzufolge der andere nur radial ausgeführt werden. Aus konstruktiven Gründen wird der

Gaststrom axial zugeführt. Daher musste für die reflektionsarme Einkopplung des Mikrowellenfeldes eine radiale Koppelstelle entwickelt werden. Durch die Verwendung einer standardisierten 7/16-Buchse, kann die Plasmaquelle mit gebräuchlichen Mikrowellenkomponenten verbunden werden. Da das Innere der Koppelstelle Feldüberhöhungen aufweist und der Einsatz von Dielektrika auf Grund der komplizierten Geometrie extrem schwierig ist, muss dieser Teil zur Sicherstellung der Isolationsfestigkeit im Normaldruck arbeiten. An die Koppelstelle schließt sich, zur Führung der Mikrowellenleistung, die koaxiale Struktur an. In diesem Bereich erfolgt der Übergang ins Vakuum.

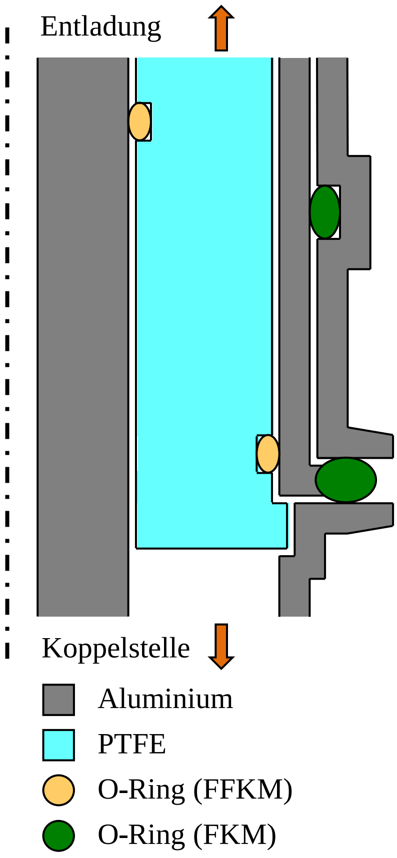

Abbildung 2.1-3 zeigt die schematische Darstellung der Mikrowellenvakuumdurchführung.

Da für die vorliegende koaxiale Struktur keine Mikrowellenvakuumdurchführung vorhanden ist, musste diese konzipiert werden. Dabei bestand die Herausforderung darin, den unterschiedlichen Anforderungen gleichzeitig gerecht zu werden. Zum einen soll das Mikrowellenfeld minimal gestört werden. Zum anderen muss die Entstehung von parasitären Entladungen unterdrückt werden und das ganze System ausreichend gasdicht sein.

Durch den Einsatz von PTFE[1] ($\varepsilon_r = 2{,}1$) als dielektrische Füllung, kann die Durchschlagsfestigkeit signifikant erhöht werden. Zwar führt das zu einer Reduktion des Leitungswellenwiderstandes von $Z_L = 48\ \Omega$ auf $Z_L = 33\ \Omega$, doch ist der Anteil der reflektierten Leistung an dieser Störstelle mit $3\ \%$ tolerierbar. Da PTFE, zum Aufbau von dauerhaft gasdichten Verbindungen, keine ausreichenden elastischen Eigenschaften hat, wurden zu diesem Zweck mehrere Kolben- und Stangendichtungen implementiert, dargestellt in Abbildung 2.1-3. Dabei wurden für den Einsatz im Mikrowellenfeld O-Ringe aus FFKM[2] gewählt, da sie ausreichend geringe dielektrische Verluste haben und bei Temperaturen von bis zu $260\ ^\circ C$ einsetzbar sind. Auf Grund der direkten Abhängigkeit des Leitungswellenwiderstands von den Durchmessern der leitenden koaxialen Struktur, wurden die Nuten für die Aufnahme der O-Ringe in die dielektrische Füllung integriert. Die Plasmaquelle wurde in ihrem Außendurchmesser so bemessen, dass sie kompatibel zum Vakuumflansch vom Typ *ISO KF DN 40* ist und über einen solchen Port in einen Reaktor integrierbar ist. Die Dichtung der Quelle in diesem äußeren Bereich wird mittels O-Ringen aus FKM[3] bewerkstelligt. Um die O-Ringe bei der

---

[1] Polytetrafluorethylen, Handelsname: Teflon

[2] Perfluorkautschuk, Handelsname: Perlast

[3] Fluorkautschuk, Handelsname: Viton

Montage nicht zu beschädigen, wurden für die Kolben- und Stangendichtungen Montagehilfen konzipiert.

Mit diesem Konzept ist es möglich, die Mikrowellenleistung aus dem Normaldruck zur Entladung im Grobvakuum zu führen, ohne parasitäre Entladungen und mit einer tolerierbaren Störung des Mikrowellenfeldes. Des Weiteren ist der Außenleiter der koaxialen Struktur so bemessen, dass der grundlegende Rundhohlleitermodus H_{11} am Ende der Quelle nicht ausbreitungsfähig ist. Das garantiert das Einhalten der Grenzwerte bezüglich Mikrowellenleckstrahlung (*DIN EN 60519-6*) im Havariefall eines nicht zündenden Plasmas.

2.2 Mikrowelleninterferometrie

Eine der wichtigsten Kenngrößen zur Charakterisierung eines Plasmas ist seine Elektronendichte, zu dessen Bestimmung eine Vielzahl an Methoden in den letzten Jahrzehnten entwickelt wurden [62]. Die am häufigsten verwendeten Methoden sind in Tabelle 2.2-1 zusammengetragen. Beginnend mit den Sondenmessungen, die weiter unterteilt werden können in Langmuir-Sonden und Mikrowellenresonanz-Sonden, die räumlich aufgelöste Elektronendichten bereitstellen. Allerdings sind diese Methoden invasiv und können auch nur bis leicht über die Grenzen des Feinvakuums hinweg eingesetzt werden ($10\,mbar$). Eine andere Möglichkeit, um räumlich aufgelöst Elektronendichten zu messen, ist die Thomson-Streuung [63], die zwar nicht invasiv, aber erst ab relativ hohen Elektrondichten einsetzbar ist. Dieses gilt auch für die Stark-Verbreiterung, die die Besonderheit hat, eine passive Methode zu sein. Die letzte aufgeführte Technik ist die Mikrowelleninterferometrie, welche linienintegrierte Resultate bereitstellt.

Methode	**Referenzen**	**n_e-Min**	**n_e-Max**	**Auflösung**	**Anmerkung**
Langmuir-Sonde	[64-66]	10^{8} m^{-3}	10^{18} m^{-3}	ortsaufgelöst	nur im Feinvakuum
Mikrowellenresonanzsonde	[67-70]	10^{14} m^{-3}	10^{18} m^{-3}	ortsaufgelöst	nur im Feinvakuum
Thomson-Streuung	[21, 71]	10^{18} m^{-3}		ortsaufgelöst	
Stark-Verbreiterung	[40, 72, 73]	10^{19} m^{-3}		linienintegriert	
Mikrowelleninterferometrie	[74-76]	10^{13} m^{-3}	10^{20} m^{-3}	linienintegriert	

Tabelle 2.2-1 gibt einen Überblick über die gängigen Methoden zur Elektronendichtebestimmung.

Auf Grund der am INP gesammelten Erfahrungen mit einem Festfrequenz-Interferometer ($150\,GHz$) [77] wurde nach alternativen Konzepten zum Aufbau eines Mikrowelleninterferometers gesucht. Ein vielversprechender Ansatz schien dabei, auf etablierte Hochfrequenzmesstechnik aus dem Bereich der Telekommunikationstechnik zurückzugreifen [78]. Zu diesem Zweck wurde ein Vektornetzwerkanalysator (VNA) des Typs *ZVA 50* der Firma Rohde & Schwarz angeschafft, um sowohl Festfrequenz- als auch frequenzaufgelöste Interferometer bis $50\,GHz$ zu implementieren. Die mit dieser Frequenz verknüpfte Freiraumwellenlänge ($\lambda_0 = 6\,mm$) bietet zwar nur begrenzte Ortsauflösung im Vergleich zu anderen Systemen [77, 79, 80], doch eröffnet sie die Möglichkeit des Einsatzes von flexiblen

Hochpräzisions-Koaxialkabeln (*ZV-Z97*). Im Gegensatz zu den erwähnten Systemen basierend auf Hohlleitern können mit den Koaxialkabeln einfacher und schneller unterschiedliche Interferometeraufbauten realisiert werden.

Um die Möglichkeiten des frequenzaufgelösten Mikrowelleninterferometers zu testen, wurden Untersuchungen an einer Fluoreszenzlampe gemacht, wobei sogar der Einfluss des Glasrohres der Lampe auf die Interferometrie untersucht werden konnte. Des Weiteren wurde ein Eintor-Interferometer zur Elektronendichtemessungen an einem Induktiv Gekoppelten Plasma (ICP) aufgebaut und die Resultate mit vorhandenen Langmuir-Sondenmessungen verglichen. Basierend auf den gesammelten Erkenntnissen wurde abschließend ein Zweitor-Interferometer für die Untersuchungen zur Mikrowellenplasmawechselwirkung aufgebaut.

2.2.1 Frequenzaufgelöste Mikrowelleninterferometrie

Um die Einsatzmöglichkeiten des VNA’s, sowie die der Antennen und Linsen zu testen und zu charakterisieren wurde ein frequenzaufgelöstes Mikrowelleninterferometer im Frequenzbereich zwischen $42{,}5\ GHz$ und $50\ GHz$ implementiert. Dabei ist die Einschränkung im Frequenzbereich durch die verwendeten korrugierten Hornantennen (Cernex *CCA22424820-XX*) bedingt. Für einen detaillierten Einblick in den experimentellen Aufbau und die erzielten Resultate wird auf [81] verwiesen, dennoch werden kurz die drei wichtigsten Experimente vorgestellt.

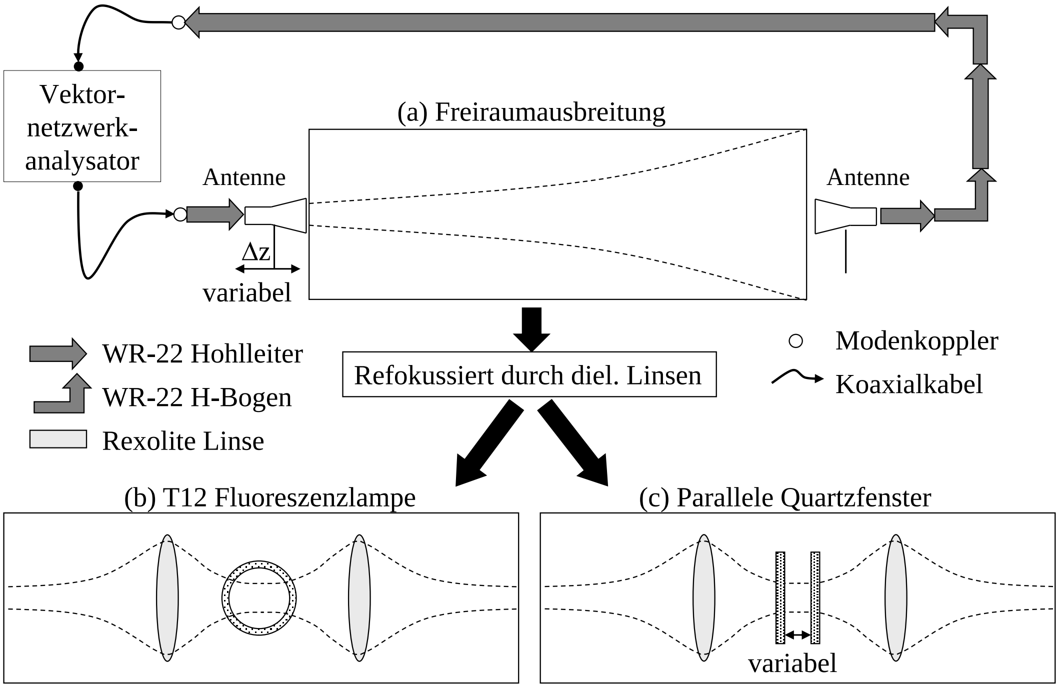

Abbildung 2.2-1 zeigt die Aufbauten zu den systematischen Untersuchungen des frequenzaufgelösten Mikrowellen-Interferometers. (a) stellt den Aufbau zur Längendetektion dar, wobei die Sendeantenne entlang der Ausbreitungsrichtung verschiebbar ist. (b) zeigt den Aufbau zur Messung an einer Fluoreszenzlampe und (c) die Experimente an zwei verschiebbaren Quartzfenstern.

Die Untersuchungen begannen mit einem Aufbau zur Messung der Phasendifferenz $\Delta\varphi$ hervorgerufen durch eine Verschiebung der Sendeantenne Δz, dargestellt in Abbildung 2.2-1 (a). Beide Antennen haben an der Ausgangsposition, der zur Referenzierung der Phasenlage genutzt wird, einen Abstand von etwa $0{,}7\ m$ zueinander. Für eine elektromagnetische Welle, die sich entlang der z-Achse im Freiraum ausbreitet, ergibt sich folgende frequenzabhängige (f) Phasendifferenz mit c_0 als Vakuumlichtgeschwindigkeit:

$$\Delta\varphi = \frac{2\pi}{c_0}\Delta z \cdot f \tag{1}$$

Nach der Entfernung der 2π-Phasensprünge und der additiven Anpassung, zur Gewährleistung der DC-Phasenbeziehung $\Delta\varphi(f = 0) = 0$ erhält man die absoluten Phasendifferenzen.

Durch simple Umstellung von Gleichung (1) lässt sich daraus $\Delta z(f)$ für die eingestellten Verschiebungen zwischen $10\ mm$ und $50\ mm$ ermitteln. Dies ist dargestellt in Abbildung 2.2-2. Es ist deutlich zu erkennen, dass die Phasendetektion und die daraus ermittelten Wegdifferenzen über den gesamten untersuchten Frequenzbereich hervorragend funktionieren. Allerdings ist eine kleine Störung[1] überlagert, die die minimale Phasenauflösung auf $250\ mrad$ begrenzt. Durch den Einsatz von Methoden der Digitalen Signal Verarbeitung (DSV) können die Störungen soweit unterdrückt werden, dass eine Auflösung von $2{,}5\ mrad$ erreicht wird.

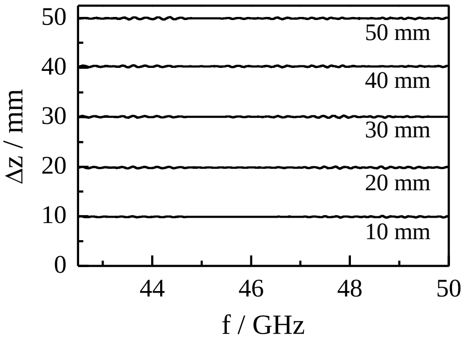

Abbildung 2.2-2 zeigt die Ergebnisse der Messungen zur Abstandsvariation zwischen den Antennen.

Im nächsten Schritt wurden dielektrische Linsen[2] zur Refokussierung in den Strahlengang eingefügt. Zur Minimierung von Reflexionen am Übergang zu den Linsen wurden definierte Rillen in die Oberfläche eingearbeitet [82], die als $\lambda/4$-Transformator fungieren. Im Fokus der Abbildung, mit einem errechneten minimalen Strahldurchmesser von $14{,}8\ mm$, wurde die positive Säule einer Fluoreszenzlampe[3] platziert. Hierbei wurde die Phasendifferenz zwischen ein- und ausgeschaltetem Plasma gemessen. Mit Hilfe der folgenden Gleichung wird dabei aus der ermittelten Phasendifferenz die Elektronendichte n_e ermittelt:

---

[1] Der Frequenzverlauf der Störungen ist sensibel zu Änderungen im Nahfeld der Antennen. Daher wird vermutet, dass die Störungen durch die korrugierten Hornantennen hervorgerufen werden.

[2] Hergestellt aus vernetztem Polystyrol, Handelsname: Rexolite

[3] Typ T12, Außendurchmesser $38\ mm$, mit einer Argon-Krypton-Füllung (90 zu 10) von $3{,}3\ mbar$ und $5\ mg$ Quecksilber

$$n_e = \frac{n_c \cdot \lambda \cdot \Delta\varphi}{\pi \int_{z_1}^{z_2} f(z) dz} \tag{2}$$

Da es sich um eine linienintegrierte Methode handelt, ist zur Interpretation die Kenntnis über die räumliche Verteilung $f(z)$ der Elektronendichte entlang des Interferometerstrahles notwendig. Auf Grund der radialen Symmetrie wird diese Verteilung als Bessel-Funktion der ersten Art und nullter Ordnung angenommen [83]:

$$f(z) = J_0\left(2{,}405 \left|\frac{z}{z_P}\right|\right) \tag{3}$$

Dabei ist $z_P = 17{,}7\ mm$, bedingt durch den Innenradius der Lampe. Durch die Annahme dieses Profils bezeichnet n_e die maximale Elektronendichte auf der Rotationsachse der Fluoreszenzlampe. Die Grenzdichte des Mikrowelleninterferometers n_c hängt primär von der verwendeten Frequenz ab und ist die theoretisch maximal detektierbare Elektronendichte[1]. Für genauere Details sei auf [81] verwiesen.

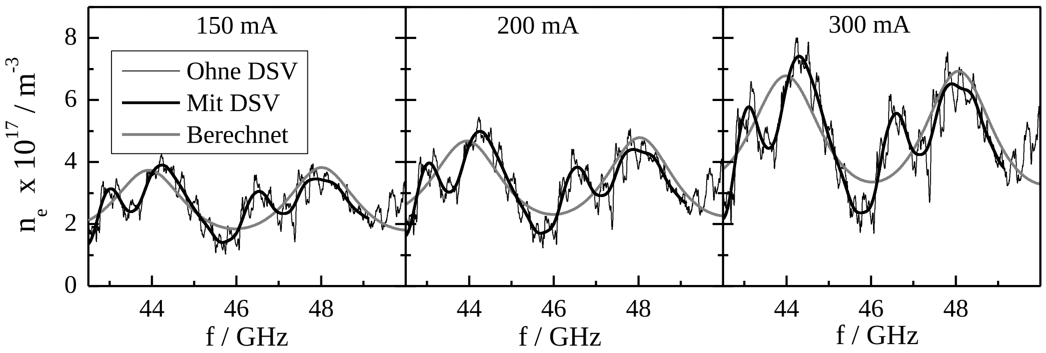

Abbildung 2.2-3 zeigt die frequenzabhängige gemessene Elektronendichte einer Fluoreszenzlampe im Vergleich zu den Ergebnissen eines Ersatzschaltbildes für verschiedene Lampenströme.

Betrachtet man die Resultate der frequenzaufgelösten Interferometermessung, so fallen die überlagerten Störungen auf, deren Einfluss mittels DSV signifikant reduziert wird, siehe Abbildung 2.2-3. Auch steigt die Elektronendichte mit dem Lampenstrom an. Entscheidend aber ist, dass die gemessene Elektronendichte nicht invariant gegenüber der Interferometerfrequenz ist und um bis zu 53 % von der frequenzgemittelten Elektronendichte abweicht.

Unter der Annahme, dass für diese Abweichung das Glasrohr der Fluoreszenzlampe verantwortlich ist, wird ein Modell entwickelt, um dessen Einfluss nachzubilden. Dabei werden zur Beschreibung der Übergänge der elektromagnetischen Welle aus dem Freiraum in das Glas Ersatzschaltungen aus dem Bereich der Hochfrequenztechnik verwendet. Die grundlegende Idee ist dabei, dass der Übergang aus dem Volumen 1 mit dem Wellenwiderstad $\underline{Z}_1$ in das Volumen 2 sich für die Welle als Abschluss mit einer fehlangepassten

---

[1] Im tatsächlichen Messeinsatz liegt diese Grenze um den Faktor $10 - 100$ niedriger, da zum einen die mathematischen Näherungen nicht mehr zutreffend sind und zum anderen das Plasma den Interferometerstrahl abzulenken beginnt.

Last $\underline{Z}_2$ darstellt, siehe Abbildung 2.2-4 (a). Die gleiche Methode wird für die Beschreibung des Überganges aus dem Volumen 2 heraus benutzt (Abbildung 2.2-4 (b)). Daraus lassen sich die Größen für Transmission und Reflektion ermitteln. Dabei müssen die Übergänge sowohl in als auch aus dem Volumen 2 derart kombiniert werden, dass die einzelnen Komponenten phasenrichtig addiert werden.

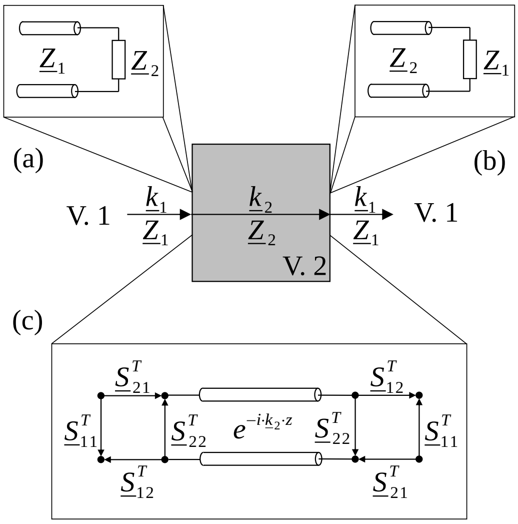

Abbildung 2.2-4 zeigt die Ersatzschaltungen zur Beschreibung der dielektrischen Umhüllung bei der Mikrowelleninterferometrie

Zu diesem Zweck wird jeder Übergang auf ein Zweitor mit dessen Streuparametern $\underline{S}_{ij}^T$ abgebildet und die Länge des Volumens 2 mithilfe einer verlustlosen Leitung berücksichtigt, dargestellt in Abbildung 2.2-4 (c). Durch Lösung des zugehörigen linearen Gleichungssystems lässt sich das System der vorderen dielektrischen Barriere auf ein Zweitor $\underline{S}_{ij}^B$ überführen. Durch eine nochmalige nummerische Kombination der resultierenden vorderen und hinteren Zweitore $\underline{S}_{ij}^B$ und der Einbeziehung der frequenzgemittelten Phasendrehung des Plasmas, kann das Transmissionsverhalten der Lampe nachgebildet werden.

Das Resultat dieses Modells ist in Abbildung 2.2-3 dargestellt, wobei ein geringer Frequenz-Offset[1] hinzugefügt wurde. Die gute Übereinstimmung hinsichtlich der Amplitude und der Periodizität der Abweichung ist zu erkennen. Daraus lässt sich schlussfolgern, dass die dielektrischen Eigenschaften des Glasrohres für die Frequenzvarianz bei der Elektronendichtemessung mittels Mikrowelleninterferometrie verantwortlich sind.

Um die Anwendbarkeit des Modells auch auf Amplitudenmessmethoden zu überprüfen, wurden die Untersuchungen durch Messungen an einem dielektrischen Resonator mit dem frequenzaufgelösten Interferometer abgeschlossen. Dabei wurden im Fokusbereich des Strahlenganges zwei Quarzfenster platziert, deren Abstand zueinander variiert werden kann, siehe Abbildung 2.2-1 (c). Auf Grundlage der Dimensionen und der Permittivität der Fenster wurden mit Hilfe des Modells ebenfalls die Transmissionseigenschaften ermittelt. Der Einfluss der Resonatoren ist in Abbildung 2.2-5 vergleichend dargestellt und zeigt eine sehr gute Überstimmung sowohl in Phase als auch Amplitude zwischen Messung und Modell. Damit ist das Modell auch in der Lage Fabry-Pérot-Interferenzen zu beschreiben, wie

---

[1] Die Modellannahmen vernachlässigen sowohl den Einfluss der Krümmung des Glasrohres als auch den der Wellenfronten. Daher ist der Frequenz-Offset zur Kompensation notwendig.

sie beispielsweise bei der Laserabsorptionsspektroskopie auftreten [84, 85]. Weiterführende Untersuchungen zur Verkippung eines Fensters [86] zeigten keine signifikante Reduktion der Resonatoreffekte.

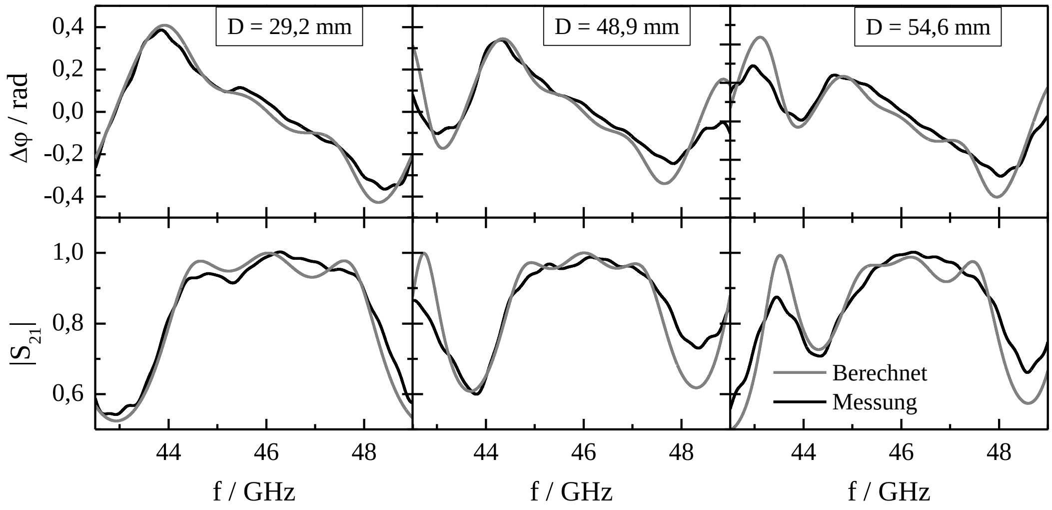

Abbildung 2.2-5 zeigt die frequenzabhängigen Transmissionseigenschaften eines dielektrischen Resonators aufgebaut aus zwei Quarzfenstern, positioniert mit verschiedenen Abständen zueinander.

2.2.2 Vergleichsmessungen an einem ICP

Um die Resultate des Mikrowelleninterferometers mit einer anderen Methode zur Elektronendichtebestimmung zu vergleichen, wird mit diesem an einem induktiv gekoppelten Plasma im Feinvakuum gemessen. Durch die vorhandene Datenbasis von ortsaufgelösten Langmuir-Sondenmessungen, die in Kooperation mit Dr. Harhausen entstanden sind, können die erzielten Resultate verglichen werden. Darüber hinaus bieten die Sondenmessungen einen direkten Zugang zur räumlichen Verteilung der Elektronendichte, um die Phasendifferenz nach Gleichung (2) zu interpretieren.

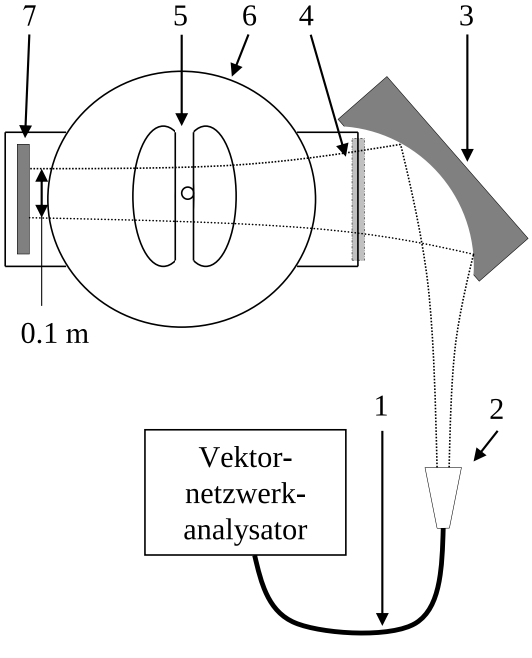

Abbildung 2.2-6 zeigt den experimentellen Aufbau des Eintor-Interferometers zur Messung an einer ICP. 1: Präzisions-Koaxialkabel, 2: Hornantenne, 3: elliptischer Spiegel, 4: Quarzfenster, 5: RF-Antenne, 6: Reaktor, 7: ebener Spiegel

Auf Grund der Möglichkeiten des VNA's hin- und rücklaufende Wellen voneinander zu trennen, kann trotz nur eines zugänglichen Ports am Reaktor, ein Interferometer aufgebaut werden. Dabei wird die vom VNA erzeugte elektromagnetische Welle über eine Hornantenne emittiert. Mittels eines elliptischen Spiegels wird sie dann umgelenkt und refokussiert. Durch die Platzierung eines weiteren ebenen Spiegels innerhalb des Reaktors im Fokus des Strahlenganges wird die einfallende Welle über den gleichen Weg bis hin zum VNA zurückreflektiert, dargestellt in Abbildung 2.2-6. Dieses zweimalige Passieren des Plasmas, wird mit einem Faktor 2 in Gleichung (2) berücksichtigt. Um den Einfluss des Quarzfensters, der im Detail im vorangegangenen Kapitel beschrieben wurde, auf die Phasenmessung zu minimieren, wurde dieses ausgebaut und seine Transmissionseigenschaften ermittelt. In einem Frequenzbereich um $45{,}75\ GHz$ hat das Fenster minimale Reflektion, wegen seines ganzzahligen Vielfaches von $\lambda/2$ [1]. Für weitere Details sowohl zum Experiment, als auch zu den Ergebnissen sei auf [87] verwiesen.

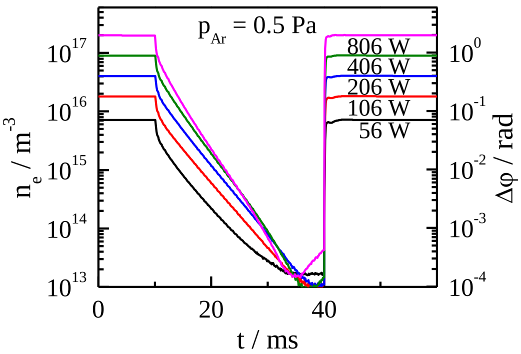

Abbildung 2.2-7 zeigt die zeitliche Entwicklung der Elektronendichte des An-Aus-Modulierten ICP’s.

Im Gegensatz zu den frequenzaufgelösten Messungen an der Fluoreszenzlampe stand hier die Untersuchung der zeitlichen Entwicklung der Elektronendichte des ICP‘s im Vordergrund. Durch die An-Aus-Modulation des Plasmas mit einer Periodendauer von $60\ ms$ konnte dessen Verlauf während des Aus-Zyklus über einen großen Dynamikbereich untersucht werden, dargestellt in Abbildung 2.2-7.

Die zeitliche Entwicklung lässt sich dabei in fünf Phasen unterteilen, beginnend mit dem eingeschwungenen Zustand der An-Phase, deren Werte für verschiedene Leistungen und Drücke in Abbildung 2.2-8 (b) dargestellt sind. Neben der Zunahme der Elektronendichte mit dem Druck p sind unterschiedliche Abhängigkeiten von der Leistung P zu erkennen. Dieses ist auf den Wechsel des Kopplungsmodus des ICP’s zurückzuführen, der sich von einer typischerweise induktiven zu einer kapazitiven Kopplung ändert [88]. Dieser Wechsel zwischen beiden Modi weist sogar bei einem Druck von $p = 0{,}1\ Pa$ einen Hysterese-Effekt auf. Diese Hysterese ist auf nicht lineare Effekte, sowohl in der Absorption der Leistung als auch in der Umsetzung der Leistung in Ionisation, zurückzuführen [89].

Der Vergleich mit den Ergebnissen der Langmuir-Sonde, bei einem Druck von $0{,}5\ Pa$, zeigt einen Unterschied von ca. dem Faktor 2 zur detektierten der Elektronendichte des Mikrowelleninterferometers. Dieser Unterschied ist auch von anderen gemessen worden [90] und seine Ursache ist bis zum jetzigen Zeitpunkt nicht hinreichend geklärt. Doch sei darauf hingewiesen, dass die Übereinstimmung bis auf den Faktor 2 bei der Bestimmung der Elektronendichte ein sehr gutes Ergebnis ist.

---

[1] Durch die Anpassung der Messfrequenz entfällt die Verwendung definiert dicker Fenster.

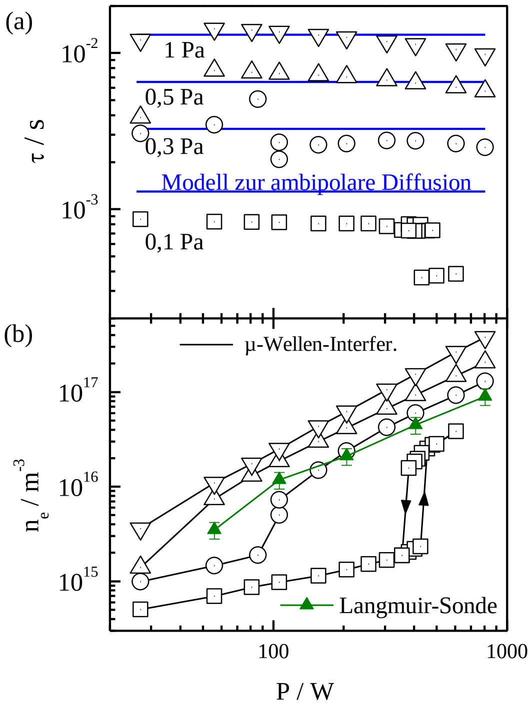

Abbildung 2.2-8 zeigt die Ergebnisse der Elektronendichtemessungen an dem ICP. (a) zeigt die experimentell ermittelten Zeitkontenstange des Abfalls in Aus-Phase im Vergleich zu einem Diffusionsmodell. (b) zeigt die Elektronendichte der An-Phase.

Bezüglich der folgenden Phasen der zeitlichen Entwicklung schließt an die An-Phase ein Übergangsbereich an, dem ein exponentielles Abfallen der Elektronendichte folgt. Für diesen Bereich wurde die Abklingkonstante τ bestimmt und mit den Ergebnissen eines analytischen, ambipolaren Diffusionsmodells verglichen. Dieses Modell löst die partielle Differentialgleichung der Diffusion in Zylinderkoordinaten, mittels des Ansatzes der Separation in drei Ortsfunktionen und eine Zeitfunktion. Durch die Thermalisierung der Ionen mit dem Neutralgas [91] und die schnelle Abkühlung der Elektronen[1] zu Beginn der Aus-Phase können die Temperaturen (T) als annähernd gleich betrachtet werden. Das führt zur Gleichung (4), wobei m_i die atomare Masse der Argonionen und δ den Stoßquerschnitt zwischen den Argonionen und Argonatomen bezeichnet. Die Boltzmann-Konstante ist mit k_B benannt. Die Konstanten a und c beziehen sich auf die Geometrie des Reaktors. Unter der Annahme einer Temperatur von $T = 470\ K$ [92] ergeben sich für die untersuchten Drücke die in Abbildung 2.2-8 (a) dargestellten Abklingkonstanten. Es ist deutlich erkennbar, dass die Ergebnisse zwischen Messung und Modell für Drücke oberhalb von 0,1 Pa sehr gut übereinstimmen.

$$\tau = \frac{3\ln(10)}{a^2 + c^2}\sqrt{\frac{\pi m_i \delta^2}{8k_B^3}}\frac{p}{T^{3/2}} \tag{4}$$

An den Bereich des exponentiellen Abfalls, der über die Grenzen des Auflösungsvermögens des Interferometers hinausgeht, schließt sich der dynamische Bereich des An-Zyklus an. Durch die gute Übereinstimmung im Vergleich der absolut gemessenen Elektronendichten mit den Sondenmessungen und der Abklingkonstanten wird die Funktionsweise des Mikrowellen-Interferometers als verifiziert betrachtet.

---

[1] Der Übergangsbereich am Anfang der Aus-Phase, beginnt sehr steil durch die hohe Elektronentemperatur. Im Anschluss wird der Anstieg dann aber in Folge der Abkühlung der Elektronen flacher.

2.3 Reflektometrie

Die Entwicklung des Magnetrons machte es möglich, elektromagnetische Strahlung im Mikrowellenbereich kostengünstig zu erzeugen, was wiederum zu diversen Anwendungen führte. Beispielsweise seien die Erwärmung unterschiedlicher Materialien [93], oder das Betreiben vom Mikrowellenplasmaquellen (1.1 Stand der Technik) erwähnt. Beiden Anwendungen gemeinsam ist der Fakt, dass zur maximalen Energieeinkopplung die Impedanz der Last auf die der Quelle angepasst werden muss. Für den Fall von zeitinvarianten Lasten werden dafür typischerweise Hohlleiterkomponenten wie E-H-Tuner oder Stab-Tuner benutzt, deren Einstellungen bis zum Erreichen der minimalen reflektierten Leistung variiert werden. Zu diesem Zweck muss mindestens der Absolutwert der hin-und rücklaufende Welle ermittelt werden [12, 13, 39, 94]. Dies ermöglicht gleichzeitig eine simple Form der Mikrowellenprozessüberwachung. Ist allerdings der komplexe Reflektionskoeffizient erforderlich, muss die hin- und rücklaufende Welle phasenaufgelöst detektiert werden. Für Anwendungen im Milliwatt-Bereich kann anstelle des Magnetrons direkt ein VNA eingesetzt werden, um sowohl die Impedanz der Last als auch die Güte der Anpassung zu detektieren [95, 96]. Ist die Bestimmung der Impedanz allerdings im Kilowatt-Bereich erforderlich, ist der Einsatz eines solch präzisen Messgerätes nicht länger möglich. Dennoch kann zumindest die zugrundeliegende Messmethode genutzt werden [97], um ein heterodynes Reflektometer zu entwickeln. Dieser Ansatz ist weit komplizierter als die skalare Detektion auf der Grundlage von gleichrichtenden Dioden, doch liefert sie alle benötigten komplexen Informationen mit einer hohen Zeitauflösung [98]. Ist diese hohe Zeitauflösung nicht erforderlich, so gibt es verschiedene Methoden, um aus skalaren Messungen den komplexen Reflektionskoeffizienten zu rekonstruieren [99, 100]. Des Weiteren ist es möglich, für Lasten, die einen Kurzschlussschieber beinhalten, den komplexen Reflektionsfaktor durch die Variation des Kurzschlussschiebers zur ermitteln [37]. Darüber hinaus gibt es die sogenannte 6-Port-Technik, die auf Basis der Detektion von vier skalaren Werten funktioniert [101-104].

Auf Grund der vorliegenden Anforderungen, bedingt sowohl durch die Mikrowellen- als auch die Plasmaquelle, ist ein heterodynes Reflektometer mit einer robusten Detektion erforderlich. Zu diesem Zweck wurde zum einen die Schaltungstechnik für einen Amplitudenmodulator und des Weiteren die Algorithmen für die Signalverarbeitung entwickelt. Zur Ermittlung der erreichbaren Auflösung des Messsystems und zum Nachweis der korrekten Funktion wurden abschließend verschiedene Testmessungen durchgeführt. Diese Thematiken, die Entwicklung und Testung, werden in den nächsten beiden Abschnitten kurz zusammengefasst. Für weiterführende Informationen sei auf [105] verwiesen.

2.3.1 Messtechnischer Ansatz

Zur Separation von hin- und rücklaufender Welle, der eingesetzten Mikrowellenquelle, ist ein Richtkoppler nachgeschaltet. Durch einen Koppelfaktor von 60 dB werden die Signalpegel aus dem Kilowatt-Bereich an die üblichen Pegel in der Messtechnik im Milliwatt-Bereich angepasst. Die so gewonnenen Signale könnten prinzipiell mittels eines analogen oder digitalen Detektionssystem ausgewertet werden, doch sind dafür Bandbreiten von mindestens 2,5 GHz und Abtastraten von 5 $GSample/s$ erforderlich. Dies ist zwar mit heutigen zur Verfügung stehenden Systemen umsetzbar, allerdings in Anbetracht der zu erwartenden Bandbreiten nicht sinnvoll. Beispielsweise begrenzt die Bandbreite des Richtkopplers von ca. 100 MHz die möglichen zeitlichen Änderungen. Daher werden die Signale von der Arbeitsfrequenz des Magnetrons (ca. 2,455 GHz) auf eine Zwischenfrequenz (ZF) umgesetzt, dessen technische Zugänglichkeit wesentlich einfacher ist.

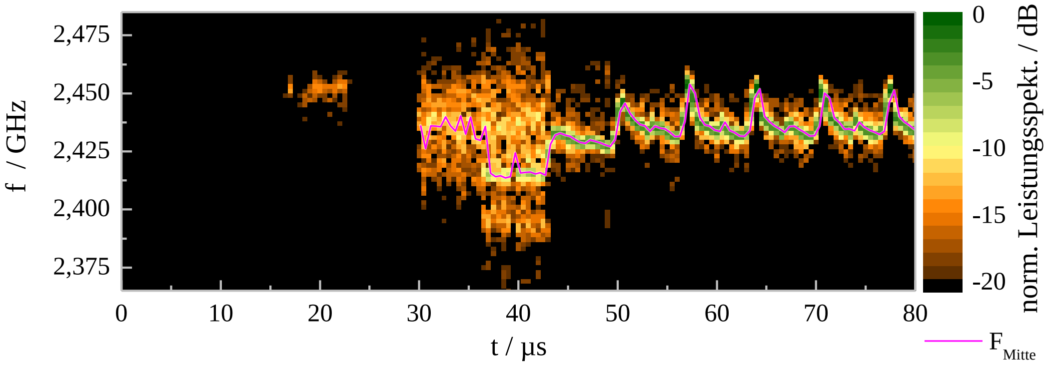

Abbildung 2.3-1 zeigt das zeitaufgelöste Spektrum des Einschwingverhaltens der Mikrowellenquelle und den Verlauf der Mittenfrequenz.

Zu diesem Zweck wurde ein Amplitudenmodulator entwickelt, dessen Lokaloszillator, implementiert mittels Frequenzsynthesizer (*TLSD05003000-100K*), in einem Bereich von 500 MHz bis 3 GHz frei einstellbar ist. Durch die Wahl der Breitbandmischer (*ZEM-4300*) kann das Modulationssystem auch für andere Anwendungen, beispielsweise 915 MHz-Technik eingesetzt werden. Auf Grundlage dieses Modulationssystems wurde im ersten Schritt das Einschaltverhalten der Mikrowellenquelle untersucht, um den Einsatz von möglichen Detektionsverfahren zu bewerten.

Dazu wurde das modulierte Signal abgetastet und für jedes Zeitfenster von 0,5 μs das Spektrum mittels diskreter Fourier-Transformation ermittelt, dargestellt in Abbildung 2.3-1. Da die typischen Zeitskalen des Einschwingens eines Magnetrons in der Größenordnung von 100 ns liegen [106], ist das gemessene Verhalten hauptsächlich durch die zum Treiben des Magnetrons verwendete Spannungsversorgung bedingt. Das Einschalten der Quelle lässt sich dabei in drei Phasen unterteilen. Die ersten 30 μs sind durch eine Totzeit des Systems geprägt. Daran schließt sich eine Übergangsphase von 13 μs an, die, auf Grund der geringen Ausgangsleistung, zu einem sehr breiten und verschmierten Spektrum führt. Zum Zeitpunkt von 43 μs beginnt die dritte Phase der eingeschwungene Zustand. Die verwendete Spannungsversorgung kann zu diesem Zeitpunkt genügend Leistung zum Treiben des Magnetrons zur Verfügung stellen, wodurch das Spektrum schmalbandiger wird. Erwähnt sei, dass es sich bei dem verwendeten Netzteil um einen Vollbrücken-Gegentaktwandler mit einer Schaltfrequenz von $150\ kHz$ handelt, der auf schnelle Anstiegszeiten optimiert wurde. Dadurch ist die Schaltfrequenz eindeutig im Spektrum der dritten Phase erkennbar. Diese Rückwirkung des treibenden Stromes auf die Mittenfrequenz des Magnetrons wird als „frequency pushing" bezeichnet [107, 108]. Des Weiteren wurde die Anwendbarkeit des Bunnemann-Frequenzschätzers [109] zur Ermittlung der Mittenfrequenz getestet und als einsetzbar bewertet. Auf Grund der hohen Dynamik der Frequenz der Mikrowellenquelle müssen sehr robuste Detektionsverfahren angewendet werden, um den zeitaufgelösten komplexen Reflektionsfaktor verlässlich zu ermitteln.

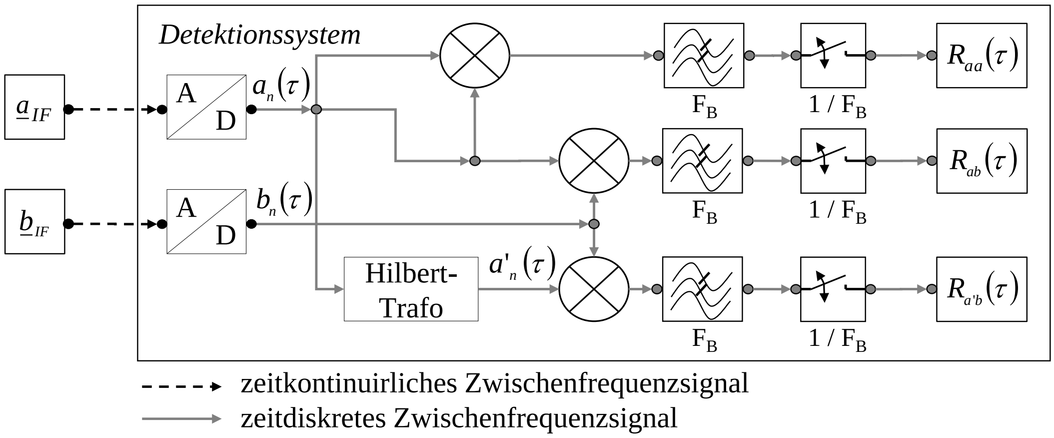

Abbildung 2.3-2 zeigt das Signalflussdiagramm des Detektions-Systems des heterodynen Reflektometers.

Da der Einsatz des Messsystems vorrangig für die Einschaltphase der Plasmaquelle geplant ist, entfallen damit die Einschränkung von Echtzeitsystemen. Dies ermöglicht den Einsatz von rechenintensiven Methoden der digitalen Signalverarbeitung zur Ermittlung des Reflektionsfaktors. Nach dem Abtasten und Speichern der Signale des Modulationssystems, erfolgt die weitere Verarbeitung auf Grundlage der Quadraturamplitudenmodulation [110], dargestellt in Abbildung 2.3-2. Da die Frequenz der Signale stark fluktuiert, wird für jeden Zeitschritt τ das Trägersignal auf Grundlage des ZF-Signales der hinlaufenden Welle gebildet. Seine dazu notwendige orthogonale Komponente wird mittels Hilbert-Transformation erzeugt. Solange die Frequenz der Mikrowellenquelle über den Zeitraum τ konstant bleibt, lassen sich auf diese Weise die Amplituden und die Phasenlagen der einzelnen Signalanteile ermitteln.

2.3.2 *Funktionsverifizierung*

Um die korrekte Funktion des Reflektometers zu überprüfen wurden verschiedene Testszenarien durchlaufen. Begonnen wurden mit einer Leistungskalibrierung, mit dessen Hilfe ein sättigungsfreier Dynamikbereich von 15 μW bis 1 mW, an den Eingängen des Modulationssystems nachgewiesen werden konnte.

Zur Bestimmung der Genauigkeit der Messung des Reflektionsfaktors wurde hinsichtlich der Phasenbestimmung ein Kurzschlussschieber verwendet, dargestellt in Abbildung 2.3-3 (a). Dabei konnte die genaue Position mittels einer Handschraube mit der Steigung 1,5 mm eingestellt werden. Nach der Referenzmessung für die kürzeste Länge wurde der Kurzschlussschieber soweit justiert, bis ein Phasenunterschied von $-360°$ detektiert wurde.

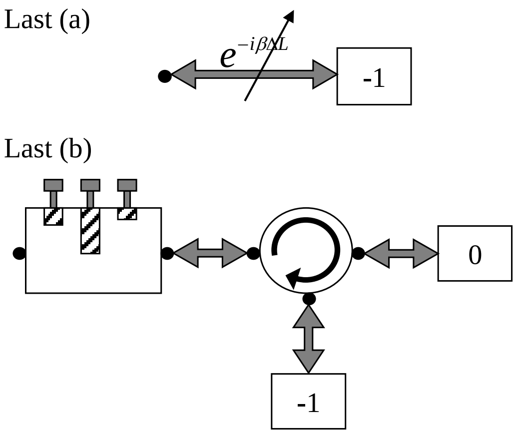

Abbildung 2.3-3 zeigt die verwendeten Referenzen zur Bestimmung der Genauigkeit des Reflektometers. (a) ein Kurzschließschieber für die Phasenbestimmung. (b) 3-Stab-Tuner angepasst abgeschlossen für die Amplitudenbestimmung.

Durch die genaue Kenntnis der Positionsänderung kann die daraus resultierende Phasenänderung berechnet und zum Vergleich herangezogen werden. Zur Bestimmung der Amplitudengenauigkeit des Reflektometers wurde ein 3-Stab-Tuner verwendet. Dieser wurde mit Hilfe eines Zirkulators, in Kombination mit einer Wasserlast, reflektionsarm abgeschlossen (Abbildung 2.3-3 (b)). Zur Bestimmung des genauen Wertes des Reflektionsfaktors für verschiedene Stab-Positionen wurde die Last (b) an einen VNA (ZVRE) angeschlossen.

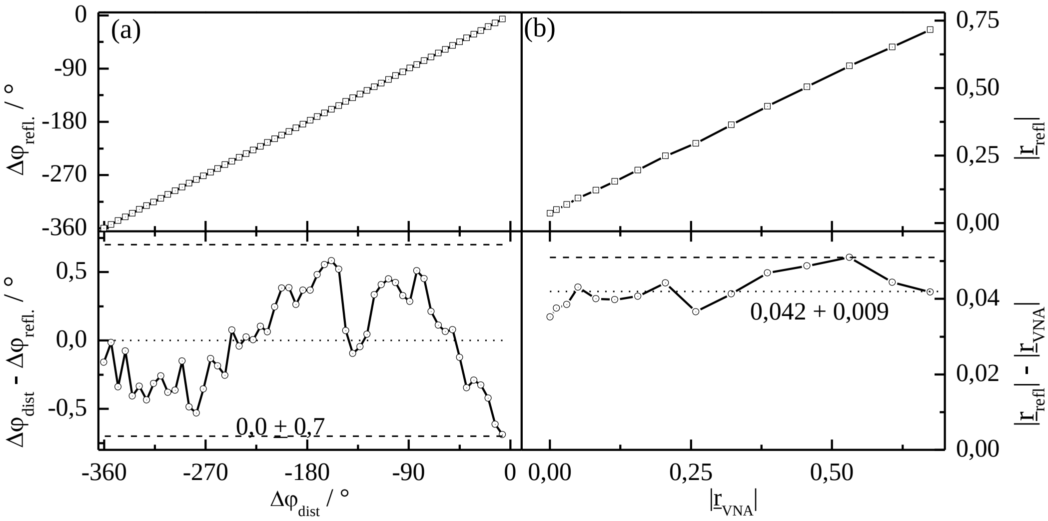

Abbildung 2.3-4 zeigt das Auflösungsvermögen des Reflektometers. (a) zeigt die Ergebnisse der Phasenmessung. (b) zeigt die Resultate der Amplitudenmessung.

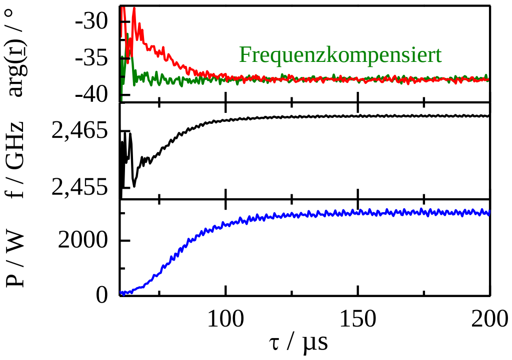

Abbildung 2.3-5 zeigt das Einschwingen der Mikrowellenquelle und die durch die Frequenzänderung hervorgerufene Phasendrehung, sowie dessen Kompensation.

Die Ergebnisse dieser Messungen sind in Abbildung 2.3-4 dargestellt. Dabei wird bei der Phasenmessung über den gesamten Detektionsbereich von $360\,°$ eine Auflösung von mindestens $\pm 0{,}7\,°$ erreicht. Bezüglich der Messung des Absolutwertes in einem Bereich zwischen $6{,}5 \cdot 10^{-4}$ und 0,7 ist ebenfalls eine sehr gute Übereinstimmung erkennbar. Allerdings zeigt ein Blick auf die Differenz zwischen Soll und Ist einen mittleren Offset von 0,043 über den gesamten Bereich. Die Ursachen hierfür sind zum einen die Kreuzkopplung des Richtkopplers von $27\ dB$ und zum anderen der nicht reflektionslose Abschluss des 3-Stab-Tuners durch den Zirkulator mit Wasserlast.

Darüber hinaus konnte die durch die Frequenzänderung des Magnetrons verursachte Phasendrehung kompensiert werden. Auf Grundlage der zeitaufgelösten Detektion der Mittenfrequenz und einem Leitungsmodell des Hohlleiters wird die durch die Frequenzänderung hervorgerufene Phasenänderung ermittelt und subtrahiert. Zu diesem Zweck wurde das Einschwingen einer Mikrowellenquelle gegen einen Kurzschluss gemessen, dargestellt in Abbildung 2.3-5. Die erzielten Resultate zeigen eindeutig, dass ein heterodynes Reflektometer für die Messungen an den vorliegenden Mikrowellenquellen, mit ihren Frequenzfluktuationen, erfolgreich entwickelt wurde.

2.4 Diagnostik zur Plasmamikrowellenwechselwirkung

Nachdem die beiden Diagnostiken, Mikrowelleninterferometrie und Reflektrometrie, etabliert waren und die zu untersuchende Plasmaquelle einsatzbereit war, wurden alle Komponenten zum Experiment, hinsichtlich der Plasmamikrowellenwechselwirkung, zusammengeführt. Die so gewonnenen Resultate sollen dabei sowohl der weiteren Verbesserung des biologischen Dekontaminationsverfahrens dienen als auch die Entwicklung der Plasmaquelle für die GaN-Kristallzüchtung untersützen. Dabei wurde die Plasmaquelle in einen Vakuumreaktor integriert, in dem ein minimaler Druck von $10^{-3}\ mbar$ erreicht wird.

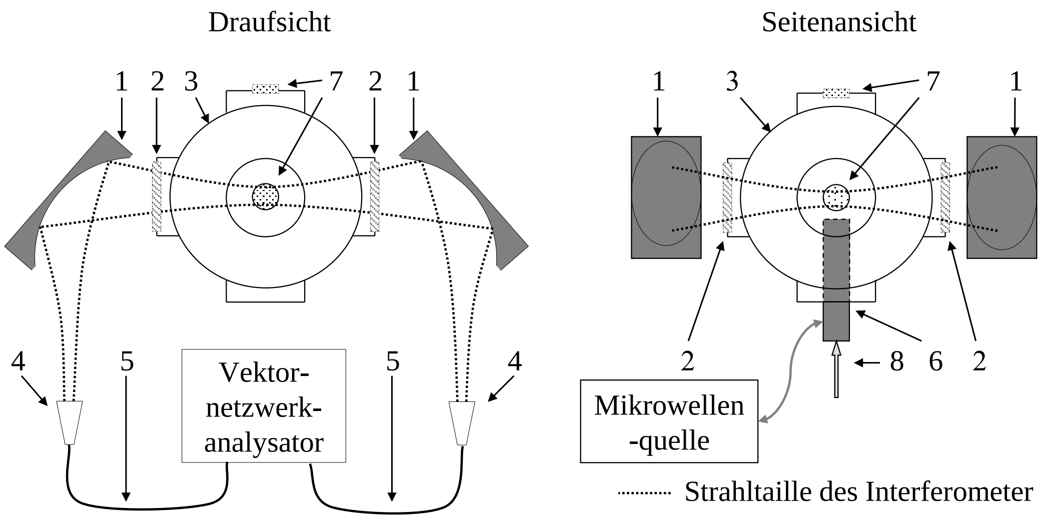

Abbildung 2.4-1 zeigt den experimentellen Aufbau des Interferometers und der Plasmaquelle. 1: elliptische Spiegel, 2: PTFE-Fenster, 3: Reaktor, 4: Hornantenne, 5: Präzisions-Koaxialkabel, 6: Plasmaquelle, 7: Quarzfenster, 8: Gaseinlass.

Um dem Interferometer ($45{,}75\ GHz$) möglichst störungsfreien Zugang zur Afterglow-Zone, in einem Abstand von $28\ mm$ zur Plasmaquelle, zu gewähren, werden PTFE-Fenster, mit einer angepassten Dicke ($\lambda/2$-Trafo) verwendet, dargestellt in Abbildung 2.4-1. Des Weiteren ist die Entladung durch zwei Quarzfenster beobachtbar und mittels eines Koaxialkabels (*Ecoflex 15*) mit der Mikrowellenquelle verbunden, die im Detail in Abbildung 2.4-2 dargestellt ist.

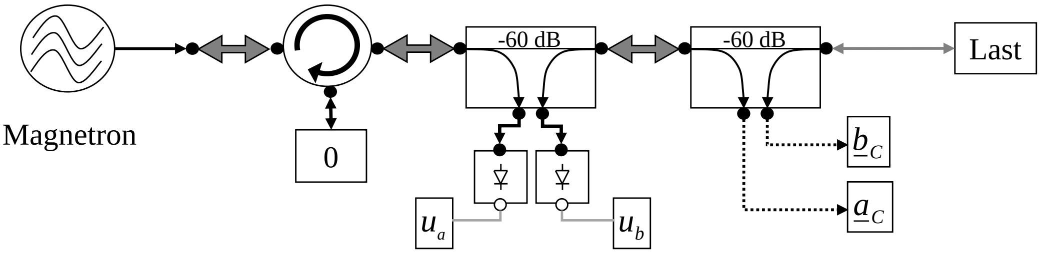

Abbildung 2.4-2 zeigt die Mikrowellenquelle mit ihren diagnostischen Zugängen.

Dabei wird die Entladung mit einem Puls-Pause-Verhältnis von $23\ ms$ zu $87\ ms$ betrieben. Durch das spezielle Design der Plasmaquelle und den Verzicht eines Anpassnetzwerkes, kann der Reflektionsfaktor bestimmt werden, der hauptsächlich durch die Plasmamikrowellenwechselwirkung beeinflusst ist. Dabei wird zur Detektion der dynamischen Anfangsphase das heterodyne Reflektometer verwendet. Zusätzlich wird zur Überwachung des gesamten Pulses und zur Ermittlung der stationären Werte ein skalares Verfahren eingesetzt.

3. Kombinierte Ergebnisse

Die Ergebnisse, die mit Hilfe des Interferometers und des Reflektometers an der Mikrowellenplasmaquelle erzielt wurden, werden in diesem Kapitel zusammen mit ausgewählten Resultaten der Modellierung, letzteres durchgeführt von Dr. Baeva, präsentiert. Dabei wird bei der Betrachtung der Ergebnisse zwischen zwei Bereichen unterschieden. Im ersten Schritt werden die Resultate bezüglich der absorbierten Leistung und der Elektronendichte, über den Verlauf des gesamten Pulses und der Aus-Phase diskutiert. Im Anschluss daran folgt, auf Basis der untersuchten Wellengrößen, eine detaillierte Betrachtung der Anfangsphase. Für genauere Informationen zu den Ergebnissen sei auf [111] verwiesen. Diesen Ergebnissen vorangestellt ist eine kurze allgemeine Untersuchung der Heizleistungsdichte in einem mikrowelleninduzierten Argon-Plasma, welche bei der Interpretation der Resultate helfen soll.

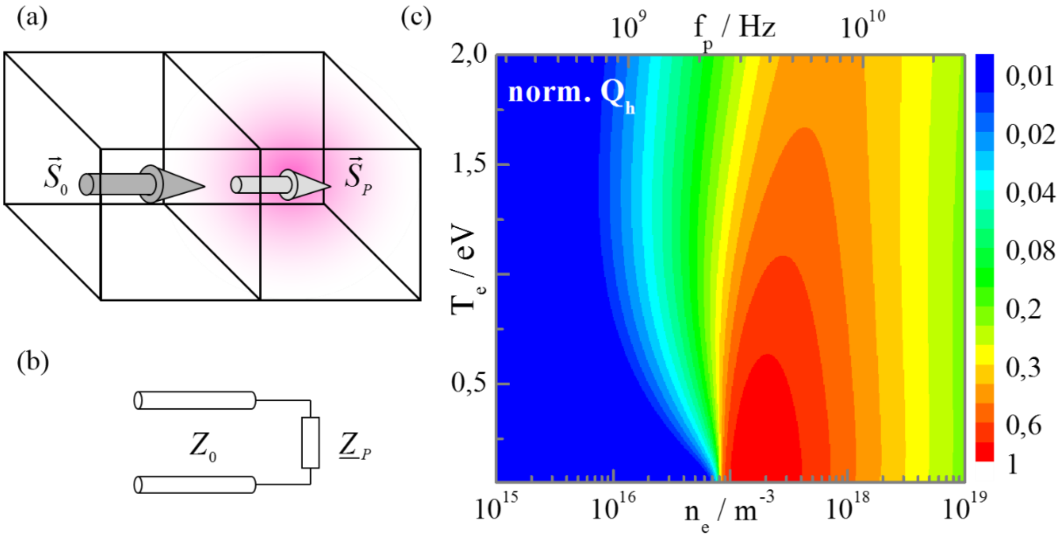

Abbildung 3-1 zeigt die Modellannahmen zur Abschätzung (a) und (b) zur Berechnung der Abhängigkeit der Heizleistungsdichte von Elektronendichte und Elektronentemperatur (c).

Ein gängiger Weg, um die Wirkung des Plasmas auf das Mikrowellenfeld zu beschreiben, ist die Lorentz-Gleichung, aus der sich eine Leitfähigkeit ableiten lässt. Damit kann bei Kenntnis des elektrischen Feldes und der Stoßfrequenz ν_m die Heizleistungsdichte Q_h berechnet und diskutiert werden [40]. Um ohne die explizite Lösung des elektrischen Feldes dennoch Aussagen über die Abhängigkeit der Heizleistungdichte von der Elektronendichte und Temperatur zu treffen, wird folgender Ansatz gewählt. Für den Poynting-Vektor $\vec{S}_0$ einer transversalen elektromagnetischen Welle an der Grenzfläche zum Plasma mit $\vec{S}_P$ (Abbildung 3-1 (a)) kann mittels der Lorentz-Gleichung und den Gleichungen für die Stoßfrequenz [111] der Wellenwiderstand ermittelt werden. Kombiniert man das mit dem Modell einer fehlangepassten Last (Abbildung 3-1 (b)) so erhält man beispielsweise für ein Argon-Plasma bei 20 $mbar$ die in Abbildung 3-1 (c) dargestellte Abhängigkeit.

Die maximale, in das Plasma eingekoppelte Heizleistungsdichte erhält man in diesem Beispiel für Elektronendichten von ca. $2 \cdot 10^{17}\ m^{-3}$. Damit liegt die korrespondierende Plasmafrequenz $f_P = 4\ GHz$ knapp oberhalb der Anregungsfrequenz der Mikrowelle. Eine Erhöhung der Elektronentemperatur führt in allen Bereich zu einer Verringerung der Heizleistungsdichte, wobei das Maximum in einem Bereich von $0{,}05\ eV$ ($\nu_m = 3 \cdot 10^8\ 1/s$) bis $0{,}5\ eV$ ($\nu_m = 3 \cdot 10^9\ 1/s$) liegt.

3.1 Zeitentwicklung des Pulses

Die Ergebnisse, die für die beiden untersuchten Drücke bei $20\ mbar$ und $40\ mbar$ sowie für verschiedene Leistungen experimentell ermittelt wurden, sind zusammen mit den Ergebnissen der Modellierung in Abbildung 3.1-1 dargestellt.

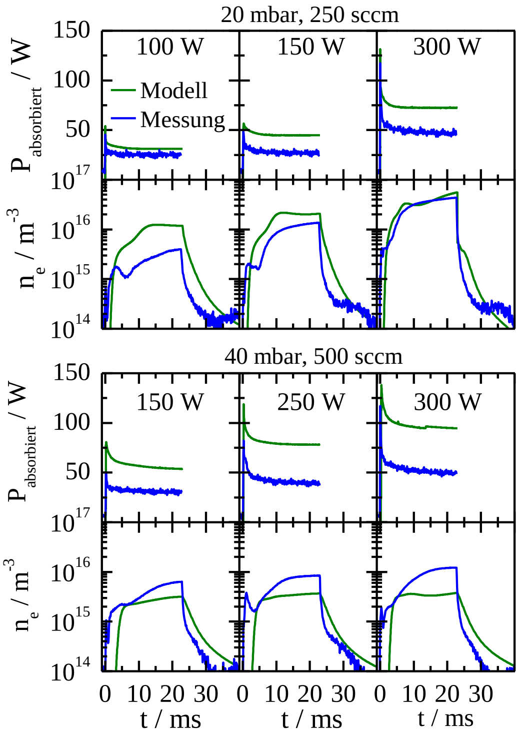

Abbildung 3.1-1 zeigt zeitaufgelöst die absorbierte Leistung und Elektronendichte für verschiedene Arbeitspunkte in Druck und Leistung.

Allen untersuchten Arbeitspunkten gemeinsam ist der schnelle Anstieg der absorbierten Leistung zu Beginn des Pulses, der nach Erreichen des Maximums langsam abfällt und dann konstant bleibt. Des Weiteren fällt die geringe Umsetzung der Mikrowellenleistung im Plasma auf, was der Verwendung von Argon geschuldet ist. Vergleicht man die gemessenen Leistungen bei einem Druck von $20\ mbar$ mit den Ergebnissen der Modellierung, so ist eine gute Übereinstimmung von $36\ \%$ zu erkennen. Diese sinkt für einen Druck von $40\ mbar$ auf ca. $45\ \%$, verursacht durch die zunehmende Ausprägung von Filamenten, die das rotationssymmetrische Modell nicht abbilden kann. Betrachtet man den Verlauf der gemessenen Elektronendichten, so erkennt man, dass dieser ebenfalls mit einem starken Anstieg beginnt und langsam zum Maximalwert ausläuft.

Während der Aus-Phase fällt diese dann relativ langsam zum Detektionslimit von $2 \cdot 10^{14}\ m^{-3}$ ab. Vergleicht man dazu die Ergebnisse des Modells, so fällt ein Zeitverzug auf, der mit steigendem Druck zunimmt. Dieser Unterschied ist, durch den ortsintegrierenden Charakter des Interferometers, sowohl radial als auch axial zu erklären. Dadurch befinden sich zu einem früheren Zeitpunkt Elektronen im Detektionsbereich, wohingegen das Modell die Elektronendichte an nur einem weiter entfernteren Ort auswertet. Bezüglich der

Elektronendichte im statischen Bereich, am Ende des Pulses, ist ein gute bis sehr gute quantitative Übereinstimmung zu erkennen.

Die Untersuchungen zeigen zum einen, dass die dynamische Wechselwirkung zwischen Plasma und Mikrowelle sich in einer Zeitskala unterhalb von 1 ms bewegt. Zum anderen fällt auf, dass die Elektronendichte im Afterglow der Quelle mit zunehmendem Druck stark abfällt und sich damit das Plasma hauptsächlich auf den aktiven Teil der Quelle beschränkt. Des Weiteren zeigen das Experiment und das Modell gute Übereinstimmungen im Verlauf des gesamten Zyklus.

3.2 Betrachtung der Anfangsphase

Auf Grund der kurzen Zeitskala in dem sich die schnellen Änderungen zu Beginn des Pulses abspielen, kann zur genaueren experimentellen Untersuchung dieses Bereiches nur das heterodyne Reflektometer mit seiner Zeitauflösung von 500 ns eingesetzt werden. Die Ergebnisse für den Arbeitspunkt von 20 $mbar$ und 300 W sind in Abbildung 3.2-1 dargestellt, wobei es sich bei den Phasenergebnissen um relative Verläufe handelt.

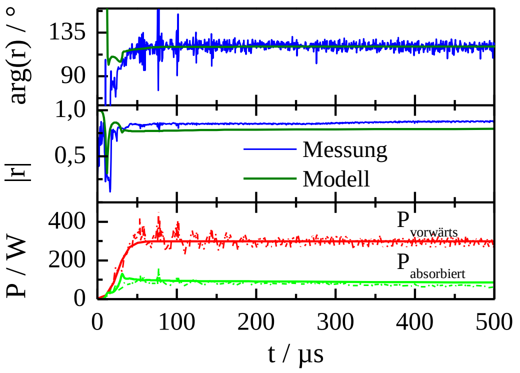

Abbildung 3.2-1 zeigt die Ergebnisse des Reflektometers für die Startphase bei 20 $mbar$.

Es ist erkennbar, dass sich die Dynamik im Verlauf auf die ersten 50 μs beschränkt. Daher wird sich die folgende Diskussion auf diesen Bereich konzentrieren. Da auf Grund des Einschwingverhaltens der Mikrowellenquelle (Abbildung 2.3-1) mit ihrem verschmierten Spektrum keine verlässliche Phasenbestimmung in diesem Zeitraum möglich ist, werden nur die Amplitudenverläufe betrachtet. Dennoch sei erwähnt, dass der statische Verlauf der Phasenlage, vom Modell vorhergesagt, durch das Experiment bestätigt werden konnte.

Um einen genaueren Einblick in die Plasmamikrowellenwechselwirkung während der Startphase der Entladung zu erhalten, sind in Abbildung 3.2-2 für ausgewählte Zeitpunkte und im Verlauf der Amplitudengrößen die Ergebnisse des Modells hinsichtlich des Betrages der elektrischen Feldstärke (a), der Elektronentemperatur (b) und der Elektronendichte (c) dargestellt.

Zum Zeitpunkt $t = 0\ \mu s$ reicht das Mikrowellenfeld bis zum Ende der koaxialen Struktur, ohne dabei in Wechselwirkung mit der Hintergrund-Elektronendichte von $1 \cdot 10^{11}\ m^{-3}$ zu treten. Deutlich erkennbar ist die Wirkung der resonanten Struktur durch die Ausbildung einer elektrischen Feldüberhöhung, an deren Position $2\ \mu s$ später die Entladung einsetzt.

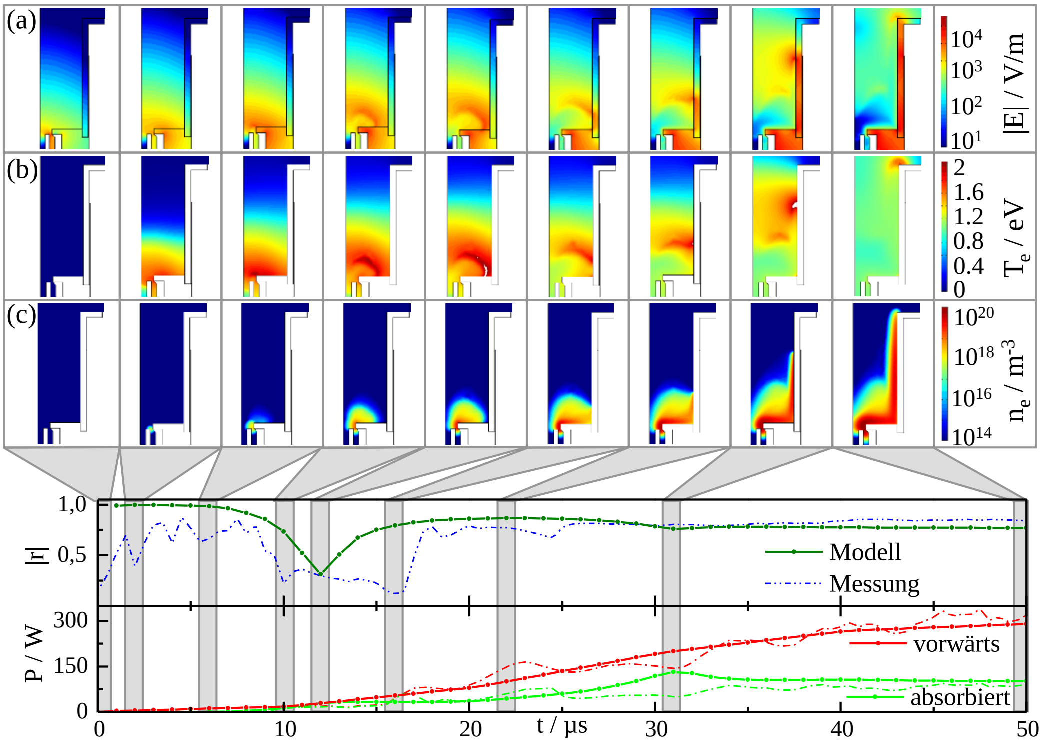

Abbildung 3.2-2 zeigt den Verlauf der Amplitudengrößen des Reflektometers und für ausgewählte Zeitpunkte den Betrag der elektrischen Feldstärke (a), die Elektronentemperatur (b) und die Elektronendichte (c).

Schon der Einfluss dieses kleinen Plasmavolumens führt zu einer Verstimmung der Resonanzeigenschaften der Zündstruktur. Dies ist erkennbar an der Reduzierung der lokalen Feldstärke, was zu einem inhärenten Schutz dieser führt. Das Volumen der Entladung vergrößert sich und kann zum Zeitpunkt $t = 10\ \mu s$ signifikant Energie aus dem elektrischen Feld umsetzen. Dies führt $2\ \mu s$ später zu einem Minimum im Reflektionsfaktor. Auf Grund der Nähe der Plasmafrequenz zur Anregungsfrequenz kann die Welle das Plasma sehr effizient heizen, was zu lokalen Elektronentemperaturen von bis $2\ eV$ führt. Durch die weitere Zunahme der Elektronendichte wird zum einen der Anteil der reflektierten Leistung erhöht und zum anderen das elektrische Feld in das Quarzrohr gedrängt. Dort setzt dann eine zusätzliche Wanderwellenentladung ein, die die aktive Plasmazone bis zum Ende des Rohres verlängert. Nach diesen dynamischen Anfangsprozessen stellen sich Elektronentemperaturen von ca. $1\ eV$ und Elektronendichten von bis zu $1 \cdot 10^{20}\ m^{-3}$ ein, die das elektrische Feld komplett aus dem Volumen in die dielektrischen Strukturen verdrängen. Damit wird auch die eigentliche Wechselwirkungszone zur Absorption der elektrischen Energie vom Plasma auf diesen Bereich beschränkt.

4. Zusammenfassung und Ausblick

Die Forschung an mikrowelleninduzierten Atmosphärendruckplasmen am INP führte zu verschiedenen potentiellen Applikationen. Dabei besitzt die mikrobiologische Dekontamination sowohl von thermolabilen Medizinprodukten als auch von Lebensmitteln schon zum jetzigen Zeitpunkt ein hohes industrielles Anwendungspotential. Neben diesen weiter fortgeschrittenen Applikationen wurden ebenfalls Untersuchungen zum Einsatz dieser mikrowelleninduzierten Plasmen für die Galliumnitrid-Kristallzüchtung durchgeführt (Publikation: *PVT Grow of GaN Bulk crystals*). Den aufgeführten Anwendungen gemeinsam ist, dass für eine erfolgreiche Weiterentwicklung der Prozesse, sowie der Plasmaquelle, ein grundlegendes Verständnis der vorliegenden dynamischen Mikrowellenplasmawechselwirkung notwendig ist. Durch den begrenzten diagnostischen Zugang der zu untersuchenden Plasmaquelle wird ein kombinierter Ansatz aus diagnostischen Methoden und Modellierung gewählt.

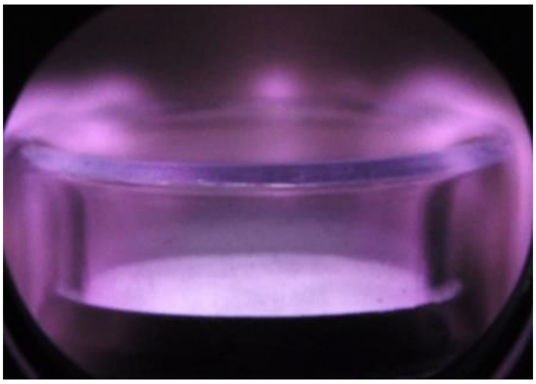

Abbildung 4-1 zeigt eine Fotografie der untersuchten Mikrowellenentladung.

Die Entladung wird in Argon bei reduziertem Druck (ab $10\,mbar$) zur Vereinfachung des Modells betrieben. Daher musste die Plasmaquelle für diesen Einsatz weiterentwickelt werden. Dieses beinhaltete zum einen die Neuauslegung der Prozesswärmeabfuhr, auf Grund der nicht oder nur teilweisen Anwendbarkeit von etablierten Verfahren im Atmosphärendruck (hohe Gasflüsse, Wasserkühlung). Mit Hilfe der Ergebnisse zur Entladungsbildung (Publikation: *Observation of microwave volume plasma ignition in ambient air*) wurde eine Prozessführung auf Basis der Pulsweitenmodulation, mit einer Pulsdauer in der Größenordnung von $10\ ms$ und einer variablen Pulspause, zur Anpassung der thermischen Last etabliert. Zum anderen ist eine Mikrowellenvakuumdurchführung zur Versorgung der Entladung mit Energie und Gasfluss entwickelt worden.

Die Plasmamikrowellenwechselwirkung dieser Quelle ist anschließend mit Methoden zur Charakterisierung des Plasmas und des Mikrowellenfeldes für unterschiedliche Arbeitspunkte in Druck und Leistung untersucht worden.

Zur Bestimmung der Elektronendichte des Plasmas wurde ein frequenzvariables Mikrowelleninterferometer auf Basis eines Vektornetzwerkanalysators erstmalig etabliert. Dieses neue Messsystem wurde im Vorfeld detailliert untersucht, um das korrekte Zusammenspiel aller Komponenten, sowohl kommerzielle (Kabel, Modenkoppler, Antennen) als auch selbstentwickelte Komponenten (Linsen und Spiegel), zu überprüfen.

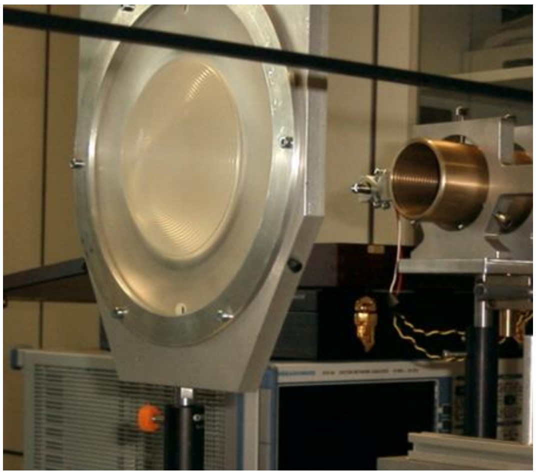

Abbildung 4-2 zeigt Linse und Antenne des Mikrowelleninterferometers zur Untersuchung an einer Fluoreszenzlampe.

In diesem Zusammenhang wurde ein frequenzaufgelöstes Mikrowelleninterferometer zur Messung der Elektronendichte in einer Fluoreszenzlampe aufgebaut (Publikation: *Influence of dielektric surrounding of plasma on the electron density measurement by microwave interferometer*). Durch diesen neuartigen Ansatz konnte der Einfluss der dielektrischen Umhüllung (Glasrohr der Lampe) auf die Mikrowelleninterferometrie untersucht werden. Es zeigt sich, dass die gemessene Elektronendichte je nach Interferometerfrequenz um bis zu 53 % abweicht. Um diesen Effekt der dielektrischen Umhüllung nachzubilden, wurde ein Modell auf Basis von Ersatzschaltungen aus dem Bereich der Hochfrequenztechnik entwickelt und zusätzlich an einem dielektrischen Resonator in guter Übereinstimmung getestet.

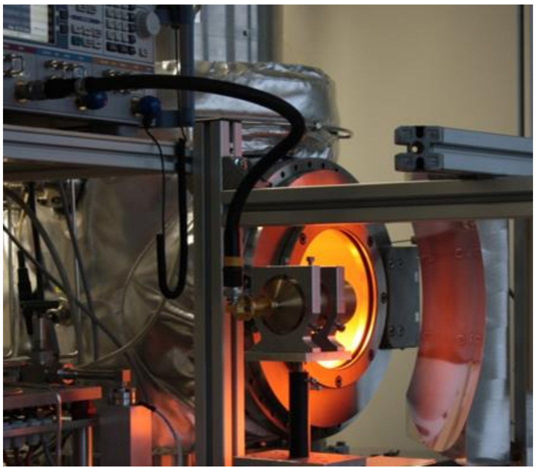

Abbildung 4-3 zeigt das Mikrowelleninterferometer an einem induktiv gekoppelten Plasmareaktor.

In einer weiteren Untersuchung an einem Induktiv Gekoppelten Plasma wurden die Resultate dieses Messsystems mit denen von Langmuir-Sondenmessungen verglichen (Publikation: *Electron density measurement on an inductively coupled plasma with a one-port microwave interferometer*). Auf Grund der konstruktiven Gegebenheiten des Reaktors ist das Plasma nur über ein Fenster für das Mikrowelleninterferometer zugänglich. Durch die Reflektion des Strahlengangs innerhalb des Reaktors und den Einsatz von direktiven Elementen zur Trennung der hin- und rücklaufenden Welle konnte das Messsystem dennoch etabliert werden. Durch die separate Ermittlung der Transmissionseigenschaften des Fensters und die darauf abgestimmte Interferometerfrequenz wurde der Einfluss des Fensters auf das Messsystem minimiert. Der Vergleich der ermittelten Elektronendichten ergab einen Unterschied von Faktor zwei zwischen Interferometer und Langmuir-Sonde. Die Gegenüberstellung der zeitaufgelösten Messungen des exponentiellen Abfalls der Elektronendichte in der Aus-Phase des Plasmas mit den Ergebnissen eines analytischen, ambipolaren Diffusionsmodells in Zylinderkoordinaten ergab ebenfalls eine gute Übereinstimmung.

Die Untersuchungen an der Fluoreszenzlampe und dem Induktiv Gekoppelten Plasma zeigten zum einen die korrekte Funktion des neu etablierten frequenzvariablen Mikrowelleninterferometers mit erreichbaren Phasenauflösungen unterhalb von $0{,}1\ mrad$. Zum anderen wurde festgestellt, dass die dielektrische Umhüllung des Plasmas zu einem systematischen Fehler von bis $53\ \%$ bei der Elektronendichtebestimmung führen kann.

Diese gewonnenen Erkenntnisse hatten bei der Konzipierung des Mikrowelleninterferometers zur Untersuchung der Plasmamikrowellenwechselwirkung einen entscheidenden Einfluss, was beispielsweise zur Verwendung von PTFE-Fenstern führte. Mit Hilfe dieses Messsystems wird die Elektronendichte im Afterglow der Mikrowellenentladung zeitaufgelöst ermittelt, um das Plasma zu charakterisieren und Vergleichswerte für die Modellierung bereitzustellen.

Abbildung 4-4 zeigt Antenne und Spiegel des Mikrowelleninterferometers zur Untersuchung der Mikrowellenentladung.

Neben der Untersuchung des Plasmas ist ebenfalls eine Diagnostik des Mikrowellenfeldes nötig, um die Plasmamikrowellenwechselwirkung dieser Entladung experimentell zu charakterisieren. Auf Grundlage dieser Daten können die Resultate des Modells bewertet werden, die einen Einblick in die Plasmaquelle und ihrer dynamischen Vorgänge erlaubt, was für die Weiterentwicklung der Applikationen essentiell ist. Durch das spezielle Design der Plasmaquelle werden die hin- und rücklaufende Mikrowellen nur schwach gestört. Daher wird deren Verhältnis, der Reflektionsfaktor, primär durch die Plasmamikrowellenwechselwirkung bestimmt.

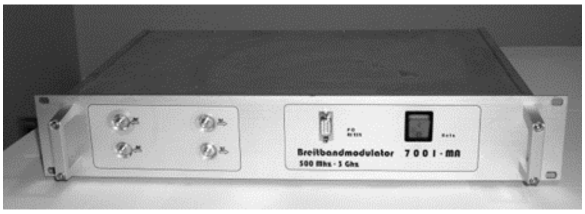

Abbildung 4-5 zeigt das entwickelte heterodyne Reflektometer.

Aus diesem Grund ist ein heterodynes Reflektometer entwickelt wurden (Publikation: *A heterodyne reflectometer for detecting the time depending complex reflection coefficient optimised for the usage with oven magnetrons*), das trotz der Verwendung von Ofenmagnetrons, mit deren typisch schlechten Signaleigenschaften, den Reflektionsfaktor robust detektieren kann. Dieses Messsystem wurde umfangreich getestet und kann mit einer maximalen Zeitauflösung von $100\ ns$ den komplexen Reflektionsfaktor mit einer Phasengenauigkeit von $10\ mrad$ bestimmen. Darüber hinaus können Phasenfluktuationen, hervorgerufen durch Frequenzänderungen des Magnetrons, kompensiert werden. Das Reflektometer erlaubt einen experimentellen Zugang zur aktiven Zone schon in der Frühphase der Entladung, der mit üblicher Messtechnik (Detektordioden) nicht aufgelöst werden kann.

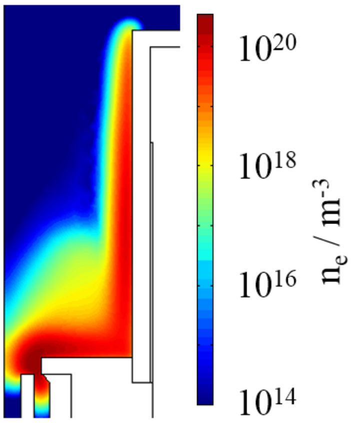

Abbildung 4-6 zeigt die räumliche Verteilung der modellierten Elektronendichte.

Mit Hilfe der Diagnostiken zur Untersuchung des Plasmas und des Mikrowellenfeldes wurde die Entladung von der Zündung bis zur stationären Phase charakterisiert und mit den Ergebnissen des Modells verglichen (Publikation: *Temporally and spatially resolved characterization of microwave induced argon plasmas: Experiment and modeling*). Es zeigte sich eine gute Übereinstimmung hinsichtlich der Elektronendichte und eingekoppelten Leistung für die untersuchten Arbeitspunkte im Millisekundenzeitbereich, sowie eine starke Dynamik im Reflektionsfaktor in der ersten Millisekunde, hervorgerufen durch die Plasmamikrowellenwechselwirkung. Durch die hohe Zeitauflösung des Reflektometers konnten diese Vorgänge im Mikrosekundenzeitbereich erstmalig experimentell aufgelöst werden, was die Interpretation mittels des Modells möglich macht. Zur besseren Interpretation dieser Ergebnisse wurde der Einfluss der Elektronendichte und Elektronentemperatur auf die Heizleistungsdichte modellhaft untersucht.

Es konnten die Vorgänge während der Zündung des Plasmas detailliert untersucht werden und damit die Richtigkeit von Annahmen, die bei der Entwicklung der Zündtechnologie [47] getroffen wurden, überprüft werden. Dieses erworbene grundlegende Verständnis ermöglicht eine Weiterentwicklung dieser Technologie. Das Ziel die Plasmaquelle für die Kristallzüchtung einzusetzen, konnte nicht erreicht werden. Während der Entwicklung der Quelle für diese Applikation, stellte eine andere Forschergruppe fest, dass die Verwendung von Plasma zwar prinzipiell möglich ist [112], aber andere Verfahren ein weitaus höheres Potential für die Züchtung von massiven GaN-Einkristallen haben [113]. Im Gegensatz dazu konnte die Einsetzbarkeit dieser Entladung für die mikrobiologische Dekontamination von Lebensmitteln und thermolabilen Medizinprodukten signifikant verbessert werden. Mit Hilfe der erzielten Ergebnisse wurde eine neue Optimierungsstrategie für die Abstimmung der Mikrowellenplasmaquelle entwickelt. Dies führte zu einer wesentlichen Verbesserung der Reproduzierbarkeit der mikrobiologischen Ergebnisse [114] (Publikation: *Inactivation of Vegetative Microorganisms and Bacillus atrophaeus Endospores by Reactive Nitrogen Species (RNS)*). Darüber hinaus bilden die erzielten Ergebnisse eine solide Grundlage für weitere experimentelle und theoretische Untersuchungen dieser Entladung in beispielsweise anderen Arbeitsgasen.

5. Originalpublikationen

Darstellung des Eigenanteils bei kumulativen Dissertationen

- PVT Grow of GaN Bulk crystals

  Siche, D., Gogova, D., Lehmann, S., Fizia, T., Fornari, R., **Andrasch, M**., Pipa, A., and Ehlbeck, *Journal of Crystal Growth*, 2011. 318(1): p. 406-410

  Eigenanteil: M. A. entwickelte den Ansatz zur Umsetzung der Plasmaquelle für die Kristallzüchtung und war an der Erstellung der Publikation beteiligt.

- Observation of microwave volume plasma ignition

  Pipa, A.V., **Andrasch, M.**, Rackow, K., Ehlbeck, J., and Weltmann, K.D.,. *Plasma Sources Science & Technology*, 2012. 21(3)

  Eigenanteil: M. A. war verantwortlich für die Entwicklung der Hochfrequenzkomponenten des Experimentes, einschließlich deren Simulation, und wirkte beim Schreiben der Publikation mit.

- Electron density measurements on an inductively coupled plasma with a one-port microwave interferometer

  Andrasch, M., Ehlbeck, J., Foest, R., and Weltmann, K.-D., *Plasma Sources Science and Technology*, 2012. 21(5): p. 055032

  Eigenanteil: M.A. konzipierte und führte die Experimente durch, mit Ausnahme der Sondenmessungen. M. A. schrieb das Manuskript mit der Unterstützung der Co-Autoren.

- Inactivation of Vegetative Microorganisms and Bacillus atrophaeus Endospores by Reactive Nitrogen Species (RNS)

  Schnabel, U., **Andrasch, M.**, Weltmann, K.-D., and Ehlbeck, J., *Plasma Processes and Polymers*, 2014. 11(2): p. 110-116.

  Eigenanteil: M.A. optimierte die Plasmaquelle, führte die Temperaturmessungen durch und wirkte an der Erstellung der Publikation mit.

- Temporally and spatially resolved characterization of microwave induced argon plasmas: Experiment and modelling

  Baeva, M., **Andrasch, M.**, Ehlbeck, J., Loffhagen, D., and Weltmann, K.-D., *Journal of Applied Physics*, 2014. 115(14): p. 143301

  Eigenanteil: M.A. war für die Experimente verantwortlich und wirkte bei der Interpretation der Simulationsergebnisse sowie bei der Erstellung des Manuskriptes mit.

- Influence of the dielectric surrounding of plasma on the electron density measurement by microwave interferometer

  Andrasch, M., Ehlbeck, J., and Weltmann, K.-D., *Measurement Science and Technology*, 2014. 25(7): p. 075004.

  Eigenanteil: M.A. konzipierte und führte die Experimente durch. M. A. schrieb das Manuskript mit der Unterstützung Co-Autoren.

- A heterodyne reflectometer for detecting the time dependent complex reflection coefficient optimised for the usage with oven magnetron

  Andrasch, M., Ehlbeck, J., and Weltmann, K.-D., *Maesurement Science and Technology*, submitted

  Eigenanteil: M.A. konzipierte und führte die Experimente durch. M. A. schrieb das Manuskript mit der Unterstützung der Co-Autoren.

Bestätigt:

Ort, Datum

Prof. Dr. Klaus-Dieter Weltmann

5.1 PVT Grow of GaN Bulk crystals

Journal of Crystal Growth 318 (2011) 406–410

Contents lists available at ScienceDirect

Journal of Crystal Growth

journal homepage: www.elsevier.com/locate/jcrysgro

PVT growth of GaN bulk crystals

D. Siche [a,*], D. Gogova [a], S. Lehmann [a], T. Fizia [a], R. Fornari [a], M. Andrasch [b], A. Pipa [b], J. Ehlbeck [b]

[a] Leibniz-Institut für Kristallzüchtung, Max-Born-Strasse 2, 12489 Berlin, Germany
[b] Leibniz-Institut für Plasmaforschung und Technologie e.V., Felix-Hausdorff-Str. 2, 17489 Greifswald, Germany

ARTICLE INFO

Available online 8 November 2010

Keywords:
A1. Substrates
A2. Single crystal growth
A2. Growth from vapor
A3. Physical vapor deposition processes
B1. Nitrides
B2. Semiconducting III-M materials

ABSTRACT

Limitations in ammonia-based vapour growth of bulk GaN require the search for a replacement of ammonia as a precursor of reactive nitrogen. We propose the implementation of a plasma-activated nitrogen source instead. In this contribution we present the current development status of a long-term stable plasma source for reactive nitrogen supply as well as a novel gallium source setup, both of which serve as the basis of a new approach to grow GaN bulk crystals. Following the characterization of the Ga source, the evaporation energy was determined as (284 ± 9) kJ/mol and the transport becomes saturated at a carrier gas flow of 200 sccm N_2. Short microwave pulses are applied to operate the plasma source. Crystal growth conditions require high power and stable currents of the microwave pulses – which will be achieved using a custom-built power supply – to reduce the thermal loads at the desired high-pressure operation.

1. Introduction

The direct and wide band gap semiconductor gallium nitride (GaN) offers a great potential for optoelectronic applications, e.g. in LEDs, laser diodes, and UV-optical devices. Homo-epitaxial growth would be the basis for an essential decrease in defect density, which in turn would lead to an increase in life time and improved performance of GaN-based devices. However, the demand for native substrates remains a major challenge for crystal growers.

GaN growth from the melt is impossible and therefore alternative methods are under development. Apart from solution, like the ammonothermal growth [1], single crystalline GaN can be grown from the gas phase. The halide vapour phase epitaxy (HVPE) is well-established [2,3], but its application for growing "bulk" crystals is just a temporary solution. Considerable problems arise, e.g. the NH_4Cl by-product formation, which is the main limitation for extended process durations.

The earliest approach to grow single-crystalline GaN was the direct reaction of elemental gallium vapour and ammonia [4]. However, this process is complicated due to contradictory process temperature requirements. On the one hand, the liquid Ga source has to be kept at temperatures of about 1400 °C, high enough to provide adequate amounts of gaseous Ga in order to achieve reasonable growth rates. On the other hand, the growth temperature cannot essentially exceed 1100 °C, which is required due to the difficulty of providing sufficient reactive nitrogen via ammonia decomposition and to maintain the positive supersaturation over the substrate.

In this paper we review the ammonia-assisted vapour growth of GaN and propose a new crystal growth method for bulk GaN where reactive nitrogen is provided by a plasma source instead of thermally cracked ammonia. A particular challenge of this approach is the use of relatively high pressures and the presence of a Ga stream in the reaction cell. The Ga evaporation data and the current status of the nitrogen plasma source development will be presented—for the latter optical emission spectra for 100 mbar nitrogen pressure.

By means of this plasma-enhanced growth process, the existing limitations are to be overcome and a stable process with growth rates well above10 μm/h should be achievable.

2. Ammonia-based vapour growth

The ammonia pyrolysis starts already at about 500 °C [5] and can be minimized using quartz (activation energy of 33.7 kcal/mol) for the reaction cell [6]. However, quartz limits the growth temperature, as SiO_2 gets reduced by the hydrogen arising from ammonia pyrolysis, which in turn results in Si- and O-donor doping of the grown material [7]. Eventually, the GaN decomposition itself increases with growth temperature and hydrogen concentration [8]. Therefore an increased partial pressure of activated nitrogen is needed to overcome this issue and assure an enhanced growth rate.

The large temperature difference between the hot Ga source and the colder substrate plus the lack of reactive nitrogen may result in

---

[*] Corresponding author. Tel.: +49 30 6392 3046; fax: +49 30 6392 3003.
E-mail address: siche@ikz-berlin.de (D. Siche).

0022-0248/$ - see front matter © 2010 Elsevier B.V. All rights reserved.
doi:10.1016/j.jcrysgro.2010.10.030

Ga condensation and even droplet formation, which finally leads to polycrystalline growth.

In the past, efforts were made to work at moderate source temperatures by searching for appropriate transport agents, alternatively to chlorine in the HVPE process, which has some draw backs as mentioned in Section 1. The advantage of the HVPE growth are very high growth rates, few hundred μm/h are possible, but good crystal quality is related to growth rates <100 μm/h. For iodine transport lower maximum growth rates were reported (78 μm/h) and the by-product NH_4I was formed, which was even harder to remove than chlorine counterpart NH_4Cl [9]. The Ga-hydride growth yielded 20 μm/h growth rate only, which cannot be increased, due to the accelerated GaN decomposition at higher hydrogen content [10]. Using the volatile suboxide Ga_2O by reducing Ga_2O_3 powder with H_2 gas at 1000 °C, a growth rate of 6 μm/h was achieved, a value which is not reasonable for bulk crystal growth. Nevertheless, the oxygen doping level was surprisingly low (1.5×10^{18} atoms/cm^3) [11] for this approach. In this context the "pseudo-halide vapour phase epitaxy" (PVPE) process was found to be a new method. The basics of this process and the growth reactor geometry were published in [12]. The pseudo-halide hydrogencyanide (HCN) acts as a transport agent for Ga, forming volatile $Ga(CN)_g$. Unfortunately, the growth rate increases with carbon concentration and at reasonable values, above10 μm/h, the carbon solubility limit is already exceeded resulting in poor crystalline quality of the layers. In Fig. 1a, a typical PVPE-grown sample is shown, where a 10 μm thick GaN layer was grown on a 3 μm GaN/SiC template at a growth temperature of $T_g = 1090$ °C, a source temperature of $T_s = 1390$ °C, 200 sccm NH_3 flow and a total pressure of $p_{tot} = 600$ mbar. As the carbon concentration was strongly reduced, the growth rate decreased to about 1 μm/h. The growth process was conducted without substrate rotation and Fig. 1b reveals the resulting inhomogeneous distribution of carbon inclusions as analyzed by SEM-EDX. The varying surface morphologies are shown for inclusion free as well as high-inclusion density areas (Fig. 1c and d, respectively). Experiments with higher carbon concentration resulted in growth rates up to 60 μm/h, but the layer quality was strongly degraded [12]. Without carbon and rising T_s to more than 1400 °C only polycrystalline growth could be observed. We assume that this was caused by supercritical super-cooling of the Ga vapour and resultant Ga droplet formation. Therefore the focus was changed from using ammonia as a reactive nitrogen precursor to plasma-activated nitrogen. This is well established for molecular beam epitaxial growth and is characterized by low growth rates at low pressures. However, nothing is known about the use of nitrogen plasma at higher pressures and growth rates. As the latter is our main focus, we firstly characterized and improved the operation stability of the Ga source, which will be described in the following section and checked the potential of high-pressure nitrogen plasma sources for an application in GaN bulk crystal growth.

3. Ga source study

The Ga evaporation and re-condensation is used to find a range of parameters for temperature, temperature difference between source and seed, pressure and nitrogen carrier gas flow, which enables bulk growth-relevant growth rates. Before running growth processes, these evaporation experiments were carried out without a supply of reactive nitrogen in a specially designed setup situated in an inductively heated vertical growth reactor. The growth reactor was separated by a diaphragm into two different temperature regions. The lower zone of the setup was the high-temperature source zone, where the Ga source was heated up in a carbon crucible and then evaporated. The second zone – the upper growth area – was kept at lower temperature. The role of the diaphragm was discussed elsewhere [12]. Nitrogen purge gas was introduced from the bottom into the evaporation system configuration as can also be seen in Ref. [12]. All setup parts were made of graphite since graphite is an inexpensive material with good thermal and chemical stability at elevated process temperatures ($T_{melt} = 3550$ °C). In order to optimize the crucible geometry, numerical simulations of the temperature field and gas flows in the reactor (software package ANSYS [13]) were carried out in addition to the Ga evaporation experiments, where the position of the moveable inductive main heater and the growth regime for maximal growth rate without exceeding the critical supercooling of the Ga vapour were checked.

In the Ga evaporation experiments the three investigated parameters were: the source temperature, the N_2 carrier gas flow, and the

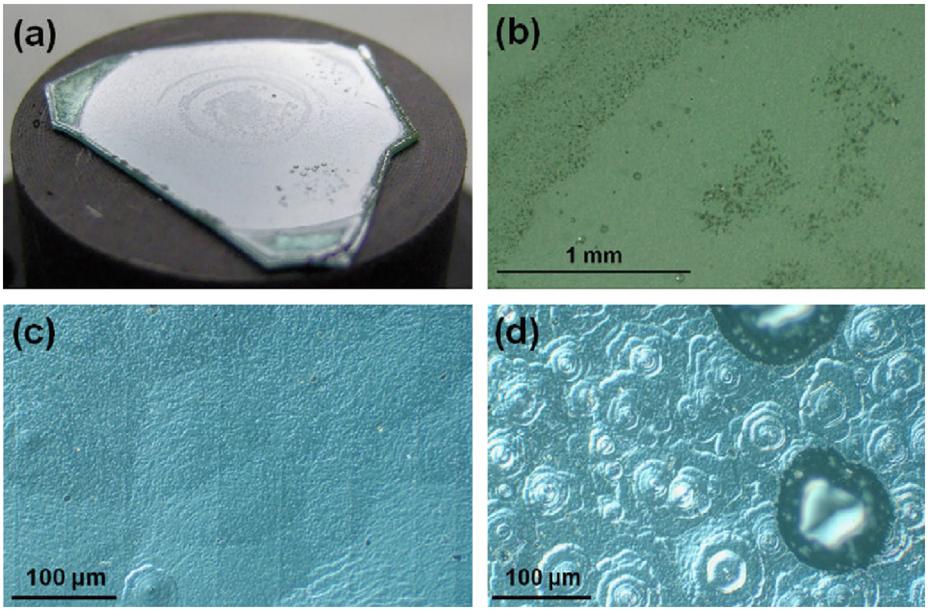

Fig. 1. (a) PVPE grown sample on the 25 mm diameter substrate holder (digital camera), (b) inhomogeneous distribution of inclusions, (c) smooth surface of a particle-free area and (d) growth hillocks and pits in areas of higher carbon particle contamination (optical microscope).

total pressure (p_{tot}) in the reactor. Their impact on the evaporation rate of Ga was studied in detail. The monitored setting of them made it possible to precisely control the Ga transport and provide sufficient Ga in the vapour phase to assure bulk crystal GaN growth with reasonably high growth rates. Due to setup-defined limitations however, the gas flow and total pressure were controlled and solely the loss of Ga and the pyrometrically accessible temperatures of source and seed were measured. Determining also the mass difference of all involved setup parts served as a crosscheck for the amount of evaporated Ga and proved a good recovery rate of the evaporated gallium. The Ga loss was determined by the weighted mass difference of the Ga crucible before and after the processes. Overall, a range of variables was tested including the source temperature (T_{source}=1100–1400 °C), the total pressure (p_{tot}=50–800 mbar), and the N_2 carrier gas flow in the range of 0–800 sccm. As mentioned earlier high T_{source} is required to supply enough Ga by physical vapour transport (PVT) to the seed holder. The evaporation time was kept constant at 4 h for all experiments. In addition to experimentally determined Ga losses, these results were qualitatively compared with theoretical values from the FactSage software [14] package in order to gain a better insight into the evaporation process.

Fig. 2 shows the molar ratio between gaseous and liquid gallium for varying pressures and temperatures in a closed system containing 1 mol Ga and 5 mol N_2, calculated for thermodynamic equilibrium by FactSage [14]. As expected, the balance shifts towards gaseous Ga corresponding to higher temperatures and lower pressures. Note that the ratio is given on a logarithmic scale and reasonable values are reached only at "extreme" parameters of low pressures and high temperatures. This would correspond to process parameters, which were actually excluded due to the decomposition behavior of GaN. However, the data reflect the situation in a static thermodynamic equilibrium. Since the growth system is open, N_2 carrier gas is permanently supplied into the system, kinetic effects occur. The simulations should reveal general trends, but do not provide quantitative usable values. Fig. 3 shows an Arrhenius plot of data yielded from evaporation experiments at a total process pressure of 200 mbar, varying source temperatures in the range from 1100 to 1350 °C, and two different N_2 carrier gas flow rates of 0 and 200 sccm. The expected evaporation increase is well observed for increasing temperatures as well as decreasing pressures (not shown). The effect of the N_2 carrier gas is obvious from the shift of the zero flow data compared to an applied flow. This means that an increase in Ga transport is observed by applying carrier gas flows, but, nevertheless, a maximum was reached already at 200 sccm and no significant increase was observed for higher fluxes (not shown). The determination of the activation energy for experiments with 200 sccm carrier gas flow yielded a value of (284 ± 9) kJ/mol, which is in good agreement with the literature data [15]. Due to very low evaporation rates without a carrier gas (a few tens of milligrams), only few data points were taken for these conditions and we desisted from fitting these data. Nevertheless, a line parallel to the fit of the other data is given as a guide for the eye reflecting the good agreement.

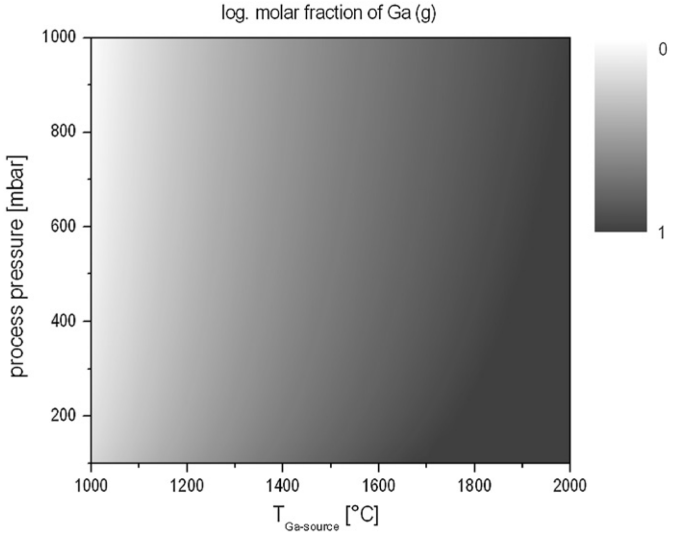

Fig. 2. Ratio of gaseous to liquid gallium vs. temperature and total pressure determined by FactSage for a closed system containing 1 mol Ga and 5 mol N_2.

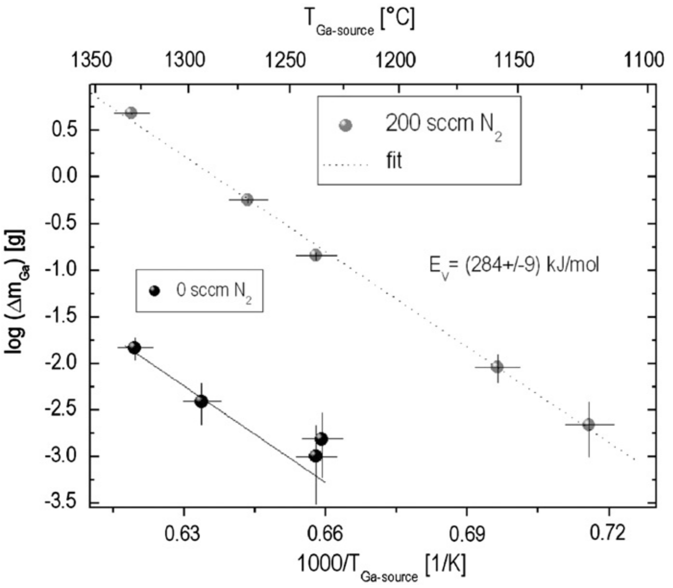

Fig. 3. Arrhenius plot of the experimentally determined Ga loss vs. source crucible temperature at 200 mbar, 4 h, and two N_2 carrier gas flows. The data for the 200 sccm experiments were fitted to determine the corresponding activation energy. A line with the same slope as the fit is given as a guide for the eye for the 0 sccm data also.

In summary, we have tested the evaporation characteristics of Ga from our growth setup and found both, a very good suitability for the planned application in the plasma-assisted processes due to reasonably high evaporation rates and a good correspondence of the activation energy of gallium between the literature and the experimental data. However, due to the partly contradictory requirements for GaN growth in terms of process temperature and pressure (as discussed earlier) the presented results might not totally reflect the optimal situation, but up to our opinion the developed Ga source provides sufficient room for any necessary parameter variations.

The efficiency of the Ga evaporation – ratio of Ga deposited on the seed holder vs. mass loss of the Ga source – should be maximal. The deposited mass should correspond to a minimal growth rate of R=10 μm/h, i.e. after 4 h of process and on a substrate of 2 cm diameter 64 mg of gallium should be found, calculated with:

$$m_{Ga} = \frac{M_{Ga}}{M_{Ga}+M_N} \times \frac{\pi}{4} d^2 h \rho_{GaN} \qquad (1)$$

where the molar masses of Ga and N are M_{Ga}=69.72 g/mol and M_N=14.007 g/mol, respectively and the density of GaN (300 K) is ρ=6.15 g/cm^3.

Assuming that the entire evaporated Ga is deposited on the seed, one derives from Fig. 3 that the minimum source temperature is 1220 °C (with log 0.064 ~ −1.2).

4. Plasma source development

Designing a suitable nitrogen plasma source is a highly challenging task and before starting the manufacturing process, some

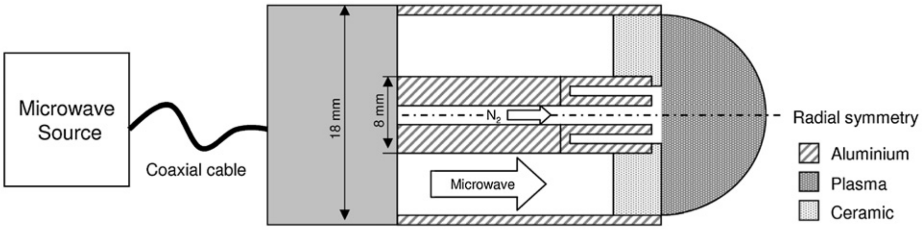

Fig. 4. Schematic drawing of the coaxial plasma source.

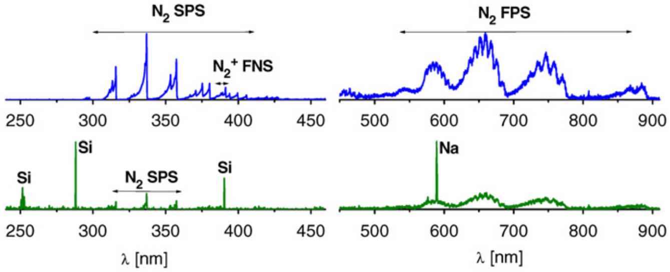

Fig. 5. Emission spectra of the pulsed microwave discharge in nitrogen at 100 mbar split in two wavelength regions. Spectra on the top and the bottom of the figure measured at microwave pulse duration of 2 and 100 ms, respectively. The spectral sensitivity of the instrument was not taken into account.

assumptions regarding the required amount of reactive nitrogen species should be estimated and will be presented in the following. The minimum flow density of reactive nitrogen N at the substrate surface (j_N) and the rate of N formation or flow I_N can be estimated from the rate R of growing GaN per second ($m_{GaN}=\rho RA$) as follows (data from Eq. (1)):

From the mass rate necessary for layer growth:

$$m_N = \frac{M_N}{M_N + M_{Ga}} \times \rho RA \tag{2}$$

the mol number is derived:

$$n_N = \frac{m_N}{M_N} = \frac{\rho RA}{M_N + M_{Ga}} \tag{3}$$

with $L=6.024\times10^{23}$ as Loschmidt number the flow of reactive nitrogen $I_N=n_N\ L\sim1.23\times10^{16}\,\mathrm{s}^{-1}$ follows and finally $j_N=I_N/A=3.9\times10^{15}\,\mathrm{cm}^{-2}\,\mathrm{s}^{-1}$ for a substrate diameter of 2 cm.

Nowadays no suitable standard nitrogen plasma source exists and the implementation of a microwave-based discharge source is favored in this study. The main challenge of sustaining microwave plasma at high pressures in nitrogen is the extremely high gas temperature in the discharge, estimated to be about 5000 K [16], and special efforts have to be considered in order to prevent the decomposition of surrounding materials. For this purpose, gas flows as high as 50 slm are usually applied (plasma torches), which have the disadvantage that crystal growth might be disturbed by highly turbulent flows. The application of short discharge pulses is another way to control the thermal load of the plasma. The repetitive and stable ignition can be achieved by inserting a resonant structure into the microwave field [17]. This concept was successfully realized in air ambient [18,19] together with the negative effect of a plasma propagation towards the magnetron within the waveguide.

In summary, the demands for the plasma source are:

- plasma formation in the growth area and controlling the thermal load (high pressures required)
- long-term stability and homogeneity as well as reproducibly formed plasma across an 1" wafer in order to achieve low defect density single crystals
- choice of suitable materials for the design of the plasma setup with respect to the high temperature and the presence of reactive species during the actual GaN crystal growth
- high rate of reactive nitrogen formation ($j_N\sim3.9\times10^{15}\,\mathrm{cm}^{-2}\,\mathrm{s}^{-1}$).

For the GaN crystal growth a new plasma source is under development, which does not include the requirements of a fixed enclosure in a rigid waveguide rather than being more flexible in mounting due to the use of a coaxial cable for the transport of microwave energy. In Fig. 4a sketch of this source is shown. The microwave source is a 2.45 GHz magnetron with a maximal output power of 2 kW and a custom-built power supply to drive the magnetron operation. This power supply can be operated in a continuous wave mode and a pulsed mode, the latter with stable current pulses of up to 1 A at 4 kV, pulse widths below 1 ms, and rising times of about 100 μs. Additionally, a wide range of pulse width settings is adjustable. The plasma is ignited at the end of the source. A ceramic barrier, nearly transparent for microwaves, is placed as shown in Fig. 4 to prevent the plasma back-traveling inside the source. The plasma source is mounted into a vacuum chamber and the N_2 gas is supplied through the inner tube of the source.

Emission spectra of a N_2 discharge at 100 mbar are presented in Fig. 5. Spectroscopic bands of neutral molecular nitrogen, belonging to the first and second positive system (FPS and SPS), as well as bands of ionic molecular nitrogen, namely first negative system (FNS), can be identified. The atomic lines of silicon and sodium are dominant for longer pulse duration indicating that the ceramics is thermally damaged under prolonged plasma contact. Both lines can be used as a sensitive indicator for critical thermal load, which can be reduced by shorter microwave pulses. Higher pressures require higher densities of the microwave power for the ignition and sustaining of the discharge, which in turn increases the gas temperature in the plasma. Therefore, a power supply for short pulses of high power with stable current together with the resonance structure for plasma ignition is critical for the development of a high pressure pulsed microwave discharge.

5. Conclusions

Based on the review of the ammonia-based GaN vapour growth it was concluded that the development of long-term stable sources for both gallium and reactive nitrogen is essential to overcome the restrictions in growth temperature and temperature gradients. For the case of the gallium source, operated with a N_2 carrier gas flow of 200 sccm, a moderate Ga source temperature of about 1300 °C can be realized in order to achieve reasonable evaporation rates. However, the design of the high-pressure plasma source is more challenging as not only the development itself is time consuming, but also the desired high-pressure operation causes extreme temperature conditions. One solution for reduced thermal loads could be the supply of short microwave pulses of high power and stable currents.

References

[1] R. Dwilinski, R. Doradzinski, J. Garczynski, L.P. Sierzputowski, A. Puchalski, Y. Kanbara, K. Yagi, H. Minakuchi, H. Hayashi, J. Cryst. Growth 311 (2009) 3015.
[2] H.P. Maruska, J.J. Tietjen, Appl. Phys. Lett. 15 (1969) 327.
[3] K. Fujito, S. Kubo, H. Nagaoka, T. Mochizuki, H. Namita, S. Nagao, J. Cryst. Growth 311 (2009) 3011.
[4] R. Juza, H. Hahn, Z. Anorg. Allg. Chem. 239 (1938) 282.
[5] I. Rahinov, N. Ditzian, A. Goldman, S. Cheskis, Appl. Phys. B 77 (2003) 541.
[6] J. Völter, M. Schön, Z. Anorg. Allg. Chem. 322 (1963) 212.
[7] D. Gogova, G.Yu. Rudko, D. Siche, H.-J. Rost, R. Fornari, A new approach to grow C-doped GaN thick epitaxial layers", pssc.201001005.R1.
[8] D.D. Koleske, A.E. Wickenden, R.L. Henry, J.C. Culbertson, M.E. Twigg,J. Cryst. Growth 223 (2001) 466.
[9] W.J. Mecouch, Z.J. Reitmeier, J.-S. Park, R.F. Davis, Z. Sitar, Phys. Status Solidi (c) 2 (7) (2005) 2129.
[10] M. Imade, M. Kawahara, F. Kawamura, M. Yoshimura, Y. Mori, T. Sasaki, Mater. Lett. 59 (2005) 4026.
[11] M. Imade, H. Kishimoto, F. Kawamura, M. Yoshimura, Y. Kitaoka, T. Sasaki, Y. Mori, J. Cryst. Growth 312 (2010) 676.
[12] K. Jacobs, D. Siche, D. Klimm, H.-J. Rost, D. Gogova, J. Cryst. Growth 312 (2010) 750.
[13] 〈http://www.ansys.com/〉.
[14] 〈http://www.factsage.com/〉.
[15] N.N. Greenwood, A. Earnshaw, Chemistry of the Elements, VCH Whily, Weinheim, 1990.
[16] M. Leins, L. Alberts, M. Kaiser, M. Walker, A. Schulz, U. Schumacher, U. Stroth, Plasma Process. Polym. 6 (2009) 227.
[17] U. Krohmann, T. Neumann, J. Ehlbeck, K. Rackow, patent 2007, WIPO Pub.No WO/2007/028813.
[18] J. Ehlbeck, R. Brandenburg, T. v. Woedtke, U. Krohmann, M. Stieber, K.-D. Weltmann, G.M.S. Krankenhaushygiene, Interdisziplinär 3 (2008) 1 〈http://www.egms.de/static/en/journals/dgkh/2008-3/dgkh000112.shtml〉.
[19] J. Ehlbeck, A. Ohl, M. Maass, U. Krohmann, T. Neumann, Surf. Coatings Technol. 174 (2003) 493.

5.2 Observation of microwave volume plasma ignition in ambient air

IOP Publishing | Plasma Sources Science and Technology

Plasma Sources Sci. Technol. **21** (2012) 035009 (8pp) doi:10.1088/0963-0252/21/3/035009

Observation of microwave volume plasma ignition in ambient air

A V Pipa, M Andrasch, K Rackow, J Ehlbeck and K-D Weltmann

Leibniz Institute for Plasma Science and Technology (INP Greifswald), Felix-Hausdorff-Str. 2 17489
Greifswald, Germany

E-mail: pipa@inp-greifswald.de and pipa@pisem.net

Received 14 November 2011, in final form 21 February 2012
Published 24 May 2012
Online at stacks.iop.org/PSST/21/035009

Abstract

A pulsed microwave (MW) plasma was maintained in a waveguide with an ignition pin. Images of the MW discharge were recorded during ignition in ambient air with millisecond time resolution and correlated with measurements of absorbed MW power. This work is focused on the quantification of ignition stability and observation of the plasma structure. Additionally, a time- and space-integrated emission spectrum in the range 220–770 nm is presented.

(Some figures may appear in colour only in the online journal)

1. Introduction

Maintaining a microwave (MW) discharge at high pressures is a challenging task, which can be interesting for a number of applications such as bio-decontamination [1], crystal growth [2], decomposition of NO in exhaust gases [3, 4] and volatile organic compounds [5], hydrogen production [6–8], enhancement of combustion [9, 10] and others [11–13]. The main problems are related to the high thermal energies of the plasma and difficulties with discharge ignition.

Several concepts of high-pressure MW plasma sources have been presented in the literature. One of them is MW microplasmas. They can be realized in a number of ways and only some of them are mentioned here: split-ring [14, 15] or slot [16] resonators, compact re-entrant cavity applicators [10], planar transmission line configuration corresponding to linear resonators [17] or microstripline applicators [18, 19], end of coaxial line [20] or in small torches [21, 22]. Small dimensions and low consumed power (1–100 W) allow avoidance of high thermal load, and spontaneous ignitions can be observed in high-quality resonators.

Other types of high-pressure MW discharges are plasma torches. They can be successfully operated with noble gases [11, 12, 23, 24]. The nozzle of the torch forms the electric field and works as a field applicator for stable plasma generation. The nature of the ignition process is not often mentioned. In case of operation in nitrogen a metallic nozzle is not usually used. The plasma is generated in a fused silica or quartz tube and a high gas flow (20–150 slm) is applied to avoid the detrimental wall burning and to stabilize the plasma [3, 4, 25].

The idea of using a pulsed MW discharge in order to control thermal load from a plasma looks very attractive but it is necessary to ensure stable and repetitive plasma ignition. The ability for repetitive plasma ignition limits the plasma off-time and therefore the reduction in thermal load. Lowering the pressure or provoking an arc by an external electric-spark system, for example as used in [9, 26], could not support repetitive ignition. Even at low pressures repetitive and stable ignition often requires additional effort. An axial short circuit was applied in [27]. The same short circuit in combination with $BaTiO_3$ pellets, which have a high dielectric permittivity ($\varepsilon = 1000$), facilitates pulsed MW discharges at 800 mbar in air-like gas mixtures [5]. Construction of the short circuit is not described.

The ignition can be initialized with an external resonance cavity [3, 4], but it does not support pulses with long off-time and thus the ability to control thermal load from the plasma are rather limited. A pulsed MW discharge was successfully obtained at high powers (15–100 kW, 9.04 GHz) at the end of a tungsten needle inserted into the waveguide system [6, 7]. The discharge is formed from a bundle (about ten) of filaments on the top of the needle and does not occupy a large volume. At higher MW powers (>1 MW, 110 GHz) focused MWs can cause a free-space breakdown in air at near-atmospheric pressure [28]. The plasma is highly filamentary with dimensions of several millimeters.

0963-0252/12/035009+08$33.00

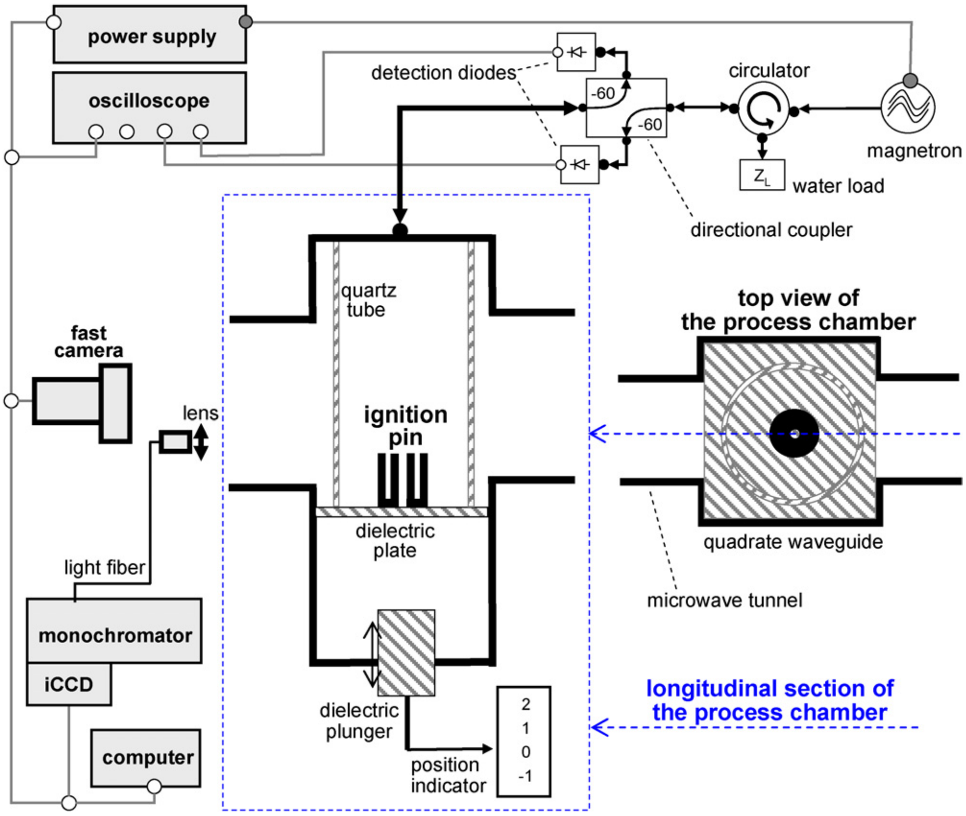

Figure 1. Experimental setup.

In [29] a resonant structure was applied as the ignition device (ignition pin) for volume plasmas, which propagate through a waveguide system. The concept of ignition pin has fundamental peculiarities and it should be distinguished from all those presented above. A resonance structure amplifies the electric field quite strongly in comparison with the metallic nozzle used in torches [11, 12, 23, 24] or tungsten needle applied in high power discharges [6, 7]. The ignition pin provokes plasmas with relatively large volume and consumes higher power in contrast to microplasmas [10, 14–22]. The principal difference from resonant cavities [3, 4] is that the volume discharge is maintained outside the resonator.

The idea was further developed by two different research groups. Axially symmetric resonator designs suggested in [30, 31] are used for ignition of MW torches but a vortex gas flow has been applied for protection of the reactor walls instead of pulse operation mode. Another improved design of the ignition pin [32] allows one to obtain stable and repetitive plasma ignition in ambient air. This invention has been used to treat plastic bottles by MW plasmas [1] without any external gas flow, which indicates an excellent control of the thermal load from the plasma.

The goal of this work is to observe and characterize MW discharge ignition in ambient air induced by a pin developed in [32]. The appearance of the volume plasma and stability of its ignition define the performance of the ignition pin in the present development stage. To the best of the authors' knowledge the ignition stability of MW plasmas at atmospheric pressure has not yet been demonstrated. Thus, it could not be compared with other investigations.

2. Experimental setup

The experimental setup is schematically shown in figure 1. A home-made power supply was used to drive a 2.455 GHz magnetron with maximal output power of 2 kW. The magnetron was decoupled from the rest of the MW setup by a circulator, which directed the reflected power to a matched water load. MW energy was transported by R 26 waveguides. Forwarded and reflected MW power was separated by a directional coupler with a coupling factor of −60 dB. To measure the powers detection diodes were used.

A quadrate waveguide with an edge length of 92 mm served as the process chamber. A special MW coupling system was developed to predominately excite the E11-modus. This MW setup has the advantage that the wavelength increases to 354 mm inside the reactor. Due to this fact the plasma is more homogeneous along the propagation direction. The process chamber has two rectangular open areas on opposite sides, with a cross section of 52 mm × 170 mm. To reduce the leakage of MW radiation through the open areas a special MW tunnel has been designed [33]. The tunnel allows visual observation of the discharge and protects the operator from the MW power, which was kept below the standard (DIN EN 60519-6) value outside the chamber.

The chamber is terminated by a short cut, which is adjustable by a movable dialectical plunger. Thus, the position of the electric field maxima in the process chamber can be controlled by the movement of the plunger. Millimeter paper is used as a position indicator for the plunger. The displacement of the standing MW in dependence on the plunger location,

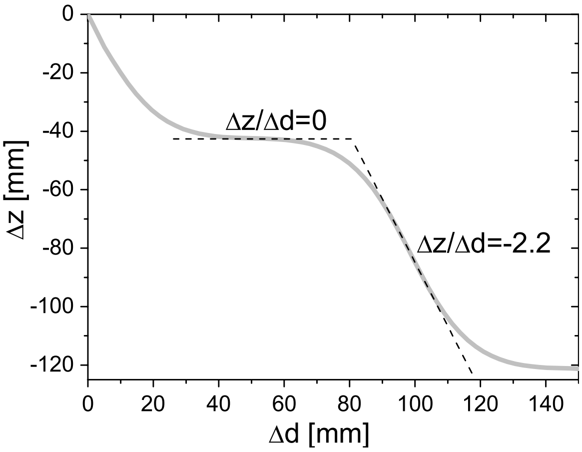

Figure 2. Simulated relative position of the standing wave (Δz) in dependence on the relative dielectric plunger position (Δd). Straight lines indicate situations when the position of the plunger does not influence the standing wave and when shift of the plunger by 1 mm leads to a change in the standing wave position up to 2.2 mm.

which was simulated with CST Microwave Studio, is presented in figure 2. According to the simulations a shift of the plunger by 1 mm can lead to a change in the standing wave position up to 2.2 mm.

The ignition pin is placed on a dielectric plate, which is fixed on the walls of the chamber. The ignition pin is an axially symmetrical resonator, see figure 1 developed in [32]. The same pin structure has been used in [1, 34]. A quartz tube, 55 mm external diameter, protects the conductive walls of the chamber from plasma attachment.

The images of the discharge were recorded by a fast camera (Photron FastcamPCI-R2) with millisecond time resolution. High time resolution restricts the working area of the CCD chip on the fast camera. In order to increase the discharge observation area the camera was moved couple of meters away from the discharge. The final images correspond to an observation area of approximately $8 \times 8\,\mathrm{cm}^2$. The camera and power supply were synchronously triggered by a computer-generated TTL pulse.

An iCCD camera (PI-MAX 1024-E.25/G/II P43, Princeton instruments) and a 0.5 m spectrograph (Acton SpecPro 500i) were used for recording the emission spectra. The triple turret of the spectrometer was equipped with two gratings: $150\,\mathrm{gr\,mm}^{-1}$, 300 nm blazed and $2400\,\mathrm{gr\,mm}^{-1}$, 500 nm blazed. A quartz light fiber leads the light into the spectrometer. The entrance aperture of the light fiber was placed in the focal plane of a quartz lens, which has collected parallel light from the volume slightly above the ignition pin.

3. Time development of the discharge ignition

The fast camera is adjusted to record images every millisecond of a single discharge ignition. A set of images is selected for presentation in figures 3 and 4 in correlation with trigger pulse and absorbed power. The first 10 ms after switching on the MW power are shown in detail and the subsequent images are selected with a larger time step. In order to have intuitive impression of the time scale the time difference between two scale ticks was kept equal to 1 ms. Figures 3 and 4 represent observation under similar experimental conditions but recorded with different apertures in front of the camera objective.

The trigger pulse is proportional to the voltage applied to the magnetron and its shape is similar to the forward power. A small ramp was applied at the beginning of the pulse in order to improve the stability of the power supply at the moment when the magnetron was switched on. The magnetron starts to generate MW power when the threshold voltage is reached. This moment can be indicated by means of artificial signals from the power measurements during the first millisecond (in figure 3 it is in the negative direction).

The images in figure 4 are recoded a with larger aperture when the system is more sensitive for photon detection. Microplasma emission is seen immediately after supplying the MW power. The appearance of the seed plasma will not guarantee a volume breakdown which requires longer times to be developed. Manufacturing defects in the ignition pin or in other parts of the setup can disturb the discharge expansion from the seed plasma.

In the presented examples, figures 3 and 4, absorbed MW power stays under the detection limit for the first 3 ms. Then the absorbed power starts to increase and reaches its maximum (about 1 kW) at 6 ms, which correlates with the growth of the plasma volume. The time moment between 5 and 7 ms can be considered as the time of volume plasma ignition. The images after 5 ms appear as if different plasma channels compete for further development. At about 10–15 ms the plasma structure is stabilized and discharge development slows down. From the photos made with a larger aperture, figure 3, it is possible to see clearly that the luminescent area still increases. Its width becomes restricted by the internal walls of the quartz tube and the top part expands above the camera field of view (40–60 ms). During this time two bright plasma channels, which are rotating around the top of the ignition pin, are formed. The channels merge into a large-volume plasma. The structure recalls an arrow-head in the time interval 60–100 ms. The plasma channels, which are attached to the ignition pin, lose their brightness with growth of the plasma volume, 100–160 ms. At 160–165 ms the luminescent area is almost de-attached from the ignition pin and the lowest plasma border starts to propagate along the quartz tube. At 166 ms the MW power is switched off and the subsequent photos represent discharge afterglow, which can be observed for longer than 30 ms.

The photos made with a small aperture, figure 4, indicate the complex internal structure of the discharge. The ignition filament (14–15 ms) develops into a toroidal structure (19–30 ms) which then stretches (30–40 ms) and transforms into two top-merged filaments (40–80 ms). Then the filaments form one dominant discharge channel (80–160 ms). One end of the channel is attached to one side of the ignition pin and the other end is stretched out along the middle of the quartz tube. On the first afterglow photo (166 ms) the bright central part of the channel is clearly visible but soon it becomes diffuse and then the intensity decreases relatively homogeneously.

Thus, the ignition of the volume plasma takes several milliseconds and is associated with an increase in absorption

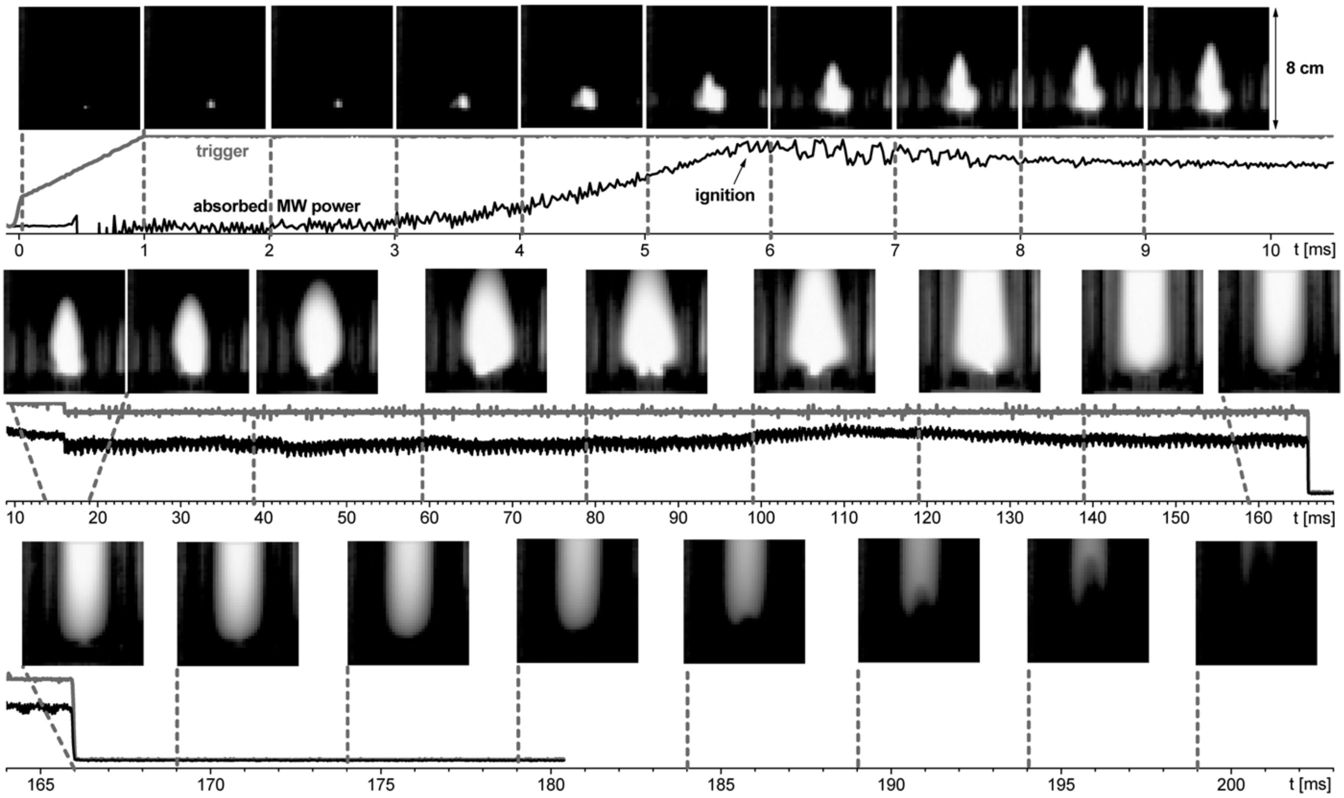

Figure 3. Fast camera photos and absorbed power during discharge ignition development. Exposure time of the photos is 1 ms. Broken lines indicate the moment when the exposition starts.

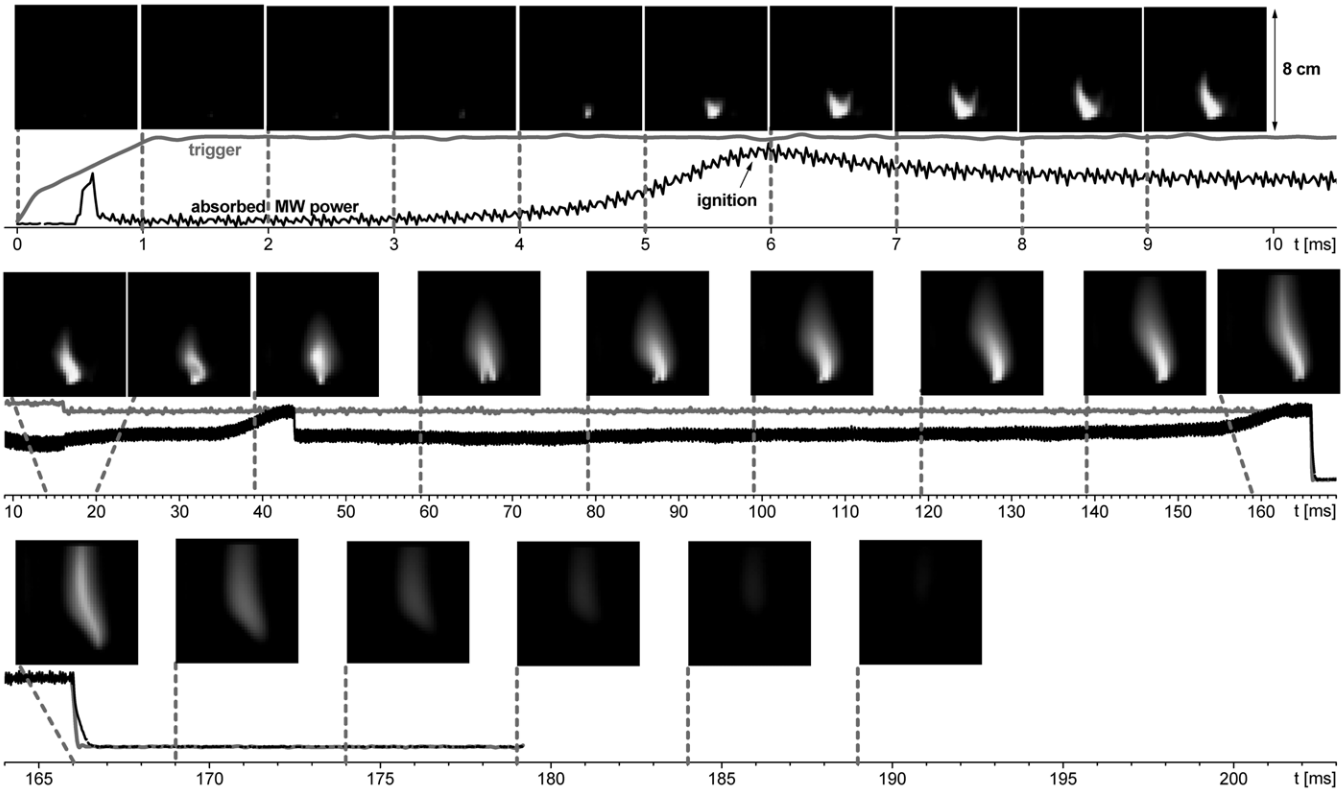

Figure 4. Fast camera photos with reduced aperture and absorbed power during discharge ignition development. Exposure time of the photos is 1 ms. Broken lines indicate the moment when the exposition starts.

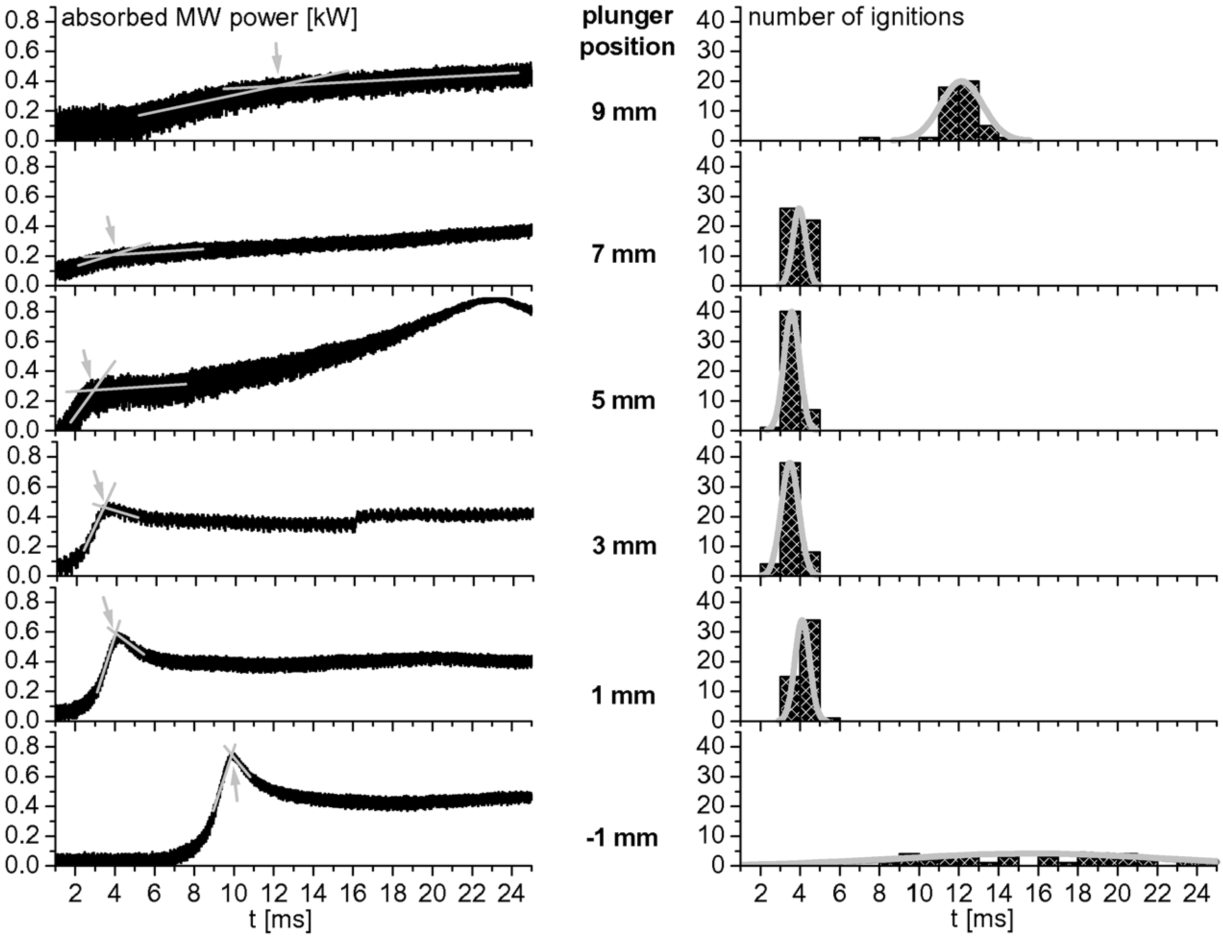

Figure 5. Examples of absorbed MW powers (left) and number of plasma ignitions (right) as a function of time measured at different plunger positions. Gray straight lines on the left side indicate an algorithm for determination of ignition times, which are marked by arrows. Gray lines on right side are fits of the histogram data points by Gaussian function.

power. The local maximum of the absorption power waveform can be considered as the moment of ignition with a precision of ±1 ms. Discharge development pass is through different stages and in 150 ms a self-propagating plasma is formed.

4. Stability of the ignition

The idea for generation of the self-propagating plasma [29] is as follows. The electric field of MWs builds maxima and minima along the process chamber. The configuration of the electric field can be predicted by means of standard calculations [34]. The ignition pin is placed slightly below a maximum in a such way that the strength of the electric field is sufficient for plasma ignition and after ignition the plasma should move toward the field maximum, i.e. away from the pin. The optimum position is a compromise between stable plasma ignition and plasma propagation.

Fine adjustment of the electric field configuration is done by movement of the dielectric plunger, which terminates the waveguide system. In order to understand the stability of discharge ignition it was observed for different plunger positions. The position used for measurement in figures 3 and 4 was marked as zero, as an optimum one. A plunger shift toward the magnetron was selected as the positive direction. The measurements were focused on the first 25 ms of the MW pulse. Examples of the measured absorbed powers and discharge ignition statistics for different plunger positions are shown in figure 5.

The time of ignition was assigned from the measured time dependence of the absorbed powers. The assignment is unambiguous for plunger positions from −1 to 3 mm due to the relatively sharp local maximum of the absorbed power. The histogram on the right-hand side of figure 5 shows how many ignitions from 50 experiments were detected at a certain time in intervals of 1 ms.

Scattering of the time lag and its relatively large value for position −1 mm indicate that the ignition pin is exposed to a low electric field. The electric field at position −2 mm is insufficient for discharge ignition. If the maximum of the electric field were above the ignition pin in optimum position 0, see figure 1, then the negative shift of the plunger should move it in the positive direction, away from the pin, see figure 2. The positive shift of the plunger brings the electric field maximum closer to the pin. Thus, the decrease in the time lag and improvement in ignition stability with positive shift of the plunger (1 and 3 mm) can be interpreted as an increase in the electric field in front of the ignition pin. Additionally, at large positive shifts, 3 mm and more, the discharge tends to stay on the pin and the self-propagating plasma is not observed.

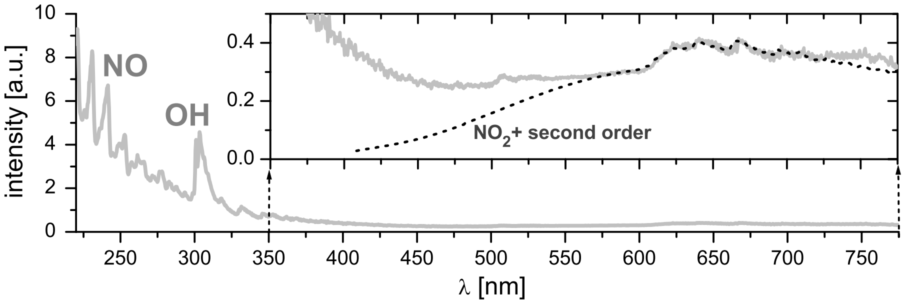

Figure 6. Overview spectrum of the MW discharge corrected for relative spectrometer sensitivity.

When the plunger moved from position −1 to 3 mm the maximum of the absorbed power became lower and wider. Ignition time for positions 5–9 mm was assigned to a change in the growth of the absorbed power. Two local parts of the power dependence were intuitively selected and approximated by a straight line, as shown in figure 5. Crossing points of the lines were considered as ignition moments, and are indicated by arrows in figure 5. This algorithm coincides with the selection of maxima for smaller plunger shifts (−1, 1 and 3 mm) and also follows the trends in modification of absorption power time dependence with plunger shift. The existence of the volume plasma can be confirmed by well-detected absorbed power because power absorbed by the microplasma is under our detection limit, see figure 3. Thus, statistical histograms were completed for larger shifts (5, 7 and 9 mm). The histograms were approximated by a Gauss function as an assumption for refection of the ignition probabilities, see figure 5.

The maximum of ignition probability has the smallest time lag at the plunger position 3–5 mm. It is plausible to assume that the ignition pin interacts with the maximum electric field at the middle position of 4 mm. At lower plunger positions (<4 mm) the maximum of the electric field is above the tip of the ignition pin, and at higher positions (>4 mm) below it. If the plunger shift from the middle position is larger than 6 mm (positions −2 and 10 mm) then repetitive plasma ignition is not observed. Thus, present observations are consistent with the idea of self-propagating plasma, indicating that the zero plunger position is a compromise between stable ignition and propagation of the discharge.

Finally, from the statistical diagrams in figure 5 the following can be concluded for the experimental setup under investigation: (i) the ignition pin is exposed to the maximum electric field at the plunger position of about 4 mm, (ii) ignition of the volume plasma takes longer than 2 ms, (iii) the uncertainty in the ignition time can be as low as ±1.5 ms. Additionally, the measured time dependence of the absorbed MW power can indicate whether the ignition pin is situated above or below the maximum of the electric field.

5. Emission spectrum

As a first spectral characterization of the discharge the time- and space-integrated (with 300 ms exposure time) overview spectrum is measured, see figure 6. The emission spectra are taken in two spectral windows 200–530 nm (blue) and 450–780 nm (red) with a low-resolution grating (150 gr mm^{-1}). A glass plate was used as the UV filter with the edge at 300–320 nm. Figure 6 is constructed from three parts: 200–402 nm is the blue window measured without a glass plate, 400–530 nm and 450–780 nm are blue and red windows measured with a glass plate. Relative spectral sensitivity, which was measured with tungsten ribbon and deuterium lamps, was taken into account before plotting the spectra together.

The main emission appears in the UV region, see figure 6. But the discharge has a powerful emission in the visible part of the spectra as well. Observation of the discharge through a 2 mm thick glass plate can be painful for the eye. For interpretation of the visible part of the recorded spectrum it is compared with the shape of chemiluminescent continuum of the NO$_2$ molecule. The data on spectral distribution of the continuum were taken from [35] and normalized at 600 nm. Above 600 nm the glass plate could not suppress light from the second order of the diffraction grating. An additional spectral window 200–400 nm was measured with the glass plate. The obtained data were added to the continuum data after scaling of the intensities and wavelength. Thus, the influence of the second-order emission was estimated. From the good agreement between spectral shape of the NO$_2$ continuum, corrected for second-order disturbance, and measured spectra it is possible to conclude that the emission of NO$_2$ molecule dominates in the spectrum above 550 nm.

The UV part of the spectra can be assigned to molecular bands of NO and OH with high rotational temperatures. The spectral region of the OH band was measured with a high spectral resolution, which was reached at second order of the 2400 gr mm^{-1} grating, for accurate identification of the emission and probable estimation of the rotational temperature. The presented spectrum, see figure 7, was recorded in one spectral window. The measurements are compared with simulations of OH band with rotational temperatures 3000 and 7000 K [36]. Differences between simulated and measured spectra as well as the large uncertainty in rotational temperature can be related to several facts: (i) non-Boltzmann distribution of the population densities over rotational levels [37], (ii) overlapping with an emission of other molecules, (iii) inhomogeneous structure of the discharge with high temperature gradients and (iv) difficulties with accurate subtraction of the background and sensitivity calibration for second order of the grating.

The conclusion about the emission of NO molecules was based on the simulation of the low-resolution spectrum,

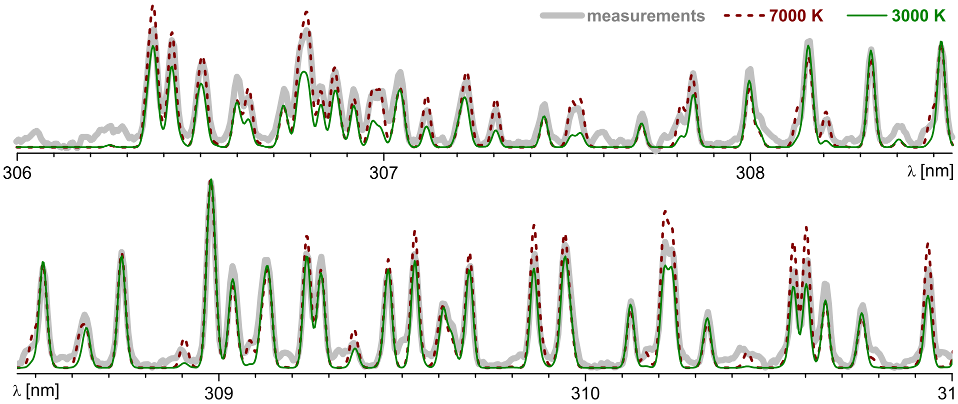

Figure 7. Spectrum of OH radical measured with high resolution and simulated with [36] for 3000 and 7000 K rotational temperatures.

shown in figure 6. The spectral part (220–290 nm) can be described as the superposition of the spectra of the NO_γ system calculated with rotational and vibrational temperatures in the range 10 000–30 000 K. The fit of the low-resolution spectrum is considered as less relevant and is hence omitted in this work.

6. Summary

The current state of the art for repetitive ignition of volume MW discharges in ambient air is presented. Recent development of the ignition pin structure significantly improves the stability of plasma ignition that allows investigation of the microwave plasma in ambient air in more detail.

Due to the enhancement of the electric field by the resonant structure, a seed plasma appears on top of the ignition pin immediately after switching on the microwave power. Strong interaction of the seed plasma with applied microwaves leads to the development of discharge structures in the volume. Ignition of the volume plasma requires several milliseconds and can be indicated as an increase in absorbed power. The jitter in the ignition time of volume plasma can be below ±2 ms for the present development. Additionally, the volume plasma is characterized by a long afterglow which can be observed over 30 ms after switching off the power. Due to the afterglow it is difficult to visually separate the active plasma region, where electrons gain energy from the electric field, and the recombination region, where chemical energy of the active species leads to the emission.

The main emission of the plasma is concentrated in the ultraviolet part of the spectra which originate from the optical transition of NO molecules. Strong emission of OH radicals is recognized in the spectra as well and indicates rotational temperature above 3000 K. At wavelengths higher than 550 nm chemiluminescence continuum of the NO_2 molecule dominates.

Acknowledgments

The authors are grateful to Andre Schella for statistics measurements and discharge images with reduced aperture, Udo Krohmann and Torsten Newmann for useful discussions and Alfred Scholz for technical assistance. This work was partly supported by the Leibniz Society (SAW project) and partly through BMBF funded network project ‘Plasmose’ (FKZ 13N8666).

References

[1] Ehlbeck J, Brandenburg R, v Woedtke T, Krohmann U, Stieber M and Weltmann K-D 2008 PLASMOSE—antimicrobial effects of modular atmospheric plasma sources *GMS Krankenhaushygiene Interdisziplinär* **3** 1

[2] Siche D, Gogova D, Lehmann S, Fizia T, Fornari R, Andrasch M, Pipa A and Ehlbeck J 2011 PVT-growth of GaN bulk crystals *J. Cryst. Growth* **318** 406–10

[3] Pott A, Doerk T, Uhlenbusch J, Ehlbeck J, Höschele J and Steinwandel J 1998 Polarization-sensitive coherent anti-Stokes Raman scattering applied to the detection of NO in a microwave discharge for reduction of NO *J. Phys. D: Appl. Phys.* **31** 2485–98

[4] Baeva M, Gier H, Pott A, Uhlenbusch J, Höschele J and Steinwandel J 2001 Studies on gas purification by a pulsed microwave discharge at 2.46 GHz in mixtures of $N_2/NO/O_2$ at atmospheric pressure *Plasma Chem. Plasma Process.* **21** 225–47

[5] Rousseau A, Dantier A, Gatilova L, Ionikh Y, Röpcke J and Tolmachev Y 2005 On NO_x production and volatile organic compound removal in pulsed microwave discharge in air *Plasma Sources Sci. Technol.* **14** 70–5

[6] Babaritskii A I, Gerasimov E N, Demkin S A, Zhivotov V K, Knizhnik A A, Potapkin B V, Rusanov V D, Ryazantsev E I, Smirnov R V and Sholin G V 2000 The repetitive microwave discharge as catalyst for a chemical reaction *Techn. Phys.* **45** 1411–16

[7] Rusanov V D, Babaritskii A I, Bibikov M B, Gerasimov E N, Zhivotov V K, Knizhnik A A, Potapkin B V and Smirnov R V 2001 Properties of a catalytically active pulsed microwave discharge at atmospheric pressure *Dokl. Phys.* **46** 242–6

[8] Uhm H S, Kim J H and Hong Y C 2007 Disintegration of water molecules in a steam-plasma torch powered by microwaves *Phys. Plasmas* **14** 073502

[9] Hong Y C, Cho S C, Bang C U, Shin D H, Kim J H, Uhm H S and Yi W J 2006 Microwave plasma burner and temperature measurements in its flames *Appl. Phys. Lett.* **88** 201502

[10] Hemawan K W, Wichman I S, Lee T, Grotjohn T A and Asmussen J 2009 Compact microwave re-entrant cavity applicator for plasma-assisted combustion *Rev. Sci. Instrum.* **80** 053507

[11] Al-Shamma'a A I, Wylie S R, Lucas J and Pau C F 2001 Design and construction of a 2.45 GHz waveguide-based microwave plasma jet at atmospheric pressure for material processing *J. Phys. D: Appl. Phys.* **34** 2734–41

[12] Zajickova L, Elias M, Jasek O, Kudrle V, Frgala Z, Matejkova J, Bursik J and Kadlecikova M 2005 Atmospheric pressure microwave torch for synthesis of carbon nanotubes *Plasma Phys. Control. Fusion* **47** B655–66

[13] Dani I, Mäder G, Dresler P, Linaschke D, Lopez E, Kaskel S and Bayer E 2009 Atmospheric-pressure plasma for solar cell manufacturing *Contrib. Plasma Phys.* **49** 662–70

[14] Iza F and Hopwood J A 2003 Low-power microwave plasma source based on a microstrip split-ring resonator *IEEE Trans. Plasma Sci.* **31** 782–7

[15] Iza F and Hopwood J A 2005 Split-ring resonator microplasma: microwave model, plasma impedance and power efficiency *Plasma Sources Sci. Technol.* **14** 397–406

[16] Gesche R, Kühn S and Andrei C 2008 Plasma ignition in a quarter-wavelength microwave slot resonator *J. Phys. D: Appl.Phys.* **41** 194003

[17] Gregorio J, Leroy O, Leprince Ph, Alves L L and Boisse-Laporte C 2009 Design of a microwave microplasma source at atmospheric pressure *IEEE Trans. Plasma Sci.* **37** 797–808

[18] Narendra J J, Grotjohn T A and Asmussen J 2008 Microstripline applicators for creating microplasma discharges with microwave energy *Plasma Sources Sci. Technol.* **17** 035027

[19] Kim J and Terashima K 2005 2.45 GHz microwave-excited atmospheric pressure air microplasmas based on microstrip technology *Appl. Phys. Lett.* **86** 191504

[20] Kiss'ovski Zh, Kolev M, Ivanov A, Lishev St and Koleva I 2009 Small surface wave discharge at atmospheric pressure *J. Phys. D: Appl. Phys.* **42** 182004

[21] Stonies R, Schermer S, Voges E and Broekaert J A C 2004 A new small microwave plasma torch *Plasma Sources Sci. Technol.* **13** 604–11

[22] Yuji T, Fujii S, Mungkung N and Akatsuka H 2009 Optical emission characteristics of atmospheric-pressure nonequilibrium microwave discharge and high-frequency DC pulse discharge plasma jets *IEEE Trans. Plasma Sci.* **37** 839–45

[23] Moisan M, Zakrzewski Z and Rostaing J C 2001 Waveguide-based single and multiple nozzle plasma torches: the TIAGO concept *Plasma Sources Sci. Technol.* **10** 387–94

[24] Castanos-Martinez E, Moisan M and Kabouzi Y 2009 Achieving non-contracted and non-filamentary rare-gas tubular discharges at atmospheric pressure *J. Phys. D: Appl. Phys.* **42** 012003

[25] Fleisch T, Kabouzi Y, Moisan M, Pollak J, Castanos-Martinez E, Nowakowska H and Zakrzewski Z 2007 Designing an efficient microwave-plasma source, independent of operating conditions, at atmospheric pressure *Plasma Sources Sci. Technol.* **16** 173–82

[26] Potts H and Hugill J 2000 Studies of high-pressure, partially ionized plasma generated by 2.45 GHz microwaves *Plasma Sources Sci. Technol.* **9** 18–24

[27] Chabert P, Rousseau A, Gousset G and Leprince P 1998 On the influence of the gas velocity on dissociation degree and gas temperature in a flowing microwave hydrogen discharge *J. Appl. Phys.* **84** 161–7

[28] Cook A, Shapiro M and Temkin R 2010 Pressure dependence of plasma structure in microwave gas breakdown at 110 GHz *Appl. Phys. Lett.* **97** 011504

[29] Ehlbeck J, Ohl A, Maaß M, Krohmann U and Neumann T 2003 Moving atmospheric microwave plasma for surface and volume treatment *Surf. Coat. Technol.* **174–175** 493–7

[30] Leins M, Baumgärtner K-M, Walker M, Schultz A, Schumacher U and Stroth U 2007 Studies on a microwave-heated atmospheric plasma torch *Plasma Process. Polym.* **4** S493–7

[31] Leins M, Alberts L, Kaiser M, Walker M, Schultz A, Schumacher U and Stroth U 2009 Development and characterisation of a microwave-heated atmospheric plasma torch *Plasma Process. Polym.* **6** S227–32

[32] Krohmann U, Neumann T, Ehlbeck J, Rackow K Method and device for ignition and generating an expanding diffuse microwave plasma and method and device for plasma treating surfaces and substances by using this plasma *Patent 2007, WIPO Pub.No WO/2007/028813*

[33] Ehlbeck J, Andrasch M, Schnabel U, Rackow K, Neumann T, Krohmann U and Weltmann K-D 2010 Dekontamination von Primärverpackungen mittels Atmosphärendruckplasmen *Vakuum Forschung Praxis* **22** 10-6 (in German)

[34] Rackow K, Ehlbeck J, Krohmann U and Baeva M 2011 An atmospheric pressure microwave-driven plasma source for surface treatment *Plasma Sources Sci. Technol.* **20** 035019

[35] Sutoh M, Morioka Y and Nakamura M 1980 Absolute rate constant for the chemiluminescent reaction of atomic oxygen with nitric oxide *J. Chem. Phys.* **72** 20–4

[36] Luque J and Crosley D R 1999 LIFBASE: Database and Spectral Simulation Program (Version 1.5) *SRI International Report* MP 99-009 http://www.sri.com/psd/lifbase/

[37] Bruggeman P, Iza F, Guns P, Lauwers, Kong M G, Gonzalvo Y A, Leys C and Schram D C 2010 Electronic quenching of OH(A) by water in atmospheric pressure plasmas and its influence on the gas temperature determination by OH(A–X) emission *Plasma Sources Sci. Technol.* **19** 015016

5.3 Electron density measurements on an inductively coupled plasma with a one-port microwave interferometer

IOP Publishing Plasma Sources Science and Technology

Plasma Sources Sci. Technol. **21** (2012) 055032 (7pp) doi:10.1088/0963-0252/21/5/055032

Electron density measurements on an inductively coupled plasma with a one-port microwave interferometer

M Andrasch, J Ehlbeck, R Foest and K-D Weltmann

INP Greifswald, Felix-Hausdorff-Straße 2, 17489 Greifswald, Germany

E-mail: Andrasch@inp-greifswald.de

Received 10 January 2012, in final form 20 August 2012
Published 4 October 2012
Online at stacks.iop.org/PSST/21/055032

Abstract

A one-port microwave interferometer has been employed to measure the electron density in a conventional reactor for plasma-enhanced chemical vapour deposition (PECVD). As opposed to standard two-port configurations, which require two accessible viewports in the reactor, this setup uses only one port and is therefore readily coupled to standard industrial vacuum equipment. The interferometer works at 45.75 GHz and separates forwarded and reflected waves. A microwave mirror is positioned at the reactor wall opposite the viewing port. The capability of the method is demonstrated on the basis of exemplary measurements in an inductively coupled plasma (ICP, 13.56 MHz) suitable for PECVD. Line-integrated electron densities are measured for different conditions (Ar, $p = 0.1$–1 Pa, $P_{\mathrm{rf}} = 30$–1000 W). Langmuir probe measurements provide radial profiles of the electron density and are used as a comparative reference. These profiles are fitted with Bessel functions and serve as the basis for the interpretation of the interferometric data in terms of peak density, where the amplitude of these generic profiles is used as the free parameter. The densities obtained are in good agreement with the Langmuir probe results. Maximum values $1 \times 10^{18}\,\mathrm{m}^{-3}$ are obtained in the centre of the vessel at an axial distance of 0.24 m from the antenna window of the ICP source.

1. Introduction

Surface techniques assisted by non-thermal low-temperature plasmas have attained a respectable level of technological maturity over the last three or four decades. Objects with superior and unique surface properties and nm-scale structures can be processed. Plasma-assisted dry etching, e.g. has become fundamental in the semiconductor industry for processing integrated circuits [1]. Plasma- and ion-assisted deposition techniques create thin film optics such as interference filters or functional coatings [2] with unrivalled precision. It is widely acknowledged that optical coatings deposited under ion or plasma-ion assistance show promising properties like surface smoothness, low porosity and high optical homogeneity [3]. This can be attained with enhanced knowledge of the basic plasma parameters, such as densities, energies and fluxes of the relevant species for the specific plasma device [4]. In non-thermal plasmas, free electrons are the primary source of energy by virtue of inelastic collisions that lead to excitation and ionization. Therefore, the determination of the electron density can be considered as one of the fundamental tasks for the optimization of existing processes and the development of new ones. Moreover, the significance of models and simulations for predictive studies can be enhanced by providing reliable data on the prevailing electron densities.

Typical diagnostic methods to determine the electron density in non-thermal discharges are based on the measurement of the charge-carrier flux to electrostatic probes, the electromagnetic emission of (bound) electrons, the scattering of their electromagnetic radiation or their interaction with electromagnetic waves [5, 6]. The last principle involves resonant probes, such as the hairpin resonator [7, 8] or the multipole resonance probe [9], and interferometric methods [10–14], which are particularly favourable for reactive plasmas, e.g. the deposition of thin dielectric films. Here, they can provide measurements with a better reliability as compared with, e.g., Langmuir probes that are gradually coated during the process.

Standard methods for microwave interferometry often imply a two-port measurement, which requires two

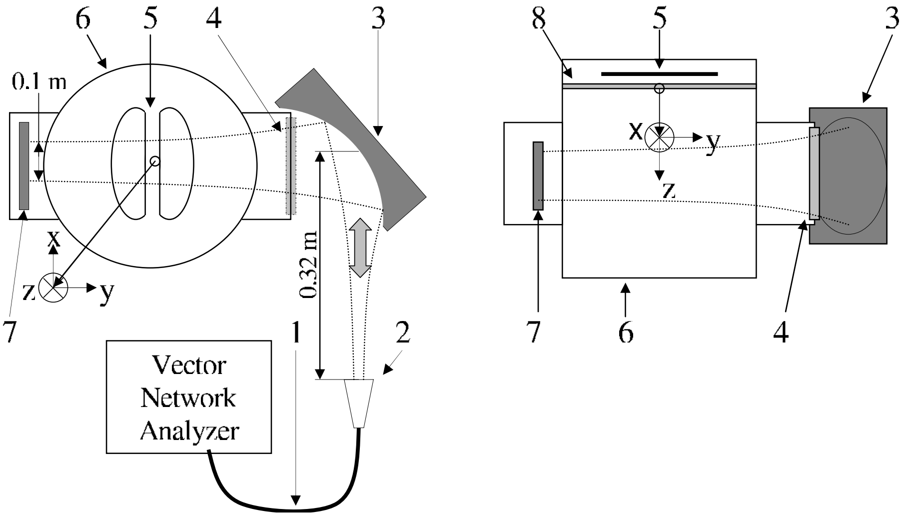

Figure 1. Schematics (left: top view, right: side view) of the experimental setup. 1—high precision flexible coaxial cable; 2—conical horn antenna; 3—elliptical mirror; 4—viewing port (silica); 5—RF antenna; 6—reactor vessel; 7—plane mirror; 8—coupling window (silica).

accessible ports with a direct line of sight through the region under study. As this is not the case for most industrial plasma reactors, the aim of this work is to demonstrate the applicability of microwave interferometry to a standard vacuum vessel with only one accessible viewport.

In order to realize the flexible interferometer configuration presented here, which is easily adaptable to different vacuum vessel diameters, we had to sacrifice in part the generally accepted design rule set by Goldsmith [15]. According to that rule, the curvature radii of the input and output Gaussian beam at the elliptical mirror should equal their distances from the focal points to the mirror-surface centre to reduce the excitation of high-order modes. In an attempt to validate this deviation from the rule, the transformation characteristics of the mirror are investigated using Comsol Multiphysics® to analyse the excitation of high-order modes and thus to evaluate the mirror configuration.

Exemplary measurements are carried out in technical vacuum equipment suitable for plasma-enhanced chemical vapour deposition (PECVD), to study the influence of varying power and duty cycle in particular. In a first step, however, the gas mixtures are restricted to Ar to allow a comparison with Langmuir probe measurements and to adopt the radial profiles obtained there. By fitting the values of the radial profiles with Bessel functions, quasi-spatially resolved density values from the microwave interferometric measurements can be derived. A parametric study on the process parameters—pressure and applied power—is a necessary prerequisite to applying the method for monitoring the electron density in plasma vessels used for PECVD.

2. Experimental setup

2.1. Discharge chamber

The ICP reactor consists of a cylindrical vacuum vessel (stainless steel, $D = 0.4\,\mathrm{m}$, $H = 0.45\,\mathrm{m}$, figure 1). A radio-frequency (RF) antenna with two D-shaped loops is positioned on top. The RF energy is coupled through a silica window into the reactor. The antenna is driven by a commercial RF generator (Cesar 1325 400V) working at 13.56 MHz with a maximum power output of 2500 W. A matching network adjusts the antenna to the 50 Ω line impedance of the RF generator output. The vacuum system is composed of a gas supply via a mass flow meter, a pumping system (turbomolecular pump with backing pump), a gate valve and pressure gauges. Thus, process pressures are stabilized and controlled. A front door (mounted on a DN 350 CF flange) is equipped with a viewing port (silica, $D = 0.2\,\mathrm{m}$) granting diagnostic access to the plasma region. The size of the viewing port could be reduced with regard to the microwave interferometer, if a higher frequency of the interferometer was used. On the opposite side of the cylindrical vessel, another DN 350 CF blind flange carries several diagnostic ports along with a socket for mounting the plane mirror on the vacuum side (No 7 in figure 1). If a plane surface, perpendicular to the direction of propagation of the interferometer beam, with a sufficient conductivity is present in the reactor, the setup can be established without a mounted plane mirror.

2.2. Microwave interferometer

A vector network analyser (Rohde & Schwarz ZVA 50) generates the electromagnetic wave for the interferometer (45.75 GHz). The wave is guided by a high precision flexible coaxial cable (Rohde & Schwarz ZV-Z97) to a mode coupler (Cernex CWK22335004F), which converts the radial symmetric transversal electromagnetic field distribution into the H_{10}-mode of a waveguide of the standard rectangular type WR-22. The conical horn antenna (Cernex CCA22424820-XX) is connected using a rectangular to circular transition (Cernex CRC220188). The wave emitted by the horn antenna is redirected and refocused by an elliptical mirror with a focal length of 300 mm. Goldsmith describes in [15] that the radii of curvature of the Gaussian beams at the elliptical mirror, so-called R_{in} and R_{out}, should be the same as the distances

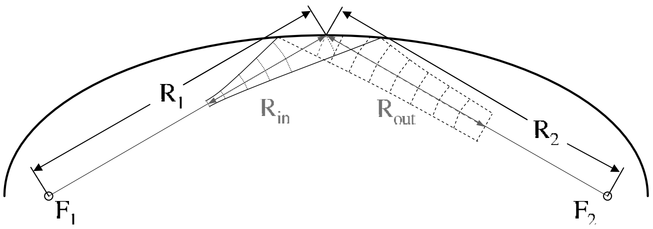

Figure 2. Schematics of the beam transformation at an elliptical mirror.

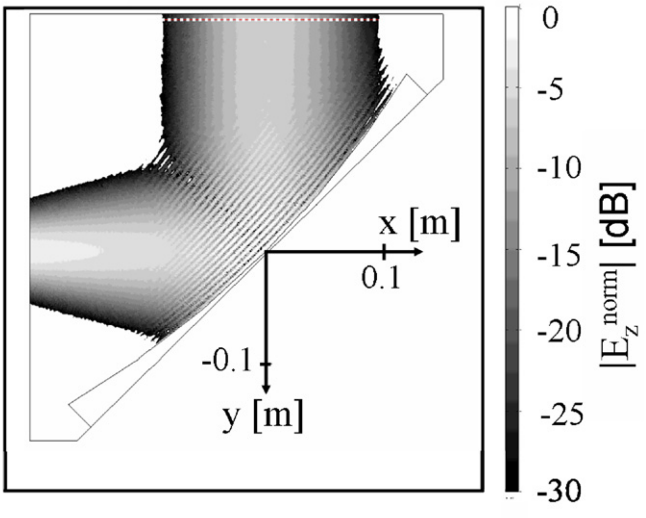

Figure 3. FEM results for the elliptical mirror. Shown is a two-dimensional plot of the normalized absolute value of the z component of the electric field for an input distance of $d_1 = 320\,\mathrm{mm}$.

from the focal points F_1 and F_2 to the centre of the mirror surface, named R_1 and R_2 (figure 2), to reduce the excitation of high-order modes. In this setup using the described reactor, the radius of curvature R_{in} is about 324 mm and R_{out} is about 2.5 m, whereas R_1 and R_2 are 600 mm. Hence, the ratio between these two radii does not meet the design rule of Goldsmith. Therefore, in order to estimate the influence of the setup on the excitation of high-order modes and thereby the operating range of the mapping, the transformation characteristics of the mirror were investigated for input distances d_1 from 300 to 340 mm with an increment of 10 mm using Comsol Multiphysics® (figure 3), this includes the used distance of 320 mm. In the investigated range of d_1 an ABCD matrix analysis was performed to estimate the undisturbed beam transformation of the mirror (figure 5). Due to the large value of R_{out} (2–5 m) the computed spherical phase front of the output beam can be approximated by the dashed line in figure 3 and was compared with the results of the ABCD matrix analysis (figure 4). Small deviations caused by the excitation of higher-order modes between both results were observed, but for the particular cases investigated here, the excitation of higher-order modes was found to be insignificant. Therefore, it is possible to set up different mappings matching different vessels with this mirror.

This Gaussian beam passes a silica window, which has the electrical length of an even-numbered multiple lambda-half transformer, and is reflected collinearly by a plane mirror placed in the focal point of the beam inside the reactor (No 7 in figure 1). The backward-directed wave is travelling to the vector network analyser, in which the forward and reflected waves are separated and the phase shift is resolved.

Directional elements, which are needed to separate forward and reflected waves independently, cannot be considered as components with ideal properties. For this reason, a calibration is necessary to reduce systematic errors. An overview of the calibration methods used in radio technology is given in [16]. In this experiment, the three-term method OSM is used, For this kind of calibration, the end of the coaxial cable is connected to an open, a short and a matching standard (Rohde & Schwarz ZV-Z36). This also ensures that the influence of the coaxial cable used is negligible. The relative phase difference is measured using the blanking method [17], where the plasma is turned off periodically to measure the phase shift caused by free space propagation. Using this method reduces errors caused by changes in the geometrical dimensions of the experiment (e.g. by thermal expansion) and provides the relative phase difference $\Delta\varphi$.

2.3. Langmuir probe

Since the concept of interferometry provides line-integrated data, additional information on the spatial distribution of the plasma density is required. The automated Langmuir probe [18] system is employed here (Smart Probe, Scientific Systems). The single-probe design consists of a wire connected to an LC element for RF compensation [19] and an additional reference probe which serves to compensate for low-frequency shifts in the plasma potential. The probe tip is made of tungsten and its length and diameter are $l = 5\,\mathrm{mm}$ and $d = 0.1\,\mathrm{mm}$, respectively. The probe tip is mounted on a lever which allows positioning within the whole plasma volume. A simplified analysis scheme is adopted for the determination of the electron density n_{e}. The zero crossing of the second derivative of the current–voltage characteristics is identified as the plasma potential V_{p}. From the probe current at V_{p}, n_{e} is inferred, where the electron temperature T_{e} needs to be known. T_{e} in turn is related to the integral value of the characteristics ranging from the floating potential V_{f} to V_{p}, assuming a Maxwellian electron energy distribution function (EEDF). This algorithm features a good robustness, although the accuracy of the results is limited. The more accurate method would be to consider the relation described by Druyvesteyn [20] which links the EEDF to the second derivative of the electron current. In order to take advantage of this ansatz, a model for the ion current also has to be adopted. The comparison of the different schemes—the second method contains a certain degree of uncertainty—revealed that it is appropriate to assign an error margin to n_{e} of $\Delta n_{\mathrm{e}}/n_{\mathrm{e}} = 20\,\%$.

2.4. Data analysis

The spatially resolved probe measurements provide profiles of n_{e}. On the other hand, it is known that the radial profiles in this arrangement can be described by a zero-order Bessel function of first kind $J_0(c\rho)$ [21], where ρ is the radial distance and c is a scaling parameter, thus providing the means to

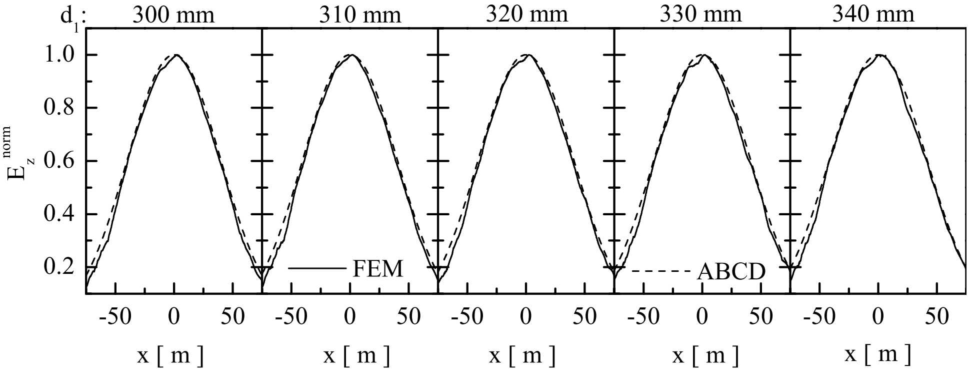

Figure 4. Normalized electrical field along the dashed line in figure 3 for different input distances d_1. Comparison of FEM analysis to ABCD matrix analysis of the mirror.

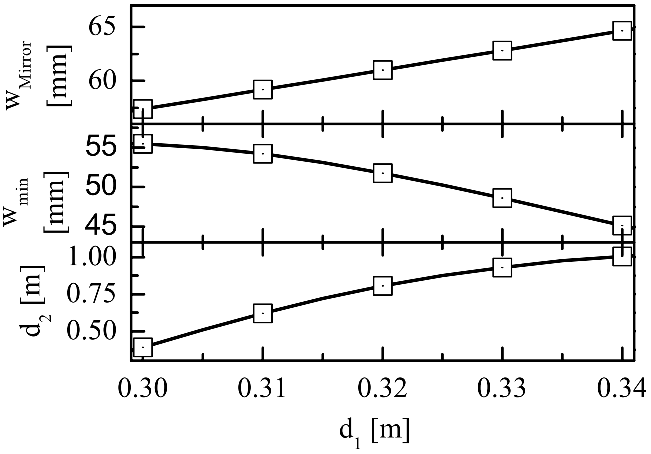

Figure 5. ABCD analysis of the elliptical mirror depending on the input distance d_1. The beam width of the input beam on the mirror plane is displayed by w_{Mirror}, the minimal beam width of the output beam by w_{min} and the distance from the focal point of the output beam to the mirror by d_2.

calculate the profiles for n_{e} along the line of sight of the microwave interferometer in the y-direction. The maximum of the electron density in the centre of the Bessel profile is

$$n_{\mathrm{e}}(y) = \hat{n}_{\mathrm{e}} f(y) = \hat{n}_{\mathrm{e}} J_0(|cy|). \tag{1}$$

With a known electron density profile it is possible to determine the absolute electron density, which is represented by its maximum in the centre of the Bessel profile $\hat{n}_{\mathrm{e}}$, from the relative phase difference $\Delta\varphi$ according to the following equation, which is based on [22] and modified by a factor of two to consider the twice-passing microwave beam through the plasma:

$$\hat{n}_{\mathrm{e}} = \frac{n_{\mathrm{c}} \lambda \Delta\varphi}{2\pi \int_{y_1}^{y_2} f(y)\,\mathrm{d}y}, \qquad n_{\mathrm{c}} = \left(\frac{2\pi c_0}{\lambda}\right)^2 \left(\frac{\varepsilon_0 m_{\mathrm{e}}}{e^2}\right), \tag{2}$$

where n_{c} is the cut-off electron density of the used interferometer. Electron mass and charge are m_{e} and e, respectively, c_0 represents the speed of light in vacuum, λ is the free space wavelength of the interferometer and ε_0 is the electric permittivity.

3. Results

The results of the Langmuir probe measurements are fitted by zero-order Bessel functions of first kind (equation (1)) to determine $\hat{n}_{\mathrm{e}}$ and c. The microwave passes the reactor at an axial position $z = 0.24\,\mathrm{m}$ and $z = 0\,\mathrm{m}$ is the surface of the coupling window. Hence, $c = 11\,\mathrm{m}^{-1}$ is calculated by linear interpolation of the profiles with $z = 0.16\,\mathrm{m}, 0.29\,\mathrm{m}$, shown in figure 6.

The results of the power-dependent static electron density for pressures in the range 0.1 –1 Pa are plotted in figure 7. For the investigated pressures, the electron density increases with power and also pressure. Taking into account that the recombination at the inner wall of the reactor is the main electron loss process, the equilibrium between electron generation and loss is determined by ambipolar diffusion to the inner walls. The diffusion constant D_{a} decreases with increasing pressure and thus the dominant loss process of the electrons is reduced. On the other hand, with increasing pressure, collisions between electrons and neutrals, which lead to regular electron generation, become more frequent. This ionization frequency also depends on the electron temperature, but due to the small change over pressure as reported by [23] this influence is weak. Accordingly, the equilibrium between electron generation and loss is shifted to higher electron densities in order to sustain the plasma.

Typically, inductively coupled plasmas exhibit two electromagnetic interactions between antenna and plasma [24]. The standard coupling is inductive (H-mode), but a capacitive coupling (E-mode) is also possible and characterized by relatively low electron densities. For the investigated pressures, 0.1 and 0.3 Pa, two regions with a different slope in the power-dependent electron density are detected. For low powers, the plasma is in the E-mode state. Above a certain threshold power, the electron density increases abruptly, caused by the transition from the E-mode to the H-mode. In addition, for the pressure 0.1 Pa, a hysteresis structure in the power-dependent electron density can be found. Above the threshold power for the H-mode, it is possible to reduce the power by 50 W without switching back to the E-mode. The two working modes also require different setups in the matching network for minimizing the reflected power, due to different plasma impedance.

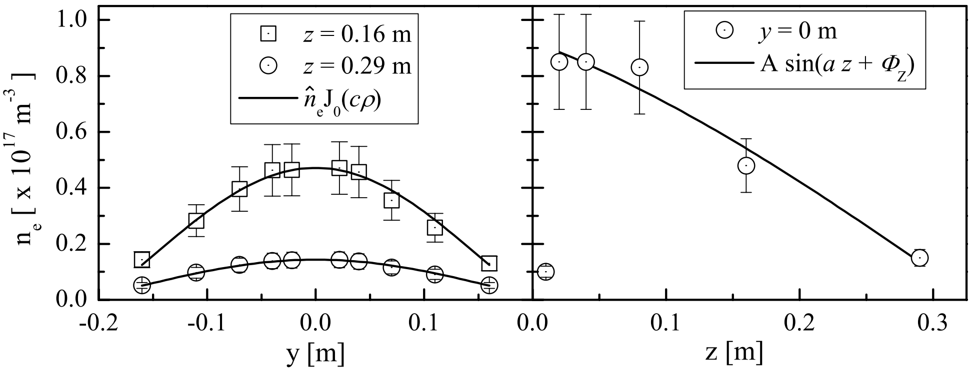

Figure 6. Electron density profiles determined by Langmuir probe measurement.

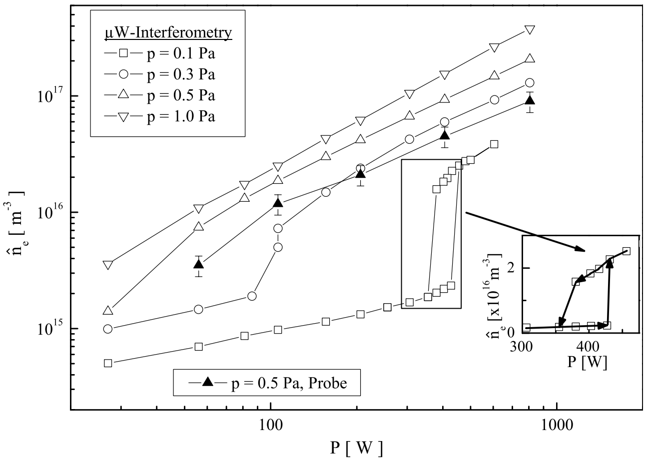

Figure 7. Power-dependent electron density of an argon ICP plasma for different pressures, measured with a microwave interferometer and Langmuir probe.

Furthermore, the results of the Langmuir probe measured for the pressure of 0.5 Pa are plotted for comparison.

It is obvious that the electron densities for the pressure of 0.5 Pa detected by the microwave interferometer are approximately twice as high. These deviations between both methods are known and reported in [1]. In addition to the error of the Langmuir probe, sources of uncertainty in the electron density detection by the used microwave interferometer could be an error in the phase detection, which can be neglected due to the high signal-to-noise ratio, or a deviation in the assumed electron density profile. Taking into account the influence of the view port to the profile and the uncertainty by the detection of profile with an invasive method, the deviation of a factor of two can be explained.

In addition, the dynamic behaviour of the electron density is investigated by turning on and off the plasma periodically (figure 8) and detecting the time dependence with a temporal resolution of 100 μs. Due to the minimum detectable phase difference of about 0.1 mrad, the minimum detectable electron density is 1×10^{13} m^{-3}. After an initial dip, the electron density decays linearly in a semi-logarithmical plot. In this region, the time decay coefficient τ is determined by fitting a linear function.

The initial dip, meaning a fast decay of the electron density, is caused by the still hot electrons at the beginning of the off phase. Gorchakov *et al* [25] reported that the electron temperature after turning off the power reduces to gas temperature within approximately 1 ms. Therefore, at the beginning of the decay, the electrons are still hot and so the time decay coefficient τ is very small. Then, the electron temperature decreases and hence the decay coefficient increases. In addition, for the pressure of 1 Pa a power switch-on dip is detected. When turning on the power the remaining electrons are heated rapidly and so the decay coefficient decreases before the generation of new electrons comes into account. The reason for detecting this effect only at 1 Pa is that a minimum density of electrons is required.

4. Discussion

To verify the time-dependent electron density, measured by microwave interferometry, the time decay coefficient is determined analytically.

The decay behaviour of the electron density in the off phase of the plasma is characterized by ambipolar diffusion of electrons and ions, which is well known e.g. [26]. For this low-pressure case, ionization and recombination processes in the plasma volume can be neglected and hence the electron diffusion is given by

$$\frac{\partial n_e}{\partial t} = D_a \nabla^2 n_e, \tag{3}$$

where D_a is the ambipolar diffusion coefficient. Using cylindrical coordinates, with z-orientation as given in figure 1 the electron density can be written as a product of three independent space and one time function:

$$n_e(\rho, \varphi, z, t) = R(\rho) \cdot \Psi(\varphi) \cdot Z(z) \cdot T(t). \tag{4}$$

The solutions of the four functions from equation (3) are then given by

$$\begin{aligned} T(t) &= C \exp\left(-\frac{t}{\tilde{\tau}}\right), \\ R(\rho) &= J_b(c\rho), \\ \Psi(\varphi) &= \sin(b\varphi + \Theta_\psi), \\ Z(z) &= \sin(az + \Theta_Z). \end{aligned} \tag{5}$$

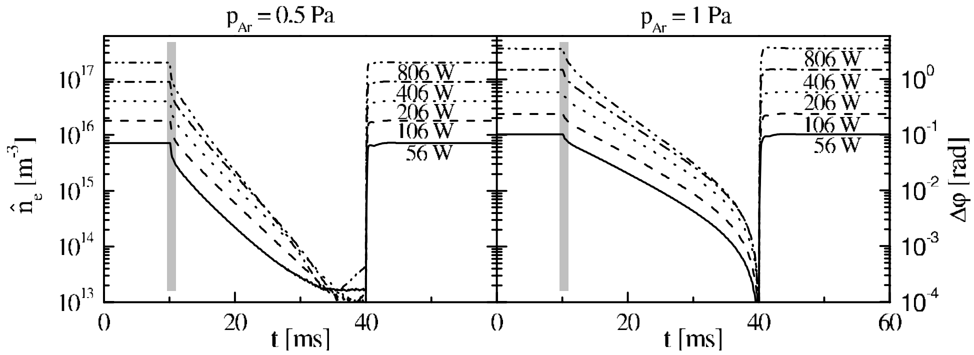

Figure 8. Time-dependent electron densities for different powers and pressures (left and middle y-axis), with the corresponding phase difference (right y-axis). At $t = 10$ ms the power source is turned off and at $t = 40$ ms the power source is turned on. The grey bar marks the initial dip of the off phase.

The constant a, and Θ_Z, scale the harmonic solution for $Z(z)$, which describes the dependence of n_e in the z-direction. Due to the fact that $\Psi(\varphi) = \Psi(\varphi + 2\pi)$, the scaling constant b has to be an integer. Furthermore, the constant b defines the order of the Bessel function. If a rotational symmetry is assumed, then $\Psi(\varphi) = \text{const}$ and $b = 0$. For this case the time decay coefficient $\tilde{\tau}$ of the electron density is

$$\tilde{\tau} = ((a^2 + c^2)D_a)^{-1}. \tag{6}$$

In a weakly ionized plasma, the diffusion coefficient can be written as $D_a = D_i(1 + T_e/T_i)$ [27], where T_e is the electron and T_i the ion temperature. In addition, the diffusion coefficient of argon ions is given by $D_i = 1/3\bar{v}\cdot l$ [28], with $\bar{v}$ as the mean velocity and can be approximated by a Maxwell distribution:

$$\bar{v} = \sqrt{\frac{8k_B T_i}{\pi m_i}}, \tag{7}$$

where k_B is the Boltzmann constant and m_i the atomic mass of the argon ion. The mean free path l can be written as

$$l = \frac{k_B T}{p\delta}, \tag{8}$$

where p is the pressure, T is the neutral gas temperature and δ is the collision cross section of argon with argon ions, which are provided by Gorchakov. Combining equations (6), (7) and (8) leads to the time decay coefficient $\tilde{\tau}$:

$$\tilde{\tau} = \frac{3}{a^2 + c^2}\sqrt{\frac{\pi m_i \delta^2}{8k_B^3}}\,\frac{\sqrt{T_i}\,p}{T(T_i + T_e)}, \tag{9}$$

where the coefficient a is related to the axial and the coefficient c to the radial flux of the electrons and ions. With the spatially resolved Langmuir probe measurements of the electron density, shown in figure 6, the coefficients of the solutions in equation (5) can be estimated to $a = 3.1\ \text{m}^{-1}$, $b = 0$ and $c = 11\ \text{m}^{-1}$. The magnitude of these coefficients leads to the conclusion that the main ambipolar flux is radial to the inner walls of the reactor. Assuming a thermalization of the ions with the neutral gas [29], and taking into account that the electrons are cooled down to gas temperature, T, T_i and T_e are approximated for the investigated powers and pressures to 470 K. Chevolleau and Fukarek [30] reported neutral gas temperatures in an inductively coupled argon discharge, which are in the range of 50% of this temperature assumption.

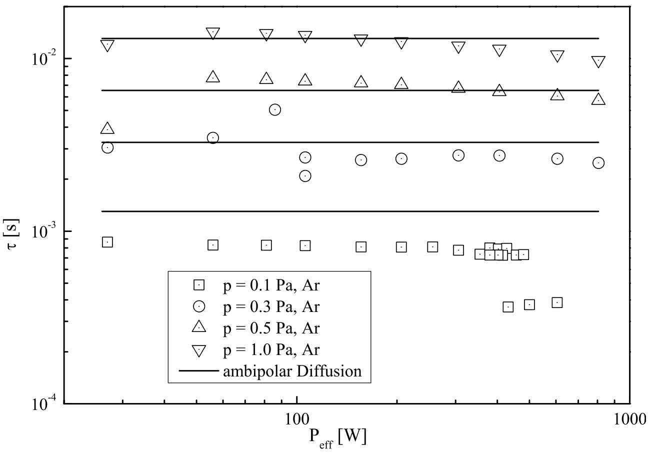

Figure 9. Power-dependent electron density decay coefficient τ for different pressures. Points show experimental results, lines show the results of equation (9).

Including this assumption in equation (9) leads to

$$\tilde{\tau} \sim \frac{p}{T^{3/2}} \tag{10}$$

the time decay coefficient increases with increasing pressure and decreasing gas temperature, due to the connection to the mean free path l. Using equation (9) and following scaling:

$$\tau = \ln(10)\cdot\tilde{\tau} \tag{11}$$

the time decay coefficient is calculated for the investigated pressure and plotted for comparison with the measured coefficients in figure 9.

The experimental time decay coefficient, determined by the exponential decay of the electron density (figure 8), has a strong dependence on the pressure, as expected. The decreasing of the time decay coefficient with increasing power can be explained by an increase in the gas temperature with power.

For pressures above 0.1 Pa, both results are in excellent agreement. The deviation between the results at 0.1 Pa could be caused by the fact that at low pressures, due to the lower particle density, the decay time is much faster. This leads to values below the detection limit already after 2 ms. This relatively short time is not sufficient to thermalize the electrons with the background gas completely. Therefore, the detected time decay coefficient is lower. Thus, the assumption of recombination at the inner walls of the reactor, determined by ambipolar diffusion as being the main electron loss process, is justified and the time-dependent electron density measurement is verified.

5. Conclusion

The efficiency of a single-port microwave interferometer, working at 45.75 GHz for investigating the electron density, in an industrial plasma environment has been demonstrated. The static and dynamic behaviour of the electron density in the afterglow of an ICP reactor was investigated in the pressure range 0.1–1 Pa and the power range 27–800 W.

The Gaussian beam transformation by the elliptical mirror was investigated using Comsol Multiphysics®. It was demonstrated that the excitation of higher-order modes could be negligible for this setup.

The applicability of the method was checked by comparing the results with spatially resolved Langmuir probe measurements. The measured electron density profile can be approximated with a Bessel function, so absolute values for the radial electron density profile can be calculated from the phase difference $\Delta\varphi$ measured with the microwave interferometer. The densities are in good agreement with the Langmuir probe results. Maximum values $1 \times 10^{18}\,\mathrm{m}^{-3}$ are obtained in the centre of the vessel at an axial distance of 0.24 m from the antenna window of the ICP source.

The measuring setup is able to monitor the E to H transition of the ICP source at pressures below 0.3 Pa. In addition, a hysteresis structure in electron density for the pressure of 0.1 Pa is detected.

To explain the measured electron density decay in the afterglow phase, the ambipolar diffusion equation is solved. With the results of the spatially resolved Langmuir probe measurements, the radial and axial electron fluxes are calculated and the time decay coefficient τ is estimated. Both results are in very good agreement for pressures above 0.1 Pa.

Furthermore, a dip in the temporal electron density decay at the beginning and at the end of the off phase is detected and is attributed to a fast change in the electron temperature.

Acknowledgments

The authors would like to thank S Gorchakov for his support. The study is supported by the Bundesministerium für Bildung und Forschung (13N9320).

References

[1] Malyshev M V and Donnelly V M 2001 *J. Appl. Phys.* **90** 1130–7

[2] Schulz-von der Gathen V *et al* 2001 *Plasma Sources Sci. Technol.* **10** 530–9

[3] Stenzel O *et al* 2011 Plasma and optical thin film technologies *Advances in Optical Thin Films IV* 1st edn (Marseille, France: SPIE) 81680L-1

[4] Harhausen J *et al* 2012 *Plasma Sources Sci. Technol.* **21** 035012

[5] Hutchinson I H 2002 *Principles of Plasma Diagnostics* (Cambridge: Cambridge University Press)

[6] Manos D M *et al* 1991 *Thin Solid Films* **195** 319–36

[7] Stenzel R L 1976 *Rev. Sci. Instrum.* **47** 603–7

[8] Piejak R B *et al* 2004 *J. Appl. Phys.* **95** 3785–91

[9] Lapke M *et al* 2011 *Plasma Sources Sci. Technol.* **20** 042011

[10] Courteille C *et al* 1996 *Plasma Sources Sci. Technol.* **5** 210–5

[11] Tuszewski M and Tobin J A 1996 *Plasma Sources Sci. Technol.* **5** 640–7

[12] Behle S, Brockhaus A and Engemann J 2000 *Plasma Sources Sci. Technol.* **9** 57–67

[13] Berndt J *et al* 2006 *Plasma Sources Sci. Technol.* **15** 18–22

[14] Brockhaus A *et al* 2006 *Plasma Sources Sci. Technol.* **15** 171–7

[15] Goldsmith P F 1998 *Gaussian Beam Quasioptical Propagation and Application* (Piscataway, NJ: IEEE)

[16] Hiebel M 2005 *Grundlagen der Vektoriellen Netzwerkanalyse* (München: Rohde & Schwarz)

[17] Rackow K, Sigeneger F, Ehlbeck J, Uhrlandt D, Weltmann K-D, Lieder G and Lieberer M 2010 Emitter erosion in fluorescent lamps *Proc. 12th Int. Symp. on the Science and Technology of Light Sources and the 3rd Int. Conf. on White LEDs and Solid State Lighting (Eindhoven, Netherlands)*

[18] Chung P M, Talbot L and Touryan K J 1975 *Electric Probes in Stationary and Flowing Plasmas: Theory and Application* (New York: Springer)

[19] Hannemann M and Sigeneger F 2006 *Czech. J. Phys.* **56** B740–8

[20] Druyvesteyn M J 1930 *Z. Phys.* **64** 781–98

[21] Zakrzewski Z *et al* 1992 *Plasma Sources Sci. Technol.* **1** 28–35

[22] Hartfuss H J, Geist T and Hirsch M 1997 *Plasma Phys. Control. Fusion* **39** 1693–769

[23] Halfmann H *et al* 2007 *J. Phys. D: Appl. Phys.* **40** 4145–54

[24] Cunge G *et al* 1999 *Plasma Sources Sci. Technol.* **8** 576–86

[25] Gorchakov S *et al* 2006 *Phys. Rev.* E **73** 056402

[26] McDaniel E W 1964 *Collision Phenomena in Ionized Gases* (New York: Wiley)

[27] Lieberman M A and Lichtenberg A J 2005 *Principles of Plasma Discharges and Materials Processing* (Hoboken, NJ: Wiley)

[28] Demtröder W 2005 *Experimentalphysik 3* (Heidelberg: Springer)

[29] Alves L L 2007 *Plasma Sources Sci. Technol.* **16** 557–69

[30] Chevolleau T and Fukarek W 2000 *Plasma Sources Sci. Technol.* **9** 568–73

5.4 Inactivation of Vegetative Microorganisms and Bacillus atrophaeus Endospores by Reactive Nitrogen Species (RNS)

Plasma Processes
and Polymers

Inactivation of Vegetative Microorganisms and *Bacillus atrophaeus* Endospores by Reactive Nitrogen Species (RNS)

Uta Schnabel,* Mathias Andrasch, Klaus-Dieter Weltmann, Jörg Ehlbeck

Plasma is used as a common technology for the treatment and modification of surfaces in a variety of industrial branches. Decontamination of inorganic materials by plasma is possible with deterioration of the materials properties of a few nanometres. The inactivation efficacy of microwave plasma processed air against vegetative bacteria and bacterial endospores was investigated. The gained results provide inactivation rates up to 6 log in total treatment times (15–30 min) comparable to sterilization treatment times of thermo-sensitive medical devices with ethylene oxide, formaldehyde or H_2O_2. Additions like O_2 or O_3 did not promote the antimicrobial efficacy. Moreover, this new method is characterized by advantages like no thermal influence, no toxicity for human and environment and low costs.

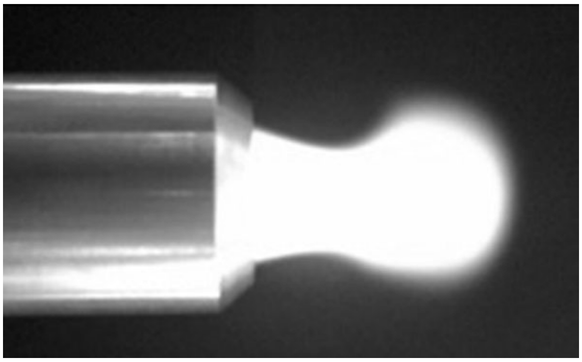

1. Introduction

Plasma is an excited gas which is used as a common technology for the treatment and modification of surfaces in a variety of industrial branches, like electrical engineering, textile, and packaging industry, optics, automotive industry, printing as well as environmental technology, and much more.[1–3] The usage of physical plasma for decontamination is under active research, because it allows a fast and safe sterilization of different materials from glass over polymers to human tissue.[4–6] Decontamination of inorganic materials such as metals, plastics, and glass by plasma is possible with deterioration of the materials properties in the scale of a few nanometres, only. Plasma is the fourth state of matter, after the solid, liquid or gaseous states. It is composed of ions and electrons in a neutral background. In case of molecule containing gas composition molecules can be ionized or dissociated by an energy transfer due to inelastic collision. Low-temperature gas plasmas used for technical applications are generated from vacuum conditions up to a few bar. The high electrical field strengths which are needed to ignite and sustain the plasma can be varied from DC up to several tenth of GHz. Gases such as oxygen or hydrogen peroxide in the plasma state have shown antimicrobial activity.[7–9] A lot of medical devices are thermo- and hydro-sensitive. For materials such as polyethylene terephthalate and polyethylene, which importance as packaging material increasing not only in food but also in pharmaceutical and medical industries, low-temperature gas plasma may be a useful alternative in relation to other low-temperature decontamination procedures taking the drawbacks and limitations of them into account. Currently used methods in medical fields for the non-thermal sterilization of heat-sensitive items are ionizing radiation, ethylene oxide (EO), formaldehyde, and hydrogen peroxide (H_2O_2). The disadvantages of high toxic EO are residues absorbed in the

U. Schnabel, M. Andrasch, K.-D. Weltmann, J. Ehlbeck
Leibniz Institute for Plasma Science and Technology, Felix-Hausdorff-Straße 2, 17489, Greifswald, Germany
E-mail: uta.schnabel@inp-greifswald.de

DOI: 10.1002/ppap.201300072

plastics, which is resulting in storage times for venting.[10] Gamma irradiation is costly and may modify materials like PP.[11] In case of aseptic packaging H_2O_2 is the main utilized agent for the decontamination of thermal-sensitive medical materials.[12] These harmful chemicals require threshold limit values (correct amount) and removal of residual chemicals from the packaging. Therefore their handling is very difficult and in consequence expensive. Hence, new decontamination methods are necessary. Low-temperature plasma may have the ability to replace or complete with current decontamination technologies in the food and medical industries. For nitrogen (N_2) gas plasma a short period of exposure is required, decomposition for exhaust gas is not as much as necessary to safe conditions like for H_2O_2 or EO and deterioration in the material can be obviated.[13]

The aim of this work is to investigate the efficiency of microwave plasma processed air by selected test strains which are used as biological indicators. Endospores of *Bacillus atrophaeus* are test strains for EO and H_2O_2 sterilization.[14,15] *Staphylococcus aureus* is a facultatively anaerobic, Gram-positive coccus. It is still one of the five most common causes of nosocomial infections, often causing postsurgical wound infections.[16] *Escherichia coli* is a Gram-negative rod-shaped bacterium that is commonly found in the lower intestine of warm-blooded organisms. Most *E. coli* strains are harmless, but some, such as serotype O157:H7 (EHEC) can cause serious food poisoning in humans.[17,18] *E. coli* are not always confined to the intestine, and their ability to survive for brief periods outside the body makes them an ideal indicator organism to test environmental samples.[19,20] It is necessary to investigate a wide range of microorganisms for optimization and validation of a newly developed decontamination method.

Plasma offers the possibility of varying parameters like process gas, pressure or applied power density. Air seems to be very efficient for microbiological inactivation, because air plasmas are excellent sources of reactive oxygen-based and nitrogen-based species, such as $O^\cdot$, $O_2^\bullet$, O_3, $OH^\cdot$, $NO^\cdot$, and $NO_2^\bullet$.[21] In our study, we investigated the inactivation of different microorganisms, endospores of *B. atrophaeus*, furthermore *S. aureus* and *E. coli* K12, caused by microwave plasma treatment with plasma processed air.

2. Experimental Section

2.1. Strains

For all microbiological experiments *B. atrophaeus* Nakamura 1989 (ATCC 9372, DSM 675) in the sporulated form was used. The vacuum dried culture achieved from the DSMZ (German Collection of Microorganisms and Cell Cultures, Braunschweig, Germany) was cultivated on sporulation agar for two weeks at 37 °C and after harvest stored in a refrigerator in sterile distilled water for preventing spore germination. The used sporulation agar consisted of 8.0 g of Tryptic Soy Broth, 4.0 g Yeast extract, 20.0 g Agar Agar and 0.03 g Manganese(II) sulfate (Merck KGAA, Carl Roth GmbH & Co. KG) filled up with distilled water to 1.0 liter. *E. coli* K12 (NCTC 10538, DSM 11250) and *S. aureus* (ATCC 6538, DSM 799) have been kindly provided by Institute of Hygiene and Environmental Medicine, Ernst Moritz Arndt University Greifswald, Germany.

2.2. Contamination of Glass Bottles

In preparation for the plasma treatment sterile laboratory bottles (DURAN Group GmbH, Wertheim/Main, Germany) with a volume of 250 ml were contaminated with microorganisms. All microorganisms, vegetatives or endospores were diluted in sterile distilled water in order to achieve concentrations of 10^7 cfu specimen^{-1} and for loaded experiments of 10^6 cfu specimen^{-1}, respectively. Investigations for realistic circumstances were done after DIN EN 13704 with 3 g $\cdot$ L^{-1} bovine serum albumin (BSA) in bacterial suspension.[22] Laboratory bottles were contaminated by a spray coating method. 100 μl bacterial suspension with or without BSA-load were sprayed (200 kPa) by air brush into an overhead bottle. Afterwards bottles were dried under sterile conditions for 1 h. Only for plasma treatment, bottles were opened, apart from that they stay closed.

2.3. Treatment of Microorganisms by Microwave Plasma Processed Air (PPA)

The non-thermal plasma treatment of the contaminated glass bottles was done with microwave plasma processed air. The used microwave plasma setup (PLexc®: Plasma excited) is shown in Figure 1. The microwaves have a frequency of 2.45 GHz and the consumed power is in the range of 1.1 kW. Accordingly, the gas temperature in the centre of the plasma is about 4 000 K at a gas flow rate of 18 slm air. The distance between the torch and the contaminated glass bottles is about 25 cm connected via a metal tube.

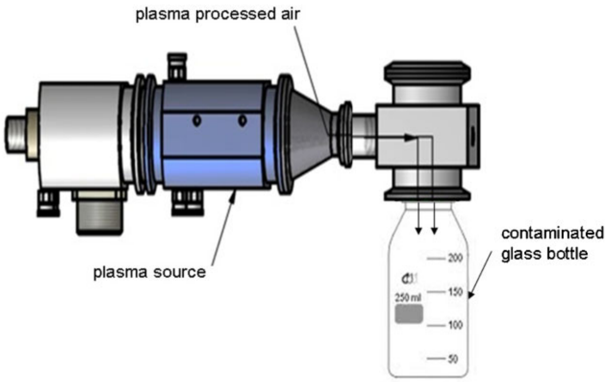

Figure 1. The microwave setup PLexc® for decontamination of glass bottles.[42,43] Plasma settings: frequency of 2.45 GHz; consumed power of 1.1 kW; gas flow rate of 18 slm air; plasma on time of 7 s.

In order to estimate the possible influence of the hot gas used for the decontamination in the PPA process on the specimens temperature the following Equation (1) has to be considered:

$$\frac{\Delta T_{bottle}}{\Delta T_{air}} = \frac{m_{air}c_{air}}{m_{bottle}c_{bottle}} \approx \frac{m_{air}}{m_{bottle}} = \frac{0.3\,g}{228\,g} = \frac{1}{760} \qquad (1)$$

Due to the fact that the specific heat capacity of glass and air with 0.6–0.8 kJ/(kg · K) and 1.0 kJ/(kg · K), respectively, is very similar the equation can be reduced to the ratio of masses. Thus, an upper limited for the temperature increase of the specimen is given.

The gas temperature at the end of the metal tube is 117 °C measured by Fiber Optic Temperature measurements (FOTEMP, Optocon AG Dresden, Germany). In contact with the bottles the gas temperature is immediately cooled down. Fiber Optic Temperature measurements (FOTEMP, Optocon AG Dresden, Germany) showed a temperature of 26 °C inside and thermographic measurements (Figure 2, FLIR E50 thermal imaging camera, FLIR Systems Inc., Oregon, USA) of 26.9 °C outside the glass bottle wall.

Since the main decontamination process is induced by plasma chemistry the discharge is ignited for 7 s, thus ensuring a eightfold gas exchange, the reactive gas is introduced into the glass bottle and could interact there for 5, 10, 15, 30, 45, and 60 min with the contamination.

Figure 2. The thermographic measurements of glass bottle wall temperature at plasma processed air (PPA) treatment. In the middle of the cross 26.9 °C are measured. Microorganisms are sprayed in the lower wall part and bottle bottom.

Additions of oxygen 4.5 (Air Liquide) and ozone (ozonizer: Laborozonisator 300, Erwin Sander Elektroapparatebau GmbH Uetze-Eltze, Germany) were realized by mixing 13 slm air with 5 slm O_2 (working gas) or adding 2 000 ppm ozone (1.67 slm O_2) after the plasma ignition zone to 16 slm plasma processed air by mass flow controller (MKS Instruments).

2.4. Recovery of Microbial Contamination

The recovery of viable and proliferating cells followed by shaking (190 cycles per minute, HS 501 digital, IKA-Werke GmbH & Co.KG Staufen, Germany) the bottles with 10 ml tryptic soy broth (CASO-Bouillon, Merck KGAA, Darmstadt, Germany) for 15 min. In the case of *B. atrophaeus* endospores treated bottles were heated for 10 min at 80 °C after shaking to destroy any vegetative bacteria which could occur due to the opening of the bottles under non-sterile conditions for plasma processed air treatment. The remaining concentration of residues was detected by the surface-spread-plate count method using tryptic soy agar plates (CASO-Agar, Merck KGAA, Darmstadt, Germany). The detection limit of this procedure was 10 cfu · ml^{-1}. Inactivation kinetics of microorganisms are depicted in semi-logarithmic plots. If the number of microorganisms fell below the detection limit, i.e., no viable microorganisms have been found, these values in the graphs are set at the detection limit.

3. Results and Discussion

3.1. Inactivation of Vegetative Microorganisms and Bacterial Endospores by PLexc® Plasma Processed Air

To investigate the antimicrobial efficacy of plasma processed air primarily *E. coli* and *S. aureus* were chosen as vegetative germs. In Figure 3, the survival curves for both microorganisms are shown in a time dependent treatment.

It can be observed that the inactivation of *E. coli* bacteria increases with longer time duration after initial gas filling of glass bottles. This effect is very evident between the initial time point and 15 min. After a 15 min interaction between plasma processed air and *E. coli* bacteria, until the detection limit of 10 cfu · ml^{-1}, no proliferating/viable cells were measured. The inactivation of *S. aureus* was done under the same conditions. Unlike *E. coli*, *S. aureus* requires shorter interaction between plasma processed air and itself. The exposure of processed air for 10 min leads to an inactivation of 5 log. After 15 min no residues could be detected until the limit of 10 cfu ml^{-1}. This indicates that the mortality of vegetative bacteria increases up to 6 log by elevating the treatment time. Moreover the inactivation was not proportional to time, which indicates a multi-phase kinetic. This phenomenon is also described by others.[23] This may be in correlation with the limited penetration depth of plasma of a few nanometers. Therefore, stacked bacteria or surface layers may gradually slow down the inactivation process.

DOI: 10.1002/ppap.201300072

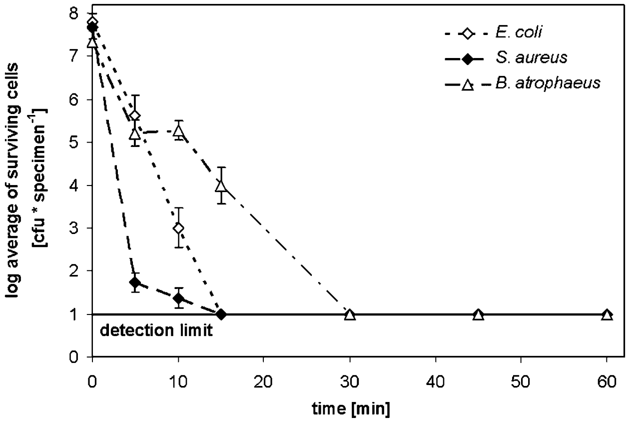

Figure 3. Effect of different incubation times on inactivation of *Escherichia coli* (◇), *Staphylococcus aureus* (◆), and endospores of *B. atrophaeus* (Δ) with plasma processed air. References without plasma treatment are set at time point t_0. Values are the average of triplicate. Plasma settings: frequency of 2.45 GHz; consumed power of 1.1 kW; gas flow rate of 18 slm air; plasma on time of 7 s.

Further, Figure 3 shows the inactivation curve of *B. atrophaeus* endospores using the microwave plasma processed air. The longer the incubation time with plasma processed air, the higher the inactivation value of the endospores. As *Bacillus* endospores are highly resistant to many disinfectants a longer interaction time for a complete reduction until the detection limit was expected. However, no germinating/viable endospores were detected after 30 min treatment. During the first 5 min a reduction of 2 log and over the next 10 min a further decrease of 1.3 log was observed. The strongest increase in inactivation of the *B. atrophaeus* endospores was measured between 15 and 30 min time of interaction. This three-step kinetic indicates a second-step mechanism of inactivation, thereby, in the first phase isolated endospores or the first layer of stacked endospores is influenced. The second phase, which had the slowest kinetics, could be attributed to the conversion of $NO^\bullet$ to $NO_2^\bullet$. Finally, the third phase was initiated after endospores and debris had been cleared or passed through and $NO_2^\bullet$ interaction is possible.[9,24]

3.2. Inactivation of Bacterial Endospores with BSA-Load by PLexc Processed Air and Additives

To give consideration to a more realistic environment and requirements after DIN EN 13704, *B. atrophaeus* endospores were suspended in a $3\,g \cdot L^{-1}$ bovine serum albumin solution. It could be expected that the protein (organic load) protect the endospores from the inactivation effects of plasma processed air. The inactivation kinetic of *B. atrophaeus* endospores with load is shown in Figure 4. Using PPA nearly similar inactivation rates for *Bacillus* endospores with a BSA load compared to endospores in distilled water were obtained.

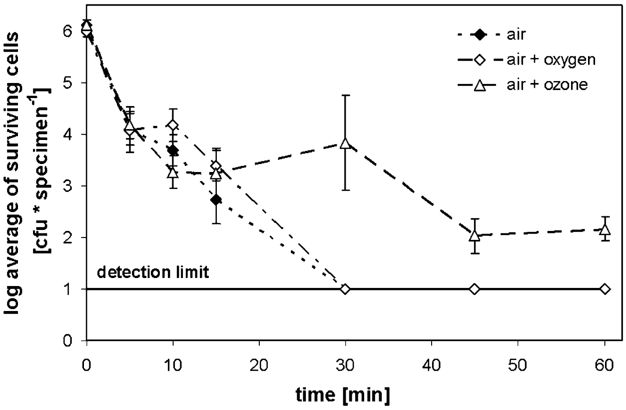

Figure 4. Effect of different incubation times on inactivation of endospores of *B. atrophaeus* with a $3\,g\,L^{-1}$ BSA load by plasma processed air alone (◆), by processed air with oxygen (◇) and with ozone (Δ). References without plasma treatment are set at time point t_0. Values are the average of triplicate. Plasma settings: frequency of 2.45 GHz; consumed power of 1.1 kW; gas flow rate of 18 slm air/13 slm air and 5 slm oxygen/16 slm air and 1.67 slm oxygen (2000 ppm ozone); plasma on time of 7 s.

The ISO 15883-5 requires in some cases the investigation with organic load, e.g., BSA. The nearly similar result for PPA treatment of endospores with and without BSA showed that the relatively low load of BSA which is required by ISO 15883-5 did not influence the sporicidal compounds of the PPA. A complete inactivation was reached after 30 min of incubation in processed air. The measurements during the first 30 min suggest a nearly linear decrease in spore activity. To improve the inactivation effects additions like oxygen (O_2) and ozone (O_3), which themselves are disinfectants or may have catalytic properties, were done. In both cases, the addition was done immediately before the plasma processed air reached the bottle. Thereby, O_2 or O_3 could react with the processed air and afterwards interact with the endospores. The combination of processed air and O_2 led to a nearby inactivation curve as processed air did alone. Moreover, between 5 and 30 min treatment the inactivation rate was worse. Nevertheless, the addition of O_2 caused as well as air alone a complete inactivation after 30 min. O_3 in adequate concentrations has the ability of inactivating microorganisms.[25] Surprisingly, a decrease for inactivation rates by a combined treatment with processed air and O_3 in a concentration of $2\,g \cdot L^{-1}$ was observed. After 45 min the maximum reduction of 4 log was achieved. During the first 15 min of treatment the inactivation was 2.8 log, afterwards, for the next 15 min a little recovering was seen. However, the error bar was very high in this case. The fast decomposition of ozone by organic materials like BSA is well known. This may be one reason for the stagnant inactivation of *B. atrophaeus* endospores after 45 min and lower decrease after 15 min. All in all the inactivation of *B. atrophaeus* endospores with BSA load had its highest efficacy in the presence of microwave plasma processed air alone, the investigated additions O_2 and O_3 were not able to offer improvements.

3.3. Inactivation of Bacterial Endospores by Synthetic Nitrogen Monoxide ($NO^{\bullet}$) Gas

To investigate whether nitrogen monoxide ($NO^{\bullet}$) or the cocktail of RNS ($NO^{\bullet}$, $NO_2^{\bullet}$, HNO_2, HNO_3) generated by microwave plasma is responsible for the antimicrobial properties, synthetic $NO^{\bullet}$ gas was used in the setup of PLexc. The $NO^{\bullet}$ was used under the same conditions like processed air. A total gas flow of 18 slm consisting of N_2 and 2 000 ppm $NO^{\bullet}$ has been made sure by mass spectrometry. The plasma ignition was not initiated. The results for these experiments are shown in Figure 5. Synthetic $NO^{\bullet}$ itself was not longer able to decontaminate *B. atrophaeus* endospores in the level like the RNS did.

After 15 min of interaction between $NO^{\cdot}$ and the endospores a reduction of 3 log was gained. Furthermore, the reduction increases over the next 15 min to a maximum of 4.6 log after 30 min. A longer incubation time did not escalate the inactivation efficacy. In conclusion $NO^{\bullet}$ is not the only plasma generated reactive nitrogen species responsible for the noticed inactivation effects.

The aim of this study was to investigate the inactivation efficiency of microwave plasma processed air with RNS against vegetative microorganisms and bacterial endospores with or without organic load. *B. atrophaeus* endospores were chosen because of their high resistance to disinfectants. To examine the efficiency of plasma processed air to a wide range of bacteria simultaneously, *E. coli* (Gram-negative) and *S. aureus* (Gram-positive) were selected.

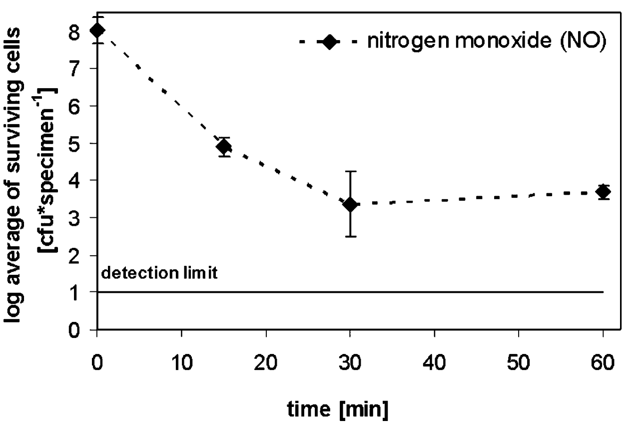

Figure 5. Effect of different incubation times on inactivation of endospores of *B. atrophaeus* with synthetic $NO^{\bullet}$ gas (◆). References without plasma treatment are set at time point t_0. Values are the average of triplicate.

The composition of microwave plasma processed air was analyzed by mass spectrometry. The mass spectrometry showed that only 2.7% of the compressed air (working gas) is transformed into $NO_2^{\bullet}$ (1.8%), $NO^{\bullet}$ (0.6%), and a 0.23% mixture of HNO_2, HNO_3, CO_2, and H_2O. No ROS were found due the high gas temperature in the centre of the plasma. Possible, but not detected ROS are $O^{\bullet}$, $O_2^{\bullet}$, $OH^{\bullet}$, and O_3. The ozone production in plasma is significantly reduced by elevated temperatures. Experiments with ozone generators at 800 °C with air resulted in the production of NO_x, only. The effect of discharge poisoning leads to higher specific energy inputs resulting in higher NO_x concentrations due to higher temperatures. Furthermore, O_3 is unstable at high temperatues. At 145 °C the O_3 decomposition time of a relative concentration of 0.2% in dry air is 1 s, only. The same time is observed for 1% relative ozone concentration at 125 °C.[26] Applying the global kinetic model presented in Baeva et al.[27] on the plasma parameter used in the present work the dominant species after nitrogen and oxygen are NO and NO_2. All other species are under these specific conditions several orders in magnitude lower.

The properties of different electric discharges can be modified and optimized by varying parameters such as pressure, power, or process gas. Each alteration of one of these parameters changes the whole plasma chemistry and influences the electron density, concentration of charged or reactive particles, and the amount of emitted UV radiation. In the case of the PLexc setup radiation can be obviated. The studies have shown that the inactivation of vegetative bacteria can be improved by increasing the incubation time. The highest inactivation for *E. coli* of 6.8 log was found after 15 min contact to plasma processed air. For *S. aureus* the highest inactivation of 6.6 log was also detected for 15 min incubation time. As shown by the inactivation kinetics, the effect was enhanced at prolonged exposure of microorganisms to plasma processed air which indicate a time-dependent reaction. Remarkable is the strong decrease during the 15 min before reaching the detection limit. Bacterial cells have a variety of strategies to react against environmental stress. This stress regulation makes bacteria less vulnerable. Examples are the formation and transfer of resistance genes, the use of efflux pumps for chemicals (e.g., antibiotics) or the formation of resistant structures used for survival under unfavorable conditions as endospores or the transition to the VBNC (viable but non-culturable) stage.[28] In general, bacteria have a cell wall mainly responsible for the outer shape and balance of pressure differences between cell interior and cell exterior. Bacteria can be divided into Gram-positives (e.g., *S. aureus*) and gram-negatives (e.g., *E. coli*) due to their cell wall structure. Gram-positive bacteria have a thicker cell wall

DOI: 10.1002/ppap.201300072

(about 15–80 mm) compared to Gram-negative bacteria (about 2 nm). In addition, Gram-negative bacteria have an outer membrane in which membrane proteins (Omp – outer membrane protein) are playing an important role in membrane permeability. Omp FepA transports iron from outside to inside and nonspecific porines transport mainly hydrophilic and low molecular substances (e.g., sodium-, potassium-, and phosphate-ions) into the periplasmatic space.[29] The thicker cell wall of *S. aureus*, as compared to *E. coli* suggests that the inactivating effect of the PPA can be delayed and therefore, longer treatment times are required for bacterial inactivation. Furthermore, there may be a lowering of the pH due to possible humidity surrounding the bacteria. This results in a change of membrane potential. Moreover, proteins and DNA can be protonated, thereby changing their structure, including functional disability. Metabolized molecules (e.g., organic acids) can also be protonated which causes a disturbance of metabolism. Bacteria measure pH value directly by membrane potential, by membrane and cytosolic proteins and the range of protonization of organic acids. Gram-negative bacteria require a constant pH of 7.6–7.8 in the cytosol for common functions of metabolism, controlled by antiport proteins in the cell membrane. Gram-positive bacteria require a cytosolic pH of 0.5–1.0 greater than the surrounding medium, controlled via ATPases.[30,31] In support of this thesis, the complete inactivation of *B. atrophaeus* endospores was not attained until a 30-min-incubation. Structure and chemical composition of endospores play a major role in their resistance to manifold physical stresses. *Bacillus* spp. endospores are highly resistant to inactivation by physical stresses such as chemicals (e.g., hydrogen peroxide), biocidal agents, pressure, temperature, UV, and ionizing radiation due to their structure. Spores consist of thick layers of highly cross-linked coat proteins, a modified peptidoglycan spore cortex, a low water content, and abundant intracellular constituents, such as calcium chelate of dipicolinic acid and α/β-type small, acid-soluble spore proteins (α/β-type SASP), last ones protect the spore DNA.[32–36] Furthermore, DNA damage accumulated during dormancy is repaired while spore germination takes place.[34,37,38] In addition, due to their complex endospore coats and their low water content, endospores are relatively insensitive to a pH decrease.

The observed survival kinetics all in all suggest an inactivation mechanism by diffusion properties of the major gas components $NO^\bullet$ and $NO_2{}^\bullet$. Minor compounds such as CO_2, H_2O, HNO_3, and HNO_2 may play a subsidiary role. The coefficient of diffusion can be mentioned with $0.2062\,cm^2\cdot s^{-1}$ for $NO^\bullet$ at 26 °C ($0.3279\,cm^2\cdot s^{-1}$ for $NO^\bullet$ at 117 °C) and $0.1572\,cm^2\cdot s^{-1}$ for $NO_2{}^\bullet$ ($0.2547\,cm^2\cdot s^{-1}$ for $NO_2{}^\bullet$).[39,40] A higher diffusion coefficient leads to faster transport of chemical species.[41] The higher diffusion coefficient of $NO^\bullet$ possibly leads to the small decrease seen in the first 5 min, afterwards the obtained plateau may be a result from the alteration of the metastabil $NO^\bullet$ to the stabile $NO_2{}^\bullet$ (2).

$$2\,NO^\bullet + O_2 \leftrightarrows 2\,NO_2{}^\bullet + 114.2\,kJ \tag{2}$$

Finally, $NO_2{}^\bullet$ induces the second greater decrease and inactivation of the cells. We assume that the positive effect on inactivation, because of the increased incubation time, arises from the diffusion of $NO^\bullet$ and $NO_2{}^\bullet$ into and through the investigated microorganisms. Furthermore, etching mechanisms may also play a role since $NO_2{}^\bullet$ is a corrosive and toxic gas. The DIN EN 13704 and FDA requirements demand that the test organism is prepared with an inorganic and organic load. Inorganic and organic residues may protect the microorganisms from the inactivation effects of generated gas components. The inorganic or organic load on used medical devises after cleaning is unknown and should play no role for new products.

In this study, the impact of organic load, in this case $3\,g\cdot L^{-1}$ BSA, was investigated. BSA is a serum albumin protein that has numerous biochemical applications and is the most abundant blood plasma protein. The results showed nearly the same inactivation kinetic as for non-loading experiments. The expected improvement by additions of O_2 or O_3 to the processed gas was not obtained. Reasons for this variance could be the high resistance of *B. atrophaeus* endospores to oxidative agents, wherefore the positive effect of additional reactive species is not obvious in our case. However, O_3 is a strong oxidizing agent which disinfection is a complex heterogeneous phenomenon. Protein damage is caused by O_3 due to reactions with dienes, amines, or thiols and its interference with cellular respiration.[35] Bacterial inactivation is a function of O_3 concentration per viable cell, meaning that below a threshold concentration O_3 has no lethal effects.[13]

4. Conclusion

Decontamination of vegetative bacteria and bacterial endospores was achieved by microwave plasma processed air with manifold reactive nitrogen species (RNS). The treatment was successful within a treatment time of 15 and 30 min, respectively. Moreover, plasma processed air was effective against *B. atrophaeus* endospores suspended in organic load (BSA) and no additions of O_2 or O_3 were needed. The diffusion properties of RNS implicit an effective gas transport into tiny gaps and long lumen. The experimental results indicate the possibility of microwave plasma processed air with no toxic residues, low costs, and short incubation times within 1 h to decontaminate surfaces and lumen which can be found at medical devices and in pharmaceutical, packaging as well as food industries.

Acknowledgements: The authors thank Udo Krohmann for his excellent support for the conception and design of the plasma source. They also thank the *Federal Office for Agriculture and Food* of Germany (project funding reference number: 2816300707) for partly financial support.

Received: June 11, 2013; Revised: September 17, 2013; Accepted: September 26, 2013; DOI: 10.1002/ppap.201300072

Keywords: bacterial endospores; microwave discharges; nitrogen; plasma treatment; sterilization

[1] C. Tendero, C. Tixier, P. Tristant, J. Desmaison, P. Leprince, *Spectrochim. Acta B* **2006**, *61*, 2.
[2] R. Suchentrunk, G. Staudigl, D. Jonke, H. J. Fuesser, *Surf. Coat. Technol.* **1997**, *97*, 1.
[3] U. Kogelschhatz, *Plasma Phys. Control. Fusion* **2004**, *46*, B63.
[4] J. Ehlbeck, U. Schnabel, M. Polak, J. Winter, Th. von Woedtke, R. Brandenburg, T. von dem Hagen, K.-D. Weltmann, *J. Phys. D: Appl. Phys.* **2011**, *44*, 18.
[5] M. Deilmann, H. Halfmann, N. Bibinov, J. Wunderlich, P. Awakowicz, *J. Food Protect.* **2008**, *71*, 2119.
[6] P. Koulik, S. Begounov, S. Goloviatinskii, *Plasma Chem. Plasma Process.* **1999**, *19*, 311.
[7] K. Tamazawa, K. Hosobuchi, *Jpn. J. Med. Instrument.* **2004**, *74*, 285.
[8] E. Stoffels, I. E. Kieft, R. E. Sladek, E. P. van der Laan, D. W. Slaaf, *Crit. Rev. Biomed. Eng* **2004**, *32*, 427.
[9] M. Moisan, J. Barbeau, S. Moreau, J. Pelletier, M. Tabrizian, L. H. Yahia, *Int. J. Pham.* **2001**, *226*, 1.
[10] Medical Management Guidelines for Ethylene Oxide. *Medical Management Guidelines* (*MMGs*). Agency for Toxic Substances and Disease Registry. From http://www.atsdr.cdc.gov (accessed August 2011).
[11] A. J. Moreira, R. D. Mansano, Tde. J. A. Pinto, R. Ruas, L. Da. S. Zambon, M. Valero da Silva, P. B. Verdonck, *Appl. Surf. Sci.* **2004**, *235*, 151.
[12] M. D. I. A. Ansari, A. K. Datta, *Trans IChemE* **2003**, *81*, 57.
[13] H. Shintani, N. Shimizu, Y. Imanishi, T. Sekiya, K. Tamazawa, A. Taniguchi, N. Kido, *Biocontrol. Sci.* **2007**, *12*, 131.
[14] ISO 14937: Sterilization of health care products – General requirements for characterization of a sterilizing agent and the development, validation and routine control of a sterilization process for medical devices. **2009**.
[15] K. Kerkulek, "Quality control in sterilization procedures. Biological indicators." in: *Quality Control in Microbiology* J. E. Prier, Ed., Univ. Park Press, Baltimore **1975**, 25.
[16] *Sherris Medical Microbiology*, 4th edition, K. J. Ryan, C. G. Ray, Eds., McGraw Hill, New York, USA **2004**.
[17] CDC (Centers for Disease Control and Prevention), *Escherichia coli* O157:H7. CDC Division of Bacterial and Mycotic Diseases. http://www.cdc.gov/ncidod/dbmd/diseaseinfo/escherichiacoli_g.htm (accessed August 2011).
[18] R. L. Vogt, L. Dippold, *Public Health Rep.* **2005**, *120*, 174.
[19] P. Feng, S. Weagant, M. Grant, "Enumeration of Escherichia coli and the Coliform Bacteria." in: *Bacteriological Analytical Manual*, 8th edition, FDA, Silver Spring, MD, USA **2002**.
[20] A. Thompson, *E. coli* Thrives in Beach Sands. Live Science. http://www.livescience.com/health/070604_beach_ecoli.html. (accessed August 2011).
[21] P. Muranyi, J. Wunderlich, M. Heise, *J. Appl. Microbiol.* **2007**, *103*, 1535.
[22] DIN EN 13704: Chemical disinfectants – Quantitative suspension test for the evaluation of sporicidal activity of chemical desinfectants used in food, industrial, domestic and institutional areas – Test method and requirements (phase 2/step 1). **2002**.
[23] M. Laroussi, I. Alexeff, W. Kang, *IEEE Trans. Plasma Sci.* **2000**, *28*, 184.
[24] N. Philip, B. Saoudi, M.-C. Crevier, M. Moisan, J. Barbeau, *J. Pelletier. IEEE Trans. Plasma Sci.* **2002**, *30*, 1429.
[25] M. Laroussi, J. P. Richardson, F. C. Dobbs, *Appl. Phys. Lett.* **2002**, *81*, 772.
[26] A. Fridmann, *Plasma Chemistry*, Cambridge University Press, New York, USA **2012**, p. 388, ISBN 9781107684935.
[27] M. Baeva, K. Rackow, M. M. Becker, J. Ehlbeck, D. Loffhagen, Characterization of atmospheric pressure microwave plasma in $N_2/O_2/H_2O$ gas mixtures. 30th ICPIG 2011, Belfast, Northern Ireland, UK.
[28] I. Matic, F. Taddei, M. Radman, *Res. Microbiol.* **2004**, *155*, 337.
[29] M. T. Madigan, J. M. Martinko, P. V. Dunlop, D. P. Clark, *Brock – Biology of Microorganisms*, 12th edition, Pearson International Edition, Pearson, Benjamin Cummings, Pearson Education, Inc., San Francisco **2009**, ISBN 978-0-321-53615-0
[30] G. Storz, R. Hengge-Aronis, *Bacterial Stress Responses*, American Society for Microbiology, ASM Press, Washington DC **2000**.
[31] K. Munk, *Taschenlehrbuch Biologie: Mikrobiologie*, Thieme Verlag Stuttgart, Stuttgart, Germany **2008**.
[32] A. Driks, *Microbiol. Mol. Biol. Rev.* **1999**, *63*, 1.
[33] P. J. Riesenman, W. L. Nicholson, *Appl. Environ. Microbiol.* **2000**, *66*, 620.
[34] P. Setlow, *Ann. Rev. Microbiol.* **1995**, *49*, 29.
[35] P. Setlow, *J. Appl. Microbiol.* **2006**, *101*, 514.
[36] T. A. Slieman, W. L. Nicholson, *Appl. Environ. Microbiol.* **2001**, *67*, 1274.
[37] P. Setlow, *Curr. Opin. Microbiol.* **2003**, *6*, 550.
[38] W. L. Nicholoson, N. Munakata, G. Horneck, H. J. Melosh, P. Setlow, *Microbiol. Mol. Biol. Rev.* **2000**, *64*, 548.
[39] J. Hirschfelder, C. F. Curtiss, R. B. Bird, *Molecular Theory of Gases and Liquids*, Wiley, New York **1954**, ISBN 0471400653.
[40] A. K. Barua, T. K. Rai Dastidar, *J. Chem. Phys.* **1965**, *43*, 4140.
[41] M. Andrasch, J. Ehlbeck, R. Foest, K.-D. Weltmann, *Plasma Sources Sci. Technol.* **2012**, *21*, 055032.
[42] U. Schnabel, R. Niquet, U. Krohmann, J. Winter, O. Schlüter, K.-D. Weltmann, *J. Ehlbeck. Plasma Process. Polym.* **2012**, *9*, 569.
[43] DE, 102005043278, (2005), INP Greifswald e.V., U. Krohmann, T. Neumann, J. Ehlbeck.

5.5 Temporally and spatially resolved characterization of microwave induced argon plasmas: Experiment and modeling

JOURNAL OF APPLIED PHYSICS **115**, 143301 (2014)

Temporally and spatially resolved characterization of microwave induced argon plasmas: Experiment and modeling

M. Baeva,[a] M. Andrasch, J. Ehlbeck, D. Loffhagen, and K.-D. Weltmann
INP Greifswald, Felix-Hausdorff-Str. 2, 17489 Greifswald, Germany

(Received 15 January 2014; accepted 28 March 2014; published online 8 April 2014)

Experiments and modeling of the plasma-microwave interaction have been performed in a coaxial microwave plasma source at a field frequency of 2.45 GHz generating argon plasmas at pressures of 20 and 40 millibars and a ratio of flow rate to pressure of 0.125 sccm/Pa. The incident microwave power between 100 W and 300 W is supplied in a regime of a pulse-width modulation with cycle duration of 110 ms and a power-on time of 23 ms. The experiments are based on heterodyne reflectometry and microwave interferometry at 45.75 GHz. They provide the temporal behaviour of the complex reflection coefficient, the microwave power in the plasma, as well as the electron density in the afterglow zone of the discharge. The self-consistent spatially two-dimensional and time-dependent modeling complements the analysis of the plasma-microwave interaction delivering the plasma and electromagnetic field parameters. The consolidating experimental observations and model predictions allow further characterizing the plasma source. The generated plasma has a core occupying the region close to the end of the inner electrode, where maximum electron densities above $10^{20}\,\mathrm{m}^{-3}$ and electron temperatures of about 1 eV are observed. Due to a longer outer electrode of the coaxial structure, the plasma region is extended and fills the volume comprised by the outer electrode. The electron density reaches values of the order of $10^{19}\,\mathrm{m}^{-3}$. The heating of the gas occurs in its great part due to elastic collisions with the plasma electrons. However, the contribution of the convective heating is important especially in the extended plasma region, where the gas temperature reaches its maximum values up to approximately 1400 K. The temporally and spatially resolved modeling enables a thorough investigation of the plasma-microwave interaction which clearly shows that the power in-coupling occurs in the region of the highest electron density during the early stage of the discharge. In the steady state phase, however, the power in-coupling occurs close to the source walls where the electron density is significantly lower than on the discharge axis.
[http://dx.doi.org/10.1063/1.4870858]

I. INTRODUCTION

Among the variety of ways to couple electric energy and generate plasmas (ac/dc, low or high frequency electric field just to mention), plasma sources based on microwave energy[1,2] have become attractive since they enable lower costs for equipment and processing. They benefit from electrodeless and relatively simple reaction chambers and cover a wide range of applications such as gas pollution control, surface treatment, material processing, decontamination, and plasma medicine.[3–8] The microwave energy can be coupled to the plasma in various ways that makes the classification quite difficult. Microwave plasma sources are divided into six categories[9] in general or are just categorized as localized and traveling-wave discharges.[10] Among the microwave plasma sources, microwave plasma torches demonstrate three different types of discharge structure:[10–12] plasmas which are placed within a resonant cavity but are emanating as post-discharges through an aperture so that microwaves are not propagating outside of the cavity; plasmas generated in a dielectric tube placed in a structure enhancing the microwave field, e.g., a resonant cavity or a surface-wave initiating applicator; expanding plasma jets at the end of a coaxial transmission line. A significant amount of research work focused on microwave plasma sources and their applications has been done in a number of groups in Cordoba, Eindhoven, Gdansk, Lisbon, Montreal, Sofia, Stuttgart, and Wuppertal, just to mention a few, leading to a tremendous number of publication works.

At INP Greifswald, microwave plasma sources have been under investigation for many years now. The surface treatment of thermal sensitive materials has become of interest for the antimicrobial treatment of hollow packaging of pharmaceutical products,[13–15] especially with the development of a self-moving atmospheric pressure microwave plasma with low thermal load.[7] Radio frequency and microwave plasmas are widely being investigated, e.g., for sterilization applications.[16,17] From the practical point of view, each discharge may have advantages or disadvantages. Microwave torch-like plasmas are easy to handle. Depending on the power consumption, gas temperatures from room temperatures up to several thousand kelvin can be achieved. The discharge can be operated in air environment even in admixture with various precursors at moderate gas fluxes. Nevertheless, the ignition of the discharge at atmospheric pressure remains still an important challenge.

---

[a]Electronic mail: baeva@inp-greifswald.de

Recently, a new ignition technique has been invented[18] and applied to a new microwave plasma source based on a coaxial structure under pulse modulation conditions. Making use of this new technique, the generated microwave plasma has been considered as a source of nitrogen atoms applied to gallium nitride crystal growth.[19] The antimicrobial treatment has been enforced leading to a new sterilization method.[20] Investigations of the plasma under pulse modulation conditions have contributed to the further improvement of the plasma source. However, the further development and potential applications demand a better understanding of the physical processes. Particularly, the plasma source has been constructed as a microwave plasma torch based on truncated coaxial waveguide such that the one electrode of the coaxial line is shorter than the other one. Such construction differs from those in Refs. 21–24 and has more in common with the design presented in Refs. 25 and 26 as it will be shown in the description of the source head in more detail below. The inner electrode is used for the gas supply and the plasma ignites near its end. The generated plasma expands and acts as an extension of the inner electrode of the coaxial line through which the microwave can propagate to the end of the outer electrode. Afterwards, the microwave is reflected backward so that the microwave energy is primarily absorbed in the plasma. This construction allows an increase in the plasma volume. Under pulsed operation, the ignition sequence described repeats in every single on-cycle provided that the duration of the off-cycle is correspondingly long.

Another important and common feature of the microwave plasma torch applied in Ref. 25 is the pulse modulation regime which offers the opportunity to look at the plasma evolution both during the ignition and in the steady state phase. Such studies bring new insight and hence contribute to a better understanding of the processes.

Lots of diagnostic work and modeling have been done and is still in progress to investigate various types of microwave plasma sources. Recently, the ignition of a microwave plasma in a narrow dielectric tube using a surfatron cavity has been imaged and temporally resolved[27] so that the plasma propagation starting from the launcher has been followed. It has been shown that the spatial features of the ignition depend on the repetition frequency. In Ref. 25, a complex character of the formation and maintenance of the microwave torch plasma in every pulse has been observed. Our investigations have shown the need for theoretical and experimental characterization of the plasma source, as well. It is the aim of the present work to study the spatial and temporal evolution of the plasma induced in the coaxial microwave plasma torch in argon at pressures between 5 and 80 millibars and to ensure stable and reproducible operation before applications in air-like mixtures will be initiated. These studies simplify the plasma chemistry and also overcome the filamentary structure of the discharge typically observed at atmospheric pressure[13] so that the attention can been focused on the plasma-microwave interaction.

In the framework of the present studies, phase- and time-resolved measurements of the incident and reflected microwaves as well as heterodyne microwave interferometry providing the electron density in the spatial afterglow of the discharge have been performed along with numerical modeling. A previously developed time-dependent, spatially two-dimensional hydrodynamic model[28] has been extended and employed to describe in a self-consistent manner the gas flow and heat transfer, the particle budget of the different species in the plasma, and the wave electrodynamics of the microwave source. The model predictions further allow to gain deeper insight into plasma parameters, which cannot be determined experimentally.

The paper is organized as follows. Section II describes the experimental setup and methods used to generate and characterize the microwave induced plasma. Section III introduces the main features of the model used to describe the processes occurring in the device. Section IV combines the results of the measurements and the model calculations into comparison and discussion. Finally, the main findings of the current investigations are summarized in Section V.

II. EXPERIMENTAL SETUP

In what follows, the experiments with the plasma source, the reactor, as well as details of the microwave and plasma diagnostics are given.

A. Plasma source and reactor

Figure 1 shows a schematic of the microwave plasma source used for the experimental investigations. It comprises a coaxial line with a truncated inner electrode. At the end of the latter, a resonant structure is built in to enable self-ignition. The ignited plasma itself serves as a shield protecting the resonant structure from energetic stress. A large volume breakdown in atmospheric pressure ambient air at a relatively low microwave power of about 2 kW has been achieved using this system.[29,30] In argon at a pressure between 10 and 100 millibars, the coaxial line is filled with teflon (PTFE) in order to suppress parasitic discharges in the coaxial section at the inner conductor (this part is outside the sketch). To the end of the coaxial line, which is in contact with the plasma, alumina ceramic is used. A tube made of silica glass is placed inside the outer conductor to prevent the direct contact of the outer electrode with the plasma. The diameters of the inner and outer conductor have been chosen so that the wave impedance obtained is as close as possible to 50 Ω. In practice, a wave impedance of 40 Ω has been

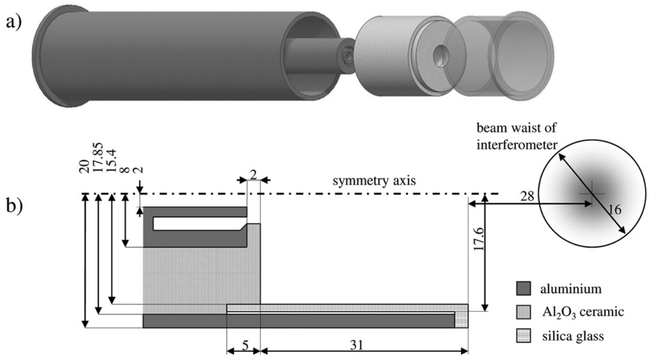

FIG. 1. (a) Plasma source in detail. (b) Schematic view of the source with the cross section of the beam of the microwave interferometer.

achieved. This results in a nearly disturbance-free access to the reflected wave which is only influenced by the plasma. The inner electrode is a tube through which the working gas is supplied. In order to protect surrounding people from microwave leakage in the case that plasma ignition fails (DIN EN 60519-6), the outer conductor is made approximately 30 mm longer than the inner one. Its diameter is taken less than the cut-off wavelength for the basic hollow waveguide mode H_{11} so that a damping of the microwave field along the tube is ensured. However, the longer outer electrode is advantageous from another point of view. In the case of electrodes of equal length, the plasma is generated and occupies the region close to the end of the inner electrode and the ceramic (Figure 1). The longer outer electrode enables the extension of the plasma insight the volume comprised. When the generated plasma expands, it acts as an extension of the inner electrode of the coaxial line through which the microwave can propagate to the end of the outer electrode. The reflected microwave is then primarily absorbed in the plasma. In that way, the energy absorbed in the plasma can be increased by 30%.

Plasma sources in the kW power range usually require active cooling in order to be operated in continuous mode. Due to the self-igniting capability, the source can be operated in a pulse-width modulation regime with a cycle duration of 110 ms and a power-on time of 23 ms. In that way, the thermal stress is reduced to a level, which requires no active cooling.

The plasma source is mounted to the plasma reactor with a volume of approximately 5 l by means of a flange (ISO-KF-40). The reactor possesses six ports of the type ISO-K 100 (shown below in Figure 3). Two of them (at the top and the backside of the vessel) are made of silica glass and ensure optical access. The others are windows made of teflon and have a thickness proportional to one-half wavelength of the microwave interferometer applied for electron density measurements (see Sec. II C). The distance between two opposing windows is about 0.5 m.

A mass flow controller regulates the incoming gas flow in the reactor. The combination of a rotary vane pump with a turbo molecular pump allows achieving a minimum pressure below 10^{-3} millibars. The pressure is controlled by an adjustable valve between the pumps and the reactor.

B. Microwave source and diagnostics

Figure 2 represents the arrangement of the microwave power line. The microwave power up to 2 kW is provided by a magnetron generator at a frequency of 2.45 GHz via a circulator with water load. Two −60 dB directional couplers have been used to supply two independent detecting systems. The scattering parameters of the directional couplers have been determined precisely using a vector network analyzer (Rohde & Schwarz ZVRE). The rectangular hollow waveguide line (WR 340) ends with a mode coupler to connect the plasma source by means of a coaxial cable (Ecoflex 15).

The first detecting system is aimed at recording the dynamic start-up behaviour of the microwave field. For that purpose, a heterodyne reflectometer is supplied with the incident and the reflected microwaves via coaxial test cables (SOCUTEST 13.0 GHz). The complex amplitudes of the power waves are denoted in Figure 2 with $\underline{a}_C$ and $\underline{b}_C$, respectively. With the available memory depth, the first millisecond of the pulse can be resolved within 500 ns so that the dynamic start-up interaction between the generated plasma and the microwave can be observed.

The second detecting system is used to monitor the established steady state phase for parasitic discharges and to estimate the steady state power. Here, a time resolution of 100 μs is sufficient to obtain the absolute values of the incident and reflected waves by means of detector diodes (ACSP-2502). In order to increase the detection accuracy, a power calibration for both the diodes has been performed using the vector network analyzer. Then, the detector voltages $\underline{u}_a$ and $\underline{u}_b$ yield the values of the incident and reflected power.

Such an intricate approach is usually regarded as unnecessary, especially if a matching network for minimizing the reflected power is applied. However, matching networks have quite a strong influence on the phase values and are hard to compensate due to the resonant structure. Furthermore, the minimization of the reflected wave complicates its detection. The advantage of the system used in the present study is that due to the absence of a matching network and the proper creation of the plasma-wave interaction zone, there is a disturbance-free access to the reflected wave. Measuring both the amplitude and the phase of the microwaves delivers additional information and enables a deeper understanding of the plasma-microwave interaction.

C. Plasma diagnostics

The spatial distribution of the electron density is closely related to the electric field distribution and to controllable discharge parameters in plasma processing such as pressure, flow rate, and power.[11,31] In the case of microwave induced plasmas, the oscillating electromagnetic field makes direct measurements in the active zone of the plasma source unfeasible. Diagnostic techniques based on Langmuir probe,[32,33] Thomson scattering,[34,35] microwave interferometer,[25,36,37] and time-resolved optical emission spectroscopy[33] are widely used for diagnostics of microwave plasmas. Results

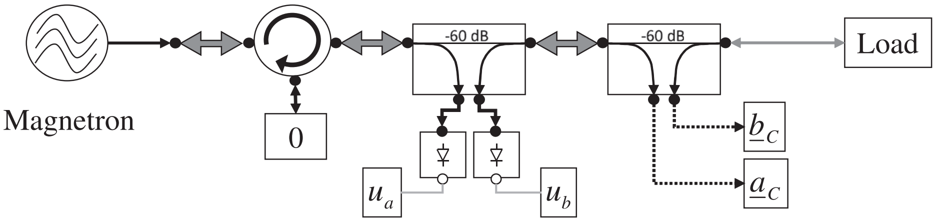

FIG. 2. Arrangement of the microwave power line.

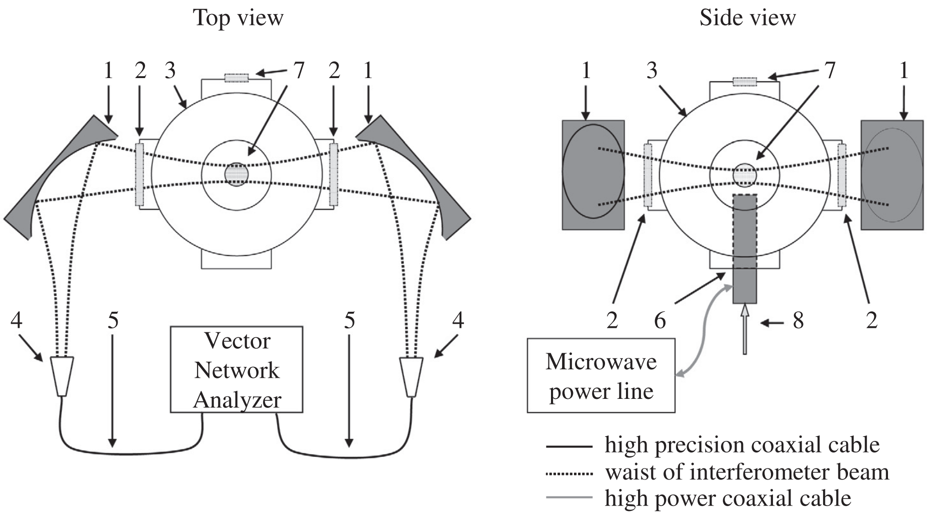

FIG. 3. Setup of the microwave interferometer. 1: elliptical mirror; 2: teflon window; 3: vacuum vessel; 4: conical horn antenna; 5: high precision flexible coaxial cable; 6: plasma source; 7: view port (silica glass); 8: gas inflow.

of Langmuir probe measurements inside a surface wave discharge are reported, e.g., in Refs. 38 and 39. It has been shown that the method is applicable in a certain distance from the intense field established close to the launcher. The diagnostic technique based on Thomson scattering provides spatially resolved electron densities and access to the electron energy distribution function.[35,40,41] However, it requires electron densities above 10^{18} m^{-3}, which can be observed in the active plasma zone. But this region is not accessible for the present plasma source. The microwave interferometer technique also needs a direct access to the investigated region. In order to provide such access, the outer electrode in Ref. 25 has a basket shape. The outer electrode of the plasma source presented in this work is constructed as a tube so that the direct access to the active zone is impossible. Because of the difficulties to measure the electron density in the active zone, microwave interferometry has been applied in the afterglow zone of the plasma. The basic principle behind this method is that the index of refraction of the travelling wave is affected by the plasma. As a result, a change in the phase shift between the reference signal and the signal with plasma appears. This variation can be used to determine the electron density.

The two-port setup used is shown in Figure 3. A vector network analyzer (Rohde & Schwarz ZVA 50) at 45.75 GHz has been used for the generation and detection[42] of the microwave. The wave is guided by a high precision flexible coaxial cable to a conical horn antenna which in turn emits a wave to be redirected and focused by an elliptical mirror. A minimal beam width of 16 mm is achieved with the elliptical mirrors used (see also Figure 1), which suits the diagnostic ports each having a diameter of 100 mm. Furthermore, the windows have a thickness proportional to one-half of the wavelength of the microwave interferometer in order to minimize their influence on the phase measurement. The windows are made of teflon, which is preferred as a material because of its low relative permittivity, e.g., lower by a factor of two as compared to silica glass.

The wave traveling through the plasma with local electron density $n_{\mathrm{e}}(y)$ undergoes over a path length dy a phase shift $\triangle\varphi = \varphi - \varphi_p = \left(\frac{2\pi}{\lambda} - \frac{2\pi}{\lambda_p}\right)dy$ with respect to the reference signal. Here, λ and λ_p denote the wavelength of the interferometer λ in free space and in the presence of plasma, respectively. Introducing the refractive index as equal to $\frac{\lambda}{\lambda_p}$, the phase shift becomes $\triangle\varphi = \frac{2\pi}{\lambda}\left(1 - \frac{\lambda}{\lambda_p}\right)$. The refractive index in turn can be expressed by means of the plasma frequency ω_p and the cut-off electron density n_{c} as $\left(1 - \frac{\omega_p^2}{\omega^2}\right)^{1/2} = \left(1 - \frac{n_{\mathrm{e}}(y)}{n_{\mathrm{c}}}\right)^{1/2}$. Considering the optical path connecting the positions y_1 and y_2, the phase shift is now being

$$\triangle\varphi = \frac{2\pi}{\lambda}\int_{y_1}^{y_2}\left[1 - \left(1 - \frac{n_{\mathrm{e}}(y)}{n_{\mathrm{c}}}\right)^{1/2}\right]\mathrm{d}y\,, \tag{1}$$

with

$$n_{\mathrm{c}} = \left(\frac{2\pi c}{\lambda}\right)^2\left(\frac{\varepsilon_0 m_{\mathrm{e}}}{e_0^2}\right), \tag{2}$$

the electron mass m_{e}, the elementary charge e_0, the speed of light c, and the vacuum permittivity ε_0, respectively. Assuming $n_{\mathrm{e}} \ll n_{\mathrm{c}}$, the root in Eq. (1) can be replaced by $1 - n_{\mathrm{e}}(y)/(2n_{\mathrm{c}})$. Notice that the cut-off electron density at the field frequency of 45.75 GHz is $n_{\mathrm{c}} \approx 2.6 \times 10^{19}\mathrm{m}^{-3}$.

Provided that a phase difference $\triangle\varphi$ between the off-cycle (serving as a reference signal) and the on-cycle of the pulse was measured, the electron density can be deduced by applying electron density profiles $f(y)$. Then, the maximum electron density reads

$$n_{\mathrm{e}}^{\max} = \frac{n_{\mathrm{c}}\lambda\triangle\varphi}{\pi\int_{y_1}^{y_2} f(y)\mathrm{d}y}\,. \tag{3}$$

Notice that the local electron density can be written as $n_{\mathrm{e}}(y) = n_{\mathrm{e}}^{\max} f(y)$ assuming that $f(y)$ is a monotonically decreasing function with a maximum value of unity at the centre. In the present study, profiles obtained by the plasma model presented in Sec. III and corresponding to the position of observation are applied in order to evaluate the electron density. The temporal resolution of the present setup was

0.1 ms. The detection range of the electron density was spread from about 2×10^{14} m^{-3} up to 10^{18} m^{-3}.

III. MAIN FEATURES OF THE MODEL

The model used in the present work is similar to the previously developed one which has been reported in detail in Ref. 28. Its main features including some differences in the reaction kinetics in comparison with the one used in Ref. 28 are described in the following.

The computational domain comprising the plasma source and a region of the plasma jet is shown in Figure 4. The model aims at a realistic representation of the plasma source, and this includes the details described in Sec. II A (see Figure 1). The coaxial line applied and the source design offer the opportunity to consider a spatially two-dimensional (2D) and axially symmetric system. The excitation boundary (segment "ab" in Figure 4) is taken sufficiently deep in the coaxial line for a pure TEM (transversal electromagnetic) field configuration. The working gas is supplied through the hollow cylindrical part of the inner conductor.

The model investigates the plasma jet together with the electromagnetic field in a self-consistent manner. Therefore, quantities describing the plasma state and motion, and the electromagnetic field have to be solved. Since no spectroscopic measurements were possible inside the plasma source, the model is based on the general case of a non-equilibrium plasma.

The collision times between the particles in the plasma are much shorter than the characteristic time scale of the flow so that the plasma behaves like a fluid. Due to frequent collisions between electrons and heavy particles, all species in the plasma attain approximately equal velocity and hence a separate momentum equation for electrons is not required. Therefore, the continuity equation and equation of motion of the plasma are written in the form of Navier-Stokes equations providing the solution for the total mass density ρ and the mass-averaged velocity $\vec{V}$, where the plasma flow is assumed to be laminar.

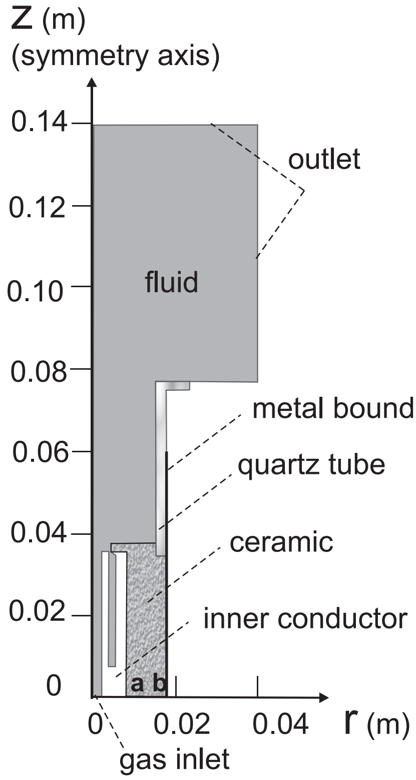

FIG. 4. Schematic representation of the computational domain.

There are separate energy balance equations for the heavy particles and electrons in a way that the heavy species (atoms and ions) are assumed to have a common temperature T and the electrons are characterized by a Maxwellian energy distribution function with a temperature T_e with $T_e \neq T$. Notice that a more precise consideration should couple the plasma model with a solution of the Boltzmann equation for the electrons in order to obtain the electron energy distribution function. Deviations from the Maxwellian distribution appear for electron energy beyond 10–12 eV due to the excitation of electronic states. From the point of view of the complexity of the present model and the relatively high wave frequency, the Maxwellian distribution seems to be a reasonable approximation.[40,43] Improvement of the model concerning non-Maxwellian electron energy distribution function and the evaluation of the corresponding transport parameters and rate coefficients[44] will be part of future studies.

Equations of species' conservation are solved for the densities N_{sp} of ions and excited atoms. The density N_g of ground state atoms is determined from Dalton's law of partial pressures and the electron density n_e results from the assumption of quasineutrality.

Furthermore, Maxwell's equations are solved assuming harmonic time variation of the components of the electric field $\vec{E}$ and the magnetic field $\vec{H}$ to obtain the Lorentz force $\vec{F_L}$ and the electric field heating Q_{fh} appearing in the momentum conservation equation and the electron energy balance, respectively. The coupled set of equations of the plasma to be solved reads

$$\frac{\partial \rho}{\partial t} + \nabla \cdot \left(\rho \vec{V}\right) = 0\,, \tag{4}$$

$$\rho \frac{\partial \vec{V}}{\partial t} + \rho(\vec{V} \cdot \nabla)\vec{V} = \nabla \cdot \left(-p\hat{I} + \hat{\tau}\right) + \vec{F}_L\,, \tag{5}$$

$$\rho C_p \frac{\partial T}{\partial t} + \rho C_p \vec{V} \cdot \nabla T = \nabla \cdot (\lambda \nabla T) + Q_{el}\,, \tag{6}$$

$$\frac{\partial}{\partial t}\left(\frac{3}{2} n_e k_B T_e\right) + \nabla \cdot \vec{F}_e = Q_{fh} - Q_{el} - Q_{in}\,, \tag{7}$$

$$\frac{\partial N_{sp}}{\partial t} + \nabla \cdot \left(-D_{sp} \nabla N_{sp} + N_{sp} \vec{V}\right) = S_{sp}\,, \tag{8}$$

$$\nabla \times \vec{E} = -i\omega\mu_0 \vec{H}\,, \quad \nabla \times \vec{H} = i\omega\varepsilon_0\varepsilon_{pl}\vec{E}\,, \tag{9}$$

$$\nabla \cdot \left(\varepsilon_0 \varepsilon_{pl} \vec{E}\right) = 0\,, \quad \nabla \cdot \vec{H} = 0\,. \tag{10}$$

In the equation of motion of the plasma, Eq. (5), p, $\hat{I}$, and $\hat{\tau}$ are the gas pressure given by the sum of the partial pressures of all species, the identity matrix, and the viscous stress tensor, respectively. The components of the latter for Newtonian flows are given by[45] $\tau_{ik} = \eta\big(\partial V_i/(\partial x_k) + \partial V_k/(\partial x_i) - 2\delta_{ik}(\nabla \cdot \vec{V})/3\big)$, where η denotes the viscosity of the fluid. C_p and λ in the energy balance (6) of the heavy particles denote the specific heat capacity and the thermal conductivity. The term Q_{el} in Eq. (6) and in the electron energy equation (7) accounts for the energy transfer from the electrons to the heavy particles in elastic collisions. Furthermore, k_{B}, $\vec{F}_{\mathrm{e}}$, and Q_{in} in (7) are the Boltzmann constant, the flux of electron energy containing the hydrodynamic flux of enthalpy and the heat conduction flux, and the rate of electron energy loss per unit volume due to inelastic collisions, respectively. Equation (8) describes the transport of the ions and excited atoms. It includes the corresponding diffusion coefficient D_{sp} and source term S_{sp}, resulting from reactions of production and loss of the species. The ambipolar diffusion coefficient has been used in the equation for the ions. Maxwell's equations (9) and (10) contain the angular field frequency ω, vacuum permeability μ_0, and the relative plasma permittivity $\varepsilon_{\mathrm{pl}}$, and $i = \sqrt{-1}$.

In order to get an estimate during the post-discharge phase, the coefficient of ambipolar diffusion of the ions is modified to account for the transition from ambipolar diffusion to free diffusion regime.[46,47] This problem has been studied in Ref. 48 considering Poisson's equation and continuity and momentum transfer equations for both electrons and ions. It has been shown that assuming equality of the electron and ion fluxes, and proportionality, an effective diffusion coefficient for the electrons in the presence of a space-charge field can be introduced according to

$$D_{se} = D_a \frac{D_e + \Lambda^2 e_0 n_e \mu_e/\varepsilon_0}{D_a + \Lambda^2 e_0 n_e \mu_e/\varepsilon_0}\,, \tag{11}$$

where D_a is the ambipolar diffusion coefficient, μ_e is the electron mobility, and $\Lambda = R/2.405$ is the characteristic diffusion length for a cylindrical volume of radius R. Applying a similar expression for the ions as done in Ref. 47, an estimation of the post-discharge conditions can be obtained avoiding a great piece of computational work, which is out of the scope of the present investigation. The ambipolar diffusion represents a good approximation for the type of description under consideration since it holds up to quite low electron densities. In any case, ambipolar diffusion gives the upper limit for the species decay.

In addition, the heat transfer in the dielectric solids, i.e., the ceramic and quartz tube, is described by the equation

$$\rho_{\mathrm{s}} C_{\mathrm{ps}} \frac{\partial T}{\partial t} = \nabla \cdot (\lambda_{\mathrm{s}} \nabla T)\,. \tag{12}$$

Here, ρ_{s},C_{ps}, and λ_{s} are the mass density, heat capacity, and thermal conductivity of the corresponding solid, respectively.

Maxwell's equations (9) and (10) have been solved in the dielectric solids with the relative dielectric permittivity ε_{s} of 1.65 in the ceramic and 3.78 in the quartz material. The relative permittivity of the plasma is expressed by the Lorentz formula

$$\varepsilon_{\mathrm{pl}} = 1 - \frac{\omega_{\mathrm{p}}^2}{\omega(\omega - i\nu_{\mathrm{m}})}\,, \tag{13}$$

with the plasma frequency $\omega_{\mathrm{p}} = \sqrt{n_{\mathrm{e}} e_0^2/(\varepsilon_0 m_{\mathrm{e}})}$ and the effective electron collision frequency for momentum transfer ν_{m}.

Equations (5)–(7) are strongly coupled with Maxwell's equations (9) and (10). The Lorentz force term in (5) is given by $F_{\mathrm{L}} = \mathrm{Re}(\sigma \vec{E} \times \vec{B}^*)/2$, where $\vec{B}^* = \mu_0 \vec{H}^*$ is the complex conjugate of the magnetic induction with the complex conjugate of the magnetic field $\vec{H}^*$. The density of energy transferred to the heavy species in collisions with electrons appearing in Eq. (6) as an energy gain, and in Eq. (7) as an energy loss term, is determined by $Q_{\mathrm{el}} = 3 m_{\mathrm{e}} n_{\mathrm{e}} \nu_{\mathrm{m}} k_{\mathrm{B}} (T_{\mathrm{e}} - T)/M$, where M is the mass of the heavy species. The field heating term in Eq. (7) describing the density of absorbed microwave power is obtained as $Q_{\mathrm{fh}} = \mathrm{Re}(\sigma \vec{E} \cdot \vec{E}^*)/2$, where $\sigma = n_{\mathrm{e}} e_0^2/[m_{\mathrm{e}}(\nu_{\mathrm{m}} + i\omega)]$ is the electric conductivity, and $\vec{E}^*$ denotes the complex conjugate of the electric field $\vec{E}$. The respective loss and gain of electron energy due to, e.g., binary inelastic collision processes of electrons with heavy particles is expressed as $Q_{\mathrm{in}} = n_{\mathrm{e}} \sum_{\mathrm{sp},r} N_{\mathrm{sp}} K_r \epsilon_r$, where K_r and ϵ_r denote the rate coefficient and the energy amount in reaction "r" with a participation of species of kind "sp."

When applying the model to an argon plasma, the considered species are the ground state argon atom (Ar), electronically excited argon atom (Ar*), which groups the 4s resonant and metastable states of argon, atomic ion (Ar$^+$), and electrons (e). The molecular ion (Ar$_2^+$) has been considered in the more general reaction scheme applied in Ref. 28. Under the conditions in the present study, its role was found to be negligible. In the active plasma zone, the density of the molecular ions is lower than that of the atomic ions by two orders of magnitude. Near the tube walls, where the gas temperature is low, the contribution of the molecular ions is below 10%. For that reason and in order to save computational costs related to the additional species equation and the more complex approach which has to be applied without using the proportionality assumption,[49,50] only the atomic ion is considered in the present work. The processes considered and the corresponding rate coefficients K_r are summarized in Table I. The electron collision frequency for momentum transfer in elastic collisions with atoms and ions is given by

$$\nu_{\mathrm{m}} = \sqrt{\frac{8 k_{\mathrm{B}} T_{\mathrm{e}}}{\pi m_{\mathrm{e}}}} (N_{\mathrm{Ar}} Q_{\mathrm{ea}} + n_{\mathrm{e}} Q_{\mathrm{ei}})\,, \tag{14}$$

where the cross sections for collisions of electrons with atoms and ions, Q_{ea} and Q_{ei}, are determined by[51,52]

$$Q_{\mathrm{ea}} = \left(3.6 \times 10^{-4} T_{\mathrm{e}} - 0.1\right) \times 10^{-20}\,\mathrm{m}^2, \tag{15}$$

$$Q_{\mathrm{ei}} = \frac{e_0^4}{24\pi(\varepsilon_0 k_{\mathrm{B}} T_{\mathrm{e}})^2} \ln\left(1.2384 \times 10^7 \sqrt{\frac{T_{\mathrm{e}}^3}{n_{\mathrm{e}}}}\right) \mathrm{m}^2, \tag{16}$$

with the electron temperature T_{e} given in kelvin.

The model is completed by the following boundary conditions. At the inlet boundary (cf. Figure 4), the flow velocity has a uniform profile and a value determined from a given flow rate. The inflow temperature is 300 K. The velocity and gradient of the electron temperature at the fluid-solid interfaces are set to zero. At the outlet, a constant pressure is specified along with zero gradients of the temperature, particle

TABLE I. List of processes considered in the present model. The rate coefficients K_r are given in m^3/s for two-body collision processes and in m^6/s for three-body collision processes. The electron temperature T_e is expressed in eV.

r	Process	Rate coefficient K_r	Reference
1	$\mathrm{e} + \mathrm{Ar} \rightarrow \mathrm{e} + \mathrm{Ar}^*$	$4.9 \times 10^{-15} T_e^{0.5} \exp(-11.65/T_e)$	55
2	$\mathrm{e} + \mathrm{Ar}^* \rightarrow \mathrm{e} + \mathrm{Ar}$	$4.8 \times 10^{-16} T_e^{0.5}$	55
3	$\mathrm{e} + \mathrm{Ar} \rightarrow 2\mathrm{e} + \mathrm{Ar}^+$	$1.27 \times 10^{-14} T_e^{0.5} \exp(-15.76/T_e)$	55
4	$\mathrm{e} + \mathrm{Ar}^* \rightarrow 2\mathrm{e} + \mathrm{Ar}^+$	$1.37 \times 10^{-13} T_e^{0.5} \exp(-4.11/T_e)$	55
5	$2\mathrm{e} + \mathrm{Ar}^+ \rightarrow \mathrm{e} + \mathrm{Ar}^*$	$8.75 \times 10^{-39} T_e^{-4.5}$ for $T_e \leq 0.26\,\mathrm{eV}$ $1.29 \times 10^{-44}(11.659/T_e + 2)$ $\times \exp(4.11/T_e)$ for $T_e > 0.26\,\mathrm{eV}$	56 57
6	$\mathrm{Ar}^* + \mathrm{Ar}^* \rightarrow \mathrm{Ar}^+ + \mathrm{Ar} + \mathrm{e}$	6.2×10^{-16}	58
7	$\mathrm{Ar}^* + \mathrm{Ar} \rightarrow 2\mathrm{Ar}^+$	3.0×10^{-21}	58
8	$\mathrm{e} + \mathrm{M} \rightarrow \mathrm{e} + \mathrm{M}$ ($\mathrm{M}=\mathrm{Ar}, \mathrm{Ar}^+$)	Cross sections Q_{ea}, Q_{ei} (see text)	51 and 52

densities, and axial velocity. Symmetry conditions with respect to the z axis (cf. Figure 4) imply zero gradients of the particle densities, temperature, and axial velocity. Surface reactions of recombination ($\mathrm{Ar}^+ \rightarrow \mathrm{Ar}$) and de-excitation ($\mathrm{Ar}^* \rightarrow \mathrm{Ar}$) on the fluid-solid boundaries supply the particle fluxes. Regarding the electromagnetic field, a perfect electric conductor is assumed at the metallic walls, absorbing boundary conditions[53] are applied at the outlet, and continuous tangential components are supposed at material interfaces. The magnetic field is set to zero at the inlet. The excitation boundary "ab" in Figure 4 is considered as active port for the incoming microwaves of the type TEM with a time-dependent power $P_{\mathrm{in}}(t)$ known from experimental data.

The initial value of the electron density was set to $10^{11}\,\mathrm{m}^{-3}$, sufficient to initiate the discharge. The initial gas temperature and electron temperature were 300 K and 0.05 eV, respectively, and the electric and magnetic field were set to zero. The flow velocity distribution follows from the established cold gas flow.

The model is realized on the computational platform COMSOL Multiphysics software[54] applying the built-in interfaces for flow and heat transfer and microwave heating, while the partial differential equation formulation has been used for the equations of species densities and electron energy. That is, the plasma module of COMSOL Multiphysics was not used for the calculations. The fully coupled and self-consistent features of the model enable a physically justified description of the interaction between the plasma and microwave.

The calculations have been performed using a mesh with about 18 000 elements. The time step size has been 10^{-12} s during the ignition phase and 10^{-6} s and 10^{-5} s during the pulse and the afterglow phase, respectively. The computations of the entire temporal development of the discharge from $t = 0$ to 50 ms took about 3 weeks on a single 3 GHz CPU computer. The computational time reduces to a couple of days on a multicore computer but remains still significantly long in consequence of the complexity of the simulation.

IV. RESULTS AND DISCUSSION

Measurements and corresponding simulations have been performed in argon for two sets of working conditions: (1) a pressure of 20 millibars and a gas flow rate of 250 sccm and (2) a pressure of 40 millibars and a gas flow rate of 500 sccm. For definiteness, we indicate that the term "peak value of the incident power" as used in the following refers to the incident microwave power established in the steady state phase of the discharge. For each set, microwave pulses with a duration of 23 ms and a variation of the peak value of the incident power have been supplied.

Figures 5 and 6 present the temporal development of two plasma characteristics, namely, the microwave power absorbed in the plasma $P_{\mathrm{abs}}(t)$ and the electron density obtained in the experiment and determined by the model. The first one is an integral quantity comprising the response of the entire medium to the incoming microwaves. The second one gives the local electron density $n_e(r = 0, z = 0.0965\,\mathrm{m}, t)$ obtained in the model at the axial position $z = 0.0965$ m (cf. Figure 4) corresponding to the position of observation, i.e., 28 mm above the upper edge of the glass tube (see Figure 1), in comparison with the experimental value n_e^{max} derived from (3) at the same position. Notice that the experimental values contain a spatial averaging due to the size of the microwave beam in the axial as well as in the radial direction even if evaluated at the same observation

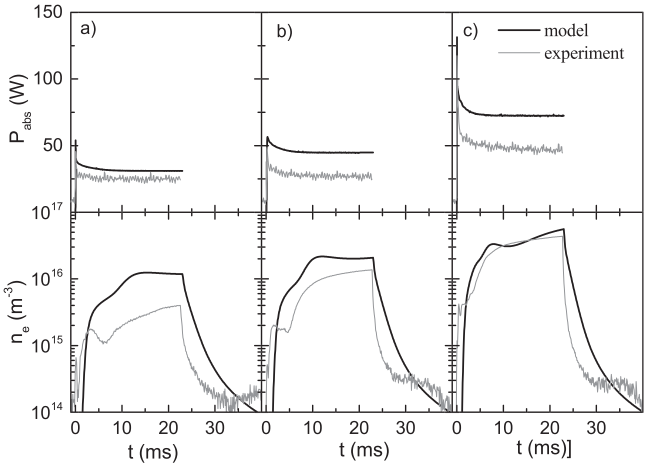

FIG. 5. Absorbed microwave power and electron density at the observation position for a gas pressure of 20 millibars and flow rate of 250 sccm at incident microwave powers with a peak value of (a) 100 W, (b) 150 W, and (c) 300 W.

position. From this point of view, the experimental results and the modeling predictions are compared to each other not for validation purposes but in order to show the trends in the discharge development. Nevertheless, the obtained values can also be discussed quantitatively.

The calculated temporal behaviour of the absorbed microwave power is similar in all cases considered. It rises within the first $20-30\,\mu$s and reaches a maximum value. Afterwards, it decreases and remains almost constant until the end of the pulse. The absorbed microwave power during the burning phase obtained with the plasma model increases nearly linearly with increasing peak value of the incident microwave power. The same behaviour is observed in the experiment.

The calculated values of the absorbed power are higher than the experimental ones, but the results agree within a factor of two for all cases. The discrepancy between predicted and measured values tends to grow with increasing peak value of the incident microwave power and the gas pressure. For the gas pressure of 20 millibars, the steady-state values of the absorbed power agree within 16% for the peak value of 100 W and within 36% for that of 300 W. When increasing the gas pressure to 40 millibars, the deviation is about 45% for all power levels. The higher values of the predicted absorbed power are not surprising since, on the one hand, the model does not account for losses at/in the walls, transmission lines, connectors, etc., and on the other hand, the experimental values contain uncertainties. The larger discrepancy at increasing power consumption can probably be explained by a stronger non-uniformity of the plasma. The two-dimensional axisymmetric model, which presumes a repetition of properties in azimuthal direction, provides an enhanced integral value. The almost equal deviation for all power levels at 40 millibars (cf. Figure 6) indicates azimuthal non-uniformity already at a power of 100 W. Indeed, photographic observations of the plasma confirmed the formation of regions of strong non-uniformity with increasing microwave power.

Consider now the temporal development of the electron density at axial position $z = 0.0965$ m (Fig. 4) obtained in the plasma model and the experimentally evaluated maximum electron density from the microwave interferometry. A rapid increase in the early pulse stage is followed by a long plateau and a relatively slow decay during the off-phase of the pulse, where the measured electron density can assume values comparable with the detection limit of about 2×10^{14} m^{-3} for times later than 23 ms. The quantitative comparison shows a very good agreement between calculated and measured electron densities at the pressure of 20 millibars and flow rate of 250 sccm for larger incident powers and higher modeling results of about 60% at the end of the steady state phase for the peak power value of 100 W (Figure 5). When doubling the pressure and flow rate simultaneously (Figure 6), the calculated densities are smaller than the measured ones, where the deviations increase up to about 60% at the end of the steady state phase. In this context, one has to keep in mind that the absorbed microwave power, which is always smaller in the experiment, is an integral quantity and that the position of the electron density measurement is in the afterglow zone, i.e., outside the active plasma zone. Thus, the non-uniformity of the plasma in the active zone as a result of the plasma-microwave interaction is expected to have a strong influence on the integral quantity and to become weaker in the afterglow zone due to the processes of convection and diffusion.

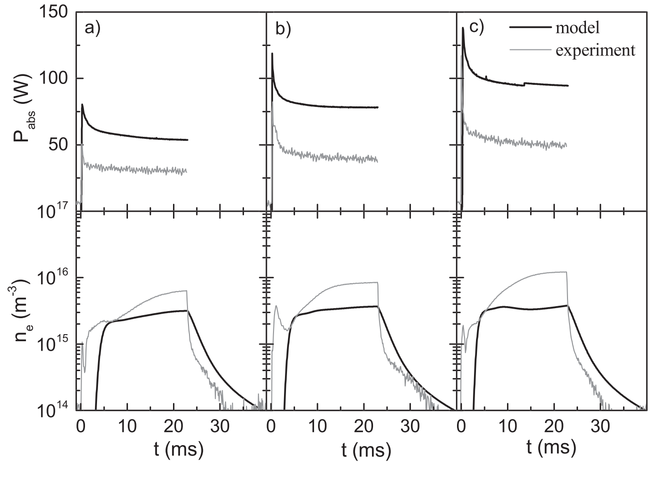

FIG. 6. Absorbed microwave power and electron density at the observation position for a gas pressure of 40 millibars and flow rate of 500 sccm at incident microwave powers with a peak value of (a) 150 W, (b) 250 W, and (c) 300 W.

Experiments with the microwave interferometer at a position closer to the active zone or a second position downstream in the afterglow zone have not been carried out. The access to the active zone is restricted by the beam diameter of about 16 mm. In the downstream afterglow zone, the electron density can fall to values comparable with the detection limit. From experimental point of view, further factors having an impact on the absolute values of the electron density are the spatial averaging in the z-direction over the cross section of the beam in the microwave interferometer and the assumption of a time-independent radial profile used in Eq. (3) for the sake of simplicity. From the point of view of the modeling, there is still an uncertainty in the rate coefficients of the processes considered in the model (cf. Table I) resulting from insufficiently known cross section data and the assumption of a Maxwellian electron energy distribution function. The deviations in the afterglow phase of the discharge at 40 millibars and 500 sccm (cf. Figure 6) indicate an uncertainty in the diffusion coefficient of the ions, which has an influence on the electron density because of the assumption of quasineutrality.

It is difficult to evaluate the experimental errors in the present investigation. Considering the analytical expression (1), the precision of $n_\mathrm{e}^\mathrm{max}$ depends on the precision of the phase shift and the profile assumed. Indeed, the phase shift has been measured within an uncertainty of about 10%. However, the power fluctuations which have an impact on the experiment as a whole are significantly larger (see, e.g., the course of $P_{in}(t)$ in Figure 7).

In the following, the plasma-microwave interaction during the discharge initiation is discussed. Figure 7 shows the temporal behaviour of the phase, the reflection coefficient of the microwave along with the incident and absorbed power during the first 0.5 ms of the discharge. The modulus of the

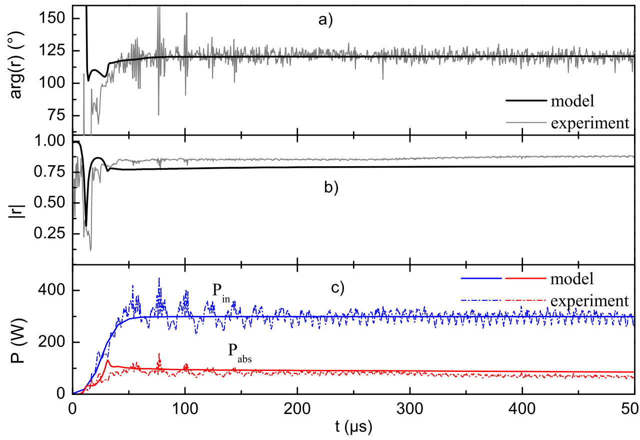

FIG. 7. Phase (a), reflection coefficient (b), and incident and absorbed microwave power (c) at a gas pressure of 20 millibars, flow rate of 250 sccm, and peak value of the incident power of 300 W.

complex reflection coefficient, $|r|$, determines the absorbed microwave power, whereas the phase of the reflected microwave has been obtained as $arg(r)$. The experimental values follow from the heterodyne reflectometry (cf. Sec. II B). In the model, the phase and the reflection coefficient have been evaluated from the complex S_{11} parameter[59] which characterizes the excitation boundary "ab" in Figure 4 and is a part of the numerical solution. The phase has an arbitrary initial value. The data correspond to the case with a gas pressure of 20 millibars, a flow rate of 250 sccm, and a peak value of the incident power of 300 W. The time-dependent measured incident microwave power $P_{\mathrm{in}}(t)$ represents an input parameter of the model. In order to avoid numerical instabilities due to fluctuations of the experimental data, the smoothed curve shown in Figure 7(c) was used for the model calculations.

It becomes obvious from Figure 7 that the phase and the reflection coefficient decrease with increasing incident power from a start value of about 180° and close to unity, respectively, at the beginning, i.e., the transmission of the microwave increases. The electric field accelerates the electrons and at sufficient wave energy, energy is imparted to the electrons to ionize the background gas at rate, which exceeds the rate of electron loss. As a consequence, the electron density grows and the plasma begins to reflect an increasing part of the incident microwave power. After about 50 μs, the phase, the reflection coefficient, and the incident and absorbed microwave power reach almost time-independent values where a good agreement between measured and calculated data is found. This stage of the discharge is worth a more detailed consideration.

In order to get a deeper insight into the plasma-microwave interaction and the ignition of the discharge, spatially two-dimensional snap-shots of the modulus of the electric field, the electron temperature, and the electron density during the first 50 μs obtained by model calculation are presented in Figure 8. The respective instants are represented in

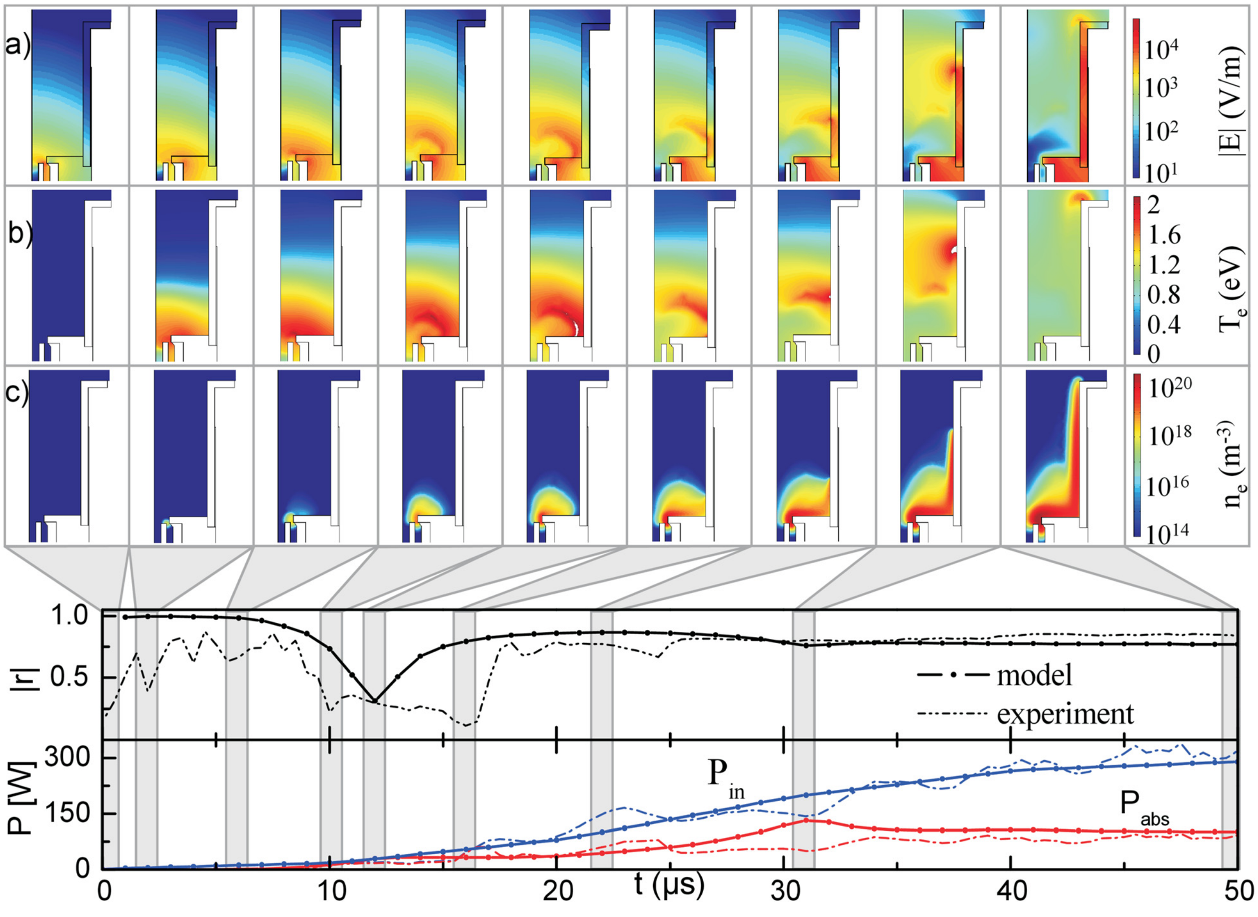

FIG. 8. Snap-shots of the electric field (a), electron temperature (b), and electron density (c) in relation to the reflection coefficient r, and incident and absorbed microwave power at a gas pressure of 20 millibars, flow rate of 250 sccm, and peak value of the incident power of 300 W.

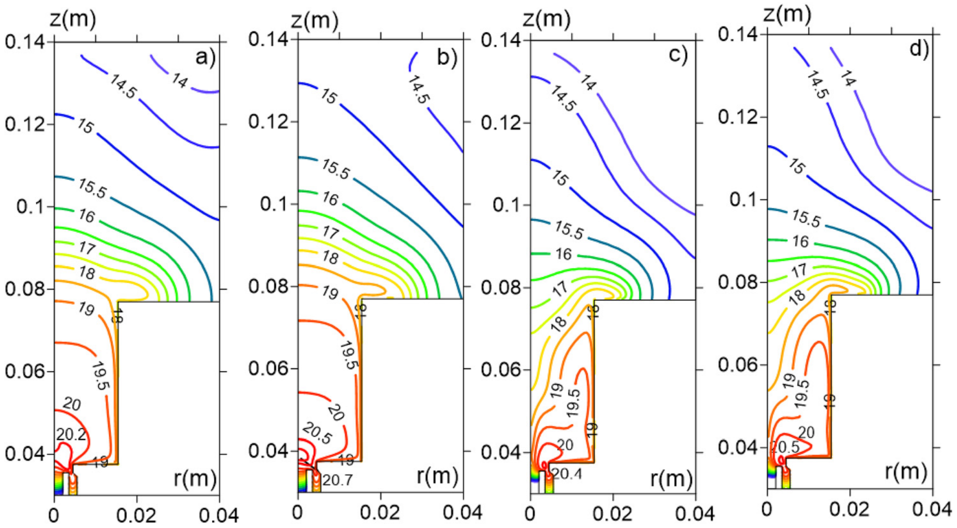

FIG. 9. Logarithmically scaled spatial distribution of the electron density at $t = 23$ ms for different working conditions specified by pressure, flow rate, and peak value of the incident power. (a) 20 millibars, 250 sccm, 150 W; (b) 20 millibars, 250 sccm, 300 W; (c) 40 millibars, 500 sccm, 150 W; (d) 40 millibars, 500 sccm, 300 W.

relation to the reflection coefficient as well as the incident and absorbed microwave power. At the start of the pulse, there are only the background electrons and ions in the fluid domain where $n_e = 1 \times 10^{11} \mathrm{m}^{-3}$ and $\omega_p = 5.6 \times 10^6 \mathrm{s}^{-1}$. The microwave is guided approximately to the end of the inner electrode. The electric field has a maximum value around the pin-shaped edge of the resonant structure (cf. Figures 1(b) and 4), where the plasma ignition starts a few microseconds later on. A short distance away from the pin, the electric field decreases by more than one order of magnitude. The electron density, the volume occupied by the plasma, and the absorbed power increase with increasing incident microwave power, whereas the reflection coefficient decreases. The generated core plasma expands towards the microwave. The rate of electron density growth depends on the mean energy that the electrons gain (and hence on T_e) and therefore on the electric field. At about $t = 12\,\mu$s, the edge of the plasma front with the cut-off electron density ($\sim 7.5 \times 10^{16} \mathrm{m}^{-3}$) approaches the quartz tube wall and the region of a high electric field is pushed in the same direction. Thereby, intensive heating of the plasma occurs and electron temperatures up to 2 eV are reached. These values indicate the state of thermal non-equilibrium of the plasma. More detailed analysis is given below. Here, we just point out that region of high electron temperatures follows the high values of the electric field and appears at the edge of the plasma front where the electron density values are close to the cut-off density. The reflection coefficient increases to an almost stable value corresponding to a certain ratio between the reflected and transmitted power. Microwave propagation and plasma expansion occur along and on the both sides of the tube walls approaching the end of the source head. The plasma plays the role of an extension of the inner electrode in the propagation of the microwave. Experimental and modelling results of r and P_{abs} agree well.

The steady state phase of the discharge ends at $t = 23$ ms, as illustrated in Figures 5 and 6. At this time, the plasma occupies the tube. The corresponding spatially two-dimensional distributions of the electron density and the heavy particle temperature are shown in Figures 9 and 10, respectively, for different working conditions. In particular, results for the peak values of the incident power of 150 and 300 W are displayed for the pressure and flow rate condition 20 millibars and 250 sccm as well as for 40 millibars and 500 sccm. Note that logarithmic scales are used for the representation of the electron density in Figure 9.

The results show that there exists a core region of the plasma around $z = 0.04$ m, where the electron density

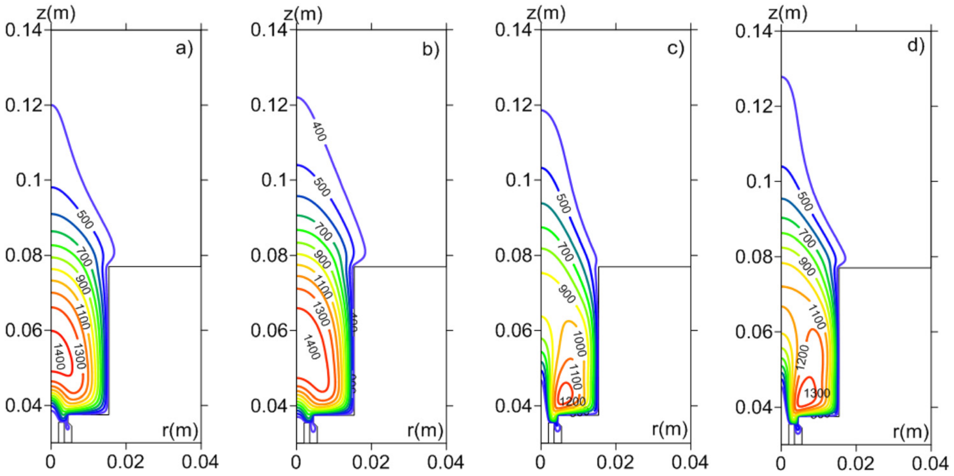

FIG. 10. Spatial distribution of the heavy particle temperature at $t = 23$ ms for the same working conditions as in Figure 9.

reaches values somewhat above $10^{20}\,\mathrm{m}^{-3}$. This region expands when increasing the power level for a given gas pressure (Figures 9(a) and 9(b)). When increasing the gas pressure, the core tends to move to the microwave and occupies the space close to the end of the ceramic (Figures 9(c) and 9(d)). Downstream of the core plasma, there is an extended region reaching the end of the source head which is caused by the longer outer electrode. Similar effects have been observed with the coaxial plasma source in Ref. 25 which also makes use of a longer outer electrode.

The region of the plasma extension is characterized by distributions of the electron density and gas temperature reaching maximum values on the symmetry axis for a gas pressure of 20 millibars (Figures 9(a), 9(b), 10(a), and 10(b)). The gas temperature reaches values up to about 1400 K for both input power values of 150 W and 300 W. However, the hottest region expands when increasing the power level. For a gas pressure of 40 millibars, the plasma extension builds a hollow structure in the distributions as shown in Figures 9(c), 9(d), 10(c), and 10(d). As a consequence, the distributions are characterized by off-axis maxima. The region of the plasma extension is further characterized by electron temperature values between 0.8 eV and 1 eV in the volume and somewhat above 1.6 eV close to the tube wall.

In order to analyze the gas heating, the corresponding terms in Eq. (6) are evaluated at the instant $t = 23\,\mathrm{ms}$, i.e., at the end of the steady state phase, along the tube radius. First, the provisional probe line passes through the core plasma region corresponding to the axial position $z = 0.04\,\mathrm{m}$. Since the plasma has reached its quasi-steady state at this instant, the contribution of the transient term is negligible. Close to the axis, the convective term $\rho C_p \vec{V} \cdot \nabla T$ is by far the biggest one with values of about $2 \times 10^7\,\mathrm{W m}^{-3}$ for a power of 150 W and a pressure of 20 millibars. The conductive term $\nabla \cdot \lambda \nabla T$ and the heating term due to elastic collisions Q_{el} get similar values of about $1 \times 10^7\,\mathrm{W m}^{-3}$, where Q_{el} is slightly larger than the conductive term. As a result, the gas is hardly heated. Toward the tube wall, the convective term vanishes, Q_{el} decreases gradually, but still prevails and the gas is heated up to about 1000 K. Close to the wall, Q_{el} is low, the conductive term increases so that the gas temperature decreases to the temperature of the wall.

Next, a probe line across the extended plasma is considered at $z = 0.055\,\mathrm{m}$ corresponding to the region of maximum gas temperature. Here, the convective term on the left hand side of Eq. (6) changes its sign with respect to that in the core region, i.e., it becomes negative and serves as a source for the gas heating. For radial positions measured from the axis up to 1/3 of the tube radius, approximately 30% of the gas heating is due to convection. On the midway to the wall, the convective contribution is about 20% and decreases toward the wall so that Q_{el} becomes the dominant heat source. The conductive term on the right hand side of (6) is negative now and provides the energy conservation. A similar behavior is found for a power of 300 W at 20 millibars. The analysis of the results along the probe line across the hollow structure of the plasma at $z = 0.055\,\mathrm{m}$ for the gas pressure of 40 millibars displayed in Figures 9(c), 10(c), 9, and 10(d) shows in particular that the convective and the conductive terms are dominant for radial positions up to approximately 3 mm. The convective term prevails over the conductive one, and Q_{el} is of minor importance. Beyond this point, the collisional term Q_{el} increases and becomes the dominant one, while the convective term vanishes. In front of the wall, the conductive term steeply increases.

The analysis in central part of the spatial afterglow ($z \geq 0.1\,\mathrm{m}$) showed that the gas heating results from the convective and conductive transport. The convective term being negative contributes to the heating. The gas temperature reaches values from about 500 K gradually decreasing below 350 K (Figure 10). The electron density is below $10^{16}\,\mathrm{m}^{-3}$ (Figure 9) so that the collisional heating is negligible.

These results show that the convection process (and conduction in the case of a hollow plasma structure) along with the elastic collisions is an important mechanism in the gas heating for the coaxial plasma source under investigation. In contrast, the investigations on the gas heating in a surfatron plasma by means of Rayleigh and Thomson scattering[60] have shown that the gas heating in this type of plasma source is only due to elastic collisions.

The detailed information provided by the model enables a better understanding of the evolution of the plasma-microwave interaction. In what follows, simulation data are analyzed for a gas pressure of 20 millibars, a flow rate of 250 sccm, and a peak value of the absorbed microwave power of 300 W, corresponding to the case in Figures 9(b) and 10(b). Figure 11 shows important characteristics of the plasma and the electric field obtained in the modeling for two instants of the discharge, along a radial line at the axial position $z = 0.04\,\mathrm{m}$. The first instant is $t = 10\,\mu\mathrm{s}$ and represents the early phase of the discharge. The second one is $t = 23\,\mathrm{ms}$ and corresponds to the late phase, where the discharge has reached its quasi-steady state. Notice that the results concerning the first instant are plotted with open symbols and dashed lines, whereas the results for the late discharge phase are plotted with solid symbols and solid lines. The temperature of heavy particles (gas temperature) is plotted with circles and the electron temperature with squares.

The common understanding based on global plasma models is that the absorbed microwave power appears in the regions of the highest electron density.[61] The electron density can even exceed the cut-off density since the collision frequency and the angular microwave field frequency are of the same order. The results obtained in the present work clearly show that the microwave power is mainly absorbed in the region of electron density values which are close to the cut-off density but in the early discharge phase while the core plasma is built. During the steady state phase, however, the maximum absorbed power corresponds to the positions close to the discharge walls. The region of intense power coupling moves toward the microwave, whereas the electron density reaches a maximum at the axis (Figure 11(a)). The spatial course of the absorbed power density follows that of the modulus of the electric field (Figure 11(b)). The power absorbed by the electrons from the electromagnetic field is distributed by the electrons in the plasma to sustain the losses due to collisional processes. Similar behavior has been observed in the modeling of microwave plasma sustained by surface waves.[62] In the early stage, the electron density is

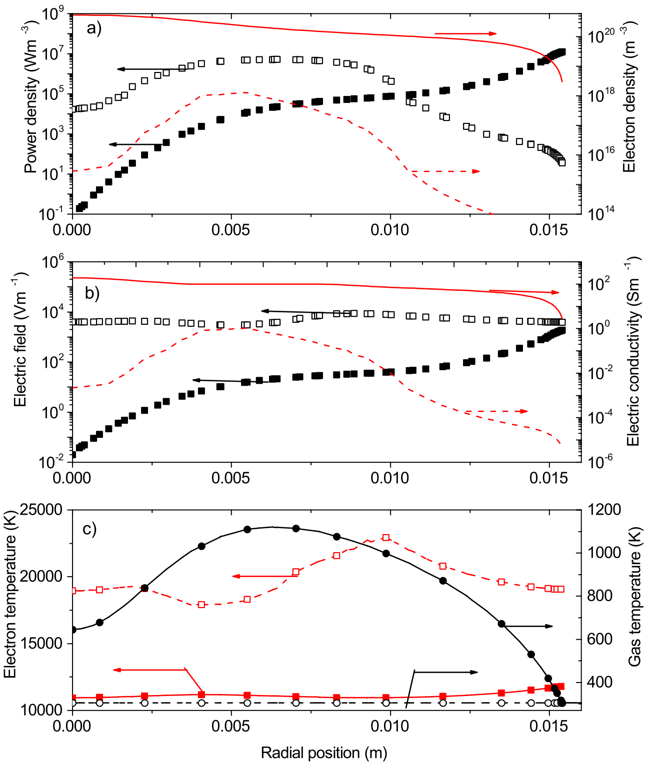

FIG. 11. Plasma and field characteristics along a radial line at the axial position $z = 0.04$ m at $t = 10\,\mu$s and $t = 23$ ms for a gas pressure of 20 millibars, a flow rate of 500 sccm, and a peak value of the incident power of 300 W. (a) The density of the absorbed microwave power and electron density; (b) the modulus of the electric field and the electric conductivity; (c) the temperatures of electrons and heavy particles. The results for $t = 10\,\mu$s are plotted with open symbols and dashed lines and the results for $t = 23$ ms are plotted with solid symbols and solid lines.

still of the order of the cut-off density so that the microwave can propagate into the plasma and the reflected microwave wave is weak. In the late phase, the electric field attenuates in the region of maximum electron density due to the strong reflection, but it is high near the walls. The electric conductivity, on the other hand, follows the spatial course of the electron density.

The heavy particle temperature increases just by a few degrees to the time $t = 10\,\mu$s, whereas the electron temperature reaches a value of about 20 000 K and above (Figure 11(c)). A significant difference between the temperatures of electrons and heavy particles is observed also in the late steady state phase where the gas temperature increases to a maximum value of about 1100 K, and the electron temperature is lower in comparison to the value during the early discharge stage, but it has values well above 10 000 K. These results confirm the state of thermal non-equilibrium of the generated plasma which is typical for low pressure microwave discharges. The profile of the electron temperature does not exactly follow the profile of the density of the absorbed microwave power due to the processes of convection and diffusion.

V. SUMMARY

The understanding of the plasma-microwave interaction is of key importance for the development and the application of plasma sources. It comprises the knowledge of the properties of the plasma and the electromagnetic field, which are strongly coupled to each another. In this work, the spatial and temporal behaviours of the plasma generated in a coaxial microwave source at a field frequency of 2.45 GHz have been investigated by means of consolidating experiments and modeling. The analysis covers incident microwave powers between 100 and 300 W in pulse modulated operation (a cycle duration of 110 ms and a power-on time of 23 ms) at the pressure and flow rate conditions with 20 millibars and 250 sccm as well as 40 millibars and 500 sccm.

The generated argon plasma is characterized by a core region, where maximum electron densities over $10^{20}\,\mathrm{m}^{-3}$ and electron temperatures of about 1 eV are observed during the steady state phase, and an extended plasma region promoted by the longer outer electrode where the electron density reaches values of about $10^{19}\,\mathrm{m}^{-3}$ and maximum gas temperatures of about 1400 K are found. The gas heating is mainly due to elastic collisions between electrons and atoms in the region of the core plasma. In the region of the extended plasma, the convection process plays an important role and contributes to the gas heating to about 20%–30%.

The temporally and spatially resolved modeling shows that the power in-coupling occurs in the core plasma region with the highest electron density in the early stage of the discharge, but during the steady state phase, it moves closer to the source walls where the electron density is not far from the cut-off density. Microwave propagation and plasma expansion occur along and on both sides of the tube walls approaching the end of the source head. The plasma plays the role of an extension of the inner electrode in the propagation of the microwave.

The temporal behavior of the measured and calculated phases, reflection coefficients, and absorbed microwave powers as well as local electron densities in the afterglow zone of the plasma agree generally well with each other for all conditions considered. With increasing input power and gas pressure, non-uniformities of the plasma appear, which are beyond the axisymmetric description of the current fluid model and require a spatially three-dimensional model which, however, implies a drastic increase of the computational time.

ACKNOWLEDGMENTS

The work was partly supported by the Leibniz SAW procedure and the BMBF (Bundesministerium für Bildung und Forschung) under Grant FZK 13N2428. The very helpful discussion with Dr. Vasco Guerra from Instituto de Plasmas e Fus̃ao Nuclear, Instituto Superior Técnico, Lisboa, Portugal, is greatly acknowledged.

[1] M. Moisan and Z. Zakrzewski, J. Phys. D: Appl. Phys. **24**, 1025 (1991).
[2] Microwave Discharges*: Fundamentals and Applications*, NATO ASI Series B: Physics, Vol. 302, edited by C. M. Ferreira and M. Moisan (Plenum, New York, 1993).
[3] A. Pott, T. Doerk, J. Uhlenbusch, J. Ehlbeck, J. Höschele, and J. Steinwandel, J. Phys. D: Appl. Phys. **31**, 2485 (1998).

[4] A. I. Babaritskii, E. N. Gerasimov, S. A. Demkin, V. K. Zhivotov, A. A. Knizhnik, B. V. Potapkin, V. D. Rusanov, E. I. Ryazantsev, R. V. Smirnov, and G. V. Sholin, Tech. Phys. **45**, 1411 (2000).

[5] A. I. Al-Shamma'a, S. R. Wylie, J. Lucas, and C. F. Pau, J. Phys. D: Appl. Phys. **34**, 2734 (2001).

[6] M. Baeva, H. Gier, A. Pott, J. Uhlenbusch, J. Höschele, and J. Steinwandel, Plasma Chem. Plasma Process. **21**, 225 (2001).

[7] J. Ehlbeck, A. Ohl, M. Maaß, U. Krohmann, and T. Neumann, Surf. Coat. Technol. **174–175**, 493 (2003).

[8] A. Rousseau, A. Dantier, L. Gatilova, Y. Ionikh, J. Röpcke, and Y. Tolmachev, Plasma Sources Sci. Technol. **14**, 70 (2005).

[9] J. Marec, E. Bloyet, M. Chaker, P. Leprince, and P. Nghiem, "Microwave discharges," in *Electrical Breakdown and Discharges in Gases*, Part B: Macroscopic Processes and Discharges, Series: NATO ASI: Physics (Plenum Press, 1983), pp. 347–382.

[10] C. Ferreira, M. Moisan, and Z. Zakrzewski, "Physical principles of microwave plasma generation," in *Microwave Excited Plasmas*, Vol. 4, Plasma Technology (Elsevier Science and Technology Books, 1992), pp. 11–52.

[11] Y. A. Lebedev, J. Phys.: Conf. Ser. **257**, 012016 (2010).

[12] H. Schlüter and A. Shivarova, Phys. Rep. **443**, 121 (2007).

[13] J. Ehlbeck, R. Brandenburg, T. von Woedtke, U. Krohmann, M. Stieber, and K.-D. Weltmann, GMS Krankenhaushyg. Interdiszip. **3**, Doc14 (2008).

[14] K. Rackow, J. Ehlbeck, U. Krohmann, and M. Baeva, Plasma Sources Sci. Technol. **20**, 035019 (2011).

[15] A. V. Pipa, M. Andrasch, K. Rackow, J. Ehlbeck, and K.-D. Weltmann, Plasma Sources Sci. Technol. **21**, 035009 (2012).

[16] M. Moisan, J. Barbeau, S. Moreau, J. Pelletier, M. Tabrizian, and L. Yahia, Int. J. Pharm. **226**, 1 (2001).

[17] J. Ehlbeck, U. Schnabel, M. Polak, J. Winter, T. von Woedtke, R. Brandenburg, T. von dem Hagen, and K.-D. Weltmann, J. Phys. D: Appl. Phys. **44**, 013002 (2011).

[18] U. Krohmann, T. Neumann, J. Ehlbeck, and K. Rackow, "Method and device for igniting and generating an expanding diffuse microwave plasma and method and device for plasma treating surfaces and substances by using this plasma," U.S. patent US8232728 B2 (31 July, 2012).

[19] D. Siche, D. Gogova, S. Lehmann, T. Fizia, R. Fornari, M. Andrasch, A. Pipa, and J. Ehlbeck, J. Cryst. Growth **318**, 406 (2011).

[20] U. Krohmann, J. Ehlbeck, T. Neumann, U. Schnabel, M. Andrasch, W. Lehmann, and K.-D. Weltmann, "Plasma-generated gas sterilization method," Europe patent EP20110724984 (13 March, 2013).

[21] M. Moisan, G. Sauve, Z. Zakrzewski, and J. Hubert, Plasma Sources Sci. Technol. **3**, 584 (1994).

[22] Q. Jin, C. Zhu, M. W. Borer, and G. M. Hieftje, Spectrochim. Acta, Part B **46**, 417 (1991).

[23] A. M. Bilgic, C. Prokisch, J. A. C. Broekaert, and E. Voges, Spectrochim. Acta, Part B **53**, 773 (1998).

[24] L. L. Alves, R. Alvarez, L. Marques, S. J. Rubio, A. Rodero, and M. C. Quintero, Eur. Phys. J. Appl. Phys. **46**, 21001 (2009).

[25] S. I. Gritsinin, V. Y. Knyazev, I. A. Kossyi, N. I. Malykh, and M. A. Misakyan, Plasma Phys. Rep. **30**, 255 (2004).

[26] S. I. Gritsinin, I. A. Kossyi, E. B. Kulumbaev, and V. M. Lelevkin, Plasma Phys. Rep. **32**, 872 (2006).

[27] E. Carbone and S. Nijdam, Plasma Sources Sci. Technol. **23**, 012001 (2014).

[28] M. Baeva, A. Bösel, J. Ehlbeck, and D. Loffhagen, Phys. Rev. E **85**, 056404 (2012).

[29] U. Schnabel, R. Niquet, U. Krohmann, J. Winter, O. Schlüter, K.-D. Weltmann, and J. Ehlbeck, Plasma Process. Polym. **9**, 569 (2012).

[30] A. Fröhling, J. Durek, U. Schnabel, J. Ehlbeck, J. Bolling, and O. Schlüter, Innovative Food Sci. Emerging Technol. **16**, 381 (2012).

[31] M. A. Heald and C. B. Wharton, *Plasma Diagnostics with Microwaves* (Wiley, New York, 1965).

[32] T. Mieno and S. Samukawa, Plasma Sources Sci. Technol. **6**, 398 (1997).

[33] T. Ohgushi, T. Okamoto, S. Watanabe, and Y. Okamoto, Appl. Surf. Sci. **169–170**, 593 (2001).

[34] D. M. Manos, J. L. Cecchi, C. W. Cheah, and H. F. Dylla, Thin Solid Films **195**, 319 (1991).

[35] S. Hübner, J. M. Palomares, E. A. D. Carbone, and J. J. A. M. van der Mullen, J. Phys. D: Appl. Phys. **45**, 055203 (2012).

[36] J. Verdeyen, J. Beberman, and L. Overzet, J. Vac. Sci. Technol. A **8**, 1851 (1990).

[37] M. Baeva, X. Luo, B. Pfelzer, T. Repsilber, and J. Uhlenbusch, Plasma Sources Sci. Technol. **9**, 128 (2000).

[38] S. Grosse, H. Schlüter, and E. Tatarova, Phys. Scr. **50**, 532 (1994).

[39] F. M. Dias, E. Tatarova, and C. Ferreira, J. Appl. Phys. **83**, 4602 (1998).

[40] E. A. D. Carbone, S. Hübner, M. Jimenez-Diaz, J. M. Palomares, E. Iordanova, W. A. A. D. Graef, A. Gamero, and J. J. A. M. van der Mullen, J. Phys. D: Appl. Phys. **45**, 475202 (2012).

[41] A. F. H. van Gessel, E. A. D. Carbone, P. J. Bruggeman, and J. J. A. M. van der Mullen, Plasma Sources Sci. Technol. **21**, 015003 (2012).

[42] M. Andrasch, J. Ehlbeck, R. Foest, and K.-D. Weltmann, Plasma Sources Sci. Technol. **21**, 055032 (2012).

[43] E. Benova, T. Petrova, A. Blagoev, and I. Zhelyazkov, J. Appl. Phys. **84**, 147 (1998).

[44] G. J. M. Hagelaar and L. C. Pitchford, Plasma Sources Sci. Technol. **14**, 722 (2005).

[45] R. J. Moreau, *Magnetohydrodynamics* (Kluver Academic Publisher, Dordrecht, 1990).

[46] V. Guerra, P. A. Sa, and J. Loureiro, Phys. Rev. E **63**, 046404 (2001).

[47] K. Kutasi, V. Guerra, and P. A. Sa, Plasma Sources Sci. Technol. **20**, 035006 (2011).

[48] W. P. Allis, *Handbuch der Physik* (Springer, Berlin, 1956), pp. 383–444.

[49] A. V. Phelps and S. C. Brown, Phys. Rev. **86**, 102 (1952).

[50] B. M. Wunderer, IEEE Trans. Plasma Sci. **6**, 406 (1978).

[51] S. V. Dresvin, A. V. Donskoi, V. M. Goldfarb, and V. S. Klubnikin, *Physics and Technology of Low-Temperature Plasmas* (Iowa State University Press, Ames, 1977).

[52] M. Mitchner and C. H. Kruger, *Partially Ionized Gases* (Wiley, New York, 1973).

[53] A. M. Bilgic, K. Garloff, and E. Voges, Plasma Sources Sci. Technol. **8**, 325 (1999).

[54] COMSOL 4.3b, 2013.

[55] K. Makasheva and A. Shivarova, Phys. Plasmas **8**, 836 (2001).

[56] Y. P. Raizer, *Gas Discharge Physics* (Springer, Berlin, 1997).

[57] M. I. Hoffert and H. Lien, Phys. Fluids **10**, 1769 (1967).

[58] D. P. Lymberopoulos and D. J. Economou, J. Appl. Phys. **73**, 3668 (1993).

[59] D. M. Pozar, *Microwave Engineering*, 2nd ed. (Wiley, New York, 1998).

[60] S. Hübner, E. Iordanova, J. Palomares, E. Carbone, and J. van der Mullen, Eur. Phys. J. Appl. Phys. **58**, 20802 (2012).

[61] M. Leins, J. Kopecki, S. Gaiser, A. Schulz, M. Walker, U. Schumacher, U. Stroth, and T. Hirth, Contrib. Plasma Phys. **54**, 14 (2014).

[62] M. Jimenez-Diaz, E. A. D. Carbone, J. van Dijk, and J. J. A. M. van der Mullen, J. Phys. D: Appl. Phys. **45**, 335204 (2012).

5.6 Influence of the dielectric surrounding of plasma on the electron density measurement by microwave interferometer

IOP Publishing Measurement Science and Technology
Meas. Sci. Technol. **25** (2014) 075004 (9pp) doi:10.1088/0957-0233/25/7/075004

Influence of the dielectric surrounding of plasma on the electron density measurement by microwave interferometer

M Andrasch, J Ehlbeck and K-D Weltmann

INP Greifswald, Felix-Hausdorff-Straße 2, D-17489 Greifswald, Germany

E-mail: Andrasch@inp-greifswald.de

Received 16 December 2013, revised 20 March 2014
Accepted for publication 4 April 2014
Published 14 May 2014

Abstract

Using a vector network analyzer a frequency resolved microwave interferometer is built up in the range of 42.5–50 GHz. Due to the frequency resolved measurement technique it is possible to investigate the influence of the surrounding dielectric material on the transmission. The experiments are performed on a fluorescent lamp, which is enclosed by a glass tube. Furthermore, a dielectric resonator is built up by two plane silica windows, placed perpendicular to the beam. It was found that the influence can be described by a one-dimensional model using equivalent circuits, which is in very good agreement with experimental results. In addition, the common technique of rotating the windows to reduce their influence is investigated.

Keywords: microwave interferometry, etalon fringes, dielectric window, equivalent circuit

1. Introduction

One of the most important parameters to characterize plasma is the electron density. Therefore, in the last decades several methods have been developed. Among several others, a small overview of commonly used techniques is presented in table 1. The probe measurements, which can be further separated into electrostatic and microwave resonance probes, provide spatially resolved densities. However, these methods are invasive and they can only be applied in low to medium vacuum discharges (up to ≈ 1000 Pa). Another method to obtain spatially resolved electron densities is the Thomson scattering [1]. Besides its non-invasive character, it requires quite a high electron density. This applies also for the Stark broadening, which is a passive method. The last listed technique is the microwave interferometry, which provides line-integrated densities and is the focus of this paper.

In the case of non-atmospheric plasmas the investigated discharge is usually ignited inside a vacuum vessel made of conductive and dielectric materials. Therefore the microwave beam, which is used for the interferometry, is transmitted through a dielectric gas barrier. A model based on equivalent networks is presented to determine the influence of the dielectric barrier to the microwave beam. This model is verified by measurements with a frequency resolved microwave interferometer to investigate the influence of the dielectric surrounding on the electron density measurements of a fluorescent lamp. In addition the complex transfer function of a system composed of two silica windows with an adjustable gap is determined and compared with the model.

2. Experimental setup

The experimental setup is split into three sections. The first deals with the signal generation and detection and also takes the microwave engineering into account. This section is followed by the description of an experiment to measure distance changes for verifying the correct operation of the interferometer. The last section of the experimental setup refers to the used dielectric lenses for the microwave mapping.

2.1. Signal generation and detection

The interferometer is built up by using a vector network analyser (VNA) (Rohde and Schwarz ZVA 50). The VNA generates the electromagnetic wave in this setup in a frequency range between 42.5 and 50 GHz, with a frequency step size of 850 kHz and an output power at the Port 1 of 20 mW.

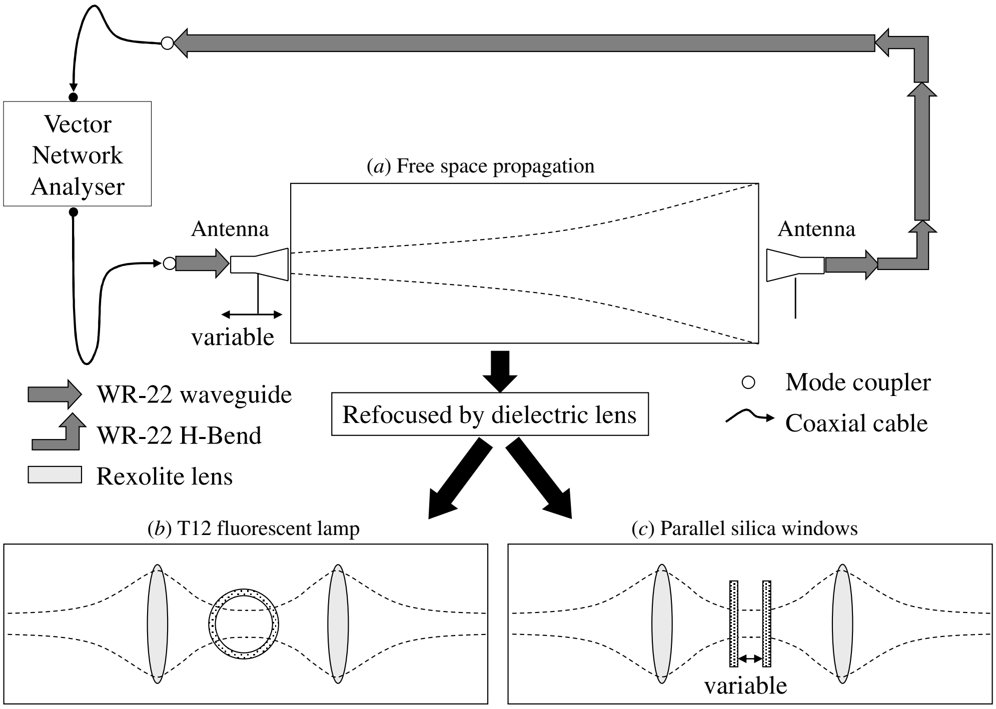

Figure 1. Schematics of the experimental microwave setup. (*a*) Illustrates the alignment for distance detection between the antennas, where the transmitting antenna is moveable along the propagation direction. (*b*) For refocusing the Gaussian beam, two dielectric lenses are used. In the focal point a fluorescent lamp of the type T12 is placed. (*c*) Two moveable windows made of silica glass are placed in the region of the focal point.

Table 1. An overview over methods to determine the electron density. Besides detection minimum and maximum, references are given. In addition, remarks and information about the spatial resolution are presented.

Method	References	n_e—Min.	n_e—Max.	Resolution	Remarks
Langmuir probe	[2, 3, 4]	10^8 m^{-3}	10^{18} m^{-3}	Spatially resolved	Only in low pressure
Microwave resonance probes	[5, 6, 7, 8]	10^{14} m^{-3}	10^{18} m^{-3}	Spatially resolved	Only in low pressure
Thomson scattering	[9, 10]	10^{18} m^{-3}		Spatially resolved	
Stark broadening	[11, 12, 13]	10^{19} m^{-3}		Line integrated	
Microwave interferometry	[14, 15]	10^{13} m^{-3}	10^{20} m^{-3}	Line integrated	

To guide the wave from Port 1 to the transmitting antenna a high precision coaxial cable is used (Rohde and Schwarz ZV-Z97), which is connected to a mode coupler (Cernex CWK22335004F). This coupler converts the radial symmetric transversal field distribution to the basic H_{10} mode of a WR 22 rectangular hollow waveguide. For attaching the corrugated horn antenna (Cernex CCA22424820-XX), which emits the electromagnetic wave to free space, a rectangle to circular transition (Cernex CRC220188) is used. The antenna has a centre frequency of 45.75 GHz and a bandwidth of 8.5 GHz. A horn antenna of the same type receives the wave, which is guided to a circular to rectangle transition and a rectangular waveguide track.

At the end of the track a mode coupler is placed to connect a high precision coaxial cable, which is attached to Port 2 of the VNA. The VNA measures the complex frequency-dependent scattering parameter $\underline{S}_{21}$ by a heterodyne technique, which includes the phase information of the interferometer. To calibrate the directional elements of the VNA a TOSM calibration is performed at the end of both precision coaxial cables; for detailed information see [16].

2.2. Distance change detection

To verify the correct operation of the interferometer a setup for measuring a distance difference is built up, see figure 1(*a*). The divergent beam transmitted by the antenna at Port 1 is received by the antenna at Port 2, in a distance of approximately 0.7 m. After recording a reference measurement the distance between the antennas is stepwise increased by 10 mm and the according phase is detected. Using a reference measurement provides the additional advantage, that the dispersion of the used hollow waveguides is compensated. The fact that the measured phase is distributed in modulo 2π, leads to fringes, which causes the loss of the absolute phase data. The electric field $\underline{\vec{E}}(z,t)$ of an electromagnetic wave propagating along the z-direction in free space can be described by equation (1), where k_0 is the wave number

$$\underline{\vec{E}}(z,t) = \underline{\vec{E}}(t) \cdot \mathrm{e}^{-\mathrm{i}k_0 z}. \qquad (1)$$

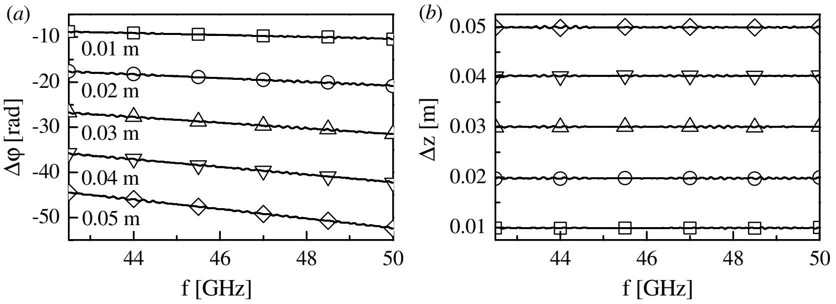

Figure 2. Distance change measurements. (*a*) Results of the measured absolute phase changes. (*b*) Results of the calculated distance changes.

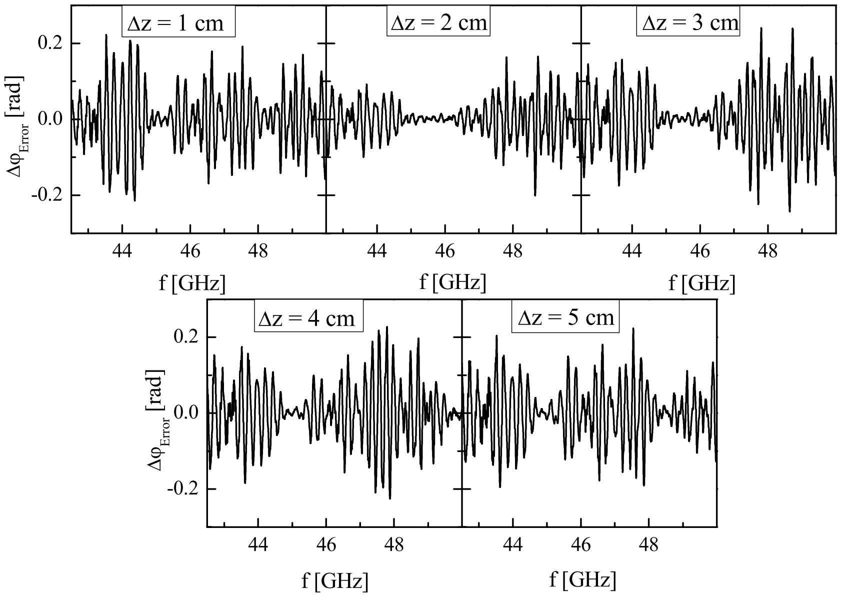

Figure 3. Relative frequency-dependent phase error for different distance changes.

By using a reference measurement the phase change $\Delta\varphi$, caused by the increasing of the propagation length Δz, can be written as:

$$\Delta\phi = -\frac{2\pi}{c_0}\Delta z \cdot f \tag{2}$$

where f is the frequency of the electromagnetic wave and c_0 the speed of light in vacuum.

By measuring in the frequency range of 42.5–50 GHz, the phase change decreases linearly. Out of this the fringes can be compensated by subtracting 2π, at the discontinuities in the phase plot. These unwrapped data were fitted by a linear function, which was extrapolated to $f = 0$ Hz. At this frequency the phase change has to be zero, which is fulfilled by an added constant. The results of this absolute phase are plotted in figure 2(*a*). By transposing equation (2), Δz can be easily calculated, as diagrammed in figure 2(*b*). The measured distance changes are in very good agreement with the adjusted distances. However some fluctuations are recognizable.

By subtracting the expected phase change out of equation (2), the relative phase error $\Delta\phi_{\mathrm{Error}}$ is calculated and plotted in figure 3. Due to the fact that the frequency dependency of the error changes with the adjusted distance, a further reduction of this phase error by referencing is not possible. This leads to an uncertainty of 250 mrad in the phase measurement. It is reasoned that the fluctuations are caused by the influence of changes near the corrugated horn antennas. This means that small changes in the surroundings of the antenna, which for example occur by adjusting them, leads to a small change in the transmitting properties.

To increase the phase resolution of the interferometer the fluctuations are separated from the rest of the phase signal. Due to the fact that the Fourier transformation of the relatively phase error is insignificant in range below 4.5×10^{-3}, in which the transformation of the interferometry measurements is dominant (figure 4(*a*)), a digital filter with finite impulse response is used for separation. This filter is a linear phase low pass filter with 2048 taps and a normalized cut off frequency of 3.3997×10^{-3}, where 1 corresponds to the Nyquist frequency. It is based on the ideal filter which is modified by a Hamming window; for more details see [17].

This digital signal processing (DSP) reduces the fluctuations to almost 1%. The effect of the DSP to the relative phase error, plotted in figure 4(*b*), is a reduction in the uncertainty from 250 to 2.5 mrad. This method is applied to all results of the other experiments to reduce the uncertainty of the phase measurement.

To compare this uncertainty of the presented system with other setups of single frequency interferometers, their phase resolution is listed in table 2. This phase resolution is mainly

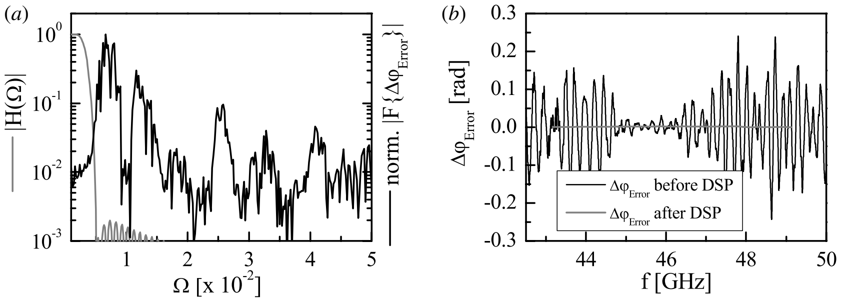

Figure 4. Implementation and results of digital signal processing. (*a*) Absolute value of the transfer function of the used FIR filter and normalized Fourier transformation of the relative phase error. Ω is the normalized frequency, where 1 corresponds to the Nyquist frequency. (*b*) Relative phase error before and after digital signal processing.

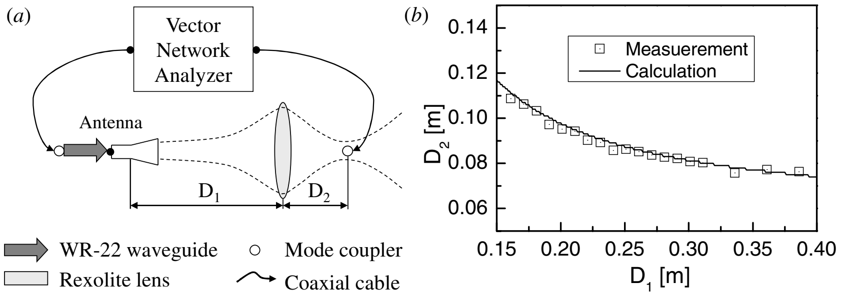

Figure 5. Mapping verification of the lenses. (*a*) Experimental setup for determining distance of the focal point for different mappings. (*b*) Experimental results of the verification in comparison to the ABCD matrix analysis.

Table 2. Detection limits of other microwave interferometers. Besides the carrier frequency, the corresponding cut off electron density and the specified phase resolution is listed, for different setups.

Name	Reference	f (GHz)	$\Delta\phi$ -Min. (mrad)	n_c
Neumann G *et al*	[18]	35	5.2	1.5×10^{19} m^{-3}
Ehlbeck J *et al*	[19]	150	5.2	2.8×10^{20} m^{-3}
Dittmann K *et al*	[20]	160	10	3.2×10^{20} m^{-3}
Lukas C *et al*	[21]	309	0.5	1.2×10^{21} m^{-3}

influenced by noise. Therefore, it depends directly on the used bandwidth and on the achievable time resolution. Due the single frequency setup, information about the relative phase error is not available. In summary, the relative phase error of this setup is in order of the phase resolutions of the compared systems. Furthermore, the cut off densities n_c are given, which is the theoretical upper detection limit of electron density.

2.3. Lenses and microwave mapping

To investigate the line integrated electron density in the positive column of a commercially available fluorescent lamp in the format T12[1], the divergent beam of the transmitting antenna is refocused by a homemade dielectric lens in a distance D_1 of 0.261 m. The lens has a radius of curvature of 80 mm, is 60 mm thick, made of Rexolite® and has a diameter of 125 mm. To reduce the reflections of the electromagnetic beam at the transition from free space to the dielectric material, a grooved layer [22] as quarter wave impedance transformer is applied to the surface of the lens. The T12 lamp is placed at a distance from the lens to the focal point D_2 of 0.085 m. The waist size of the beam in the focal point is 7.4 mm. Afterwards the Gaussian beam is refocused by a lens of the same kind and a mirror in symmetric distance to the receiving antenna. This setup is shown in figure 1(*b*). The lamp is driven with continuous current of 150, 200 and 300 mA.

By replacing the fluorescent lamp by two silica windows and increasing the waist size of the focal point to 9.7 mm by decreasing the distance D_1 to 0.19 m the effect of the dielectric surrounding to the phase measurement is investigated, pictured in figure 1(*c*). The windows with an edge length of 100 mm and a dielectric constant of 3.86 have a thickness of 9.9 and 10.1 mm. They are placed coplanar to each other and orthogonal to the direction of propagation. Both windows are placed at the same distance to the focal point and an overall gap is varied from 29.2 to 54.6 mm.

The correct function of the lenses is verified by testing different mappings. Therefore the distance between the lens and the focal point D_2 is detected for various distances D_1 between the antenna and the lens. The setup is shown in figure 5(*a*). The focal point is determined by the maximum value of the received signal. For comparison the mapping is calculated by using ABCD matrix method [22]. Both results are plotted for one lens in figure 5(*b*) and are in good agreement. The result of the other lens differs only insignificantly. By this fact the proper function of the lenses and the mapping is verified.

---

[1] Outer diameter is 38 mm.

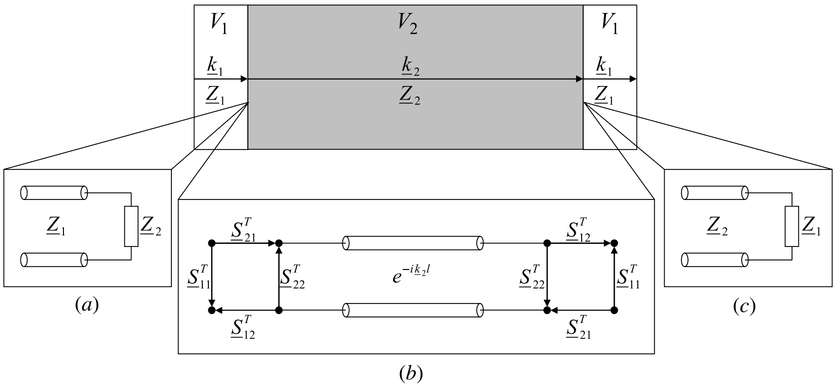

(*a*) (*b*) (*c*)

Figure 6. Dielectric barriers and their equivalent networks.

3. Equivalent circuit

To describe the influence of a dielectric surrounding, for example the glass tube, which encloses the plasma in a fluorescent lamp, to the microwave beam, an equivalent network is used. This surrounding consists of two dielectric barriers, each with two transitions between the different materials. A transversal electromagnetic wave, which propagates along the z-direction in a dielectric volume V_1 with the complex relative permittivity $\underline{\varepsilon}_r^1$ is partly reflected at this transition to the volume V_2 with the complex relative permittivity $\underline{\varepsilon}_r^2$. The value of the reflection can be calculated by using the reflection coefficient $\underline{r}$ and wave impedances of the volumes. This wave impedance is given for a transversal electromagnetic wave, for example in volume V_1, by following equation:

$$\underline{Z}_1 = \sqrt{\frac{\mu_0 \underline{\mu}_r^1}{\varepsilon_0 \underline{\varepsilon}_r^1}} \tag{3}$$

where ε_0 is the permittivity and μ_0 the permeability of free space, $\underline{\varepsilon}_r^1$ is the relative permeability and equal to 1 in this case. To describe the first transition, the equivalent network in figure 6(*a*) is used, where the wave impedance $\underline{Z}_2$ of volume V_2 is an unmatched load for the wave propagating in volume V_1. To determine the value of transmission of the wave out of volume V_1 into V_2, the simple relation of the transmission coefficient $\underline{t} = r_m + 1$ can be used. The second transition at the end of volume V_2 to a volume with the same wave impedance as volume V_1 can be described in the same way, using the equivalent network given in figure 6(*b*). The reflection coefficient $\underline{r}_{\text{in}}$ is given by equation (4):

$$\underline{r}_{\text{in}} = \frac{\underline{Z}_2 - \underline{Z}_1}{\underline{Z}_2 + \underline{Z}_1}. \tag{4}$$

This description does not take into account the interaction of the multiple reflected waves in volume V_2, caused by the reflected wave towards the first transition, which is there partly reflected again to the second transition and so on.

To include this effect the transitions are described by two port networks and the length of volume V_2 l is included by a waveguide, diagrammed in figure 6(*c*). The scattering parameter $\underline{S}_{11}^T$ describes the reflection in the same way as $\underline{r}_{\text{in}}$ at the first transition and $\underline{S}_{22}^T$ in the same way as $\underline{r}_{\text{out}}$ at the second transition. For this reason both scattering parameters are known by calculating the reflection coefficient. Due to the fact that the scattering parameters are based on normalized incident and reflected waves, the change of the wave impedance system has to be considered by calculating $\underline{S}_{21}^T$ and $\underline{S}_{12}^T$. This leads to following equations:

$$\begin{aligned} \underline{S}_{21}^T &= (\underline{r}_{\text{in}} + 1)\sqrt{\frac{\underline{Z}_1}{\underline{Z}_2}} \\ \underline{S}_{12}^T &= (\underline{r}_{\text{out}} + 1)\sqrt{\frac{\underline{Z}_2}{\underline{Z}_1}}. \end{aligned} \tag{5}$$

The wave number $\underline{k}_2$ in volume V_2 can be calculated by its permittivity constant $\underline{\varepsilon}_r^2$ using equation (6):

$$\underline{k}_2 = \frac{2\pi \cdot f}{c_0\sqrt{\underline{\varepsilon}_r^2}}. \tag{6}$$

The equivalent network in figure 6(*c*) can be combined to one two-port network, by solving the belonging linear equation system. The resulting scattering parameters of the dielectric barrier $\underline{S}_{21}^B$ and $\underline{S}_{11}^B$ can be calculated by the equations (7) and (8):

$$\underline{S}_{21}^B = \frac{\underline{S}_{21}^T \cdot \underline{S}_{12}^T \cdot e^{-i\underline{k}_2 l}}{1 - \underline{S}_{22}^T \cdot \underline{S}_{22}^T \cdot e^{-i2\underline{k}_2 l}} \tag{7}$$

$$\underline{S}_{11}^B = \underline{S}_{11}^T + \frac{\underline{S}_{22}^T\,\underline{S}_{21}^T \cdot \underline{S}_{12}^T \cdot e^{-i2\underline{k}_2 l}}{1 - \underline{S}_{22}^T \cdot \underline{S}_{22}^T \cdot e^{-i2\underline{k}_2 l}}. \tag{8}$$

Due to the symmetry of the network $\underline{S}_{11}^B$ is equal to $\underline{S}_{21}^B$ and $\underline{S}_{22}^B$ is equal to $\underline{S}_{11}^B$.

Based on the fact that the dielectric barrier fully surrounds the plasma in a fluorescent lamp, the microwave beam has to travel twice through the barrier. This behaviour can also be described with the equivalent network in figure 6(*c*). The resulting scattering parameters of the lamp $\underline{S}_{21}^L$ and $\underline{S}_{11}^L$ can be numerically calculated by equations (7) and (8), when $\underline{S}_{ij}^T$ is replaced by the results of $\underline{S}_{ij}^B$ and $\underline{k}_2$ by the wave number of the plasma $\underline{k}_p$.

The material properties of the used dielectric barriers are shown in table 3. For this experiment it is sufficient to describe the relative permittivity by real numbers.

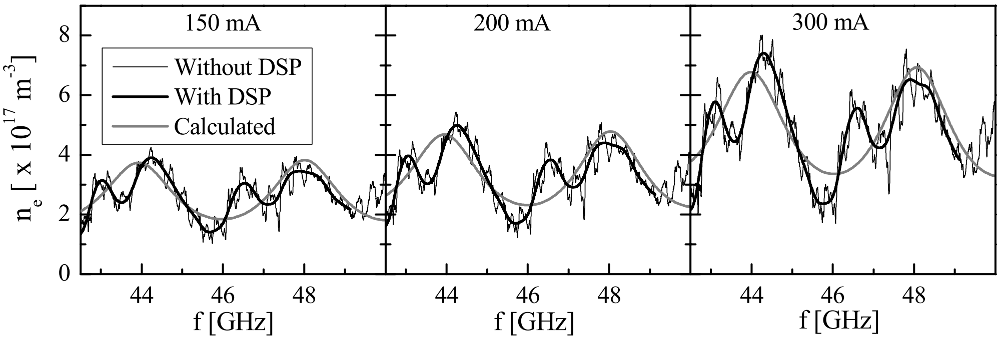

Figure 7. Results of the line-integrated frequency-dependent electron density measurements in the positive column of a fluorescent lamp in comparison to the results of the calculation.

Table 3. Material properties of the used dielectric barriers.

Object	Thickness of barrier (mm)	$\underline{\varepsilon}_r$	Distance between barriers
Glass tube	0.8	2.6	35.4 mm
Window 1	10.1	3.85	Variable
Window 2	9.9	3.85	Variable

4. Results and discussion

To investigate the electron density in a fluorescent lamp the phase change is determined. By assuming the spatial distribution of the electron density along the beam propagation through the plasma $f(z)$ as a zero order Bessel function of the first kind:

$$f(z) = J_0\left(2.405\left|\frac{z}{z_p}\right|\right) \tag{9}$$

with $z_P = 17.7$ mm the absolute number of the electron density can be calculated by the following equation, which is given by [23]:

$$n_e = \frac{n_c \lambda \Delta\phi}{\pi \int_{z1}^{z2} f(z)\,\mathrm{d}z}$$
$$n_c = \left(\frac{2\pi c_0}{\lambda}\right)^2 \left(\frac{\varepsilon_0 m_e}{e^2}\right) \tag{10}$$

where m_e is the mass and e the charge of an electron. λ is the wavelength of the interferometer and ε_0 is the vacuum permittivity. The phase change $\Delta\phi$ is determined by the interferometer, referenced by a measurement without plasma.

The fluctuations, which are recognized by the distance measurements, occur in the measurement of the electron density too. Therefore, the same digital filter is used to reduce the measurement error. It is obvious that the electron density increases with the lamp current, diagrammed in figure 7. Furthermore the measured electron density is not frequency independent as expected. A deviation up to 53% in comparison to the frequency-averaged electron density is detected.

To describe this frequency dependence of the measured electron density, the influence of the surrounding glass tube is taken into account by calculating the transfer function of the lamp. The influence of the dispersion of the plasma and the spatial distribution is considered by replacing the product of the wave number of the plasma and the inner diameter of the tube $\underline{k}_p l$ by the phase change $\Delta\varphi$ out of equation (10). The electron density for the calculation is determined by frequency averaging of the measurements. This one-dimensional model ignores the influence of the curvature of the glass tube and the Gaussian beam propagation. Due to these a frequency offset of 1 GHz has to be added for a better agreement between calculation and measurement. Concerning the amplitude of the deviation and its frequency dependence, it is obvious that the fluctuation is well described by this one-dimensional model. Therefore, it is concluded that the surrounding glass tube forms a dielectric resonator, which significantly affects the phase measurement.

To make this effect more obvious the transfer function of the lamp without plasma $I = 0$ mA is diagrammed in comparison to the ignited lamp with a current of $I = 300$ mA in figure 8. The phase change is referenced to the electric length of the glass tube, which includes the phase change along the inner region of the lamp and twice along the glass, without any resonant effects.

The transfer function of the lamp without any plasma has periodic structure with a frequency interval between two minima of 4.1 GHz. This behaviour of the transfer function is typical for waveguide resonators. Due to the fact that the beginning and the end of the resonator are not a real short circuit, the characteristic length of the frequency interval is 36.56 mm and not the inner diameter of the lamp. The dispersion character of the ignited plasma changes the characteristic length, which leads to a significant frequency shift ΔF in the transfer function of the lamp. This changes the influence of the dielectric resonator to the phase measurement by $\Delta\varphi_{\text{Resonator}}$. A detailed view to the transfer function at a frequency of approximately 47 GHz shows that the resulting phase change $\Delta\varphi_{\text{resulting}}$ consists of two parts, seen in figure 8. On the one hand the phase shift is caused by the plasma $\Delta\varphi_{\text{Plasma}}$, which is the basic effect of the electron density determination. On the other hand the transfer function of the dielectric resonator is changed and with it the phase arrangement of the resonator, which leads to the phase change $\Delta\varphi_{\text{Resonator}}$. This frequency-dependent phase change $\Delta\phi_{\text{Resonator}}$ causes the deviation in the electron density measurements, diagrammed in figure 7. Based on the calculation it is concluded that this deviation in the phase change measurement increases with the relative permittivity

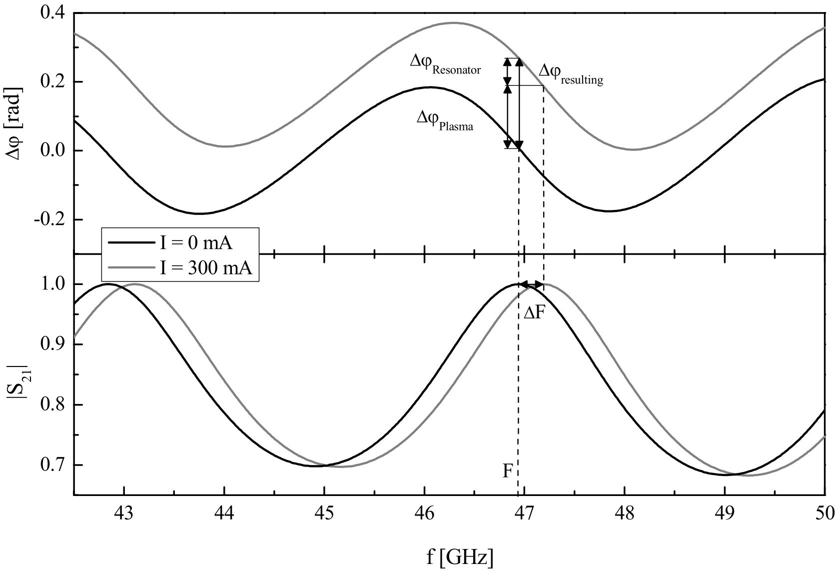

Figure 8. Influence of the surrounding dielectric resonator formed by a glass tube to the phase measurement by an interferometer.

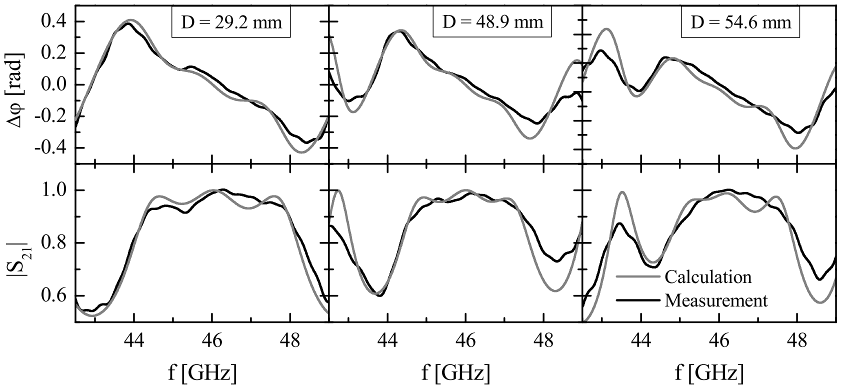

Figure 9. Transfer function of a dielectric resonator, built up by two silica windows with a variable gap.

of the dielectric barriers and with the characteristic length of the resonator.

To verify the influence of the surrounding dielectric material, the experimental setup, shown in figure 1(*c*), is used, where two silica windows are placed parallel to each other with a variable gap and orthogonal to the direction of wave propagation.

In figure 9 the absolute value of the transfer function and the phase change referenced to the electric length of the setup are diagrammed. Due to the fact that the thickness of the windows is approximately ten times larger than the shell of the glass tube and therefore in the scale of the wavelength, the characteristic length is not mainly determined by the size of the gap between the windows. To achieve a good agreement between the measurements and the calculated results, no additional frequency offset was necessary. It is obvious that the effect of the dielectric resonator is well described by the usage of equivalent networks.

The described effect does not only influence phase change measurements, it also causes deviation in measuring changes of the amplitude. For instance laser absorption spectroscopy is based on amplitude measurements, where this effect is known as etalon fringes or Fabry–Perot interference fringes [24, 25]. An often-used method to minimize these fringes is to rotate the windows by an angle Θ. By using the Brewster angle Θ_B, defined by equation (11), and a polarization parallel to the window, the reflection at the transition can be significantly reduced [26]

$$\Theta_B = \arctan\left(\sqrt{\frac{\varepsilon_r^2}{\varepsilon_r^1}}\right). \tag{11}$$

Due to the used material and frequency range the Brewster angle is 63° and therefore an arrangement of the windows is very difficult to implement. Nevertheless, it is also common to reduce the interference fringes by small misalignments. For example, wedged windows [27] or small angle rotated windows [28] are used. Therefore, the effect of small misalignments is investigated by tilting the window towards the emitting antenna by 3.4° and 6.8°. The window towards the receiving antenna is placed at a distance of 29.2 mm orthogonal to the direction of the wave propagation, shown in figure 10(*a*).

The influence of the dielectric resonator to the phase and the amplitude measurement is slightly decreasing with increasing the angle, but the deviations are still present for the investigated angles, diagrammed in figure 10(*b*).

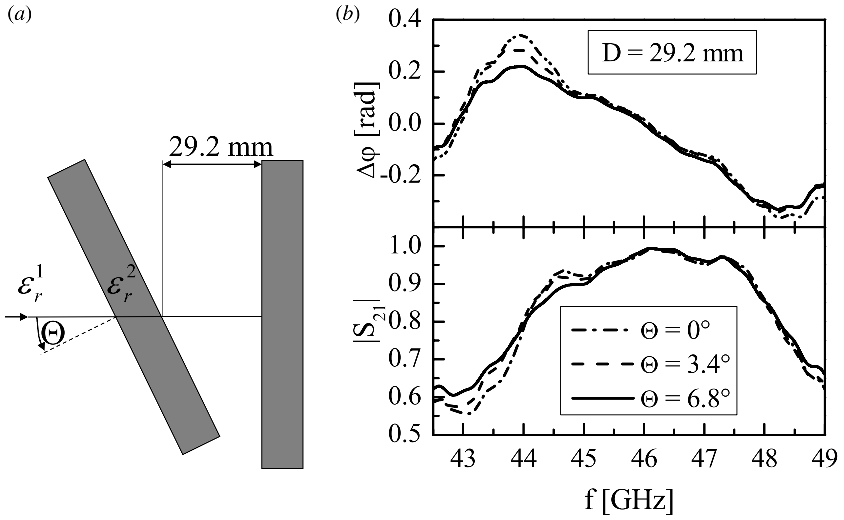

Figure 10. (*a*) Arrangement of the windows. (*b*) Transfer function of a dielectric resonator, built by two silica windows with a variable angle.

5. Conclusion

A frequency resolved microwave interferometer is built up by using a vector network analyser and dielectric lenses. To verify the correct function of the interferometer a distance change measurement without lenses is done. Based on the relative phase change, with fringes the absolute phase change and with it the distance change are determined. The detected distance changes are in very good agreement to the adjusted distances. The fluctuations in the phase measurement are reduced by digital signal processing, which leads to an uncertainty of 2.5 mrad. Furthermore the electron density in the positive column of a fluorescent lamp is determined and a frequency-dependent deviation of about 53% in the electron density detection via microwave interferometry is observed. With equivalent circuits the frequency-dependent transfer function of the glass tube is simulated and in good agreement with the measurements. This effect was also tested by a dielectric resonator built up with two silica windows, whose transfer functions are calculated and measured, too. It is concluded that a dielectric barrier, which surrounds the plasma, built up a dielectric resonator, which causes frequency-dependent deviations in phase and amplitude measurements. By using the presented frequency-resolved microwave interferometer this effect can be quantified and compensated.

In addition the effect of reducing the deviations by rotating the windows is investigated for small angles, which is a common technique in the tuneable diode laser absorption spectroscopy. It is observed that with increasing the angle the deviation is slightly decreased, but still significant.

Acknowledgment

The study is supported by the Bundesministerium für Bildung und Forschung (13N9320).

References

[1] Manos D M, Cecchi J L, Cheah C W and Dylla H F 1991 Diagnostics of low-temperature plasmas—the electron component *Thin Solid Films* **195** 319–36

[2] Chung P M, Talbot L and Touryan K J 1975 *Electric Probes in Stationary and Flowing Plasmas: Theory and Application* (New York: Springer)

[3] Cherrington B E 1982 The use of electrostatic probes for plasma diagnostics—a review *Plasma Chem. Plasma Process.* **2** 113–40

[4] Hannemann M, Koborov N and Rapp M 2003 Probe measurements in a low density large volume afterglow plasma *ICPIG'03: Proc. Int. Conf. on Phenomena in Ionized Gases* pp 131–4

[5] Stenzel R L 1976 Microwave resonator probe for localized density-measurements in weakly magnetized plasmas *Rev. Sci. Instrum.* **47** 603–7

[6] Piejak R B, Godyak V A, Garner R, Alexandrovich B M and Sternberg N 2004 The hairpin resonator: a plasma density measuring technique revisited *J. Appl. Phys.* **95** 3785–91

[7] Lapke M *et al* 2011 The multipole resonance probe: characterization of a prototype *Plasma Sources Sci. Technol.* **20** 042001

[8] Styrnoll T *et al* 2013 Process diagnostics and monitoring using the multipole resonance probe in an inhomogeneous plasma for ion-assisted deposition of optical coatings *Plasma Sources Sci. Technol.* **22** 045008

[9] van Gessel A F H, Carbone E A D, Bruggeman P J and van der Mullen J J A M 2012 Laser scattering on an atmospheric pressure plasma jet: disentangling Rayleigh, Raman and Thomson scattering *Plasma Sources Sci. Technol.* **21** 015003

[10] Hubner S, Palomares J M, Carbone E A D and van der Mullen J 2012 A power pulsed low-pressure argon microwave plasma investigated by Thomson scattering: evidence for molecular assisted recombination *J. Phys. D: Appl. Phys.* **45** 055203

[11] Yubero C, Garcia M C and Calzada M D 2006 On the use of the H alpha spectral line to determine the electron density in a microwave (2.45 GHz) plasma torch at atmospheric pressure *Spectrochim. Acta* B **61** 540–4

[12] Torres J, Palomares J M, Sola A, van Dermullen J J A M and Gamero A 2007 A Stark broadening method to

determine simultaneously the electron temperature and density in high-pressure microwave plasmas *J. Phys. D: Appl. Phys.* **40** 5929–36

[13] Leins M *et al* 2014 Microwave plasmas at atmospheric pressure *Contrib. Plasma Phys.* **54** 14–26

[14] Heald M A and Wharton C B 1965 *Plasma Diagnostics with Microwaves* (New York: Wiley)

[15] Stix T H 1992 *Waves in Plasmas* (New York: American Institute of Physics)

[16] Hiebel M 2005 *Grundlagen Der Vektoriellen Netzwerkanalyse* (Munich: Rohde and Schwarz)

[17] Kaiser J F, Hill M and Steiglitz K 1983 Design of FIR filter with flatness constraints *ICASSP'83: IEEE Int. Conf. on Acoustics, Speech, and Signal Processing* pp 197–200

[18] Neumann G, Banziger U, Kammeyer M and Lange M 1993 Plasma-density measurements by microwave interferometry and Langmuir probes in an Rf discharge *Rev. Sci. Instrum.* **64** 19–25

[19] Ehlbeck J, Rackow K, Andrasch M and Weltmann K D 2011 Electron density determination by means of tuneable 50 GHz and 150 GHz interferometers *Contrib. Plasma Phys.* **51** 131–6

[20] Dittmann K, Küllig C and Meichsner J 2012 160 GHz Gaussian beam microwave interferometry in low-density Rf plasmas *Plasma Sources Sci. Technol.* **21** 024001

[21] Lukas C, Muller M, Schulz-von der Gathen V and Dobele H F 1999 Spatially resolved electron density distribution in an Rf excited parallel plate plasma reactor by 1 mm microwave interferometry *Plasma Sources Sci. Technol.* **8** 94–99

[22] Goldsmith P F 1998 *Gaussian Beam Quasioptical Propagation and Applications* (New York: IEEE Press)

[23] Hartfuss H J, Geist T and Hirsch M 1997 Heterodyne methods in millimetre wave plasma diagnostics with applications to ECE, interferometry and reflectometry *Plasma Phys. Control. Fusion* **39** 1693–769

[24] Mansfield C D and Rutt H N 1999 Evaluation of multiple beam interference effects in infrared gas spectroscopy *Meas. Sci. Technol.* **10** 206–10

[25] Masiyano D, Hodgkinson J and Tatam R P 2008 Use of diffuse reflections in tunable diode laser absorption spectroscopy: implications of laser speckle for gas absorption measurements *Appl. Phys.* B **90** 279–88

[26] Weidmann D *et al* 2004 Mid-infrared trace-gas sensing with a quasi- continuous-wave Peltier-cooled distributed feedback quantum cascade laser *Appl. Phys.* B **79** 907–13

[27] Hodgkinson J, Masiyano D and Tatam R P 2010 Gas cells for tunable diode laser absorption spectroscopy employing optical diffusers: part I. Single and dual pass cells *Appl. Phys.* B **100** 291–302

[28] Wysocki G, Curl R F, Tittel F K, Maulini R, Bulliard J M and Faist J 2005 Widely tunable mode-hop free external cavity quantum cascade laser for high resolution spectroscopic applications *Appl. Phys.* B **81** 769–77

5.7 A heterodyne reflectometer for detecting the time dependent complex reflection coefficient optimised for the usage with oven magnetron

A heterodyne reflectometer for detecting the time dependent complex reflection coefficient optimised for the usage with oven magnetron

M Andrasch, J Ehlbeck and K-D Weltmann
INP Greifswald, Felix-Hausdorff-Straße 2, 17489 Greifswald, Germany
Andrasch@inp-greifswald.de

Abstract

A heterodyne microwave reflectometer is presented for detecting the time dependent complex reflection coefficient. Both hardware setup and detection algorithm, regarding the special requirements of using oven magnetrons, are presented. The correct function of the described measurement system is verified for frequencies in the range of 2.45 GHz. Test measurements of the reflection coefficient concerning the linearity, time resolution, accuracy in phase and amplitude detection are performed. The dynamic range is approximately two orders of magnitude and the limit in the phase detection is below 0.7 °. The accuracy in the detection of the absolute values of the reflection coefficient is better than 0.05 and a time resolution of 500 ns is achieved.

1. Introduction

Due to the development of the magnetron and its cost efficient way of generating microwave radiation, many high power microwave applications have been established. Besides the heating of different materials [1], microwave induced plasma sources, an assortment is presented in [2], working at high powers, are based on these vacuum tubes. Both types of applications have to match the impedance of the load to the source to transfer the maximum of energy. In the case of a time invariant impedance of the load this matching can be done for instance by varying the settings of E-H tuner or stub tuner until the reflected power reaches its minimum. Therefore, forwarded and reflected wave have to be detected at least by its absolute values, to run the process in an optimal way [3, 4, 5, 6]. This also comes along with the possibility of controlling the quality of plasma and heating process. However, if additionally the complex reflection coefficient of the load is required, it is necessary to detected forwarded and reflected wave phase resolved, which can for example be done by replacing the magnetron with a vector network analyser [7, 8] for measuring at powers in the mW-range. If the impedance of the load has to be determined at the working power in the kW-range, the usage of such precise devices is not possible, but the underlying technique [9] can be modified to build a heterodyne reflectometer. This method is in comparison to a scalar detection based on rectification with diodes very complex [10], but can provide all complex information with an adequate time resolution [11]. In the case of slow changes of the reflection coefficient, it is possible to use several methods to reconstruct the complex reflection coefficient out of a scalar detection. In [12] the determination of the reflection coefficient is based on a scalar detection combined with a defined phase variation of the load with a phase shifter. Also the usage of a scalar detected combined with several transmission-line transformers as described in [13] is possible, but unfortunately it is difficult to apply it to high power application due to the switching between the transmission-lines. For some loads, which have the characteristic of a two port terminated with length adjustable short, the complex reflection coefficient can be determined by varying the distance of the short, for example by using a shorting plunger[14]. Furthermore, the complex reflection coefficient can be determined by using the six-port measurement technique, which consists of four scalar detection devices [15, 16, 17, 18].

However, the detection of the complex reflection coefficient provides two main benefits. On the one hand the matching of the load can be done directly, which reduces the required time. In comparison the usage of a scalar detection system needs an iterative process and takes therefore longer. On the other hand, the complex reflection coefficient offers an additional parameter for process controlling.

2. Design

To determine the time dependent complex reflection coefficient of the load, the forwarded wave from the magnetron $\underline{a}$ and the reflected wave from the load $\underline{b}$ are separated by a directional coupler with a coupling coefficient of -60 dB. This also matches the maximum amplitude of the signals from 3 kW in the power line, built of WR 340 hollow waveguides, to 3 mW in the measuring line with the signals $\underline{a}_C$ and $\underline{b}_C$, shown in Figure 1. As high frequency source a 3 kW magnetron is used, which is isolated from the load by a circulator combined with a water load. The two key components of the reflectometer are on the hand the modulation system, which converts radiofrequency signals between 1 GHz and 3 GHz to intermediate frequency signals in the MHz-range, so they are much easier accessible. On the other hand, the second key component is the detection system, which computes the amplitudes of the forwarded and the reflected wave and the phase between them, out of the intermediate frequency signals. This detection system must able to handle oscillator fluctuations, which come a long with the use of magnetrons.

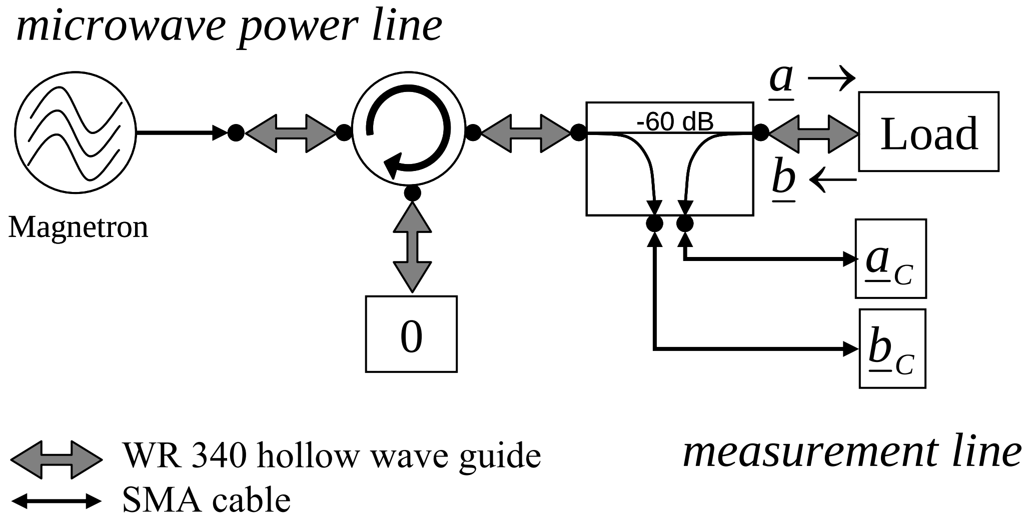

Figure 1. It shows the setup of the microwave power line, starting with the magnetron isolated by a circulator with a water load, followed by a directional coupler. This coupler provides the depending signals for the measurement line.

2.1. Modulation system

The architecture of the modulation system is shown in Figure 2.

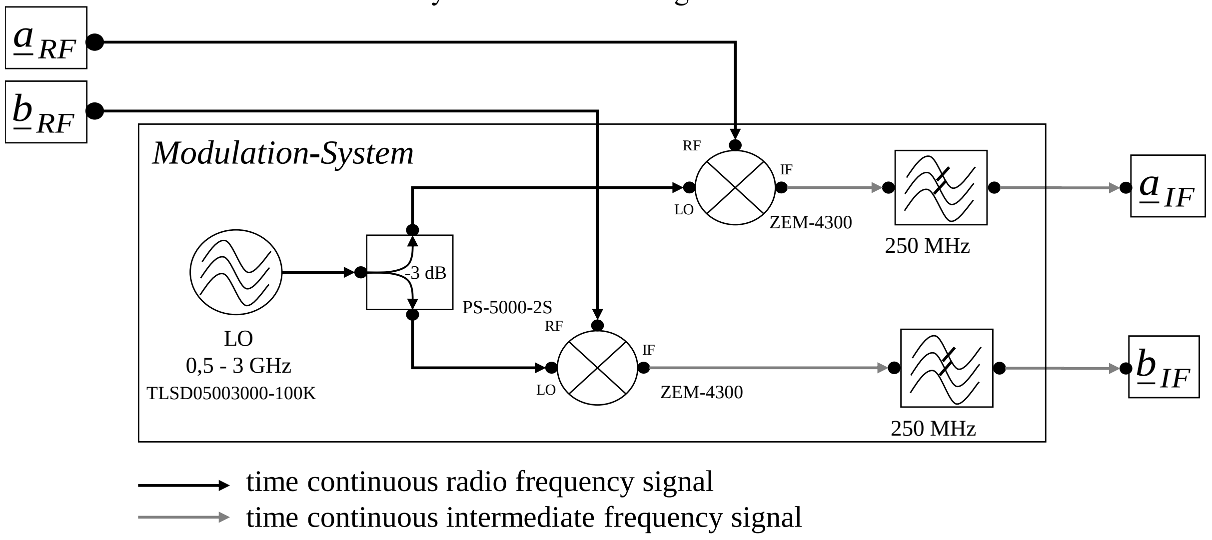

Figure 2. It shows the signal flow graph of the modulation system.

The local oscillator of the frequency conversion system is realised by a frequency synthesiser, which provides a tuneable signal between 500 MHz and 3 GHz with a step size of 100 kHz. This signal, with a minimum output power of 13 dBm, is split by a 2-way power divider (PS-5000-2S) to drive the mixers (ZEM-4300), with at least 9 dBm. The connections between synthesiser, power divider and mixers are done by coaxial test cables with SMA-connectors (SOCUTEST 13.0 GHz). To minimize aliasing effects a low pass filter with a cut off frequency of 250 MHz, at the output of the modulation system, is used. With the used components, this system can convert the radio signals, $\underline{a}_{RF}$ and $\underline{b}_{RF}$, between 1 GHz and 3 GHz to the intermediate signals, $\underline{a}_{IF}$ and $\underline{b}_{IF}$, between DC and 250 MHz. To increase the applicability all parts and the required power supplies are placed inside a 19'' case with two rack units, displayed in Figure 3. The radio and intermediate frequency signals can be accessed via SMA-jacks and the frequency synthesiser is controlled via PC over RS 232 interface.

Figure 3. Picture of the housed modulation system.

2.2. Detection system

A common affordable microwave source @ 2.45 GHz in the kW-range are oven magnetrons, which generates electromagnetic waves with a high efficiency between 50 % and 85 % [19]. However, the quality of these oscillators, concerning frequency stability and phase noise, a typical spectra is shown in [20], leads to problems by the detection of the complex reflection coefficient of the load. Therefore a robust detection method is required, which is able to handle the fast and slow frequency fluctuations of the magnetron.

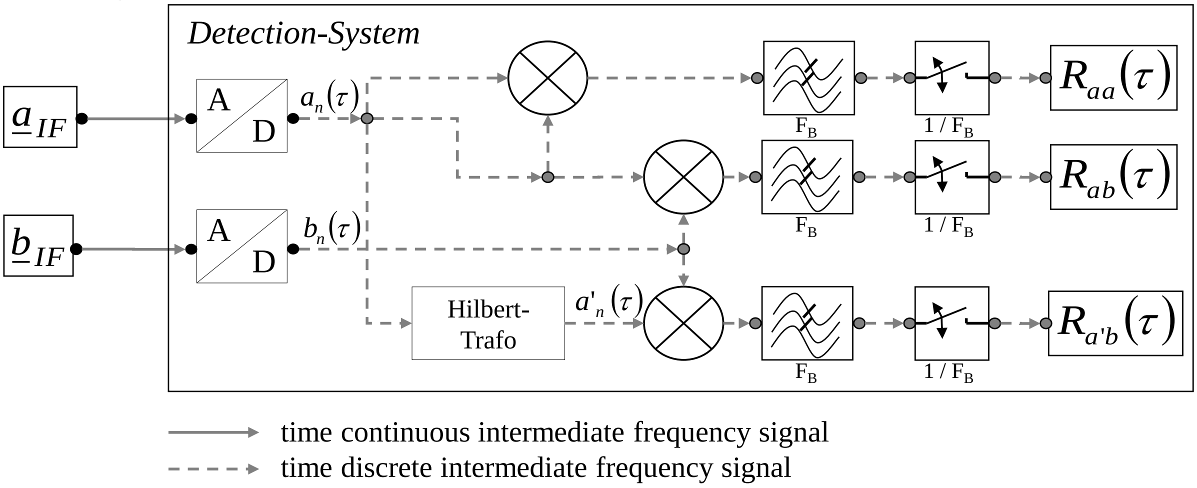

Figure 4. It shows the signal flow graph of the detection system.

Due to the fact, that the development is focussed to the investigation of non-continuous events, the detection system is not restricted to a real time operation. So the starting point of the detection is the sampling and storing of the intermediate frequency signals, $\underline{a}_{IF}$ and $\underline{b}_{IF}$, by a scope card (Gage Cobra

GS22G8), the signal flow graph is diagrammed in Figure 4. Afterwards the stored signals are processed based on the quadrate amplitude demodulation [21], by a computer. Due to the time depends of the frequency $f_{IF}(\tau)$, the amplitudes $A(\tau)$, $B(\tau)$ and the phases $\varphi_a(\tau)$, $\varphi_b(\tau)$ of the intermediate signals, caused by the fluctuation of the magnetron, a time dependent demodulation signal is required. As long as these changes have a lower bandwidth than the frequency of the intermediate signals, the signal based on the forwarded wave $a_n(\tau)$can be used for demodulation. To obtain the additional required orthogonal signal $a_n(\tau)$ a Hilbert Transformation is used, which computes the orthogonal demodulation signal $a'_n(\tau)$. Considering the reflected wave by its intermediate signal $b_n(\tau)$, these three signals can be written as:

$$\begin{aligned} a_n(\tau) &= A(\tau)\cos\left(2\pi\frac{f_{IF}(\tau)}{F_S}n+\varphi_a(\tau)\right) \\ a'_n(\tau) &= -A(\tau)\sin\left(2\pi\frac{f_{IF}(\tau)}{F_S}n+\varphi_a(\tau)\right) \\ b_n(\tau) &= B(\tau)\cos\left(2\pi\frac{f_{IF}(\tau)}{F_S}n+\varphi_b(\tau)\right) \end{aligned} \qquad 1$$

Providing that, the low pass bandwidth (F_B) matches the fluctuations of the magnetron and the sampling frequency F_S is at least greater than the sum of bandwidth of low pass filter and two times the frequency of the intermediate signals ($F_S > F_B + 2f_{IF}$), the other multiplication product is suppressed. So after multiplication, filtering and down sampling by F_S/F_B, the following results are obtained:

$$\begin{aligned} R_{aa}(\tau) &= \frac{1}{2}A^2(\tau) \\ R_{ab}(\tau) &= \frac{1}{2}A(\tau)B(\tau)\cos(\varphi_b(\tau)-\varphi_a(\tau)) \\ R_{a'b}(\tau) &= \frac{1}{2}A(\tau)B(\tau)\sin(\varphi_b(\tau)-\varphi_a(\tau)) \end{aligned} \qquad 2$$

By introducing φ as difference between reflected and forwarded signal ($\varphi = \varphi_b - \varphi_a$), all required information for calculating the time dependent complex reflection coefficient ($\underline{r} = \underline{b}/\underline{a}$) as well as forwarded and reflected power can be determined by using:

$$\begin{aligned} A(\tau) &= \sqrt{2R_{aa}(\tau)} \\ B(\tau) &= \sqrt{2\frac{R_{a'b}^2(\tau)+R_{ab}^2(\tau)}{R_{aa}(\tau)}} \\ \tan(\varphi(\tau)) &= \frac{R_{a'b}(\tau)}{R_{ab}(\tau)} \end{aligned} \qquad 3$$

Additional, the intermediate frequency is detected by splitting the stored data $a_n(\tau)$ into frames with the length of $1/F_B$ and performing a fast Fourier Transformation. To obtain the centre frequency the Buneman frequency estimator [22] is used, which is provided by the software LabVIEW form National Instruments.

3. Experimental setup

To verify the correct operation of the whole measuring system, several experiments are performed. Besides obvious test measurement concerning the detection of the complex reflection coefficient, a power calibration is performed, which includes measurements regarding the linearity of the system. To reduce systematic errors the accurate scattering matrix of the directional coupler is determined by using a vector network analyser. In addition, the time resolution is tested by measurements on a fast high ripple switching mode power supply. All used settings concerning the modulation and detection system are summarised in Table 1, where $\bar{f}_{IF}$ refers to the mean frequency of the intermediate frequency signals and T_{avg} to the time in which the time depend signals are averaged to determine the static results.

3.1 Power calibration and linearity

For an absolute estimation of forwarded and reflected power, a calibration is done for several working points, to ensure the absence of any saturation effects. As reference source for the power calibration a vector network analyser (Rohde & Schwarz ZVRE) is used. At the interesting frequency around 2.45 GHz, the uncertainty of the output power is specified below 0.5 dB, which corresponds to a relative error lower than 12 %. One after another both inputs, $\underline{a}_{RF}$ and $\underline{b}_{RF}$, were connected to the vector network analyser and the power was varied in a logarithmical scale between 15 µW and 1 mW.

3.2 Test load setup

To verify the function and determine the accuracy of the measuring system, the microwave power line, which is driven by a low ripple power supply and provides 2 ms power pulses, is equipped with two different variable test loads, shown in Figure 5. Therefore, the outputs of the measure line $\underline{a}_C$ and $\underline{b}_C$ are connected to the inputs of the modulation system $\underline{a}_{RF}$ and $\underline{b}_{RF}$. Due to the low ripple of the power supply, the frequency changes of the magnetron are less than 50 MHz. Therefore, different setting (Table 1), which leads to a lower sample rate, could be used. However, for testing different phases a shorting plunger, indicated in fig. 5 as load (a) is used which length can be precise adjusted by a screw thread with a pitch of 1.5 mm. Starting with the lowest length as reference measurement, the phase change $\Delta\varphi_{dist}$ can be calculated in dependence of the length change ΔL by using:

$$\begin{aligned} \Delta\varphi_{dist} &= -2\frac{360°}{c_0}g(f)\Delta L \\ g(f) &= \sqrt{f^2 - f_C^2} \end{aligned} \qquad 4$$

Where c_0 is the speed of light in vacuum, f the stimulus frequency of the magnetron and f_C the cut off frequency of the used WR 340 hollow waveguide. By increasing the length change stepwise by 1.5 mm to 87 mm, the resulting phase change reaches 360°. By this the phase measurement is tested in the whole region.

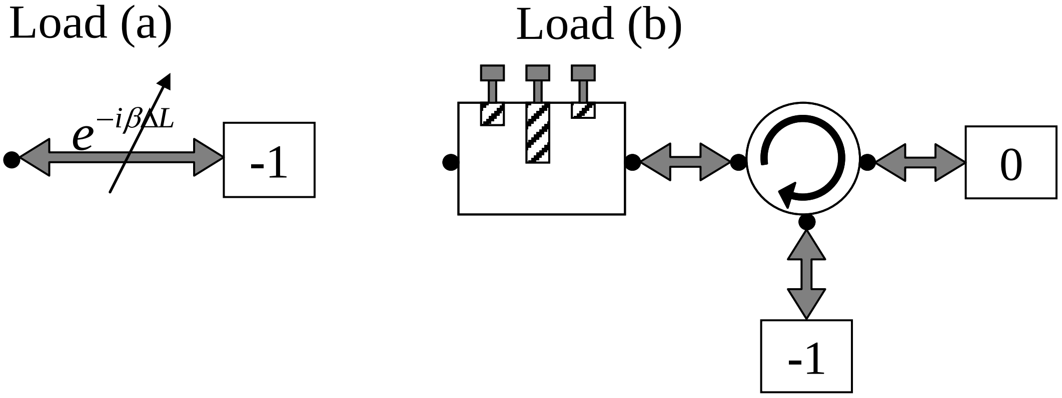

Figure 5. It shows the two different test loads. Load (a) is a shorting plunger for testing the phase accuracy. Load (b) is stub tuner, with a circulator and water load for a low reflection termination, to measure the amplitude accuracy.

For testing the detection of different absolute values of the reflection coefficient $|\underline{r}|$, the test load (b) is used. It consists of a stub tuner followed by a circulator, which is terminated with a water load for minimum reflection. Due to minimise electromagnetic radiation leakage, the other port is terminated with a short, built out an aluminium plate. With this setup, different amplitudes of the reflected wave can be obtained by changing the depth of one stub, which can be precisely adjusted by setting the screw thread. To calibrate the position of the stub to the absolute value of the reflection coefficient, the stub tuner is connected to a vector network analyser.

3.3 Time resolution

The set of test measurements are completed by several time resolved measurements of the microwave power line, composed of a 2 kW (NL10250-18) magnetron, driven by a fast high ripple switching mode power supply. These results are compared to the results of a current probe (TCP 305), which is connected to the cathode of the magnetron.

	F_{LO} [GHz]	$\bar{f}_{IF}$ [MHz]	F_S [MSamples/s]	F_B [MHz]	T_{avg} [µs]
Power calibration	2.34	100	1000	2	25
Test load measurements	2.44	28	100	2	250
Test time resolution	2.34	80	1000	2	-

Table 1. It shows the settings of the reflectometer for the different experimental setups.

4. Results and Discussion

With the presented results, the limits of the introduced reflectometer are shown, concerning the minimum dynamic range, accuracy in detecting the absolute value and the phase of the reflection coefficient and the time resolution.

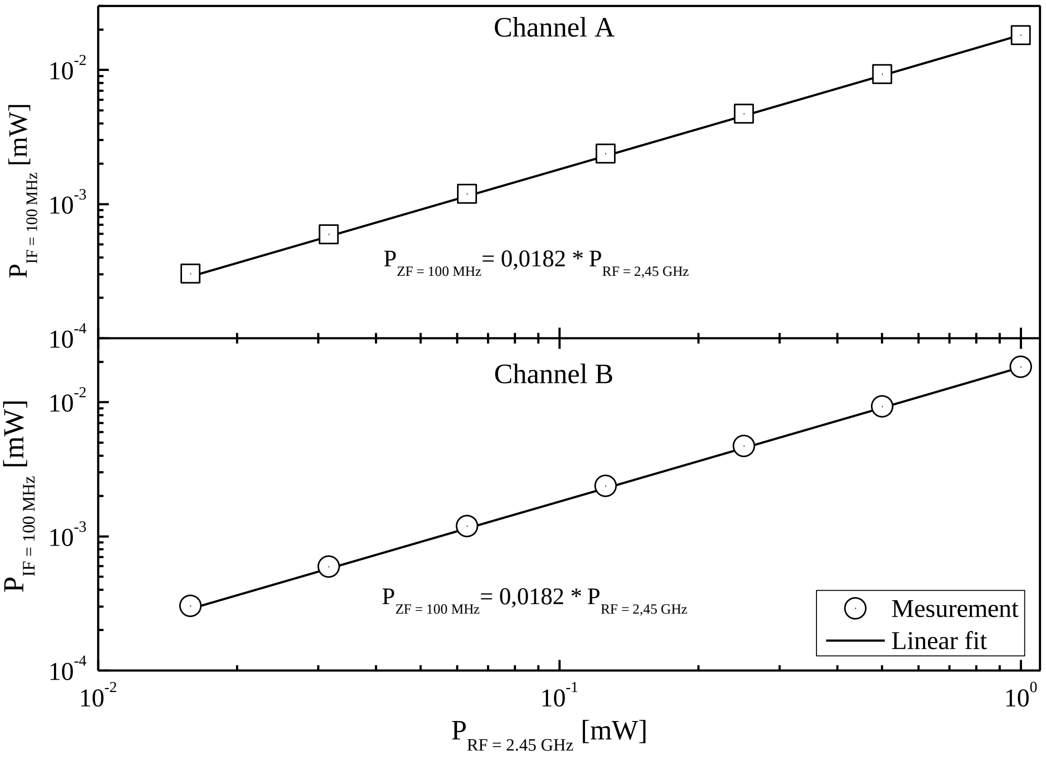

Figure 6. It shows the results of the power calibration of the combined setup.

The results of the power calibration for both channels are shown in Figure 6. First, it is obvious that the whole system works correct, concerning the frequency down conversion and the detection of intermediate frequency signals. In addition, it can be found, that the linearity of the detection is at least in the range of one order of magnitude in an amplitude scale or two orders of magnitude in a power scale, due to the absence of any saturation effects. Therefore a linear rescaling is sufficient for determine the absolute power values based on the detected. A further extension of the dynamic range of the calibration, restricted by the limits of the vector network analyser, is for instance realisable by adding external attenuators. Due to the fact, that with a reflection coefficient of 0.3 (-10 dB) the load already absorbs 90 % of the forwarded power and with 0.1 (-20 dB) even 99 %, a dynamic range of the reflectometer of 20 dB is sufficient for high power applications and a further extension is not reasonable. To match the maximum power of the calibration of 1 mW to the maximum power of 3 mW in the measuring line the signals $\underline{a}_C$ and $\underline{b}_C$ are damped by 6 dB attenuators.

Concerning the results of the test load measurement, a typical time evolution of the detected signals is shown in Figure 7. After starting the pulse, with a typical rise time (90 %) of approximately 100 µs, the microwave power ripple is below 5 % over the whole 2 ms pulse. This low ripple in the steady state leads to very stable frequency of the magnetron, the frequency changes are below 1 MHz. Furthermore, strong fluctuations in the frequency during the turn on and off phase are recognisable.

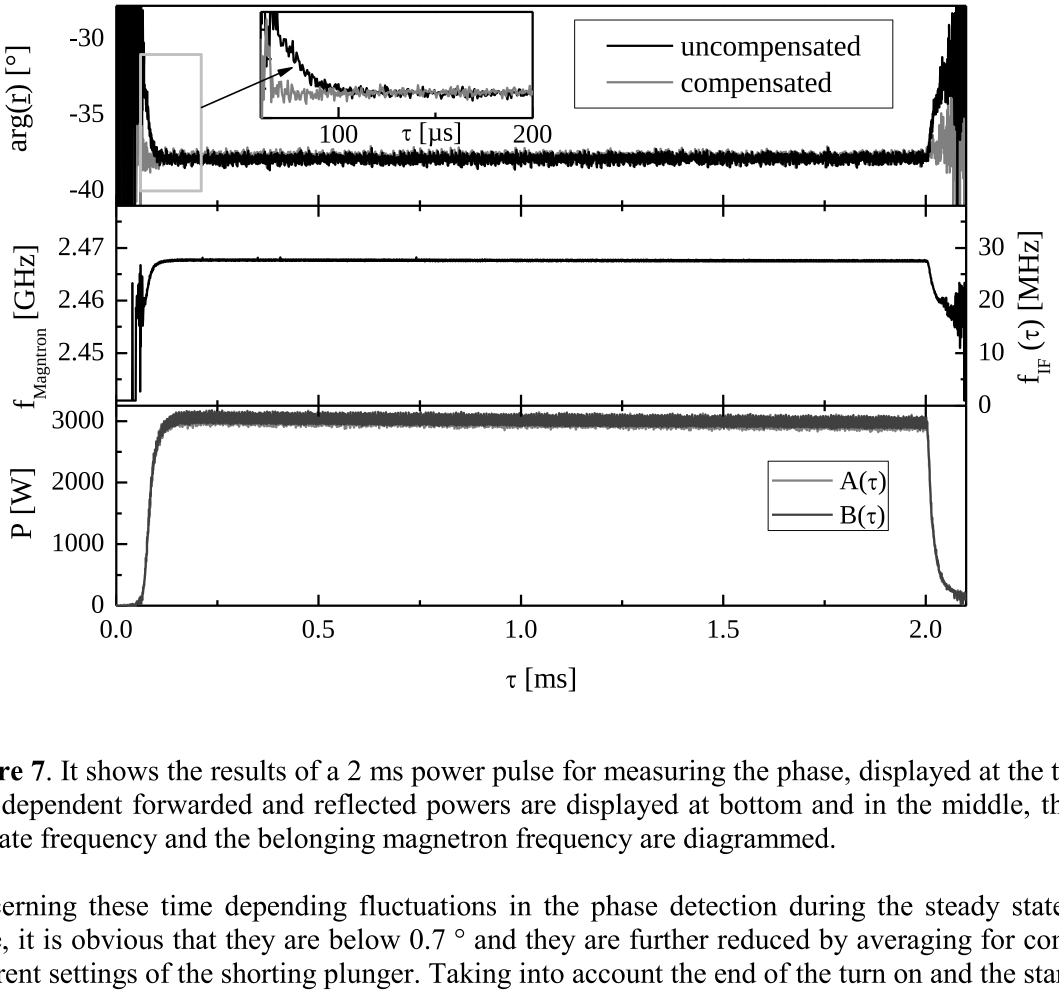

Figure 7. It shows the results of a 2 ms power pulse for measuring the phase, displayed at the top. The time dependent forwarded and reflected powers are displayed at bottom and in the middle, the intermediate frequency and the belonging magnetron frequency are diagrammed.

Concerning these time depending fluctuations in the phase detection during the steady state of the pulse, it is obvious that they are below 0.7 ° and they are further reduced by averaging for comparing different settings of the shorting plunger. Taking into account the end of the turn on and the start of the turn off phase, a continuous phase change $\Delta\varphi_{dyn}$ is observable, which is caused by the frequency change $\Delta f = f - F$ of the magnetron and the distance between directional coupler and position of the short $L \cong 0.15\ m$, for the diagrammed setup. By Taylor expansion of equation 4 the following result is obtained:

$$\Delta\varphi_{dyn}(f) = -\frac{360°}{c_0}2Lg_1\Delta f$$

$$g_1 = \left.\frac{\partial g}{\partial f}\right|_{f=F} = \frac{F}{\sqrt{F^2 - f_C^2}} \qquad 5$$

where F is the mean frequency of the magnetron in the steady state. Due to the additional time resolved frequency detection, this phase change can be predicted and so compensated. In the zoom box in Figure 7, the excellent working of this compensation is shown.

For the evaluation of the accuracy of the reflectometer in detecting the phase this measurement is performed for a bunch of setting of the shorting plunger. The detected phase change $\Delta\varphi_{refl}$ is diagrammed in dependence of the calculate phase change $\Delta\varphi_{dist}$ based on equation 4 with using the mean frequency F, shown at the top of Figure 8 (a). For a better estimation of the deviation, the difference between both results is plotted below. It is obvious, that the detection of the phase is excellent working over the whole range of 360 °. A more detailed view of the deviations leads to the accuracy limits of 0.7° in phase detection.

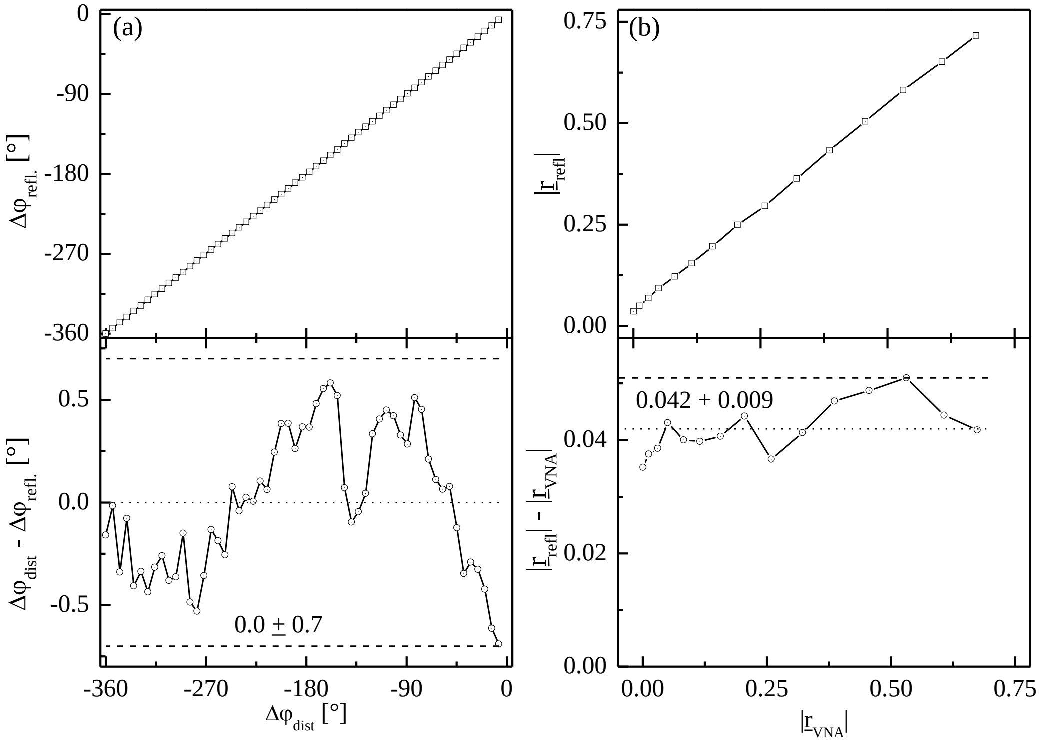

Figure 8. Diagrammed are the static results of the test measurements with the shorting plunger (a) and stub tuner (b). At the top the detected values are plotted in dependence of the expected and below the difference between them.

For determining the accuracy in detection the absolute value of the reflection coefficient $\left|\underline{r}_{refl}\right|$, the reflection of the stub tuner was varied between 6.5e-4 and 0.7 by changing the depth of one stub between minimum and maximum. Consider the whole scale of the obtained results. It is obvious that they well agree, even below the lower limit of the power calibration.

However, a small offset of 0.042 is observable, which is approximately constant and therefore not directly related to an error in the detection system. It is reasoned that a systemic error in the hardware setup causes this deviation, which is probably based on two effects. On the one hand, the directional coupler has to be addressed. Its cross coupling is only below -27 dB, which means that at maximum a quantity of 0.045 of the forwarded wave $\underline{a}_C$ is transmitted to the output $\underline{b}_C$, even if the load of the power line is perfectly matched and with it $\underline{b} = 0$. On the other hand, the not perfect termination of the stub tuner by the circulator combined with a water load is possible error source of the deviation. The measurement of the reflection of the termination with a vector network analyser shows a value of approximately 0.05. Both explanations can quantitatively explain the detected deviation and therefore it is hard to distinguish. In the case of the cross coupling, it would be in general possible to reduce this systemic error by applying a one port error model [23], which is usually used in low power vector network analysis [24]. The method is based on determine the error coefficients with different calibration standards, such as open, short, offset short and matched. To implement these calibration standards with a high precision is state of the art for low-level signals, below 1 W. However, for working in the high power range, where hollow waveguides are necessary to handle the power output of the magnetron, the implementation of some of these calibration loads is technological challenging. Therefore, for example a circulator with water load, with reflection coefficient of 0.05 is used as matched load in this experiment. In summary, the test of the detection of the absolute value of the reflection coefficient shows a good agreement to the measurements with the vector network analyser, with an error margin below 0.05.

To evaluate the time resolution of the reflectometer, measurements with a fast in-house developed switching mode power supply are performed. Due to optimisation of the power supply to fast rise times, the current ripple is quiet high, diagrammed in Figure 9.

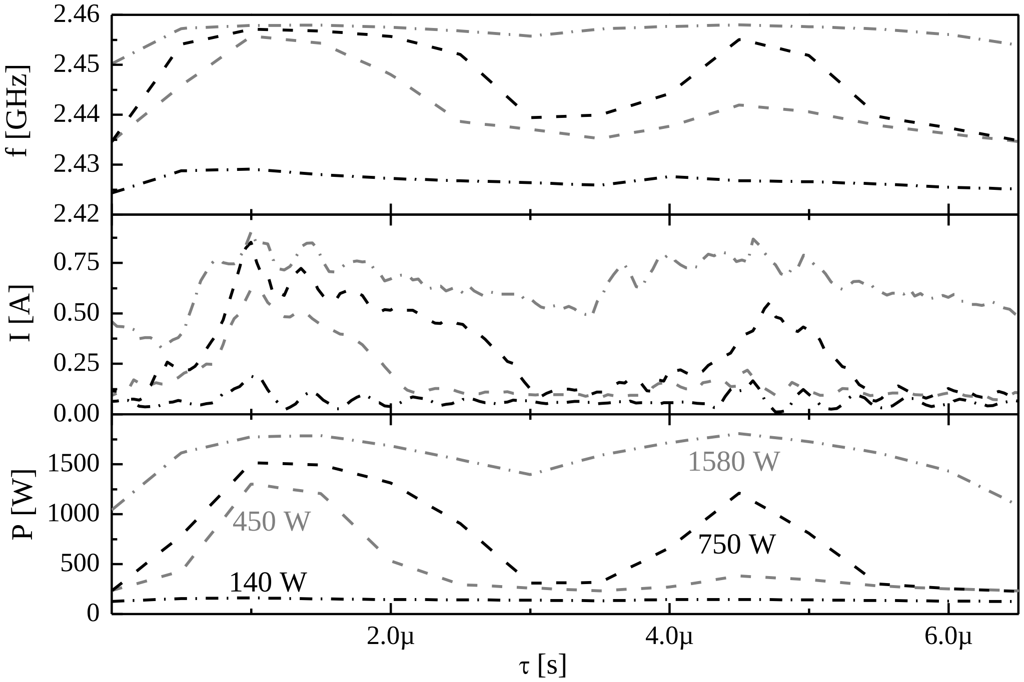

Figure 9. It shows the time dependent ripple of the magnetron frequency (at the top) and forwarded power (at the bottom), caused by the current ripple (in the middle) of the switching mode power supply, in the steady state. Working points between 140 W and 1580 W in average are displayed.

The ripple of the current is about 40 % for the maximum mean forwarded power of 1580 W and increases up to a maximum of 260 % for 450 W. The minimum achievable output power of the used 2 kW magnetron was 140 W, and the cycle duration of the full-bridge push-pull converter is around 6.8 µs. It is obvious, that for powers above 140 W a fluctuation in the detected microwave power is recognisable, and it perfectly follows the fluctuations of the driving current. Concerning the time resolved detection of the magnetron frequency there are two effects mentionable. First, the mean frequency of the magnetron changes with the mean power, starting by 2.427 GHz for a mean power of 140 W, ending by 2.457 GHz for 1580 W. This means by varying the driving current of the magnetron and with it the magnetron output power, the microwave frequency changes up to 30 MHz. Secondary, the magnetron frequency changes about 20 MHz during the cycle duration of the power supply, for mid power of 450 W and 750 W. Both effects, which are called frequency pushing [19, 25], are very meaningful to the matching of narrow-band loads with bandwidths below this 20 MHz, for example microwave cavities, which are used for atmospheric plasma sources [26, 27]. To use them in an optimal way, it has to be ensure, that the frequency fluctuation of the used microwave source is below the restriction of the matching. If this is not possible the frequency fluctuations of the magnetron can be reduced for instance by magnetron injection locking [28].

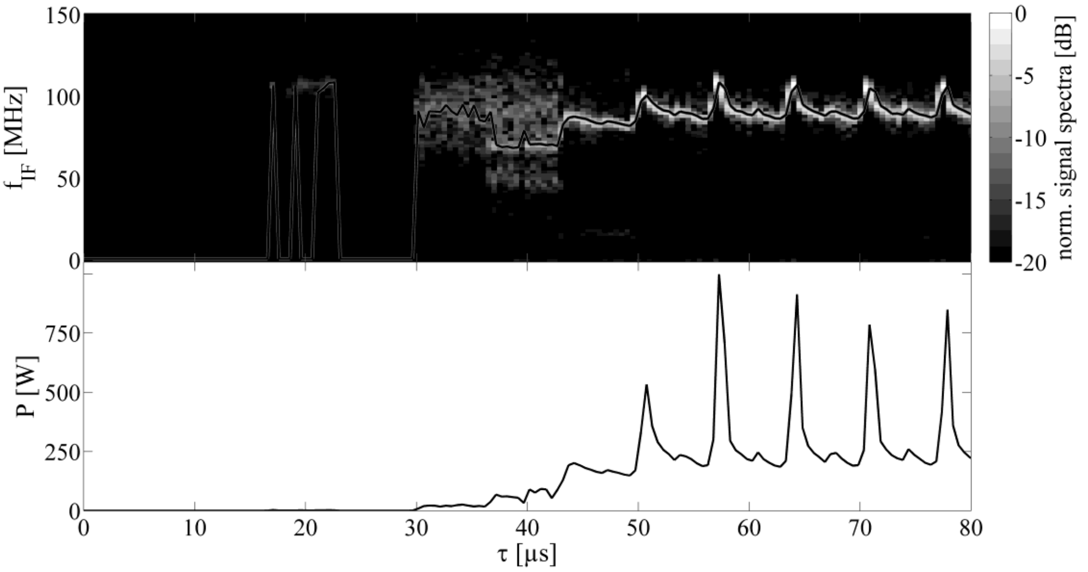

Figure 10. It shows the time dependent spectra of the intermediate signal corresponding to the magnetron, driven by a fast high ripple switching mode power supply, during the start-up (at the top). The black line, underlayed with a grey line, represents the obtained centre frequency. Below, the corresponding time dependent output power is diagrammed.

In addition, the start-up behaviour of the 450 W working point of the fast microwave setup is investigated, diagrammed in Figure 10. It is obvious, that the investigated time dependence of the start-up is related to the power supply. The typical start up times of oven magnetrons are in the range of 100 ns [29], therefore the much slower evolution has to be caused by the power supply. Concerning the development of the output power, a dead time of 30 µs is recognisable, which is followed by two cycles of the power supply (2 x 6.8 µs) with a very low output power. At 43 µs the first typical cycle shape appears with a reduced peak power and afterwards at 51 µs the start-up of the power supply is finished. Furthermore, the amplitude of the peak at beginning of each cycle varies during the start-up, until the steady state, shown in Figure 9, is reached. Regarding the time development of the signal spectra of the magnetron, a strong connection to the output power is observable. The dead time of 30 µs is also detectable as the two-cycle low output power phase. Due to the low power in this phase the spectra of the magnetron is very broad, which complicates the estimation of the centre frequency. With ending of the start-up and forming of the typical cycle shape at 43 µs, the signal spectra narrows and follows the modulation of the current, as it is shown in Figure 9. Concerning the estimation of the centre frequency after the start-up of the power supply, it is obvious that it works well and so the basic requirement to compensate phase fluctuations, which are caused by frequency changes, is fulfilled.

5. Conclusion

A reflectometer is presented for the time resolved detecting of the reflection coefficient in amplitude and phase, which is able to handle the fluctuation caused by the usage of a oven magnetron. Both the hardware setup of the modulation system, which is used to convert the radio frequency of 2.45 GHz to a more accessible intermediate frequency in the MHz-range, and the basic algorithm of the detection system, which is based on the quadrate amplitude demodulation and computes the directed powers and with it the complex reflection coefficient, are described.

After a power calibration with a vector network analyser as RF-signal source, measurements for testing the accuracy in phase and amplitude detection of the reflection coefficient are performed. In connection with the phase measurements continuous frequency changes during the turn on and off phase of the microwave source are detected, which causes phase deviations. These deviations are compensated, based on a Taylor expansion of the belonging formula and a precise detection of the time dependent frequency. However, the correct function of the reflectometer in detection the phase, with error margins below 0.7°, and the absolute value, with error margins below 0.05, of the reflection coefficient is verified.

To determine the time resolution of the reflectometer a power line was built up, which is driven by a fast high ripple switching mode power supply, and the results are compared to the detected current of the magnetron during the steady state. With a time resolution of 0.5 µs of the reflectometer, a fluctuation of the output power of magnetron, caused by fluctuation of the driving current during the cycle time of the switching mode power supply, is detected. Furthermore, a variation of the magnetron frequency, between 2.425 GHz and 2.455 GHz, with the output power, between 140 W and 1580 W, is observed. Additionally, the start-up behaviour of the high ripple power supply is investigated, by its output power and the signal spectra. Three phases are observed, starting with a dead time of 30 µs, which is followed by a low power output phase with very broad magnetron spectra ending at 43 µs. After an additional cycle of the power supply, in which the typical cycle shape appears, with a reduced peak power and narrowed spectra, the start-up is finished after 50 µs.

Thus, it had been shown that this new technique is very useful for the examination of the ignition process of microwave excited plasma sources [30] especially in combination with oven magnetrons.

6. References

[1] Jones D A, Lelyveld T P, Mavrofidis S D, Kingman S W and Miles N J "Microwave heating applications in environmental engineeringâ€"a review" *Resources, Conservation and Recycling* 2002 **34** 75-90

[2] Pipa A V, Andrasch M, Rackow K, Ehlbeck J and Weltmann K D "Observation of microwave volume plasma ignition in ambient air" *Plasma Sources Science & Technology* 2012 **21**

[3] Al-Shamma's A I, Wylie S R, Lucas J and Pau C F "Design and construction of a 2.45 GHz waveguide-based microwave plasma jet at atmospheric pressure for material processing" *Journal of Physics D-Applied Physics* 2001 **34** 2734-2741

[4] Leins M, Baumgartner K M, Walker M, Schulz A, Schumacher U and Stroth U "Studies on a Microwave-Heated Atmospheric Plasma Torch" *Plasma Processes and Polymers* 2007 **4** S493-S497

[5] Uhm H S, Kim J H and Hong Y C "Disintegration of water molecules in a steam-plasma torch powered by microwaves" *Physics of Plasmas* 2007 **14**

[6] Dani I, Mader G, Grabau P, Dresler B, Linaschke D, Lopez E, et al. "Atmospheric-Pressure Plasmas for Solar Cell Manufacturing" *Contributions to Plasma Physics* 2009 **49** 662-670

[7] Roussy G, Rochas J-F, Vuillot D and Debard C "A critical look at permittivity and permeability measurement methods in waveguide. An elementary data fusion approach" *The Journal of microwave power and electromagnetic energy : a publication of the International Microwave Power Institute* 2009 **43** 28-35

[8] Ju Y, Ohno Y, Soyama H and Saka M "Electrical characterization of doped silicon using high-frequency electromagnetic waves" *Journal of Materials Science & Technology* 2004 **20** 123-124

[9] Anderson R and Dennison O "An Advanced Network Analyzer for Sweep-Measuring Amplitude and Phase from 0.1 to 12.4 GHz" *Hewlett-Packard Journal* 1967 **2**

[10] Girbau D, Lazaro A and Pradell L "Characterization of dynamics and power handling of RF MEMS using vector measurement techniques" *Ieee Transactions on Microwave Theory and Techniques* 2004 **52** 2627-2633

[11] Fricke D "Precise Integrated Reflectometer for Cw and Pulsed Signals at 2.45 Ghz" *Journal of Microwave Power and Electromagnetic Energy* 1994 **29** 180-188

[12] Abou-Khousa M A, Baumgartner M A, Kharkovsky S and Zoughi R "Novel and Simple High-Frequency Single-Port Vector Network Analyzer" *Ieee Transactions on Instrumentation and Measurement* 2010 **59** 534-542

[13] Attiya A M "Three transmission-line transformers for phase retrieval from scalar reflection coefficients" *Microwave and Optical Technology Letters* 2004 **40** 231-235

[14] Moisan M, Zakrzewski Z, Etemadi R and Rostaing J C "Multitube surface-wave discharges for increased gas throughput at atmospheric pressure" *Journal of Applied Physics* 1998 **83** 5691-5701

[15] Samuel A L "An Oscillographic Method of Presenting Impedances on the Reflection-Coefficient Plane" *Proceedings of the Institute of Radio Engineers* 1947 **35** 1279-1283

[16] Engen G F "A (historical) review of the six-port measurement technique" *Microwave Theory and Techniques, IEEE Transactions on* 1997 **45** 2414-2417

[17] Adam S F "Microwave Instrumentation: An Historical Perspective" *Microwave Theory and Techniques, IEEE Transactions on* 1984 **32** 1157-1161

[18] Sobol H and Tomiyasu K "Milestones of microwaves" *Ieee Transactions on Microwave Theory and Techniques* 2002 **50** 594-611

[19] Gilmour A S *Microwave tubes*: Artech House, 1986

[20] Kim J I, Won J H, Park G S, Ha H J and Shon J C "Reduction of noise in strapped magnetron by electric priming using anode shape modification" *Applied Physics Letters* 2006 **88** -

[21] Werner M *Nachrichtentechnik*: Vieweg + Teubner, 2009

[22] Dwivedi V and Singh D "Electric Power Quality Monitoring (PQM) using Virtual Instrumentation" *Power Electronics Electrical Drives Automation and Motion (SPEEDAM), 2010 International Symposium on* 2010:431-436.

[23] Fitzpatrick J "Error Models for Systems Measurement" *Microwave Journal* 1978 **21** 63-66

[24] Hiebel M *Grundlagen der vektoriellen Netzwerkanalyse*: Rohde & Schwarz, 2005

[25] Tahir I, Dexter A and Carter R "Frequency and phase modulation performance of an injection-locked CW magnetron" *Ieee Transactions on Electron Devices* 2006 **53** 1721-1729

[26] Moisan M, Zakrzewski Z and Rostaing J C "Waveguide-based single and multiple nozzle plasma torches: the TIAGO concept" *Plasma Sources Science & Technology* 2001 **10** 387-394

[27] Rackow K, Ehlbeck J, Krohmann U and Baeva M "Microwave-based characterization of an atmospheric pressure microwave-driven plasma source for surface treatment" *Plasma Sources Science & Technology* 2011 **20**

[28] Pengvanich P, Neculaes V B, Lau Y Y, Gilgenbach R M, Jones M C, White W M, et al. "Modeling and experimental studies of magnetron injection locking" *Journal of Applied Physics* 2005 **98**

[29] Luginsland J W, Lau Y Y, Neculaes V B, Gilgenbach R M, Jones M C, Frese M H, et al. "Three-dimensional particle-in-cell simulations of rapid start-up in strapped oven magnetrons due to variation in the insulating magnetic field" *Applied Physics Letters* 2004 **84** 5425-5427

[30] Baeva M, Andrasch M, Ehlbeck J, Loffhagen D and Weltmann K-D "Temporally and spatially resolved characterization of microwave induced argon plasmas: Experiment and modeling" *Journal of Applied Physics* 2014 **115** 143301

Literaturverzeichnis

1. Hippler, R., Kersten, H., Schmidt, M., and Schoenbach, K.H., "*Low Temperature Plasmas: Fundamentals, Technologies and Techniques*". 2 ed. 2008: Wiley-VCH Verlag GmbH & Co. KGaA.

2. Weltmann, K.-D., Kindel, E., Woedtke, T.v., Hähnel, M., Stieber, M., and Brandenburg, R., "*Atmospheric-pressure plasma sources: Prospective tools for plasma medicine*". Pure and Applied Chemistry, 2010. **82**(6): p. 1223-1237.

3. Moisan, M. and Pelletier, J., "*Microwave Excited Plasmas*". 1992, The Netherlands: Elsevier Science Publishing.

4. Pott, A., Doerk, T., Uhlenbusch, J., Ehlbeck, J., Hoschele, J., and Steinwandel, J., "*Polarization-sensitive coherent anti-Stokes Raman scattering applied to the detection of NO in a microwave discharge for reduction of NO*". Journal of Physics D-Applied Physics, 1998. **31**(19): p. 2485-2498.

5. Baeva, M., Gier, H., Pott, A., Uhlenbusch, J., Hoschele, J., and Steinwandel, J., "*Studies on gas purification by a pulsed microwave discharge at 2.46 GHz in mixtures of N-2/NO/O-2 at atmospheric pressure*". Plasma Chemistry and Plasma Processing, 2001. **21**(2): p. 225-247.

6. Rousseau, A., Dantier, A., Gatilova, L., Ionikh, Y., Ropcke, J., and Tolmachev, Y., "*On NOx production and volatile organic compound removal in a pulsed microwave discharge in air*". Plasma Sources Science & Technology, 2005. **14**(1): p. 70-75.

7. Leins, M., Alberts, L., Kaiser, M., Walker, M., Schulz, A., Schumacher, U., and Stroth, U., "*Development and Characterisation of a Microwave-heated Atmospheric Plasma Torch*". Plasma Processes and Polymers, 2009. **6**: p. S227-S232.

8. Babaritskii, A.I., Gerasimov, E.N., Demkin, S.A., Zhivotov, V.K., Knizhnik, A.A., Potapkin, B.V., Rusanov, V.D., Ryazantsev, E.I., Smirnov, R.V., and Sholin, G.V., "*The repetitive microwave discharge as a catalyst for a chemical reaction*". Technical Physics, 2000. **45**(11): p. 1411-1416.

9. Rusanov, V.D., Babaritskii, A.I., Bibikov, M.B., Gerasimov, E.N., Zhivotov, V.K., Knizhnik, A.A., Potapkin, B.V., and Smirnov, R.V., "*Properties of a catalytically active pulsed microwave discharge at atmospheric pressure*". Doklady Physics, 2001. **46**(4): p. 242-246.

10. Hong, Y.C., Cho, S.C., Bang, C.U., Shin, D.H., Kim, J.H., Uhm, H.S., and Yi, W.J., "*Microwave plasma burner and temperature measurements in its flames*". Applied Physics Letters, 2006. **88**(20).

11. Hemawan, K.W., Wichman, I.S., Lee, T., Grotjohn, T.A., and Asmussen, J., "*Compact microwave re-entrant cavity applicator for plasma-assisted combustion".* Review of Scientific Instruments, 2009. **80**(5).

12. Uhm, H.S., Kim, J.H., and Hong, Y.C., "*Disintegration of water molecules in a steam-plasma torch powered by microwaves".* Physics of Plasmas, 2007. **14**(7).

13. Al-Shamma's, A.I., Wylie, S.R., Lucas, J., and Pau, C.F., "*Design and construction of a 2.45 GHz waveguide-based microwave plasma jet at atmospheric pressure for material processing".* Journal of Physics D-Applied Physics, 2001. **34**(18): p. 2734-2741.

14. Heinlin, J., Morfill, G., Landthaler, M., Stolz, W., Isbary, G., Zimmermann, J.L., Shimizu, T., and Karrer, S., "*Plasma medicine: possible applications in dermatology".* JDDG: Journal der Deutschen Dermatologischen Gesellschaft, 2010. **8**(12): p. 968-976.

15. Gesche, R., Kuhn, S., and Andrei, C., "*Plasma ignition in a quarter-wavelength microwave slot resonator".* Journal of Physics D-Applied Physics, 2008. **41**(19).

16. Kiss'ovski, Z., Kolev, M., Ivanov, A., Lishev, S., and Koleva, I., "*Small surface wave discharge at atmospheric pressure".* Journal of Physics D-Applied Physics, 2009. **42**(18).

17. Kim, J. and Terashima, K., "*2.45 GHz microwave-excited atmospheric pressure air microplasmas based on microstrip technology".* Applied Physics Letters, 2005. **86**(19).

18. Narendra, J.J., Grotjohn, T.A., and Asmussen, J., "*Microstripline applicators for creating microplasma discharges with microwave energy".* Plasma Sources Science & Technology, 2008. **17**(3).

19. Hoskinson, A.R. and Hopwood, J., "*A two-dimensional array of microplasmas generated using microwave resonators".* Plasma Sources Science and Technology, 2012. **21**(5): p. 052002.

20. Yuji, T., Fujii, S., Mungkung, N., and Akatsuka, H., "*Optical Emission Characteristics of Atmospheric-Pressure Nonequilibrium Microwave Discharge and High-Frequency DC Pulse Discharge Plasma Jets".* Ieee Transactions on Plasma Science, 2009. **37**(6): p. 839-845.

21. Gessel, A.F.H.v., Carbone, E.A.D., Bruggeman, P.J., and Mullen, J.J.A.M.v.d., "*Laser scattering on an atmospheric pressure plasma jet: disentangling Rayleigh, Raman and Thomson scattering".* Plasma Sources Science and Technology, 2012. **21**(1): p. 015003.

22. Schopp, C., Nachtrodt, F., Heuermann, H., Scherer, U.W., Mostacci, D., Finger, T., and Tietsch, W., "*A novel 2.45 GHz/200 W Microwave Plasma Jet for High Temperature Applications above 3600 K".* Journal of Physics: Conference Series, 2012. **406**(1): p. 012029.

23. Stonies, R., Schermer, S., Voges, E., and Broekaert, J.A.C., "*A new small microwave plasma torch"*. Plasma Sources Science & Technology, 2004. **13**(4): p. 604-611.

24. Iza, F. and Hopwood, J.A., "*Low-power microwave plasma source based on a microstrip split-ring resonator"*. Ieee Transactions on Plasma Science, 2003. **31**(4): p. 782-787.

25. Iza, F. and Hopwood, J., "*Split-ring resonator microplasma: microwave model, plasma impedance and power efficiency"*. Plasma Sources Science & Technology, 2005. **14**(2): p. 397-406.

26. Gregorio, J., Leroy, O., Leprince, P., Alves, L.L., and Boisse-Laporte, C., "*Design of a Microwave Microplasma Source at Atmospheric Pressure"*. Ieee Transactions on Plasma Science, 2009. **37**(6): p. 797-808.

27. Gregorio, J., Alves, L.L., Leroy, O., Leprince, P., and Boisse-Laporte, C., "*Microwave microplasma sources based on microstrip-like transmission lines"*. European Physical Journal D, 2010. **60**(3): p. 627-635.

28. Lebedev, Y.A., "*Microwave discharges: generation and diagnostics"*. Journal of Physics: Conference Series, 2010. **257**(1): p. 012016.

29. Schlüter, H. and Shivarova, A., "*Travelling-wave-sustained discharges"*. Physics Reports, 2007. **443**(4–6): p. 121-255.

30. Chabert, P., Rousseau, A., Gousset, G., and Leprince, P., "*The influence of the gas velocity on dissociation degree and gas temperature in a flowing microwave hydrogen discharge"*. Journal of Applied Physics, 1998. **84**(1): p. 161-167.

31. Hübner, S., Palomares, J.M., Carbone, E.A.D., and Mullen, J.J.A.M.v.d., "*A power pulsed low-pressure argon microwave plasma investigated by Thomson scattering: evidence for molecular assisted recombination"*. Journal of Physics D: Applied Physics, 2012. **45**(5): p. 055203.

32. Jimenez-Diaz, M., Carbone, E.A.D., Dijk, J.v., and Mullen, J.J.A.M.v.d., "*A two-dimensional Plasimo multiphysics model for the plasma–electromagnetic interaction in surface wave discharges: the surfatron source"*. Journal of Physics D: Applied Physics, 2012. **45**(33): p. 335204.

33. Moisan, M., Zakrzewski, Z., Pantel, R., and Leprince, P., "*A Waveguide-Based Launcher to Sustain Long Plasma Columns through the Propagation of an Electromagnetic Surface Wave"*. Plasma Science, IEEE Transactions on, 1984. **12**(3): p. 203-214.

34. Fleisch, T., Kabouzi, Y., Moisan, M., Pollak, J., Castanos-Martinez, E., Nowakowska, H., and Zakrzewski, Z., "*Designing an efficient microwave-plasma source, independent of operating conditions, at atmospheric pressure"*. Plasma Sources Science & Technology, 2007. **16**(1): p. 173-182.

35. Castanos-Martinez, E., Moisan, M., and Kabouzi, Y., "*Achieving non-contracted and non-filamentary rare-gas tubular discharges at atmospheric pressure".* Journal of Physics D-Applied Physics, 2009. **42**(1).

36. Moisan, M., Pantel, R., and Hubert, J., "*Propagation of a Surface-Wave Sustaining a Plasma-Column at Atmospheric-Pressure".* Contributions to Plasma Physics, 1990. **30**(2): p. 293-314.

37. Moisan, M., Zakrzewski, Z., Etemadi, R., and Rostaing, J.C., "*Multitube surface-wave discharges for increased gas throughput at atmospheric pressure".* Journal of Applied Physics, 1998. **83**(11): p. 5691-5701.

38. Zajickova, L., Elias, M., Jasek, O., Kudrle, V., Frgala, Z., Matejkova, J., Bursik, J., and Kadlecikova, M., "*Atmospheric pressure microwave torch for synthesis of carbon nanotubes".* Plasma Physics and Controlled Fusion, 2005. **47**: p. B655-B666.

39. Leins, M., Baumgartner, K.M., Walker, M., Schulz, A., Schumacher, U., and Stroth, U., "*Studies on a Microwave-Heated Atmospheric Plasma Torch".* Plasma Processes and Polymers, 2007. **4**: p. S493-S497.

40. Leins, M., Kopecki, J., Gaiser, S., Schulz, A., Walker, M., Schumacher, U., Stroth, U., and Hirth, T., "*Microwave Plasmas at Atmospheric Pressure".* Contributions to Plasma Physics, 2014. **54**(1): p. 14-26.

41. Moisan, M., Zakrzewski, Z., and Rostaing, J.C., "*Waveguide-based single and multiple nozzle plasma torches: the TIAGO concept".* Plasma Sources Science & Technology, 2001. **10**(3): p. 387-394.

42. Potts, H. and Hugill, J., "*Studies of high-pressure, partially ionized plasma generated by 2.45 GHz microwaves".* Plasma Sources Science & Technology, 2000. **9**(1): p. 18-24.

43. Cook, A., Shapiro, M., and Temkin, R., "*Pressure dependence of plasma structure in microwave gas breakdown at 110 GHz".* Applied Physics Letters, 2010. **97**(1).

44. Ehlbeck, J., Ohl, A., Maass, M., Krohmann, U., and Neumann, T., "*Moving atmospheric microwave plasma for surface and volume treatment".* Surface & Coatings Technology, 2003. **174**: p. 493-497.

45. Rackow, K., Ehlbeck, J., Krohmann, U., and Baeva, M., "*Microwave-based characterization of an atmospheric pressure microwave-driven plasma source for surface treatment".* Plasma Sources Science & Technology, 2011. **20**(3).

46. Ehlbeck, J., Brandenburg, R., von Woedtke, T., Krohmann, U., Stieber, M., and Weltmann, K.-D., "*Plasmose - antimicrobial effects of modular atmospheric plasma sources".* GMS Krankenhaushygiene Interdisziplinär, 2008. **3**.

47. Krohmann, U., Neumann, T., Ehlbeck, J., and Rackow, K. "*Method and device for igniting and generating an expanding diffuse mircowave Plasma and method and device for Plasma treating surfaces and substances by using this plasma".*Pub. No. **US8232728 B2** (2012-07-31)

48. Ehlbeck, J., Schnabel, U., Polak, M., Winter, J., Woedtke, T.v., Brandenburg, R., Hagen, T.v.d., and Weltmann, K.-D., "*Low temperature atmospheric pressure plasma sources for microbial decontamination".* Journal of Physics D: Applied Physics, 2011. **44**(1): p. 013002.

49. Krohmann, U., Ehlbeck, J., Neumann, T., Schnabel, U., Andrasch, M., Lehmann, W., and Weltmann, K.-D. "*Plasma-generated gas sterilization method ".*Pub. No. **EP2566524 A1** (2013-03-13)

50. Schnabel, U., Niquet, R., Krohmann, U., Winter, J., Schluter, O., Weltmann, K.D., and Ehlbeck, J., "*Decontamination of Microbiologically Contaminated Specimen by Direct and Indirect Plasma Treatment".* Plasma Processes and Polymers, 2012. **9**(6): p. 569-575.

51. Siche, D., Gogova, D., Lehmann, S., Fizia, T., Fornari, R., Andrasch, M., Pipa, A., and Ehlbeck, J., "*PVT growth of GaN bulk crystals".* Journal of Crystal Growth, 2011. **318**(1): p. 406-410.

52. Maruska, H.P. and Tietjen, J.J., "*Preparation and Properties of Vapor-Deposited Single-Crystalline Gan".* Applied Physics Letters, 1969. **15**(10): p. 327-&.

53. Fujito, K., Kubo, S., Nagaoka, H., Mochizuki, T., Namita, H., and Nagao, S., "*Bulk GaN crystals grown by HVPE".* Journal of Crystal Growth, 2009. **311**(10): p. 3011-3014.

54. Baeva, M., Bösel, A., Ehlbeck, J., and Loffhagen, D., "*Modeling of microwave-induced plasma in argon at atmospheric pressure".* Physical Review E, 2012. **85**(5): p. 056404.

55. Schafer, J., Vasina, P., Hnilica, J., Foest, R., Kudrle, V., and Weltmann, K.D., "*Visualization of Revolving Modes in RF and MW Nonthermal Atmospheric Pressure Plasma Jets".* Ieee Transactions on Plasma Science, 2011. **39**(11): p. 2350-2351.

56. Kim, K.S. and Kim, S.H., "*Epitaxial growth of GaN using reactive neutrals extracted from the nitrogen Helicon wave plasma".* Journal of Vacuum Science & Technology a-Vacuum Surfaces and Films, 2000. **18**(6): p. 2847-2853.

57. Myoung, J.M., Gluschenkov, O., Kim, K., and Kim, S., "*Growth kinetics of GaN and effects of flux ratio on the properties of GaN films grown by plasma-assisted molecular beam epitaxy".* Journal of Vacuum Science & Technology a-Vacuum Surfaces and Films, 1999. **17**(5): p. 3019-3028.

58. Ehlbeck, J., Andrasch, M., Schnabel, U., Rackow, K., Neumann, T., Krohmann, U., Weltmann, K.-D., Großjohann, B., Braun, D., Klein, M., and Schultz, G.,

"*Dekontamination von Primärverpackungen mittels Atmosphärendruckplasmen"*. Vakuum in Forschung und Praxis, 2010. **22**(5): p. 10-16.

59. Pehl, E., "*Mikrowellentechnik Band 1"*. 1984, Heidelberg: Dr. Alfred Hüthig Verlag GmbH.

60. Kummer, M., "*Grundlagen der Mikrowellentechnik"*. 1984, Berlin: VEB Verlag Technik.

61. Pipa, A.V., Andrasch, M., Rackow, K., Ehlbeck, J., and Weltmann, K.D., "*Observation of microwave volume plasma ignition in ambient air"*. Plasma Sources Science & Technology, 2012. **21**(3).

62. Hutchinson, I.H., "*Principles of plasma diagnostics"*. 2002: Cambridge University Press.

63. Manos, D.M., Cecchi, J.L., Cheah, C.W., and Dylla, H.F., "*Diagnostics of Low-Temperature Plasmas - the Electron Component"*. Thin Solid Films, 1991. **195**(1-2): p. 319-336.

64. Chung, P.M., Talbot, L., and Touryan, K.J., "*Electric probes in stationary and flowing plasmas: Theory and application"*. 1975: Springer New Yourk.

65. Cherrington, B.E., "*The use of electrostatic probes for plasma diagnostics—A review"*. Plasma Chemistry and Plasma Processing, 1982. **2**(2): p. 113-140.

66. Hannemann, M. and Sigeneger, F., "*Langmuir probe measurements at incomplete rf-compensation"*. Czechoslovak Journal of Physics, 2006. **56**: p. B740-B748.

67. Stenzel, R.L., "*Microwave Resonator Probe for Localized Density-Measurements in Weakly Magnetized Plasmas"*. Review of Scientific Instruments, 1976. **47**(5): p. 603-607.

68. Piejak, R.B., Godyak, V.A., Garner, R., Alexandrovich, B.M., and Sternberg, N., "*The hairpin resonator: A plasma density measuring technique revisited"*. Journal of Applied Physics, 2004. **95**(7): p. 3785-3791.

69. Lapke, M., Oberrath, J., Schulz, C., Storch, R., Styrnoll, T., Zietz, C., Awakowicz, P., Brinkmann, R.P., Musch, T., Mussenbrock, T., and Rolfes, I., "*The multipole resonance probe: characterization of a prototype"*. Plasma Sources Science & Technology, 2011. **20**(4): p. 042001.

70. Styrnoll, T., Harhausen, J., Lapke, M., Storch, R., Brinkmann, R.P., Foest, R., Ohl, A., and Awakowicz, P., "*Process diagnostics and monitoring using the multipole resonance probe in an inhomogeneous plasma for ion-assisted deposition of optical coatings"*. Plasma Sources Science and Technology, 2013. **22**(4): p. 045008.

71. Hubner, S., Palomares, J.M., Carbone, E.A.D., and van der Mullen, J., "*A power pulsed low-pressure argon microwave plasma investigated by Thomson scattering:*

evidence for molecular assisted recombination". Journal of Physics D-Applied Physics, 2012. **45**(5): p. 055203.

72. Yubero, C., Garcia, M.C., and Calzada, M.D., "*On the use of the H alpha spectral line to determine the electron density in a microwave (2.45GHz) plasma torch at atmospheric pressure".* Spectrochimica Acta Part B-Atomic Spectroscopy, 2006. **61**(5): p. 540-544.

73. Torres, J., Palomares, J.M., Sola, A., van Dermullen, J.J.A.M., and Gamero, A., "*A Stark broadening method to determine simultaneously the electron temperature and density in high-pressure microwave plasmas".* Journal of Physics D-Applied Physics, 2007. **40**(19): p. 5929-5936.

74. Heald, M.A. and Wharton, C.B., "*Plasma Diagnostics with Microwaves".* 1965, New York: Wiley.

75. Stix, T.H., "*Waves in Plasmas".* 1992, New York: Amercan Institute of Physics.

76. Hartfuss, H.J., Geist, T., and Hirsch, M., "*Heterodyne methods in millimetre wave plasma diagnostics with applications to ECE, interferometry and reflectometry".* Plasma Physics and Controlled Fusion, 1997. **39**(11): p. 1693-1769.

77. Ehlbeck, J., Rackow, K., Andrasch, M., and Weltmann, K.D., "*Electron Density Determination by Means of Tuneable 50 GHz and 150 GHz Interferometers".* Contributions to Plasma Physics, 2011. **51**(2-3): p. 131-136.

78. Howlader, M.K., Yang, Y.Q., and Roth, J.R., "*Time-resolved measurements of electron number density and collision frequency for a fluorescent lamp plasma using microwave diagnostics".* Ieee Transactions on Plasma Science, 2005. **33**(3): p. 1093-1099.

79. Dittmann, K., Küllig, C., and Meichsner, J., "*160 GHz Gaussian beam microwave interferometry in low-density rf plasmas".* Plasma Sources Science and Technology, 2012. **21**(2): p. 024001.

80. Lukas, C., Muller, M., Schulz-von der Gathen, V., and Dobele, H.F., "*Spatially resolved electron density distribution in an RF excited parallel plate plasma reactor by 1 mm microwave interferometry".* Plasma Sources Science & Technology, 1999. **8**(1): p. 94-99.

81. Andrasch, M., Ehlbeck, J., and Weltmann, K.-D., "*Influence of the dielectric surrounding of plasma on the electron density measurement by microwave interferometer".* Measurement Science and Technology, 2014. **25**(7): p. 075004.

82. Goldsmith, P.F., "*Gaussian Beam Quasioptical Propagation and Applications".* 1998: IEEE.

83. Zakrzewski, Z., Moisan, M., Margot, J., and Sauve, G., "*Spatial distributions of electron density and electric field in discharges sustained within microwave circuits"*. Plasma Sources Science & Technology, 1992. **1**(1): p. 28-35.

84. Mansfield, C.D. and Rutt, H.N., "*Evaluation of multiple beam interference effects in infrared gas spectroscopy"*. Measurement Science & Technology, 1999. **10**(3): p. 206-210.

85. Masiyano, D., Hodgkinson, J., and Tatam, R.P., "*Use of diffuse reflections in tunable diode laser absorption spectroscopy: implications of laser speckle for gas absorption measurements"*. Applied Physics B-Lasers and Optics, 2008. **90**(2): p. 279-288.

86. Wysocki, G., Curl, R.F., Tittel, F.K., Maulini, R., Bulliard, J.M., and Faist, J., "*Widely tunable mode-hop free external cavity quantum cascade laser for high resolution spectroscopic applications"*. Applied Physics B-Lasers and Optics, 2005. **81**(6): p. 769-777.

87. Andrasch, M., Ehlbeck, J., Foest, R., and Weltmann, K.-D., "*Electron density measurements on an inductively coupled plasma with a one-port microwave interferometer"*. Plasma Sources Science and Technology, 2012. **21**(5): p. 055032.

88. Cunge, G., Crowley, B., Vender, D., and Turner, M.M., "*Characterization of the E to H transition in a pulsed inductively coupled plasma discharge with internal coil geometry: bi-stability and hysteresis"*. Plasma Sources Science & Technology, 1999. **8**(4): p. 576-586.

89. Turner, M.M. and Lieberman, M.A., "*Hysteresis and the E-to-H transition in radiofrequency inductive discharges"*. Plasma Sources Science and Technology, 1999. **8**(2): p. 313.

90. Malyshev, M.V. and Donnelly, V.M., "*Diagnostics of inductively coupled chlorine plasmas: Measurement of electron and total positive ion densities"*. Journal of Applied Physics, 2001. **90**(3): p. 1130-1137.

91. Alves, L.L., "*Fluid modelling of the positive column of direct-current glow discharges"*. Plasma Sources Science & Technology, 2007. **16**(3): p. 557-569.

92. Chevolleau, T. and Fukarek, W., "*Ion flux, ion energy distribution and neutral density in an inductively coupled argon discharge"*. Plasma Sources Science & Technology, 2000. **9**(4): p. 568-573.

93. Jones, D.A., Lelyveld, T.P., Mavrofidis, S.D., Kingman, S.W., and Miles, N.J., "*Microwave heating applications in environmental engineeringâ€”a review"*. Resources, Conservation and Recycling, 2002. **34**(2): p. 75-90.

94. Dani, I., Mader, G., Grabau, P., Dresler, B., Linaschke, D., Lopez, E., Kaskel, S., and Beyer, E., "*Atmospheric-Pressure Plasmas for Solar Cell Manufacturing"*. Contributions to Plasma Physics, 2009. **49**(9): p. 662-670.

95. Ju, Y., Ohno, Y., Soyama, H., and Saka, M., "*Electrical characterization of doped silicon using high-frequency electromagnetic waves"*. Journal of Materials Science & Technology, 2004. **20**: p. 123-124.

96. Roussy, G., Rochas, J.-F., Vuillot, D., and Debard, C., "*A critical look at permittivity and permeability measurement methods in waveguide. An elementary data fusion approach"*. The Journal of microwave power and electromagnetic energy : a publication of the International Microwave Power Institute, 2009. **43**(4): p. 28-35.

97. Anderson, R. and Dennison, O., "*An Advanced Network Analyzer for Sweep-Measuring Amplitude and Phase from 0.1 to 12.4 GHz"*. Hewlett-Packard Journal, 1967. **2**.

98. Fricke, D., "*Precise Integrated Reflectometer for Cw and Pulsed Signals at 2.45 Ghz"*. Journal of Microwave Power and Electromagnetic Energy, 1994. **29**(3): p. 180-188.

99. Abou-Khousa, M.A., Baumgartner, M.A., Kharkovsky, S., and Zoughi, R., "*Ka-Band Vector Reflectometer Based on Simple Phase-Shifter Design"*. Ieee Transactions on Instrumentation and Measurement, 2011. **60**(2): p. 618-624.

100. Attiya, A.M., "*Three transmission-line transformers for phase retrieval from scalar reflection coefficients"*. Microwave and Optical Technology Letters, 2004. **40**(3): p. 231-235.

101. Samuel, A.L., "*An Oscillographic Method of Presenting Impedances on the Reflection-Coefficient Plane"*. Proceedings of the Institute of Radio Engineers, 1947. **35**(11): p. 1279-1283.

102. Adam, S.F., "*Microwave Instrumentation: An Historical Perspective"*. Microwave Theory and Techniques, IEEE Transactions on, 1984. **32**(9): p. 1157-1161.

103. Engen, G.F., "*A (historical) review of the six-port measurement technique"*. Microwave Theory and Techniques, IEEE Transactions on, 1997. **45**(12): p. 2414-2417.

104. Sobol, H. and Tomiyasu, K., "*Milestones of microwaves"*. Ieee Transactions on Microwave Theory and Techniques, 2002. **50**(3): p. 594-611.

105. Andrasch, M., Ehlbeck, J., and Weltmann, K.-D., "*A heterodyne reflectometer for detection the time dependent complex reflection coefficient, optimised for the usage with oven magnetron"*. Maesurement Science and Technology, 2014.

106. Luginsland, J.W., Lau, Y.Y., Neculaes, V.B., Gilgenbach, R.M., Jones, M.C., Frese, M.H., and Watrous, J.J., "*Three-dimensional particle-in-cell simulations of rapid start-up in strapped oven magnetrons due to variation in the insulating magnetic field"*. Applied Physics Letters, 2004. **84**(26): p. 5425-5427.

107. Gilmour, A.S., "*Microwave tubes"*. 1986: Artech House.

108. Tahir, I., Dexter, A., and Carter, R., "*Frequency and phase modulation performance of an injection-locked CW magnetron"*. Ieee Transactions on Electron Devices, 2006. **53**(7): p. 1721-1729.

109. Dwivedi, V. and Singh, D. "*Electric Power Quality Monitoring (PQM) using Virtual Instrumentation"*. in *Power Electronics Electrical Drives Automation and Motion (SPEEDAM), 2010 International Symposium on*. 2010.

110. Werner, M., "*Nachrichtentechnik"*. 2009: Vieweg + Teubner.

111. Baeva, M., Andrasch, M., Ehlbeck, J., Loffhagen, D., and Weltmann, K.-D., "*Temporally and spatially resolved characterization of microwave induced argon plasmas: Experiment and modeling"*. Journal of Applied Physics, 2014. **115**(14): p. 143301.

112. Zwierz, R., Golka, S., Kachel, K., Siche, D., Fornari, R., Sennikov, P., Vodopyanov, A., and Pipa, A.V., "*Plasma enhanced growth of GaN single crystalline layers from Ga vapour"*. Crystal Research and Technology, 2013. **48**(4): p. 186-192.

113. Dwiliński, R., Doradziński, R., Garczyński, J., Sierzputowski, L.P., Puchalski, A., Kanbara, Y., Yagi, K., Minakuchi, H., and Hayashi, H., "*Excellent crystallinity of truly bulk ammonothermal GaN"*. Journal of Crystal Growth, 2008. **310**(17): p. 3911-3916.

114. Schnabel, U., Andrasch, M., Weltmann, K.-D., and Ehlbeck, J., "*Inactivation of Vegetative Microorganisms and Bacillus atrophaeus Endospores by Reactive Nitrogen Species (RNS)"*. Plasma Processes and Polymers, 2014. **11**(2): p. 110-116.